NUMERICAL MODELING OF UNSTABLE ROCK FAILURE

by

Amin <u>Manouchehrian</u>

A thesis submitted in partial fulfillment
of the requirements for the degree of
Doctor of Philosophy (PhD) in Natural Resources Engineering

The Faculty of Graduate Studies
Laurentian University
Sudbury, Ontario, Canada

THESIS DEFENCE COMMITTEE/COMITÉ DE SOUTENANCE DE THÈSE
Laurentian Université/Université Laurentienne
Faculty of Graduate Studies/Faculté des études supérieures

Title of Thesis
Titre de la thèse NUMERICAL MODELING OF ROCKBURST IN DEEP TUNNELS

Name of Candidate
Nom du candidat Manouchehrian, Seyed Mohammad Amin

Degree
Diplôme Doctor of Philosophy

Department/Program   Date of Defence
Département/Programme PhD Natural Resources Engineering   Date de la soutenance September 23, 2016

APPROVED/APPROUVÉ

Thesis Examiners/Examinateurs de thèse:

Dr. Ming Cai
(Co-supervisor/Co-directeur(trice) de thèse)

Dr. Peter Kaiser
(Co-supervisor/Co-directeur(trice) de thèse)

Dr. Shailendra Sharan
(Committee member/Membre du comité)

Dr. Krishna Challagulla
(Committee member/Membre du comité)

Approved for the Faculty of Graduate Studies
Approuvé pour la Faculté des études supérieures
Dr. Shelley Watson
Madame Shelley Watson

Dr. Bibhu Mohanty   Acting Dean, Faculty of Graduate Studies
(External Examiner/Examinateur externe)   Doyenne intérimaire, Faculté des études supérieures

Dr. Graeme Spiers
(Internal Examiner/Examinateur interne)

ACCESSIBILITY CLAUSE AND PERMISSION TO USE

Abstract

Rockburst is an unstable and violent rock failure and it is a hazardous problem in deep underground mines and civil tunnels; it imposes a great danger to safety of workers and investment. Many factors that influence rockburst damage have been identified. In many rockburst case histories, the presence of geological structures such as faults, shear zones, joints, and dykes has been observed near excavation boundaries but their role in rockburst occurrence is still not fully understood. A good understanding of the role of geological structures on rockburst damage is important to anticipate and control rockbursts and constitutes the focus of this thesis.

In this research an explicit finite element tool (Abaqus-Explicit) is employed to study unstable rock failure and rockburst processes. First, uniaxial compression tests were simulated to confirm the suitability of the adopted numerical tool for simulating unstable rock failures. Two indicators namely Loading System Reaction Intensity (LSRI) and the maximum unit kinetic energy (KE_{max}) were proposed to distinguish between stable and unstable failures in laboratory testing conditions. Unstable rock failures under polyaxial unloading conditions were also simulated. The influences of loading system stiffness, specimen's height to width ratio, and intermediate principal stress on rock failure were investigated.

Next, material heterogeneity (in terms of strength and deformability) was introduced into the models using Python scripting to enhance the efficiency of Abaqus for modeling geomaterials. Numerical simulation results showed that heterogeneous models resulted in more realistic failure modes than homogeneous models. The effect of material heterogeneity on rock failure intensity in unconfined and confined compression tests was investigated. It was observed that when two

materials have the same peak strength, the heterogeneous model had more released energy than the homogeneous model due to differences in the failure mode. The tensile splitting failure mode of the heterogeneous model released more energy than the shear failure mode of the homogeneous model.

Then, the role of geological weak planes on rockburst occurrence and damage near the boundary of tunnels was studied using 2D models. Initially, a tunnel without any adjacent weak plane was modeled. Then a fault with different lengths, inclinations, and distances to the tunnel was added to the models and its effect on rock failure was simulated. The velocity and the released kinetic energy of failed rocks, the failure zone around the tunnel, and the deformed mesh were studied to identify stable and unstable rock failures. The simulation results showed that the presence of a fault near a tunnel could induce rockburst if the fault is positioned and oriented in such a way that it promotes high stress and low local loading system stiffness.

Finally, a rockburst that occurred in the Jinping II drainage tunnel in China with an observed nearby fault was simulated. The modeling results captured the field observation of rockburst damage and confirmed that the presence of weak planes in the vicinity of deep tunnels is a necessary condition for the occurrence of rockburst. The finding from this research constitutes a better understanding of unstable rock failures in both laboratory and in situ. The insights gained from this research can be useful for rockburst anticipation and control during mining and tunneling in highly stressed grounds.

Keywords

Unstable rock failure; Rockburst; Heterogeneity; Tensile failure; Confinement; Unloading; polyaxial compression; Released kinetic energy; Tunnel; Geological structures; Case study.

Original Contributions

This thesis aims at making contributions for an improved understanding of rockbursts in deep tunnels. Several challenging issues are addressed and new methods developed, and the results are presented in respective chapters. Major contributions of the thesis are listed below:

(1) Affirmation of using the Abaqus-Explicit code to study unstable rock failure and rockburst processes (Chapter 3).

(2) Development of a new index for identifying unstable rock failure in laboratory test simulations (Chapter 3).

(3) Investigation of the influence of loading system stiffness, specimen's height to width ratio and intermediate principal stress on rock failure intensity and rock failure mechanisms under polyaxial unloading conditions using numerical modelling (Chapter 3).

(4) Extension of the suitability of Abaqus-Explicit to model geomaterials by adding material heterogeneity into the models. This was fulfilled by Python scripting (Chapter 4).

(5) Exploration of the influence of material heterogeneity on the rock failure intensity in unconfined and confined compression tests (Chapter 4).

(6) Development of a new approach for simulating gradual tunnel excavation in 2D models (Chapter 5).

(7) Demonstration of the influence of weak planes representing geological structures on rockburst occurrences at tunnel walls (Chapters 5 and 6).

(8) Development of an approximate method to estimate the released kinetic energy and ejection velocity due to rockbursting in tunneling (Chapters 5 and 6).

Acknowledgements

Vijay Sharma, Kim Trapani, Alberto Romero, Subash Bastola, Negar Saeidi and Negar Sabeghi, my good friends in Iran, Canada, and United States for providing priceless support to me.

Last but not least, I would like to express my deepest appreciation to my dad, my mom, my brother Ali, my sister Shahrzad, and my grandmother for their continued support and unconditional love. Without their encouragement, I would not be able to achieve a PhD. Their belief in my abilities encouraged me to overcome all obstacles and continue to reach to the aims.

Amin Manouchehrian
MIRARCO
Laurentian University
Sudbury, Canada, 23th September 2016

Table of Contents

List of Tables

List of Figures

List of Symbols

A	Area
B	Brittleness
c	Cohesion
C_g	Competency factor
d	Distance of the fault plane to the tunnel
d'	Normal distance of the fault plane to the tunnel
E	Young's modulus
E_{pp}	Post-peak modulus
E_s	Unloading deformation modulus
F	Contact force
H	Height
k	Stiffness
KE	Kinetic energy
KE_{max}	Maximum released kinetic energy per unit volume
k_{pp}	Post-peak stiffness
L	Length of column/ specimen
l	Length of the fault
r	Tunnel radius
t	Time
T_s	Tangential stress index
U	Total strain energy
$\bar{V}$	Average velocity
$\bar{V}_{max}$	Maximum of the average velocity
V_{max}	Reaction velocity of loading system
V_o	Applied loading velocity
W	Work
Δx	Penetration of surface
ε	Strain
θ	Fault inclination angle
μ	Friction coefficient
$\mu_c / \mu_E / \mu_\varphi$	Mean value of cohesion/ Young's modulus / friction angle
ρ	Density
v	Poisson's ratio
$\sigma_1 / \sigma_2 / \sigma_3$	Maximum / Intermediate / Minimum principal stress
$\sigma_c / \sigma_E / \sigma_\varphi$	Standard deviation of cohesion/ Young's modulus / friction angle
$\sigma_r / \sigma_\theta / \tau_{r\theta}$	Radial stress/ Tangential stress/ Shear stress
σ_x / σ_z	Horizontal stress/Vertical stress
φ	Friction angle

List of Acronyms

AI	Artificial Intelligence
ANN	Artificial Neural Network
BEM	Boundary Element Method
BN	Bayesian Network
BPI	Burst Potential Index
COV	Coefficient of Variation
CWFS	Cohesion Weakening and Frictional Strengthening
DDA	Discontinuous Deformation Analysis
DDM	Displacement Discontinuity Method
DEM	Discrete/Distinct Element Method
DFN	Discrete Fracture Network
ERR	Energy Release Rate
ESR	Strain Energy Storage Rate
FAI	Failure Approach Index
FDM	Finite Difference Method
FEM	Finite Element Method
FLAC	Fast Lagrangian Analysis of Continua
GA	Genetic Algorithm
LERR	Local Energy Release Rate
LSRI	Loading System Reaction Intensity
LSS	Loading System Stiffness
PDE	Partial Differential Equation
PES	Potential Elastic Strain
PFC	Particle Flow Code
PPV	Peak Particle Velocity
PSO	Particle Swarm Optimization
RFPA	Rock Failure Process Analysis
RMi	Rock Mass index
RQD	Rock Quality Designation
SVM	Support Vector Machine
TBM	Tunnel Boring Machine
UCS	Uniaxial Compressive Strength
UDEC	Universal Distinct Element Code

Preface

This research work has been accomplished at MIRARCO − Mining Innovation and the Bharti School of Engineering, Laurentian University, under the supervision of Prof. Ming Cai, and with the financial support of the Natural Sciences and Engineering Research Council (NSERC) of Canada, Vale, LKAB, Rio Tinto, CEMI, and MIRARCO.

The results presented in Chapter 3 are published in the proceedings of *the 13th International ISRM Congress 2015*, which was organized by the ISRM and held in Montreal, Canada (Cai and Manouchehrian, 2015). More comprehensive results presented in Chapter 3 have been published in *Canadian Geotechnical Journal* (Manouchehrian and Cai, 2016d). The results presented in Chapter 4 have been published in the journal of *Computers and Geotechnics* (Manouchehrian and Cai, 2016a). The results of numerical simulation of rockburst in tunnels presented in Chapter 5 are published in the proceedings of *the 3rd International Symposium on Mine Safety Science and Engineering 2016*, held in Montreal, Canada (Manouchehrian and Cai, 2016b). More comprehensive results in Chapters 5 and 6 have been submitted for consideration for publication in *Rock Mechanics and Rock Engineering* (Manouchehrian and Cai, 2016c).

Chapter 1

1 Introduction

1.1 Background

Mankind's life is very dependent on the Earth's materials. Continuous mining in the past has depleted most surface and shallow reserves and forced us to go deeper inside the earth for more natural resources. Mining conditions are different in deep grounds; it is harder and more risky to mine at depth. One engineering hazard of mining at depth is rockburst. A rockburst is an unstable failure of rock associated with a sudden release of energy, and it imposes a great danger to safety of workers and investment.

Case histories in mining have documented violent rock failures that were accompanied by rapid ejection of debris and broken rocks into working areas of mine openings and tunnels (Andrieux et al., 2013; Blake and Hedley, 2003; Ghose and Rao, 1990; Gibowicz and Lasocki, 1997; Hedley, 1992; Shepherd et al., 1981; Young, 1993; Zhang et al., 2012). These violent unstable failures have resulted, in some cases, in a loss of life and total collapse of mine panels (Chen et al., 1997; Whyatt et al., 2006; Zhang et al., 2013; Zhu et al., 2009). Violent rock failure can occur locally in isolation, which may not affect the general stability of a mine but pose a great threat to personnel in the area. Figure 1-1 illustrates rock damages in some tunnels due to rockburst (Jiang et al., 2010; Stacey and Rojas, 2013; White and Rose, 2012). Modern mining operations take available measures to reduce the likelihood of unstable rock failures but elimination of their occurrence is difficult in practice due to the uncertainty in rock stress,

strength, stiffness, and other mechanical properties (Cai, 2013b). Over the past several decades, researchers have studied unstable rock failure and rockbursting using various means such as analytical, numerical, experimental, and statistical approaches. Many conditions leading to rockburst occurrence are not fully understood and further studies are needed to be performed to understand the mechanisms of rockbursting so as to control and mitigate rockburst risk.

There are generally two types of unstable rock failure: volume failure and contact failure (Aglawe, 1999). Unstable volume failure occurs when a mine structure, such as a pillar, becomes

Figure 1-1: Examples of rockburst damage in deep tunnels at: (a & b) Brunswick Mines, Canada (White and Rose, 2012), (c) Jinping II hydropower station, China (Jiang et al., 2010), and (d) a mine in South Africa (Stacey and Rojas, 2013).

over-stressed and fails violently. Unstable contact failure occurs when there is a sudden slip along a fault or other weakness planes. The later tends to occur when a large area of a mine has been extracted. Usually the contact failure has a greater magnitude than the volume failure, with damage over a larger area. Figure 1-2 shows the classification of unstable failures in mines.

The definition of rockburst may vary among researchers (Coates, 1966; Cook et al., 1966; Müller, 1991). Also, different mechanisms of the rockburst damaging have been hypothesized. For example different rockburst mechanisms proposed by Ortlepp and Stacey (1994) and Kaiser (1993) are presented in Table 1-1 and Figure 1-3, respectively. In this study, the word "rockburst" refers to a sudden and violent failure of overstressed rock, resulted from the rapid release of accumulated energy (Blake and Hedley, 2003).
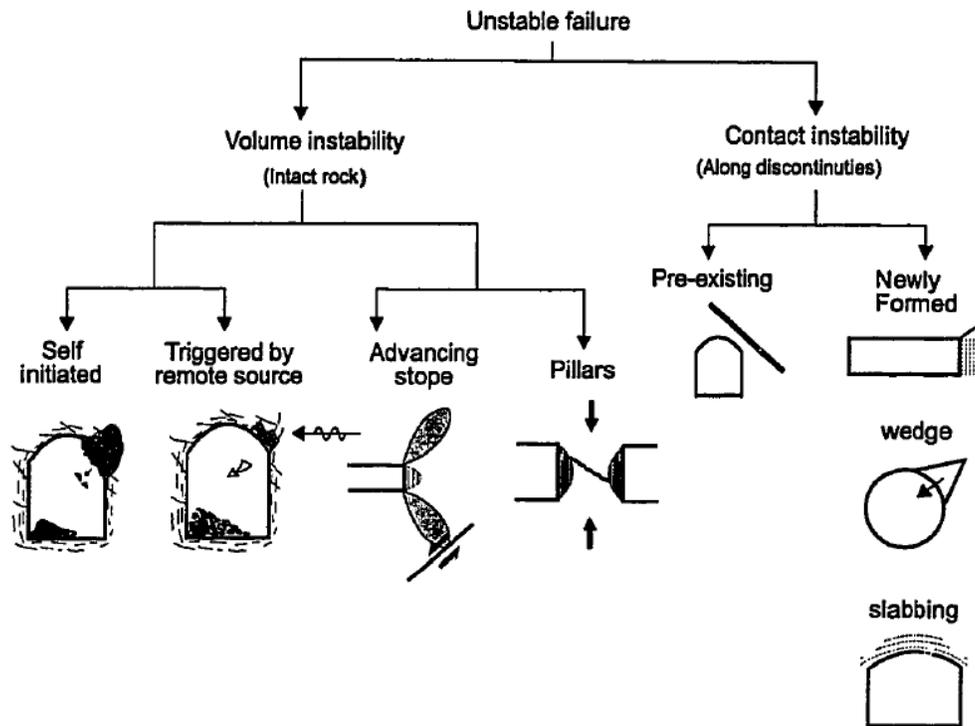
Figure 1-2: Classification of unstable failures in mining (Aglawe, 1999).

Table 1-1: Mechanisms of damaging rockbursts proposed by Ortlepp and Stacey (1994)

Seismic event	Postulated source mechanism	First motion from seismic record	Richter magnitude (M_L)
Strain Bursting	Superficial spalling with violent ejection of fragments	Usually undetected, could be implosive	-0.2 to 0
Buckling	Outward expulsion of pre-existing larger slabs parallel to opening	Implosive	0 to 1.5
Face crush	Violent expulsion of rock from tunnel face	Implosive	1.0 to 2.5
Shear rupture	Violent propagation of shear fracture through intact rock mass	Double-couple shear	2.0 to 3.5
Fault slip	Violent renewed movement on existing fault	Double-couple shear	2.5 to 5.0
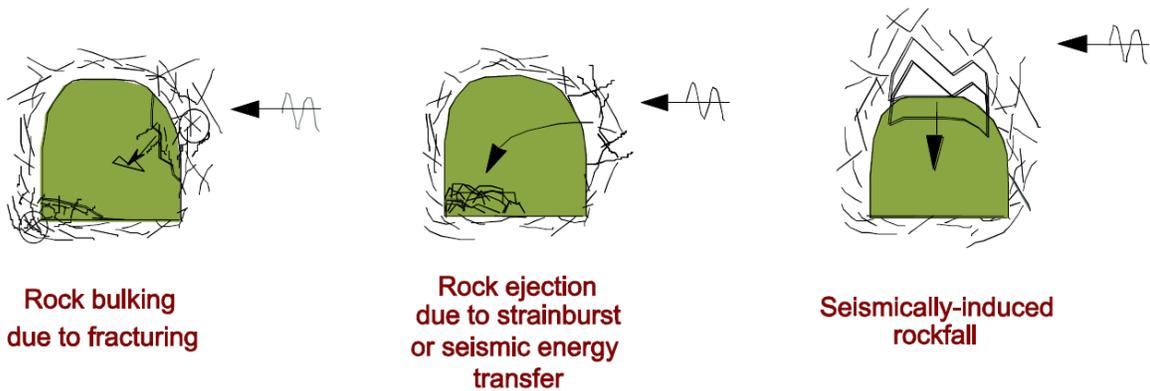
Figure 1-3: The rockburst damage mechanisms proposed by Kaiser (1993) (after Cai and Kaiser (2015) who modified from Kaiser et al. (1996)).

4

1.2 Problem statement

In the second half of the 20th century, advancement in mining technology allowed minerals to be mined in deep grounds. This resulted in frequent occurrences of rockburst in some mines. Consequently, unstable failure of rocks around underground openings became an important and challenging issue for the mining industry. Rockburst is an unstable rock failure and one of the most hazardous problems in deep underground mines. Rockburst occurrences have been increasing as mining activities progress to deeper grounds. Examples of rockburst have shown that a rockburst is accompanied by the release of energy. Some efforts have been made over the past five decades to understand why rockbursts occur, to anticipate where they will happen, and to estimate how large a rockburst event will be. Having this information about rockbursts would be valuable for rock support design. Unfortunately, there is still a long way to go.

Rock support design is strongly related to the safety and the overall cost of a mining project. Support system must be able to control rockburst damage but it should not be too costly. In a rockburst, some of the stored strain energy in the rock mass is transferred to the fractured rock mass, causing rock ejection at a high ejection velocity. The ejected rock blocks may possess kinetic energy; therefore, the applied rock support must be able to absorb or dissipate this kinetic energy (Cai, 2013b). Hence, it is essential to estimate the released energy for designing a safe and cost-effective support system.

Rockburst case histories reveal that rockburst damage is often localized and not uniform. In other words, the damage extent in a tunnel caused by a rockburst varies at different locations. Figure 1-4 presents the locations of rockburst in a tunnel at Jinping II hydropower station, showing localized rockburst damage (Jiang et al., 2010). The localized rockburst damage

originates from the complex mechanisms that drive rockbursts and the contribution of influencing factors on rockburst occurrence. Many factors that influence rockburst damage have been identified (Figure 1-5) but no one knows the exact condition for the occurrence of a rockburst in a complex underground setting. For example, geological structures such as faults, joints, and dykes are key factors that influence the stability of underground excavations; however, their role in influencing unstable rock failure is not well understood.
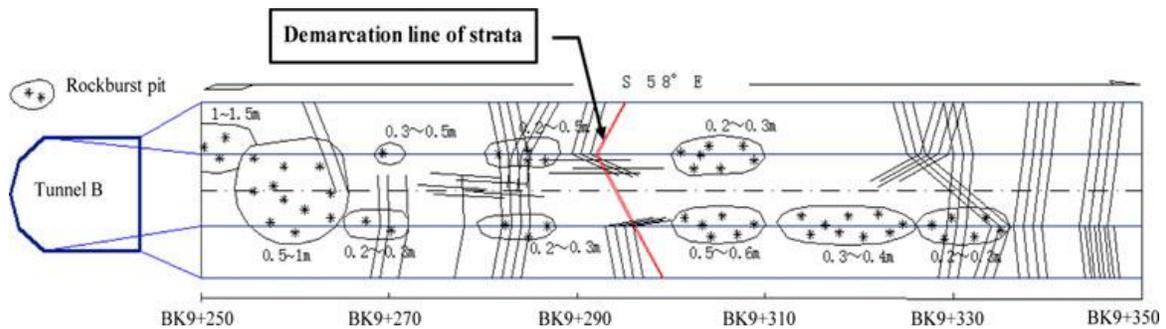
Figure 1-4: Locations of rockbursts along a tunnel at Jinping II hydropower station (Jiang et al., 2010).

Figure 1-5: Main factors influencing rockburst damage (Cai and Kaiser, 2015).

The above mentioned facts raise many questions that await answers. This study is conducted to find answers for the following challenging questions:

- Why do rocks fail in a stable or unstable manner?

- How much energy is released due to a rockburst? This is important for safe and cost-effective support system design.

- Why is rockburst damage often localized along a tunnel or around the excavation boundary, not at all locations?

- How do geological structures affect unstable rock failure and released energy?

1.3   Research hypotheses and objectives

The main goal of this research is to apply numerical modeling technique to assess the rockburst potential around underground excavation boundaries and estimating released energy when a rockburst occurs. The results from this research would be useful for rock support design. A series of research tasks are identified and listed below to achieve the goal:

- test different material models to check the capability of reproducing the mechanical behavior of hard rocks using Abaqus;

- choose a suitable candidate model by simulating a variety of laboratory tests (e.g., uniaxial compression, triaxial compression and tensile tests) and assessing its applicability for studying unstable failure under compressive loading;

- validate the ability of a calibrated explicit FEM model to simulate stable and unstable failures under laboratory compressive loading conditions (uniaxial compression and true-triaxial unloading conditions);

- find appropriate indicator(s) for identifying unstable rock failure and measuring the intensity of failure;

- validate the selected indicator(s) by applying it to known cases at laboratory scale;

- validate the models for known cases at field scale;

- study the effect of geological structures on the rock failure mode;

- assess rockburst potential around underground excavation boundaries (case study);

- calculate released energy due to unstable rock failure.

The hypotheses for the present research are:

- unstable rock failure can be simulated using Abaqus as an advanced numerical tool;

- for unstable failure to occur, some necessary conditions must be met;

- geological structures affect the rock failure mode (stable or unstable) by modifying the loading system stiffness;

- the released energy from unstable rock failure can be estimated.

1.4 Methodology

Significant advances have been made in computer science and technologies, which have made other sciences increasingly dependent on computers. For engineers, it is now possible to reproduce many physical phenomena using numerical methods in combination with powerful modern computers. Numerical methods are most useful when it is hard or impossible to study a phenomenon directly in reality. Sometimes, it is hard to explain and justify results from experiments. In such a case, numerical modeling provides an alternative or complementary means to analyze the problem and interpret the results.

Numerical models have been used to solve many geotechnical problems including studying unstable rock failure. Many investigations have been conducted to study unstable rock failure using numerical tools such as Rock Failure Process Analysis (RFPA), Fast Lagrangian Analysis of Continua (FLAC), Universal Distinct Element Code (UDEC) and Particle Flow Code (PFC), which are powerful numerical tools in the field of geotechnical engineering (Bardet, 1989; Garvey, 2013; Gu, 2013; Jia and Zhu, 2012; Kias, 2013; Müller, 1991; Oelfke et al., 1996; Zhu et al., 2010; Zubelewicz and Mróz, 1983). The degree of success of each tool for analyzing rockburst problems varies and is strongly dependent on the limitations of the applied code. For example, RFPA uses an implicit solver which is not suitable for studying dynamic problems such as the process of rockburst. UDEC and PFC are DEM-based codes that are capable of capturing micro and macro fracturing process; however, they are computationally expensive to model large-scale problems. FLAC is an FDM-based numerical tool that is not suitable for solving very large deformation problems, making it less attractive for rockburst modeling.

Abaqus is a FEM-based numerical tool developed by Dassault Systems (3DS). Application of Abaqus has resulted in very realistic simulation results of many complex problems (Ghaei and Movahhedy, 2007; Giner et al., 2009; Helwany, 2007; Zhang and Vu-Quoc, 2002). It has a broad application in industries such as automotive, aerospace, and industrial products. This numerical tool is equipped with implicit and explicit solvers, making it applicable for solving a large variety of physical and engineering problems. For example, the explicit version has been used for analyzing very large strain problems such as forging and forming of metals. In addition, it is a user friendly program.

On the other hand, there are some criticisms on the use of homogeneous models (such as Abaqus, Phase2, FLAC, etc.) to solve geotechnical engineering problems if the objective of a

modeling is to analyze the rock failure process (Diederichs, 2001; Valley et al., 2010). When a homogeneous material model is used, even if the overall stress–strain curve reflects the prescribed mechanical properties properly, the obtained failure process and pattern may be unrealistic (Valley et al., 2010). Fortunately, Abaqus provides windows for adding or improving its capability using scripting. For instance, for modeling rock-like materials, there is a possibility of introducing heterogeneity into the models so as to produce more realistic results.

Considering all the strengths and weaknesses of available numerical tools (Table 1-2), it is concluded that Abaqus should provide an ideal and efficient numerical tool for analyzing rockburst problems. Hence, Abaqus-Explicit is chosen for this research.

Using the chosen tool, the following themes are designed to complete this research:

- modeling unstable rock failure at laboratory scale; and
- modeling unstable rock failure at field scale.

Table 1-2: Comparison of some available numerical tools for solving the unstable rock failure problem

Numerical tool	Explicit solver	Very large deformation	Material heterogeneity	Computational cost	Availability in 2D and 3D	Visualization options
Abaqus$^{2D/3D}$	Yes	Yes	Potential (Script)	Low	Yes	High
FLAC/FLAC^{3D}	Yes	No	Potential (FISH)	Low	Yes	Moderate
PFC/PFC^{3D}	Yes	Yes	Available	High	Yes	Moderate
Phase^2	No	No	Available	Low	No	Moderate-High
RFPA/RFPA^{3D}	No	No	Available	Low	Yes	Moderate-High
UDEC/3DEC	Yes	Yes	Available	High	Yes	Moderate

1.4.1 Modeling unstable rock failure at laboratory scale

Unstable rock failures are violent and often accompanied with rock ejection. Implicit numerical techniques are not capable of simulating unstable failure problems but explicit numerical techniques are. In this study, the suitability of the adopted numerical tool for simulating unstable rock failures will be first tested by simulating unstable rock failure in laboratory tests including uniaxial and polyaxial compression tests. New indicators will be proposed to distinguish between stable and unstable failures in laboratory test simulation.

Failure of brittle rocks is dominated by tensile fracturing. Homogeneous models cannot capture this rock failure mechanism while heterogeneous models are proven capable of capturing it. Material heterogeneity will be introduced into Abaqus models using Python scripts for more realistic simulation of rock failure process. In addition, the effect of material heterogeneity on rock failure intensity in unconfined and confined compression tests will be investigated.

1.4.2 Modeling unstable rock failure at field scale

Underground mine development involves excavation of tunnels, shafts, pillars, etc., and these structures are subjected to plausible rockburst damage. As stated above, rockburst is one of the most difficult engineering problems in deep mining. Geological structures such as faults and shears have been observed near excavation boundaries in many rockbursts and these structures must have played a role in these rockburst events. In this research, rock failure near the excavation boundary of a tunnel with adjacent fault will be modeled. Moreover, a case study will be conducted to simulate a known rockburst in a tunnel with an observed fault nearby.

For a safe and cost-effective rock support system design, an estimate of released energy due to rock ejection is needed. This released energy must be dissipated by the support system. In this study, released energy from rockburst will be estimated.

1.5 Work scope

This thesis is composed of seven chapters. A brief summary of the chapters is provided below.

- The introductory chapter (Chapter 1) presents the background, problem statement, research hypotheses and objectives, methodology, and scope of the work.

- In Chapter 2, a brief summary of rockburst case histories is presented. The applied approaches for solving unstable rock failure and rockburst problem are categorized into different groups and a detailed review of numerical methods for studying rockburst is presented.

- In Chapter 3, numerical simulation results of unstable rock failure in laboratory tests using Abaqus-Explicit are presented. Firstly, uniaxial compression tests are simulated to confirm the suitability of the adopted numerical tool for simulating unstable rock failures. Two indicators are proposed to distinguish between stable and unstable failures. Then, unstable rock failures under polyaxial unloading conditions are simulated. The influences of loading system stiffness, specimen's height to width ratio, and intermediate principal stress on rock failure intensity are investigated.

- In Chapter 4, simulation of failure of homogeneous and heterogeneous rocks is presented. It is confirmed that homogeneous models cannot capture splitting rock. Material heterogeneity is introduced into Abaqus models using Python scripts. Moreover, the effect of loading system stiffness (LSS) and confinement as well as

material heterogeneity on rock failure intensity in terms of failed rock ejection velocity and released energy is investigated.

- In Chapter 5, the influence of weak planes around tunnels on rockburst damage is studied. Rock failure near the excavation boundary of a tunnel without any adjacent weak plane is modeled first. Then a weak plane with different lengths, inclinations and distances to the tunnel is added to the models and its effect on rock failure is studied.

- In Chapter 6, a case study of rockburst in the drainage tunnel in Jinping II hydropower station in China is conducted to demonstrate the applicability of the developed Abaqus models for rockburst modeling.

- Chapter 7 summaries the main achievements of this thesis and presents some suggestions for future work.

- The theory of stable and unstable failure, influence of loading system mass on the rock dynamic response, Abaqus input files and, Python scripts used for simulations are presented in Appendices A, B, C ,and D, respectively. At the end of this document, the author's curriculum vita is presented.

Chapter 2

2 Literature review

2.1 Rockburst case histories in some countries

Rockbursts in the gold mines in the Witwatersrand area in South Africa and the Kolar Gold Field in India were first recognized to be the consequence of mining, not natural earthquakes, at the turn of the 20th century (Aga et al., 1990; Blake and Hedley, 2003; Ghose and Rao, 1990). The rockburst problem increases as excavation activities progress to deep grounds. For example, many deep hard rock mines in Canada, South Africa, Australia, Sweden, and India and some deep civil tunnels in Switzerland, China, and Peru have experienced rockburst problems (Andrieux et al., 2013; Blake and Hedley, 2003; Ghose and Rao, 1990; Gibowicz and Lasocki, 1997; Heal, 2010; Young, 1993). It is difficult to summarize all rockbursts that have occurred in the past in one study. However, in the following sections, some major rockburst case histories in Australia, China, India, North America, and South Africa are briefly reviewed.

2.1.1 Rockbursts in Australia

Many mines in Australia have experienced rockburst problems. Heal (2010) summarized some rockburst case histories from nine mines in Australia including Barkers and Strezelecki, Big Bell, Black Swan, Darlot, Junction, Kanowna Belle, Mount Charlotte, Perseverance, and Perilya Broken Hill. The collected data from these case histories were used to develop a rockburst damage potential assessment technique.

At Barkers and Strezelecki Mine, fourteen rockbursts occurred from 2002 to 2003. Some of the recorded seismic events indicated high event magnitudes with the largest magnitude of 3.0 in Richter scale. The rockburst occurrence at Barkers and Strezelecki was strongly related to the presence of seismically active structures. The rockburst damage at the mine was partially controlled after installing the cone bolts. Big Bell Mine experienced some large seismic events (with Richter magnitudes greater than 2.0) at multiple damage locations. For instance, one rockburst event with ten separate damage locations occurred at Big Bell 7. The majority of the rockbursts at Big Bell occurred due to high stress induced by mining, affected by factors such as the steeply dipping foliation and the orientation of the excavations. In some cases, use of cone bolts along with split sets and mesh limited the rockburst damage. The Black Swan case histories consist of only three rockbursts that occurred from 2002 to 2003. Field evidence showed that geological structures played a role in all three rockbursts at Black Swan Mine (Heal, 2010).

At Darlot Gold Mine, two severe rockbursts occurred in 2003 and 2004. In one of the rockburst events at Darlot, about 200 t of broken rocks blew out into the working area. The combination of a large opening span with inadequate ground support was the main factor for the occurrence of the severe rockbursts at the mine. 16 rockburst case histories were documented for Junction Mine. One of the largest mining-induced seismic events recorded in Australia with a Richter magnitude of 3.1 occurred at Junction, which resulted in damage over multiple levels of the mine. Five rockburst case histories are documented for Kanowana Belle Mine from 2000 to 2003. Again, the presence of seismically active major structures, particularly geological contacts, was evident in most of the rockburst case histories at Kanowana Belle (Heal, 2010) .

Mount Charlotte Mine experienced some of the largest mining-induced seismic events in Australia from 1998 to 2003. For instance, a seismic event with a Richter magnitude of 3.5

occurred in 1998. This seismic event was followed by a 150,000 t production blast and it caused minor damage to surface structures in the city of Kalgoorlie. This blast caused a fault to slip over a large area. At Perilya Broken Hill Mine, only one rockburst occurred in 2005. However, it was a very large event with a Richter magnitude of 3.1. The presence of a major seismically active structure was considered to be the main factor that led to this large seismic event and associated rockburst damage. Perseverance Mine experienced seven rockbursts from 2002 to 2004. A common theme in many of the rockburst case histories at Perseverance is the inadequacy of the support system comprised of split sets and mesh (Heal, 2010).

2.1.2 Rockbursts in China

In China, rockburst has been a challenging problem in many underground mines and civil tunnels. The first recorded rockburst occurred in the Shenli Coal Mine in 1933, when the mining depth reached to 200 m (Li et al., 2007; Wu and Zhang, 1997). Wu and Zhang (1997) reported 2000 rockburst case histories in 33 coal mines from 1949 to 1997 that resulted in damages to mines, equipment, and injuries to personnel. Some of the seismic events were large with a maximum recorded Richter magnitude of 4.2.

Rockburst was a hazardous problem during the construction of the Jinping II hydropower station in China. Zhang et al. (2012) reported four intense rockburst events in the Jinping II tunnels. On November 28, 2009, an extremely intense rockburst occurred in the drainage tunnel at a depth of 2,330 m, which caused seven deaths and one injury as well as the total destruction of a TBM machine. The recorded seismic signals indicated a Richter magnitude of 2.0 of the rockburst. On July 14, 2010, an extremely intense rockburst occurred on the wall of headrace tunnel No. 4 and

it destroyed a multi-beam jumbo drill, broke and deformed some rockbolts, and damaged the rock mass and shotcrete on the wall.

On April 16, 2011, a large rockburst occurred in the headrace tunnel No. 4. This rockburst resulted in uplifting the floor in a large area. The associated seismic waves caused a moderate rockburst in the drainage tunnel that was 45 m away from the headrace tunnel No. 4. On February 4, 2010, an intense rockburst occurred in the headrace tunnel No. 2 and severely damaged the tunnel. During the rockburst, the floor shook violently, and three workers were injured and a dump truck was damaged (Zhang et al., 2012).

2.1.3 Rockbursts in India

Gold mines at Kolar Goldfield in India became seismically active at the turn of 20th century. The first recorded rockburst at Kolar Goldfield occurred in a stope of Oorgaum Mine in 1898 (Ghose and Rao, 1990). At shallow depths, rockburst was not a critical problem in those mines; however, it became a serious problem as mining advanced to deeper grounds in the 1930s. The rockburst problem was even more challenging when the ore body to be mined was near faults, dykes, and pegmatites. Mining near geological structures resulted in some intense rockbursts with Richter magnitudes as high as 5 to 6.

Mining at Kolar Goldfield resulted in a large number of rockburst case histories. Among all, the rockbursts in Glen ore shoot in 1962 and in Northern folds in 1966 in Champion Reef Mine and, in the west reef workings of Nundydroog Mine in 1971 were the most severe (Aga et al., 1990). On November 27, 1962, a major "area rockburst" occurred at Champion Reef Mine. The term "area rockburst" refers to a phenomenon wherein a major rockburst triggers a series of rockbursts of the same or smaller sizes. The first major tremor was followed by 59 tremors

recorded in the following 24 hours. Abnormal rockbursting continued for about two weeks. This area rockburst resulted in severe damage to the whole stoping areas on the wings of the Glen ore shoot and the Southern ore body. Moreover, some surface facilities were damaged. Another series of major rockbursts occurred at Champion Reef Mine on December 25, 1966. This area rockburst damaged a large area of the mine. Abnormal rockbursting continued for several days. Nundydroog Mine experienced a major rockburst on November 27, 1971, which resulted in severe damage to the mine. In addition, some surface facilities over an area of 3 km^2 were damaged. The rockburst problem at Kolar Goldfield Mines was partially mitigated by modifying the mining methods.

2.1.4   Rockbursts in North America

The first rockburst in North America occurred at the silver mines in the Coeur d'Alene District of Idaho (Blake and Hedley, 2003; Whyatt et al., 2006). In Canada, the majority of rockbursts had occurred in Northern Ontario (Andrieux et al., 2013; Blake and Hedley, 2003; Hedley, 1988, 1992; Udd and Hedley, 1987). In the United States, sixty years of rockbursting in the Coeur d'Alene district made the area well known (Whyatt et al., 2006). Blake and Hedley (2003) compiled rockburst case histories from fifteen mines in Canada and the United States including the Brunswick lead-zinc mine at Bathurst, Lake Shore, Teck-Hughes, Wright-Hargreaves, Macassa gold mines at Kirkland Lake, Falconbridge No. 5, Strathcona, Creighton mine, Copper Cliff North nickel mine, Quirke uranium mine, Campbell gold mine; Lucky Friday, Star, Galena, and Sunshine silver-lead-zinc mine. In general, these are the mines that have well-documented records and published papers and reports that analyzed the probable cause and mechanism of rockburst (Andrieux et al., 2013; Blake and Hedley, 2003; Hedley, 1988, 1992).

Rockburst problems started in Brunswick Mine in the mid-1980s when the sizes of sill pillars were reduced below 40 m. Rockbursts occurred in the mid-1990s resulted in significant ore-losses and increased mining risk. All gold mines in the Kirkland Lake District experienced rockbursts; however, the most burst-prone mine was Lake Shore Mine. A total of 1,391 rockbursts were reported from 1931 to 1965. Some of these rockbursts were very large; the largest rockburst had a Richter magnitude of 4.4, occurred in 1939 at Lake Shore, and it was one of the largest in Canada. Teck-Hughes and Wright-Hargreaves mines experienced rockbursts from the early 1930s to the 1960s. Some of rockbursts were so violent that some parts of the mines were forced to be abandoned (Blake and Hedley, 2003).

Rockburst became a serious problem at Macassa Mine after fifty years of exploitation and mining advanced to deeper ground. Continuous rockbursts resulted in the closure of the mine in 1999. At Falconbridge No. 5 Shaft Mine, the first recorded rockburst occurred in 1955. In 1984, a series of large rockbursts occurred, which resulted in the closure of the mine. Strathcona Mine experienced rockburst problems in 1988 in the central part of the sill that finally resulted in the end of exploitation in the Main Ore Zone. Moreover, a number of rockbursts occurred in the Deep Copper Zone at Strathcona Mine in 1999. With proper mitigation measures, the rockburst problem did not stop mining activities in this mine (Blake and Hedley, 2003).

The earliest rockbursts in Creighton Mine, one of the deepest operating mines in North America, were reported in 1934. These rockbursts resulted in changes in mining methods, stope sequencing, and ground support. Rockburst became a challenging problem at Copper Cliff North in 1980s. After changing the mining method to center-out paneling method, the rockburst problem was under control. Quirke Mine experienced 136 rockbursts over a five-year period in 1980s. This mine is a typical example for the mines that experienced a chain reaction of pillar

failures. Lucky Friday Mine experienced a series of rockbursts in the late 1960s. However, after changing the mining method the rockburst problem was brought under control (Blake and Hedley, 2003).

2.1.5   Rockbursts in South Africa

The Witwatersrand Basin and Bushveld Complex in South Africa hold two of the largest known gold reserves in the world. These huge gold ore bodies persist to depths of several kilometers. In South Africa, continuous extraction of gold has exposed the mining industry to the danger of rockburst. Rockbursts were first encountered in the early 1900s when extensive stopes, supported solely by small reef pillars, reached depths of several hundred meters (Durrheim, 2010). The statistical surveys show that most of the rockbursts in South Africa have occurred in the vicinity of dykes and major faults (Johnston, 1988).

The largest mining-related seismic event recorded in South Africa occurred in the Klerksdorp district on March 9, 2005, with a Richter magnitude of 5.3. This seismic event shook the nearby town of Stilfontein and resulted in serious damages to several buildings and minor injuries to 58 people. Moreover, a shaft in a nearby mine was damaged severely, two miners were killed, and 3200 miners were evacuated under difficult conditions (Durrheim, 2010).

Despite many technical advances, rockbursts remain one of the most hazardous problems facing deep mining operations and continue to pose a significant risk to investment and lives. In 1908, the Ophirton Earth Tremors committee was commissioned to investigate earth tremors originating in the Witwatersrand Gold Mines in Johannesburg (Brune, 2010). The committee found that the tremors originated in underground pillars when the pillars were loaded under high stress. This investigation did not signal the beginning of rockburst research, which actually

began two years later in 1910, with the installation of the first seismometer at observatory in Johannesburg. It was the start of research on rockburst. So far, many efforts have been made for studying and analyzing rockburst. In the following sections, a detailed review of some previous studies on unstable rock failure and rockburst is presented.

2.2   Theoretical description of stable and unstable failures

Rocks can behave in a quasi-static, controlled fashion during failure. The failure may, however, be dynamic if kinetic energy is applied to the failing rock from the loading system. If the released energy from the loading system is more than the energy amount that can be stored or dissipated by the failing rock, then the system is said to be in an unstable equilibrium. When a brittle rock is loaded by a comparatively soft loading system, unstable equilibrium exists when failure occurs. If the loading system stiffness is less than the post-failure stiffness of a rock specimen and the peak strength of the sample is reached, then the stored strain energy in the loading system is transferred rapidly into the failing rock, leading to unstable failure.

Cook (1965) first proposed to use the complete stress–strain curve and the associated energy components for studying failure instability. Later, Salamon (1970) explained the contribution of the stored energy on instability of failure in rocks using a simplified unstable equilibrium. In this section, the theoretical description of stable and unstable rock failures is presented.

The concept of the equilibrium in a simple spring-rock system is illustrated in Figure 2-1a. This simple system is composed of a loading system (a linear elastic spring) and a rock specimen. A downward displacement is applied to point O_1, adding load P_s to the system until the specimen fails completely. This system is analogous to a uniaxial compressive strength (UCS) test in laboratory. In Figure 2-1, the displacement of the upper end (O_1) and the lower end (O_2) is γ and

21
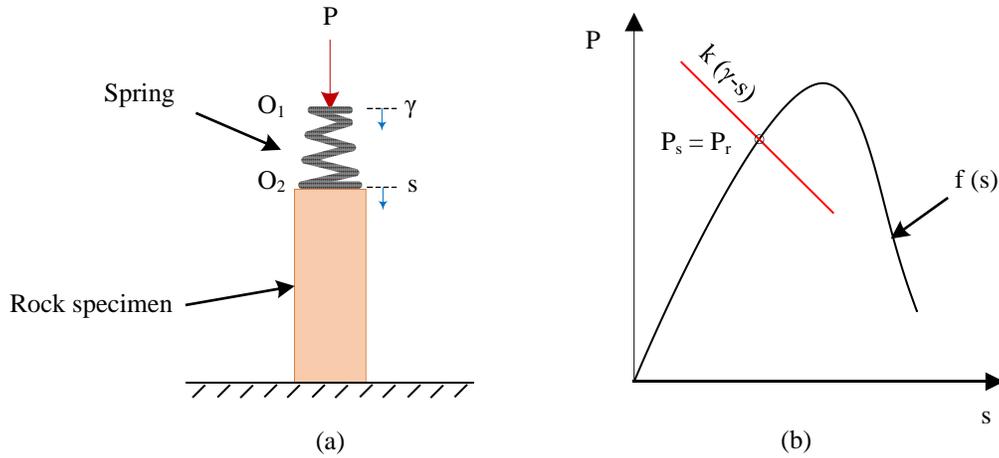
Figure 2-1: (a) Idealized loading system, and (b) the illustration of the equilibrium between load and rock resistance (reproduced and modified from Salamon (1970)).

s, respectively. The spring in the system has a linear elastic force-displacement behavior which is shown in Figure 2-1b by the red line. The spring force (F_s) is a function of the spring's stiffness (k) and the change in spring length (γ - s). The compressive force P_s on the spring can be calculated by Eq. (2-1).

$$P_s = k.(\gamma - s) \tag{2-1}$$

The force-displacement relation of the rock specimen is described by,

$$P_r = F(s) \tag{2-2}$$

For the system in equilibrium, $P_s = P_r$, that is,

$$k(\gamma - s) = f(s) \tag{2-3}$$

as shown in the pre-peak curve in Figure 2-1b.

22

The equilibrium state defined by Eq. (2-3) remains stable as long as the spring does not induce any further displacement to the specimen. It means that the spring does not transfer anymore external energy to the specimen. If γ remains unchanged ($\Delta\gamma = 0$), no external energy enters into the system. Hence, the equilibrium is stable if the work done by the spring (ΔW_s) during a virtual displacement (Δs) of point O_2 is smaller than the work required to induce the same displacement in the rock (ΔW_r), that is,

$$\Delta W_r - \Delta W_s > 0 \qquad (stable) \tag{2-4}$$

The change in the work done by the spring and the work required to deform the rock are calculated by Eqs. (2-4) and (2-5), respectively.

$$\Delta W_s = \left(P + \frac{1}{2}\Delta P_s\right).\Delta s \tag{2-5}$$

$$\Delta W_r = \left(P + \frac{1}{2}\Delta P_r\right).\Delta s \tag{2-6}$$

The changes in forces on the spring and specimen can be derived from Eq. (2-1) and Eq. (2-2), respectively ($\Delta\gamma = 0$),

$$\Delta P_s = -k.\Delta s \tag{2-7}$$

$$\Delta P_r = f'(s)\Delta s = \lambda.\Delta s \tag{2-8}$$

where λ is the slope of the force-displacement curve of the specimen. Substituting expressions in Eqs. (2-7) and (2-8) into Eqs. (2-5) and (2-6) and then into Eq. (2-4) gives,

$$\frac{1}{2}.(k+\lambda).(\Delta s)^2 < 0 \tag{2-9}$$

This result shows that the condition for the stability of the failure is

$$k+\lambda > 0 \qquad (stable) \tag{2-10}$$

Within this system, a negative slope would be observed for a brittle rock specimen under failure. The value of the spring stiffness k is always positive by definition. Therefore, if the negative slope of the rock after failure becomes greater than the stiffness of the spring, then unstable failure is initiated. In summary, instability may be characterized either from the capacity of the loading system to exert more forces than will be resisted, or through an investigation of the release of excess energy as a result of unstable equilibrium.

2.3 Numerical methods of studying rockburst

Tragic fatalities and heavy damages due to rockbursts have made researchers to work harder to find ways to control rockburst damage. In recent years, many studies have been conducted using different approaches to study different aspects of unstable rock failure, such as why it happens, where it happens, and how violent it would be. Figure 2-2 summarizes the methods employed for studying rockburst problems. This thesis focuses on the numerical modeling of rockburst; therefore a review on the numerical methods for studying unstable rock failure and rockburst is presented in this section. In addition, other methods for studying unstable rock failure and rockburst showed in Figure 2-2 are reviewed briefly in Appendix A.
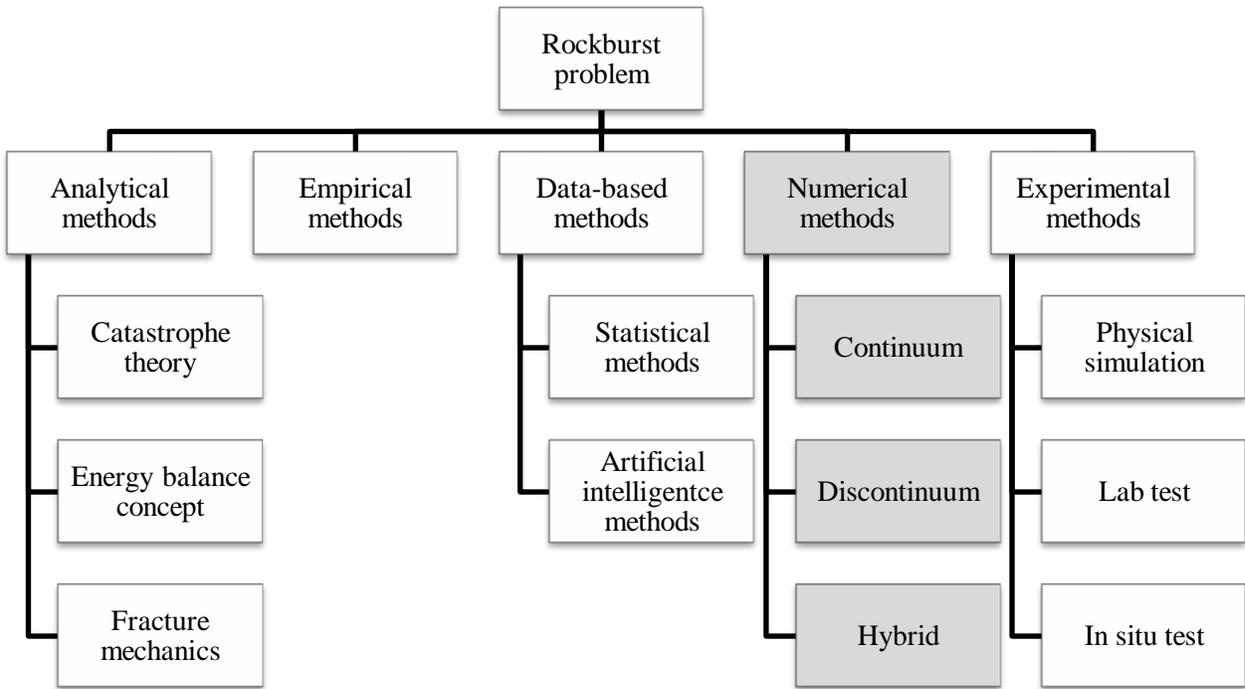
Figure 2-2: A summary of methods for studying rockburst.

2.3.1 Numerical modeling approaches in geomechanics

Some geomechanical problems can be solved using simplified analytical solutions. However, this approach is usually limited to very few problems with idealized assumptions and conditions. For example, analytical solutions that exist for excavation of a circular tunnel in a homogeneous rock mass under hydro-static field stress condition are rarely applicable to practical tunneling problems. Furthermore, experimental studies are costly and time-consuming. Engineers must revert to approximate solutions using numerical tools to solve real-life problems (Beer et al., 2008).

The mining process results in rock deformation and failure around the openings. Properties of joints and rock itself dominate the behavior of rock masses at all stages of deformation. Numerical models provide a tool to analyze the process of rock deformation and failure. The

methodology by which one investigates these processes using numerical models depends on the purpose of the modeling. For example, to design a cavern it requires building of a complex model that contains all geological features of a rock mass but a simplified model can be appropriate to design a small trench. Starfield and Cundall (1988) argued that simplification is needed in order to allow for comprehension of model results and thoughtful iteration of the experimentation process.

Continuum and discontinuum numerical methods have been used to analyze engineering problems and to eliminate assumptions imposed by the analytical approach. For continuum problems, Finite Element Method (FEM), Finite Difference Method (FDM), and Boundary Element Method (BEM) and for discontinuum problems, Discrete/Distinct Element Method (DEM), Discrete Fracture Network (DFN) and Discontinuous Deformation Analysis (DDA) are the most commonly used methods in solving geomechanics problems. The fundamental difference between the continuum and the discontinuum methods originates from the difference in the treatment of displacement compatibility conditions. In the continuum methods, the displacement compatibility must be applied between internal elements. In contrast, the displacement compatibility is not required between blocks in the discontinuum methods.

The FDM is the oldest numerical method and has been used widely for solving many engineering problems. In this method, the problem domain is divided into sub-domains of smaller size called elements (Figure 2-3b). Then the Partial Differential Equations (PDE) are approximated by replacing partial derivatives with differences at regular or irregular grids imposed over the problem domains. Indeed, the original PDEs are transferred into a system of algebraic equations in terms of unknowns at grid points. By applying the initial and boundary
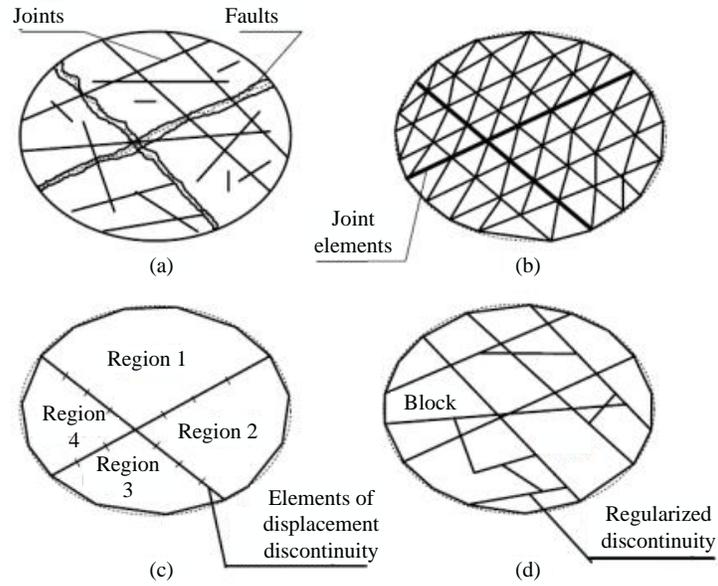
Figure 2-3: Representation of (a) fractured rock mass in (b) FDM or FEM, (c) BEM, and (d) DEM (Jing, 2003).

conditions, the solution of the system equation can be obtained. FLAC, which is a popular numerical tool in geomechanics, is based on FDM.

The FEM is the most commonly used method for finding approximate solutions for boundary and initial-value problems. In the FEM, similar to the FDM, the problem domain is sub divided into a finite number of elements (Figure 2-3b). Then variational methods from the calculus of variations are used to solve the problem by minimizing an associated error function. Being a powerful numerical method, the FEM has been employed for solving a large variety of engineering problems. The engineering world has been arguably improving with the aid of this powerful numerical method (Hastings et al., 1985). The FEM is the basis of many numerical tools in geomechanics such as Abaqus, Phase2, Plaxis, and RFPA.

Unlike the FDM and the FEM, discretization is needed only at domain boundaries in the BEM (Figure 2-3c). This makes the BEM more efficient than other numerical methods in terms of

computation costs. The information required in the solution domain is separately calculated from the information on the boundary, which is obtained by solution of a boundary integral equation, instead of direct solution of the PDEs, as in the FDM and the FEM. The BEM is the most efficient technique for fracture propagation analysis (Jing, 2003). It is also best suited for simulating infinite domains due to the use of fundamental solutions of the PDEs in such domains. Tools such as Examine$^{2D/3D}$ and Map3D, which are widely used in geomechanics, are based on BEM.

The DEM is especially designed for modeling discontinuum such as fractured or granular geological media. In the DEM, the problem domain is defined by an assemblage of blocks which are connected together (Figure 2-3d). Then, the problem is solved by solving the equations of motion of these blocks and considering the contact behavior. The blocks can be rigid or deformable. The FDM or the FEM are used for defining deformable blocks. The advantage of the DEM is its ability for solving problems with large displacements caused by rigid body motion of individual blocks, including block rotation, fracture opening and completes detachments. The DEM is the basis of some geomechanical programs such as UDEC and PFC.

From a micro-scale point of view, a rock is made up of minerals, voids, and fractures. This means that basically a rock is a discontinuum medium (Figure 2-4a). For simplification, a rock can be treated as an equivalent continuum medium if its texture is uniform. In engineering problems, where we mainly deal with meso-scale (Figure 2-4b) and macro-scale (Figure 2-4c) problems, rocks are considered as a continuum medium if no significant discontinuity exists. Existence of major discontinuities in the problem domain disables the continuum approach for solving the problem and discontinuum approach should be applied instead. Figure 2-4 illustrates the view of rocks at different scales.
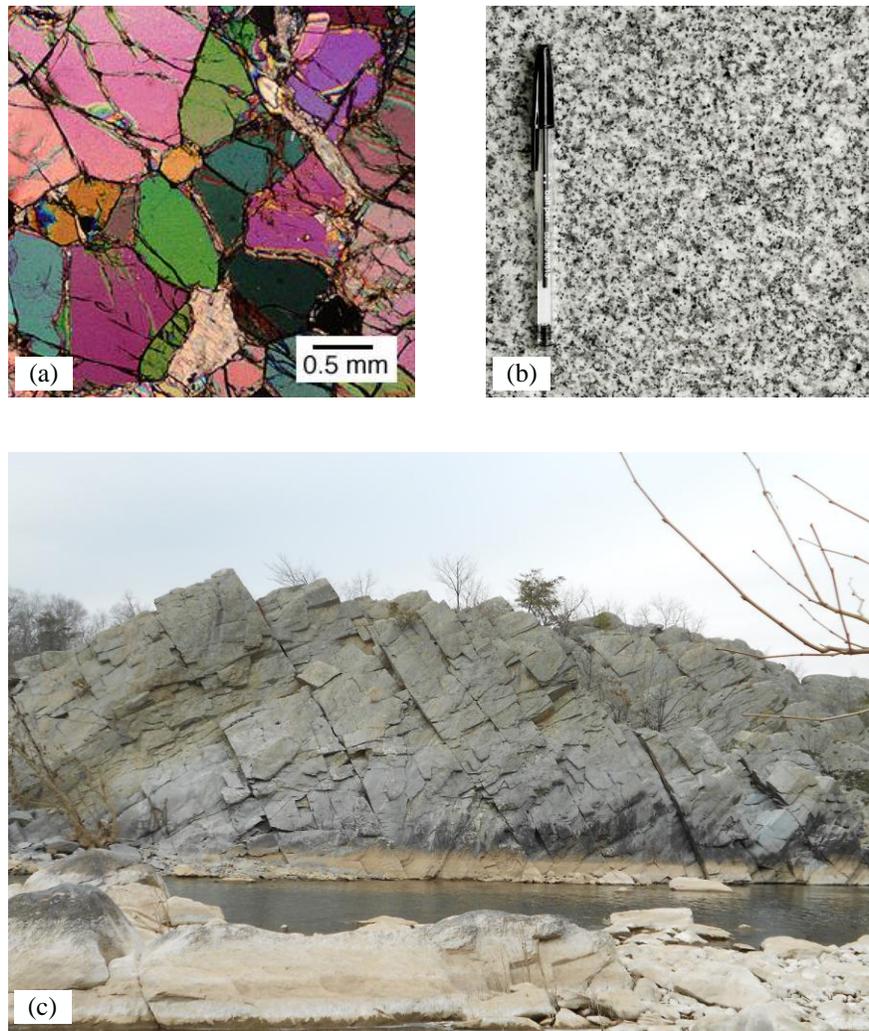
Figure 2-4: Views of rocks at (a) micro-scale (http://serc.carleton.edu/NAGTWorkshops/petrology/index.html), (b) meso-scale (http://www.affordablegranite.co.uk/salt-pepper-granite.html), and (c) macro-scale (http://whattherockstellus.blogspot.ca/2012_03_01_archive.html).

In geomechanics, the selection of a numerical modeling approach depends on many factors but the problem scale and fracture system geometry are the main factors (Jing, 2003). In general, a medium without any fractures can be modeled using the continuum approach (Figure 2-5a). Moreover, the continuum approach can be applied when too many fractures exist in the medium. In this situation an equivalent continuum approach is assumed (Figure 2-5d). Furthermore, the continuum approach is applicable where few fractures exist, if no fracture opening and no

29
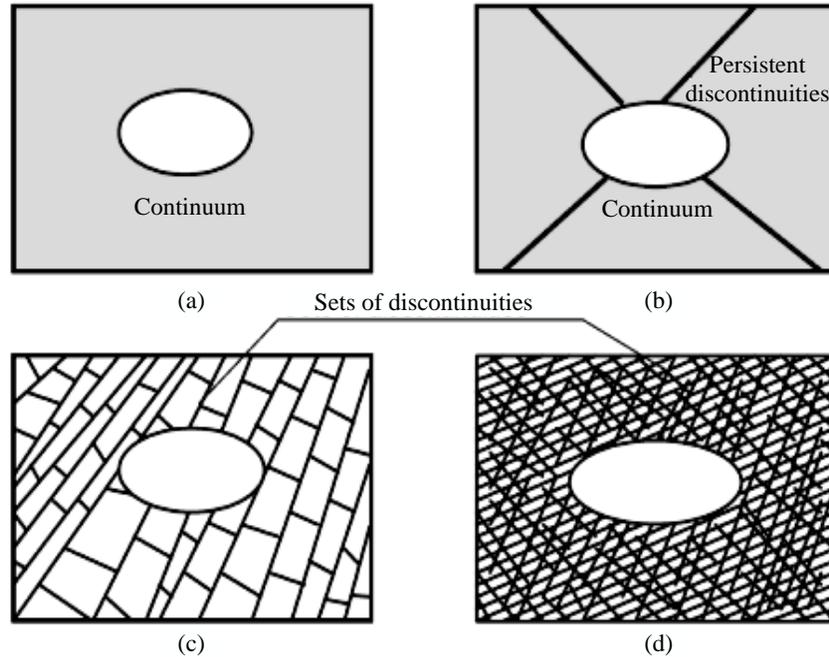
Figure 2-5: Suitability of different numerical approaches for modeling an excavation in a rock mass: (a) continuum method, (b) either continuum with fracture elements or discrete method, (c) discrete method, and (d) continuum method with equivalent properties (Jing, 2003).

complete block detachment are possible (Figure 2-5b). The discontinuum approach is usually suitable where moderately fractured rock mass exists or, where very large displacements or block detachments are expected (Figure 2-5c).

2.3.2 Implicit vs. Explicit numerical methods for simulating unstable rock failure

Rockburst damages involve rock ejection at the boundary of excavations. The ejected rock blocks possess kinetic energy (which is proportional to the square of the ejection velocity and mass of the ejected rock) and the applied rock support must be able to absorb or dissipate this kinetic energy (Cai, 2013b). Therefore, it is essential to estimate the released kinetic energy for designing a safe and cost-effective support system. Estimations of the ejection velocity due to unstable rock failure have been made by different researchers through observations in laboratory and field (He et al., 2010; Jager et al., 1990; Jiang et al., 2015; Milev et al., 2001; Ortlepp, 1993;

Stacey et al., 1995). Different ejection velocity ranges in rockbursts have been observed and tested by different researchers. Ortlepp (1993) observed that the ejection velocity of broken rocks in a rockburst could be in the range of 8 to 50 m/s. Jager et al. (1990) believed that the ejection velocity could be up to 6 m/s. Stacey et al. (1995) stated that an ejection velocity between 5 and 10 m/s could be a reasonable assumption to design a rockburst support. Desirably, a numerical model capable of capturing the rock ejection during rockbursts can be very useful for designing rockburst support.

Unstable rock failure problems are fundamentally nonlinear dynamic problems. Hence, a suitable numerical model for the simulation of unstable rock failure should be able to capture the sudden changes of the model variables during the calculation time. A special attention must be paid to selecting a numerical tool to study unstable rock failure problems. Numerical solutions are obtained using explicit or implicit solvers and depending on the types of solvers used, the simulations results could be different (Cai, 2008b). In explicit numerical methods, the state of a system at time $t + \Delta t$ is calculated from the state of the system at time t. The state of the system at time $t + \Delta t$ is

$$y\,(t + \Delta t) = \; f\big(y(t)\big) \tag{2-11}$$

where $y(t)$ and $y(t + \Delta t)$ are the states of the system at times t and $t + \Delta t$, respectively. In contrast, in implicit numerical methods the solutions are obtained by considering both the states of the system at the current times t and $t + \Delta t$ which can be expressed mathematically as

$$g\big(y(t), y(t + \Delta t)\big) = \; 0 \tag{2-12}$$

Unstable rock failure has been studied using implicit and explicit numerical models by some researchers (Bardet, 1989; Chen et al., 1997; Fakhimi et al., 2016; Fujii et al., 1997; Garvey, 2013; Gu, 2013; Gu and Ozbay, 2015; He et al., 2016; Kaiser and Tang, 1998; Kias and Ozbay, 2013; Miao et al., 2016; Mitri et al., 1999; Müller, 1991; Oelfke et al., 1996; Salamon et al., 2003; Sharan, 2007; Sun et al., 2007; Tan et al., 2009; Zhang et al., 2013). In general, the problem of convergence arises when using an implicit numerical model for solving a nonlinear dynamic problem. On the other hand, implicit numerical models are unconditionally stable while the explicit numerical models are conditionally stable, requiring that the time step used must be smaller than the critical time step. Some researchers used implicit numerical models to study unstable rock failure (Kaiser and Tang, 1998; Oelfke et al., 1996; Zhu et al., 2010). For instance, Oelfke et al. (1996) presented an implicit model for analyzing underground mine deformation. In their models, divergence of the solution was interpreted as a sign of unstable failure. In another study, Kaiser and Tang (1998) studied unstable rock failure in rib pillars using RFPA which is an implicit numerical model. In their models, the constitutive law for each element was elastic–brittle, and it was postulated that the element failure was violent. Then, it was assumed that the number of failed elements in brittle failure conditions was proportional to the seismic events or acoustic emissions. By counting the number of seismic events they indicated that the rock failure was more unstable when a softer loading system was applied. Implicit numerical models may be suitable to identify the location and magnitude of failure; however, the rock ejection process as an important feature of unstable rock failure cannot be captured.

In explicit numerical methods, the problem of convergence is eliminated, which makes the explicit approaches more suitable for solving nonlinear dynamic problems (Harewood and McHugh, 2007; Sun et al., 2000; Yang et al., 1995). Because the unstable rock failure problems

are fundamentally nonlinear dynamic problems, the explicit numerical methods are more suitable than the implicit numerical methods for studying this type of problems. The application of the explicit numerical tools such as FLAC, PFC and UDEC, have demonstrated the suitability of using explicit numerical models to study unstable rock failure (Fakhimi et al., 2016; Garvey, 2013; Gu, 2013; Gu and Ozbay, 2015; He et al., 2016; Jiang et al., 2010; Kias and Ozbay, 2013; Zhang et al., 2013). In Section 2.3.4, some examples of using explicit models for modeling unstable failure are presented.

2.3.3 Numerical simulation of unstable rock failure

Laboratory testing can reproduce the process of unstable rock failure and help to analyze the internal changing characteristics of rockburst; however, it is rather difficult to simulate rockbursts that truly mimic conditions underground. Through laboratory testing, Wawersik and Fairhurst (1970) demonstrated that failure mode depends on the relative stiffness of the rock's post-peak stiffness and LSS. For an elastic material, the stiffness of a column with a uniform cross section area and material property is calculated by:

$$k = \frac{AE}{L} \tag{2-13}$$
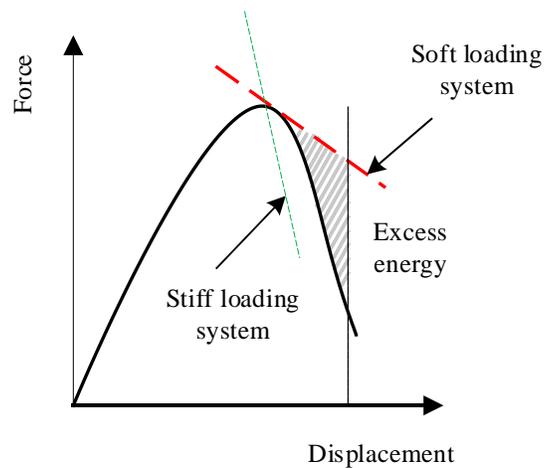
Figure 2-6: Equilibrium stability concept.

where *E* is the elastic modulus, *A* is the cross section area, and *L* is the length. Figure 2-6 illustrates the concept of equilibrium instability related to LSS and material stiffness. The slopes of the red and green dashed lines represent the loading system's unloading stiffness for soft and stiff loading conditions, respectively, and the slope of the solid line represents the material's post-peak stiffness. When the LSS is softer than the material's characteristic post-peak stiffness, failure will be violent due to a sudden release of energy stored in the loading system. On the other hand, when the LSS is stiffer than the material's characteristic post-peak stiffness, the failing material is able to absorb the energy released from the loading system and the failure is stable.

A comparison of LSS and material's post-peak stiffness can be made to study the mechanism of unstable failure. Some researchers used numerical modeling approach to compare the LSS and material's post-peak stiffness (Garvey, 2013; Kias, 2013). An advantage of the computer aided simulations is that one can conduct extensive parametric studies to find the factors such as geometry, size, material, loading system properties, contact properties, etc. that contributes to

unstable rock failure. With the aid of computer simulations, for instance, it has been understood that in an UCS test the specimen's geometry, size and material, loading system properties as well as contact properties between the specimen and the loading system influence the failure mode (in terms of stable and unstable) (Garvey, 2013; Kias, 2013). These findings can be very useful for studying the failure mode in mine pillars because there is an analogy between UCS test in laboratory and pillars in the field. For example, Fakhimi et al. (2016) conducted some experimental and numerical tests to investigate unstable failure of mine pillars. They simulated unstable rock failure of mine pillars by loading a specimen in a soft loading machine. In their laboratory setup, a steel beam was connected to the loading machine and was in contact with the specimen to accumulate energy during loading of the specimen. When the rock specimen failed, the stored energy inside the beam was released violently and in this way the unstable rock failure was captured. They also carried out some numerical investigations (Figure 2-7) to study the influence of pillar's length and diameter, friction coefficient between the pillar and the roof, compressive strength of the pillar, rock post-peak behavior, the roof stiffness, and pillar and roof rock densities on the intensity of the rock failure. They proposed a scaling model to find the significance of different parameters involved in the unstable rock failure.
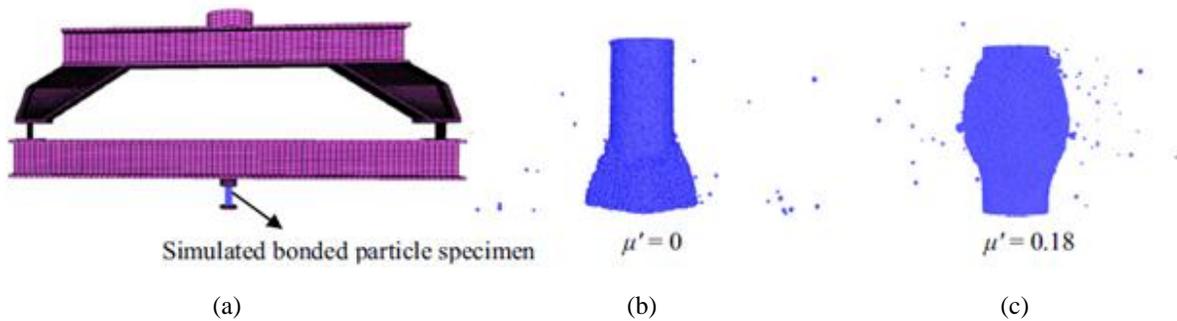
Figure 2-7: (a) FEM model of a frame structure together with the bonded particle rock specimen, and the damaged specimen after the strainburst assuming friction coefficients between the loading platens and the specimen as (b) zero, (c) 0.18 (Fakhimi et al., 2016).

Usually, laboratory testing conditions are designed in such ways that they represent the field conditions. However, the rock behavior in laboratory conditions may be very different from its behavior in the field condition. This difference originates from the different properties of intact rock and rock mass. In general, the presence of discontinuities in rock masses changes the properties of the rock masses. Moreover, due to the existence of uncertainty in geomechanical parameters, it is difficult to adjust the laboratory testing conditions similar to the in situ conditions. Therefore, despite the advantages of laboratory testing for studying the rock behavior, in situ investigations and experiments are needed to have a better understanding of rock behavior for solving practical engineering problems.

Advances in computing technology have enabled engineers to build larger and more detailed models to conduct safer constructions. Rockbursts in underground mines and tunnels can be studied using numerical models. As stated by Salamon (1993), different aspects of the rockburst problem such as the relation between mining activities and the related seismicity, source mechanism, and the effects of seismic waves on mining excavations would benefit from numerical modeling. The mechanisms that drive rockbursts in mines and tunnels are complex.

Many factors (Figure 1-5) may influence the rockburst damage and should be considered in analyses. Failure to give sufficient attention to the influencing factors on rockburst may lead to disasters. The Crandall Canyon Mine disaster, in which several miners were killed and injured, is an example of inappropriate design which resulted in rockbursts (Whyatt, 2008). Investigations have shown that in the models used to design the Crandall Canyon Mine, the strength of the coal pillars was overestimated and the potential of unstable failure was disregarded. This example highlights the necessity of careful recommendations for assessing the threat of unstable failure using numerical models.

Due to the complexity of rockbursts, computer models (which are capable of solving complex boundary value problems) are needed to determine the rockburst potential and damage locations in underground openings (Hedley, 1992). In general, computer modeling along with microseismic monitoring are conducted to determine the potential rockburst locations in underground openings. High stress concentration and energy release rates (ERR) can indicate burst-prone locations. For example, Blake (1972) developed a FEM model to simulate the mining activities in the Coeur d'Alene of Idaho. He showed that areas of high stress concentration surrounding a cut-and-fill stope coincided with rockburst locations determined by microseismic monitoring. As Hedley (1992) stated, the numerical models provide more general results than specific ones. In other words, the modeling results indicate rockburst potential locations but it does not necessarily mean that the rockburst will occur at those locations. Therefore, interpretation of computer modeling should be combined by field observations, geologic survey, seismic data and the area rockburst background in order to make reliable predictions.

In most numerical studies, the main consideration is given to exploring the influence of excavation activities, geotechnical factors, and seismic events on the rockburst occurrences and damages. It has been recognized that a deep underground opening is more burst-prone when it approaches a geological discontinuity such as fault, dyke, and contact (Hedley, 1992; Snelling et al., 2013). However, the influence of geological structures around the underground opening in many numerical studies has been neglected. Typically, the addition of joints, shears, and bedding planes brings an element of realism to the model. Investigations on the role of geological structures on rockburst occurrences and damage may draw a clearer picture of rockburst mechanisms.

2.3.4 Recognition of unstable rock failure in numerical modeling

In numerical modeling, recognition of stable and unstable rock failures is not straightforward. Usually, one or more indicators are needed to interpret the simulation results. Depending on the selected numerical tool, different indicator(s) can be selected. After reviewing the literature, different indicators were found for distinguishing between stable and unstable rock failure in numerical models. In this section, the approaches and some unstable failure indicators used by some researchers for studying the unstable rock failure in the numerical results are briefly reviewed.

Zubelewicz and Mróz (1983) developed FEM models to simulate rockburst in three different mining conditions: dynamic rupture of rock pillars, dynamic failure of excavation faces, and burst of inhomogeneous rocks in the tunnel. They showed that the mode of failure could be studied by solving the initial static and the subsequent dynamic problems. In their study, the FEM model solved full equations of motion explicitly after applying a disturbance to the system.

38

They showed that a failure was unstable when the rate of kinetic energy ($\dot{E}_k$) increased drastically (Figure 2-8).

Bardet (1989) proposed to use surface buckling as a trigger of unstable failure in FEM models. In Bardet's view, surface instability could be detected when the stiffness matrix in a finite element grid became singular. The time that the stiffness matrix value became negative was considered as the time of instability. Müller (1991) used finite element and finite difference methods to simulate rockburst and concluded that the finite difference model was more suitable for modeling rockburst. Oelfke et al. (1996) presented a FEM-DEM hybrid model for analyzing underground mine deformation. They demonstrated that mine instability was a function of local mine stiffness. In their models, divergence of the solution was interpreted as a sign of unstable failure.

Fujii et al. (1997) proposed a numerical approach for the prediction of coal face rockbursts in
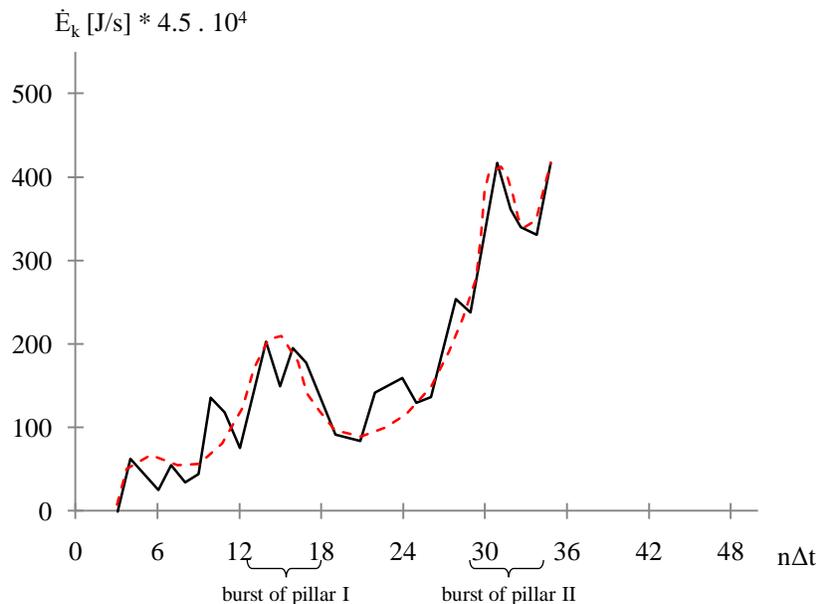
Figure 2-8: Variation of the rate of kinetic energy within the solution domain (dynamic rupture of rock pillars). Dashed line shows the trend (reproduced from Zubelewicz and Mróz (1983)).

39
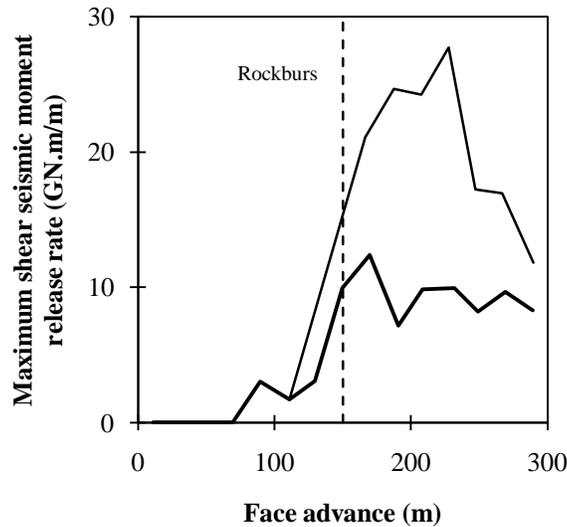
Figure 2-9: Calculated maximum shear seismic moment release rate vs. face advance at Horonai Coal Mine. Thick and thin lines denote contribution of coal seam fracture and the total rate, respectively (reproduced from (Fujii et al., 1997)).

deep longwall coal mining. They developed three dimensional (3D) elastic numerical models using the Displacement Discontinuity Method (DDM). The maximum shear seismic moment release rate was calculated for each mining step to predict the rockburst occurrence. The calculated maximum shear seismic moment release rate began to increase when the face reached the rockburst location.

Chen et al. (1997) developed a double rock sample model to study rockburst mechanism using RFPA. They simulated the progressive failure of the rock and calculated the number of seismic events due to failure. A sudden drop or quiescence of microseismic events was used to identify unstable rock failure. Mitri et al. (1999) proposed a FEM modeling approach to evaluate strainburst potential in mines. They used the computed seismic Energy Release Rate (ERR) and strain Energy Storage Rate (ESR) from the modeling results to develop a Burst Potential Index (BPI). They applied their modeling approach to a Canadian underground mine with rockburst
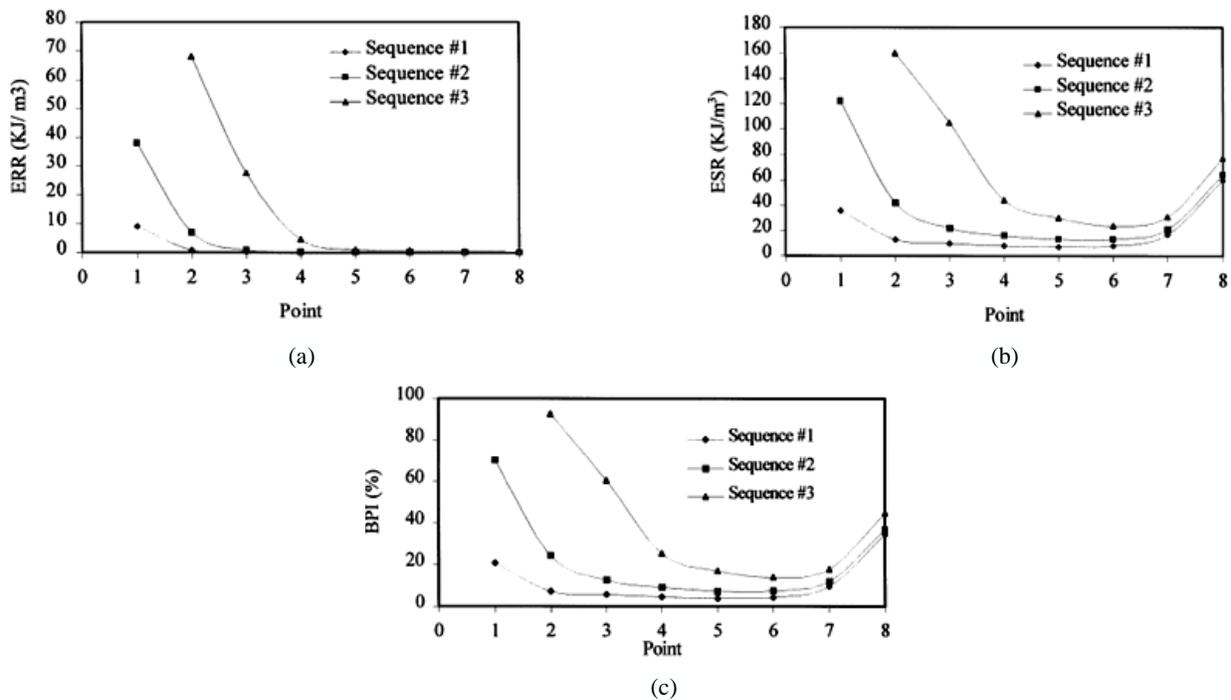
Figure 2-10: Variation of: (a) ERR, (b) ESR, and (c) BPI at monitored points (Mitri et al., 1999).

problems to estimate the rockburst potential in different mining sequences. For this purpose, ERR and ESR at eight monitoring points (p1 to p8) along the cross-section of a crown pillar were computed and then the associated BPIs were calculated (Figure 2-10). They stated that this modeling approach could be suitable for estimating strainburst potential.

Hazzard et al. (2002) used PFC to investigate unstable fault slips caused by underground excavation. They showed that many small tensile cracks were formed before the slip on the fault (Figure 2-11). Cracking/slip started at one point and propagated outwards to form an unstable failure along a large portion of the fault.
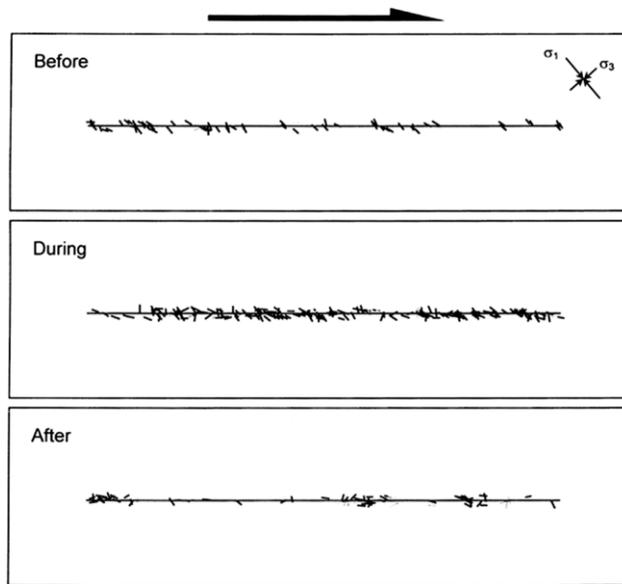
Figure 2-11: Microcracks formed before, during and after the microseismic event in the shear fault simulation. The direction of shear is shown at the top (Hazzard et al., 2002).

Sharan (2007) proposed a finite element perturbation method to study rockburst potential in underground openings using Phase2. He showed the efficiency of the proposed numerical technique by comparing finite element results with analytical solutions for deep circular openings in rock mass subject to hydrostatic in situ stress. When a loading stiffness parameter approached to zero, it was interpreted as a sign of possible rockburst.

Li et al. (2008) used FLAC to investigate the effect of underground coal mining on fault plane stress and slip displacement. Their study showed that the slip displacement increased sharply due to an increase in shear stress and a decrease in normal stress when the working face advanced in the footwall towards the fault. When the working face advanced in the hanging wall towards the fault, however, the slip displacement of the fault was small due to an increase in normal stress and a decrease in shear stress. They confirmed that a high potential of slip-type rockburst existed when the working face moved towards the fault.

Tan et al. (2009) used PFC to simulate unstable failure of pillars in coal mines; they used the velocity of the ejected particles to identify unstable failure. Jiang et al. (2010) proposed Local Energy Release Rate (LERR) as an indicator for identifying unstable failure in FLAC models (Figure 2-12). They compared the numerical results with some known cases of unstable failure at the Jinping II pilot tunnel and noted that their proposed indicator predicted the location and the depth of the rockbursts satisfactorily. However, they could not determine LERR thresholds across which rockburst would occur.

Kias and Ozbay (2013) used a DEM-FDM hybrid modeling approach to analyze unstable failure of coal pillars using PFC and FLAC. The work performed by damping in PFC was used as an indicator of unstable failure. They tested the suitability of their proposed unstable failure indicator in UCS test simulations, and then, applied this numerical approach to a series of pillar tests with different width to height ratios (Figure 2-13). They noted that the developed numerical approach was suitable for studying unstable compressive failure in coal mines.

Garvey (2013) developed PFC and FLAC models to simulate unstable rock failure in UCS test
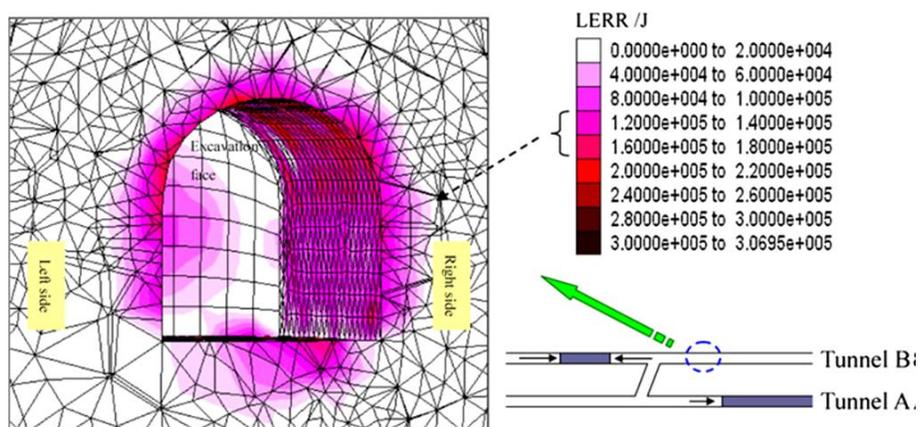
Figure 2-12: Rockburst indicated by LERR at the Jinping II pilot tunnel (Jiang et al., 2010).

and concluded that FLAC was more suitable for modeling unstable rock failure. In his study, the maximum unbalanced force, the maximum acceleration, the maximum velocity, and the maximum shear strain rate were calculated to identify unstable failure (Figure 2-14). He applied this modeling approach to evaluate the unstable failure potential in coal pillars and claimed that the proposed unstable failure indicators, as qualitative measures of unstable equilibria, were appropriate to study dynamic response in FLAC models.
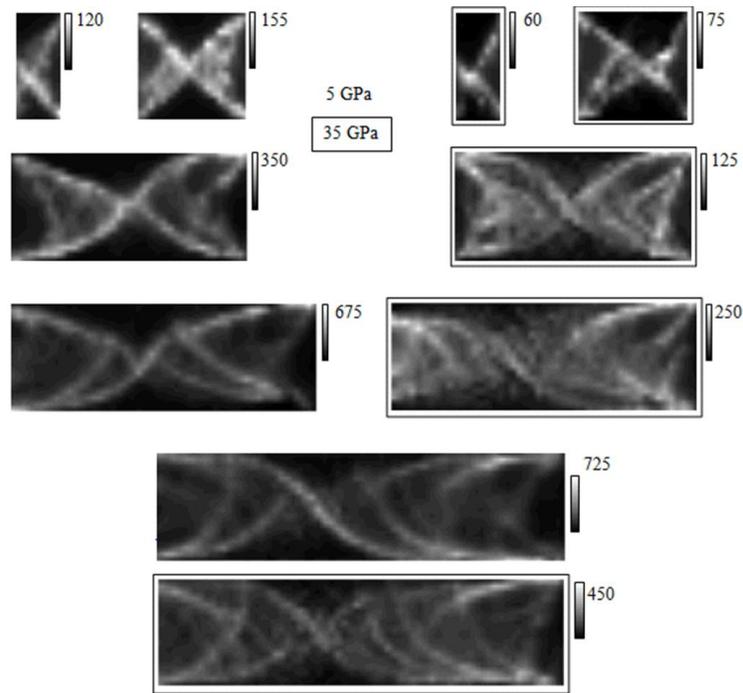
Figure 2-13: Images of cumulative work by the damping mechanism for unstable rock failure identification in pillars (Kias and Ozbay, 2013).
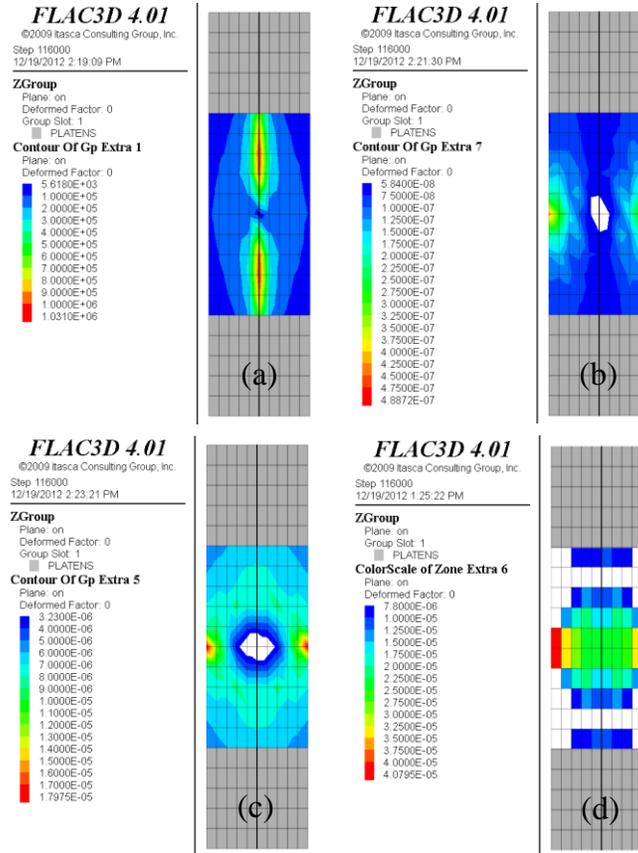
Figure 2-14: Unstable rock failure indicators in UCS test: (a) maximum unbalanced force, (b) maximum acceleration, (c) maximum velocity, and (d) maximum shear strain rate (Garvey, 2013).

Zhang et al. (2014) analyzed rock mass damages due to rockburst in two tunnels in the Jinping II hydropower station. They calculated the Failure Approach Index (FAI) using FLAC to interpret the numerical results (Figure 2-15) and concluded that the dynamic activities could not be simulated by their static numerical method. However, their model was capable of capturing the development of the damage and failure of the rock mass and the process of accumulation and release of the energy storing in the rock mass.

Gu and Ozbay (2015) studied the stability of rock and rock discontinuities in coal mines. They used UDEC models to consider failure stability of both rock discontinuities in slip and coal in compression and showed that the post-failure characteristics of the discontinuity and the loading
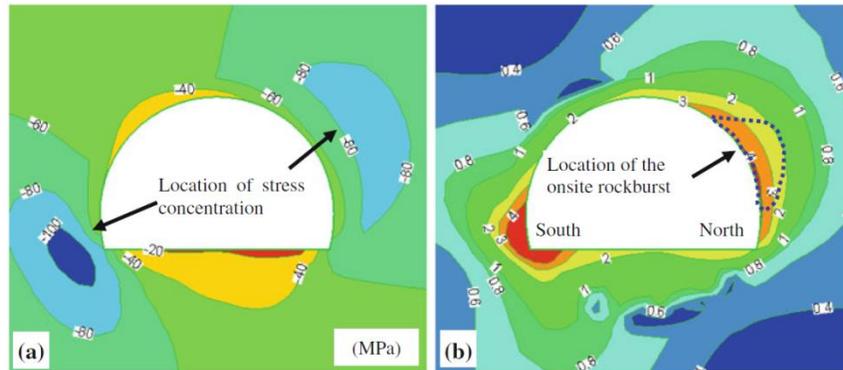
Figure 2-15: Simulated rockburst in Jinping II headrace tunnel No.2; (a) σ_1 distribution, and (b) FAI distribution (Zhang et al., 2014).

stiffness of the surrounding rock could affect the slip failure mode at an existing rock discontinuity. They concluded that unstable rock failure might occur when an unstable slip failure occurred at the coal-rock interfaces.

He et al. (2016) developed DDA models to assess rockburst potential and intensity in discontinuous rock masses (Figure 2-16). In this study, the energy components of the block system were calculated to identify rockburst. They concluded that an increase of in situ stresses and a decrease of frictional resistance of pre-existing discontinuities resulted in an increase in kinetic energy of the ejected blocks. Furthermore, they noted that the rockburst problem could be mitigated using the top heading and bench excavation technique.
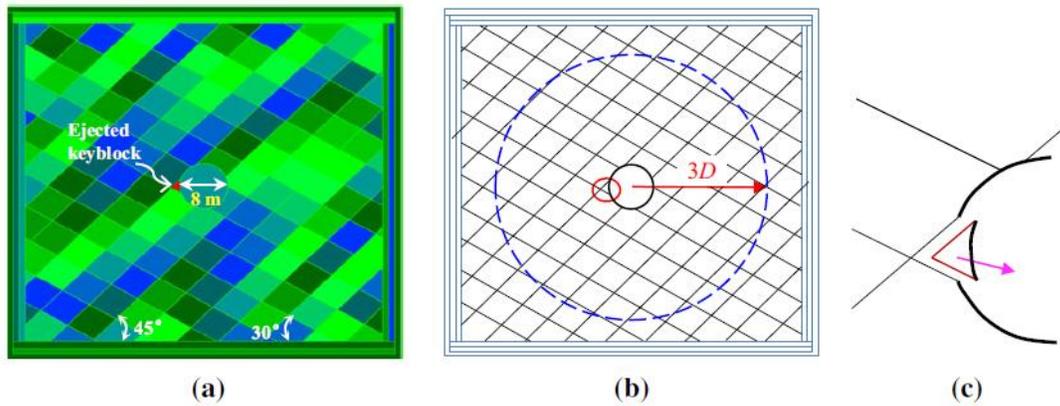
Figure 2-16: A 2D model utilizing a modified version of DDA: (a) blocky rock mass system; (b) analysis domain; and (c) ejected key block (He et al., 2016).

2.4 Final remarks

The case histories presented in this chapter clearly demonstrate the relentless face of the rockbursts. The priceless lessons taught from the rockburst case histories show that the rockburst problem becomes more serious as the excavation process advances to deeper grounds. Moreover, it is understood that underground openings are more burst-prone when they approach to geological structures.

In this chapter, numerical approaches for studying rockburst were reviewed. The studies mentioned in this chapter and many other similar studies have contributed to the understanding of rockburst. Unfortunately, rockburst is still a threatening problem, partially due to a lack of tools that can be used to investigate rockburst mechanism and damage but most importantly due to the fact that rockburst is a very complex phenomenon. More studies are needed for a better understanding of rockburst mechanism so as to control rockburst.

Some numerical studies have demonstrated the capability of using numerical method to study the unstable rock failure and rockburst. However, a missing factor in the previous numerical works is the effect of geological structures on rockburst occurrence and damage. Geological structures can control the behavior of a rock mass and influence its failure modes (stable or unstable). Including geological structures in numerical modeling may lead to revealing the sufficient condition of rockburst and explaining localized rockburst damage along excavation boundaries. Numerical analyses of rockburst considering existing weak planes in rock masses are conducted in this thesis to expand and improve the understanding of rockburst mechanism. The details of numerical simulations are presented in the following chapters.

As discussed in Section 1.4, not all numerical tools are suitable for studying unstable rock failure and rockburst. Before any numerical study, the suitability of the selected tool should be tested and if needed, improvements should be made. In the next chapter, the failure behaviors of rock specimens under uniaxial compression and polyaxial unloading conditions will be simulated using Abaqus-Explicit to confirm the suitability of the tool for simulating unstable rock failures.

Chapter 3

3 Simulation of unstable rock failure in laboratory tests

3.1 Introduction

Rocks in the ground before excavation are under a polyaxial stress loading condition. Excavation of an opening changes the stress state near the excavation boundaries. Rocks near the excavation boundaries are unloaded in the radial direction and loaded in the tangential direction. In deep grounds where rock strength is high, the tangential stress can increase to a high value before the rocks fail, which means that a large amount of strain energy can be stored in the rocks. This is one of the necessary conditions for unstable failure to occur. In some cases, unloading of the rocks due to excavation could cause the rocks to fail. Therefore, it is necessary to study the potential of unstable rock failure under unloading conditions.

Some researchers investigated rock failure behaviors under unloading conditions using analytical, experimental, and numerical methods (He et al., 2010; He et al., 2012a; Li et al., 2013; Li et al., 2014; Sun et al., 2007; Tao et al., 2012; Zhao and Cai, 2015; Zhu et al., 2014). In this chapter, the failure behaviors of rock specimens under uniaxial compression and polyaxial unloading conditions are investigated using Abaqus-Explicit. Abaqus-Explicit is equipped with an explicit solver that makes it suitable for solving problems involving unstable failure. Firstly, the capability of Abaqus-Explicit for capturing unstable failure is verified. In laboratory uniaxial compression tests, if the LSS is smaller than the rock's characteristic post-peak stiffness, the failure will be violent and unstable; otherwise the failure is stable. Thus, uniaxial compression

tests are simulated using different machine LSS to verify Abaqus's suitability to simulate unstable rock failure. Secondly, rock failure under polyaxial unloading conditions is studied and the released kinetic energy is calculated. The influences of LSS, specimen's height to width ratio (H/W), and intermediate principal stress (σ_2) on rock failure are also investigated.

3.2 Finite element modeling of post-failure behavior of rocks

Studies show that the materials subjected to compressive loads may show different post failure behaviors (Goodman, 1989; Paterson, 1958; Zheng et al., 2005). These types of post-failure behaviors can be categorized into four groups: (i) brittle, (ii) strain-softening, (iii) plastic, and (iv) strain-hardening. The typical deformation behaviors of materials under compressive loads are illustrated in Figure 3-1a, with idealized stress–strain curves shown in Figure 3-1b.

Rocks may show any of the four types of deformation behaviors depending on the loading conditions. For example, a rock specimen may show brittle or strain softening behavior after the peak load in uniaxial and low confinement triaxial compression tests. However, the same rock
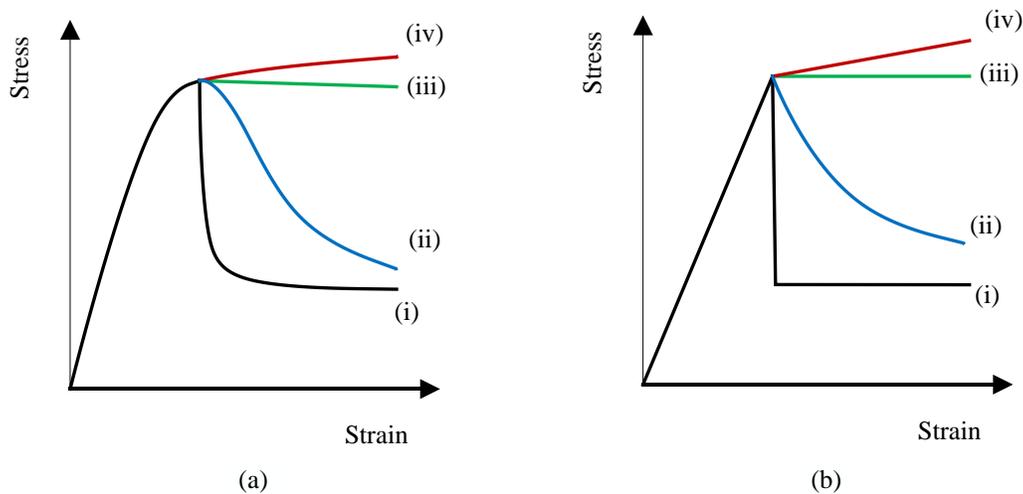
Figure 3-1: (a) Stress–strain curves observed in laboratory test of rock and soil specimen, and (b) idealized stress–strain curves for different models.

50

specimen may show plastic or strain-hardening behaviors when the confinement is increased (Hoek and Brown, 1997; Read and Hegemier, 1984; Wang et al., 2011a).

The classification of the post-failure behaviors of materials constitutes four corresponding constitutive models for modeling the material response to mechanical loads: (i) elasto-perfectly brittle-plastic, (ii) elasto-plastic strain-softening, (iii) elasto-perfectly plastic, and (iv) elasto-plastic strain-hardening models (Figure 3-1b). In these models, the following assumptions are made to simulate a material's post-failure behavior:

- in elastic-brittle-plastic models, the strength parameters drop abruptly from peak values to the residual ones;

- in elasto-plastic strain-softening models, the strength parameters decrease gradually from peak to residual values as the deformation increases;

- in elasto-perfectly plastic models, the strength parameters keep constant after the stress reaches the materials strength; and

- in elasto-plastic strain-hardening models, the strength parameters increase in the plastic state as deformation increases.

Elasto-plastic strain-softening models can be used to study the mechanical behavior of many rock types (Wang et al., 2011a). However, a limit to the rate of softening of the strain-softening material exists within the framework of the classical theory of plasticity. A fundamental problem of incorporating strain-softening materials in standard continuum models is the inherent mesh sensitivity that occurs after reaching a certain softening level (Bazant et al., 1984; Bazant and Oh, 1985; Bazant and Pijaudier-Cabot, 1988; de Borst, 2013). This mesh sensitivity goes beyond the standard discretization sensitivity of numerical approximation methods for PDEs and is not

related to deficiencies in the discretization methods. Instead, the underlying reason for this mesh sensitivity is a local change in character of the governing PDEs. This local change of character of the governing set of PDEs leads to a loss of well-posedness of the initial boundary value problem and results in an infinite number of possible solutions (de Borst, 2013). A problem is well-posed if three conditions exist: (i) a solution exists, (ii) the solution is unique, and (iii) the solution depends on the initial conditions continuously (Hadamard, 1902). Discretization of the domain results in a finite number of solutions. For a finer discretization, the number of solutions increases, which explains the observed mesh sensitivity.

The problem of mesh sensitivity is a fundamental problem and one cannot avoid this issue if a strain-softening model is used. In this thesis, a constant mesh size is selected in all models in each study so that the errors associated with the mesh size would be the same in all models. In this way, a relative comparison of the simulation results can be made.

3.3 Uniaxial compression test simulation

3.3.1 Model calibration and boundary conditions

In this section, the Abaqus-Explicit code is used to simulate unstable rock failure in uniaxial compression tests to check its applicability for solving unstable rock failure problems. Firstly, the mechanical and physical properties (Table 3-1) of Tianhu granite (Zhao and Cai, 2015) are used to calibrate the models. In the study conducted by Zhao and Cai (2015), seven rectangular prisms with four different H/W ratios (1.0, 1.5, 2.0, and 2.5) were prepared in their test to study the rockbursting behavior of Tianhu granite. Specimens were approximately 60 mm in width, 30 mm in thickness, and the height varied between 60 mm and 150 mm. Uniaxial compression and Brazilian tests were conducted on cylindrical specimens from the same rock to obtain the basic

mechanical properties of the rock. The prepared prismatic specimens were tested using the polyaxial unloading machine at China University of Mining Technology in Beijing to study the dynamic response of rock to the unloading due to excavation. The prismatic specimens were loaded in three directions: σ_1, σ_2, and σ_3. In each test, the principal stresses were increased gradually to the in situ stress level at a depth of 500 m (σ_1 = 20 MPa, σ_2 = 13 MPa and σ_3 = 12 MPa). Then, the specimens were unloaded in the minimum principal stress direction (σ_3), the intermediate principal stress (σ_2) was kept constant and the maximum principal stress (σ_1) was increased until failure of the specimens occurred. It should be noted upon unloading of σ_3, the specimens did not failure and additional loading in the axial direction was needed to bring the rock to failure. Test results showed that the peak strength decreased gradually and approached to a constant value when the H/W ratio increased from 1.0 to 2.5 (Zhao and Cai, 2015).

An elasto-plastic Mohr-Coulomb softening model is used to model the strength behavior of the rock. The laboratory tests (uniaxial compression, triaxial compression, and Brazilian tests) are simulated to calibrate the model parameters. In the uniaxial and triaxial compression test simulations, cylindrical specimens with a height of 100 mm and a diameter of 50 mm are used. In the Brazilian test simulation, discs with a diameter of 50 mm and a thickness of 10 mm are used (Figure 3-2). In the uniaxial compression test simulation, one end of the specimen is fixed in the vertical direction and the other two horizontal directions are free (roller constraint) and a constant velocity of 0.015 m/s is applied directly to the other end of the specimen to apply load. The same end boundary conditions are applied to the specimens in the triaxial compression test simulation and the confinements applied are 20, 50, and 100 MPa. In the Brazilian test simulation, the specimens are loaded by two platens; one platen is fixed and the other is moved

at a constant velocity of 0.015 m/s to apply load. Model geometry, boundary conditions, and mesh in uniaxial (and triaxial) compression and Brazilian tests are illustrated in Figure 3-2.

No data exist for the post-peak behavior of the Tianhu granite that can be used to calibrate the post-peak behavior of the rock. Hence, the post-peak stress–strain curves of a typical hard rock are assumed. The objective is to simulate unstable rock failure considering the relative values of the post-peak stiffness of the rock and the loading machine stiffness.

Table 3-2 summarizes the adjusted parameters for defining the post-peak behavior of the rock. The friction angle is fixed at 40°, and the cohesion is weakened as a function of the plastic shear strain. The tensile strength is also modeled as a function of the plastic tensile strain.
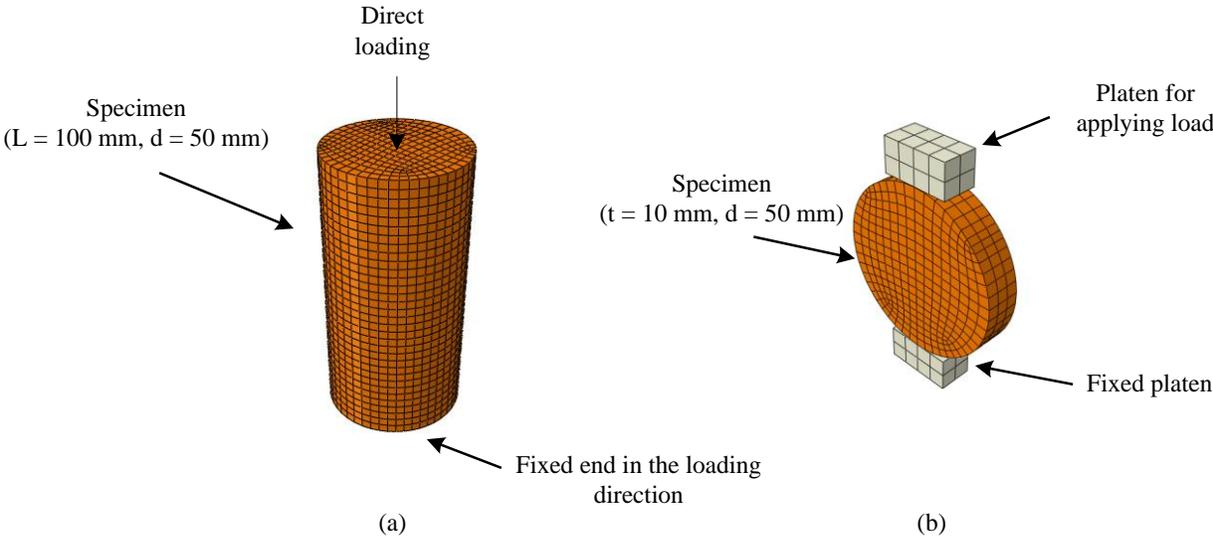
Figure 3-2: Abaqus model geometry and mesh in (a) uniaxial (and triaxial) compression and (b) Brazilian test simulations.

Table 3-1: Physical and mechanical properties of the simulated rock

Parameter	Test value	Simulated value
Density, ρ (kg/m^3)	2650	2650
Young's modulus, E (GPa)	51	51
Poisson's ratio, v	0.27	0.27
Uniaxial compressive strength, UCS (MPa)	160	160
Brazilian tensile strength (MPa)	7.1	7.4

Table 3-2: Strain-softening parameters of the model

Cohesion		Tension cut-off	
Cohesion yield stress (MPa)	Absolute plastic shear strain	Tension cut-off stress (MPa)	Tensile plastic strain
37.5	0	10.02	0
35	0.0025	0.01	0.015
30	0.009		
25	0.017		
20	0.028		
15	0.041		
10	0.058		
5	0.085		
0.01	0.11		

The platen length is varied and its elastic modulus is kept constant at E = 200 GPa to account different loading system stiffness in the numerical modeling. A cylindrical platen with a diameter of 54 mm and a length between 50 and 800 mm is simulated, and the dimension of the cylindrical specimen is 100 mm (height) × 50 mm (diameter). A model with LSS = 9.16 GN/m is presented in Figure 3-3. The LSS is calculated using Eq. (2-13). The mechanical and physical properties of the rock listed in Table 3-1 and steel properties (i.e., E = 200 GPa, v = 0.3 and ρ = 7700 kg/m^3) are assigned to the rock and the platen, respectively. Frictionless contact is assigned to the contact between the platen and the specimen to exclude the friction effect.
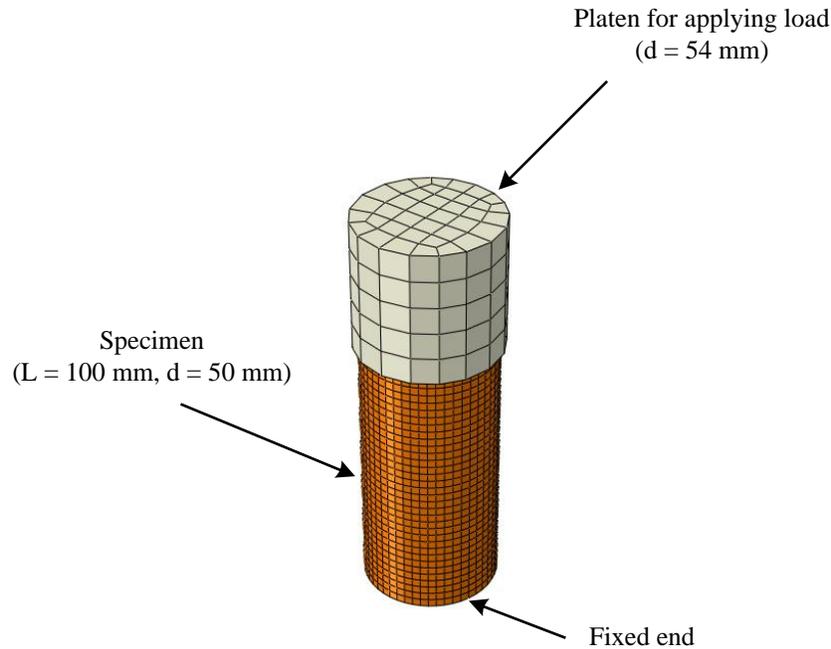
Figure 3-3: Abaqus UCS model geometry and mesh.

3.3.2 Influence of LSS on failure behavior

Figure 3-4 presents the stress–strain relations for specimens with LSS varying from 0.57 to 9.16 GN/m. To reveal the characteristic behavior of the rock, a case with rigid loading (i.e., infinite loading system stiffness) is simulated and the results is labeled as "Material" and represented by the dashed line in Figure 3-4. This rigid loading condition is simulated by applying a constant velocity of 0.015 m/s directly to the specimen's top end. The calculated post-peak stiffness of the specimen at the steepest part in the stress–strain curve is 4.23 GN/m. The simulation results show that when the LSS is smaller than the post-peak stiffness of the rock, the specimen's post-peak curve deviates significantly from the rock's characteristic post-peak curve due to a strong reaction of the platen caused by rock failure. This type of post-peak response in the form of unstable failure has been observed in laboratory test (Stavrogin and Tarasov, 1995). When the LSS is greater than the post-peak stiffness of the rock, there is only a very small deviation of the

56
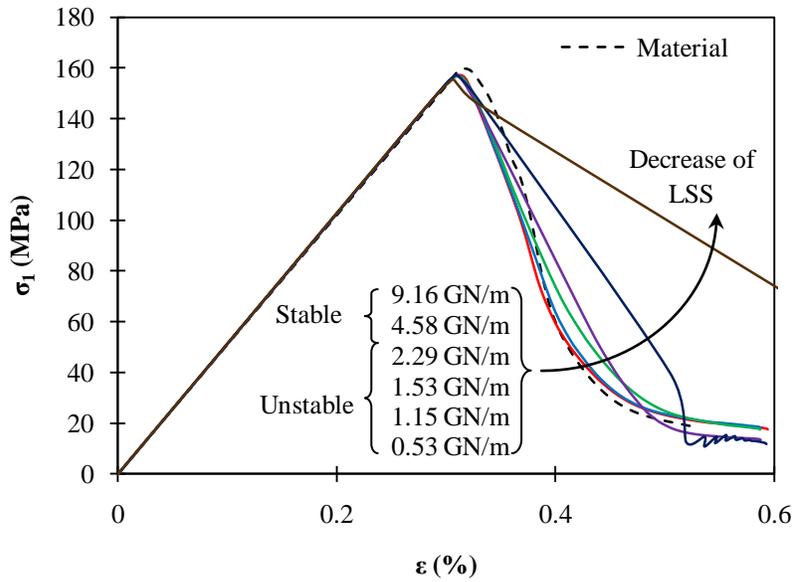
Figure 3-4: Stress–strain curves with different loading system stiffness simulated using Abaqus-Explicit.

specimen's post-peak curve from the rock's characteristic post-peak curve. The results demonstrate that the Abaqus-Explicit solver can be used to simulate unstable rock failure.

Some numerical models might be unstable; hence, it is important to ensure that the captured instabilities shown in Figure 3-4 are due physical instability, not numerical instability. As stated above, the post failure behavior of rock is controlled by the loading system in an unstable rock failure. Figure 3-5 shows the force–displacement curves of the UCS models with different LSS values (k). This figure indicates that the rock behavior is not influenced by the loading system when the rock failure is stable. For example, when k = 9.16 GN/m the post-failure behavior of the rock is stable (thin red line), and is the same as the material behavior (black dash line), but is different from the loading system behavior (thick red line). Furthermore, it can be clearly seen that for relatively softer loading systems, the post-failure behavior of the rock is controlled by the loading system. For instance, when k = 0.57 GN/m the post-failure behavior of the rock (thin
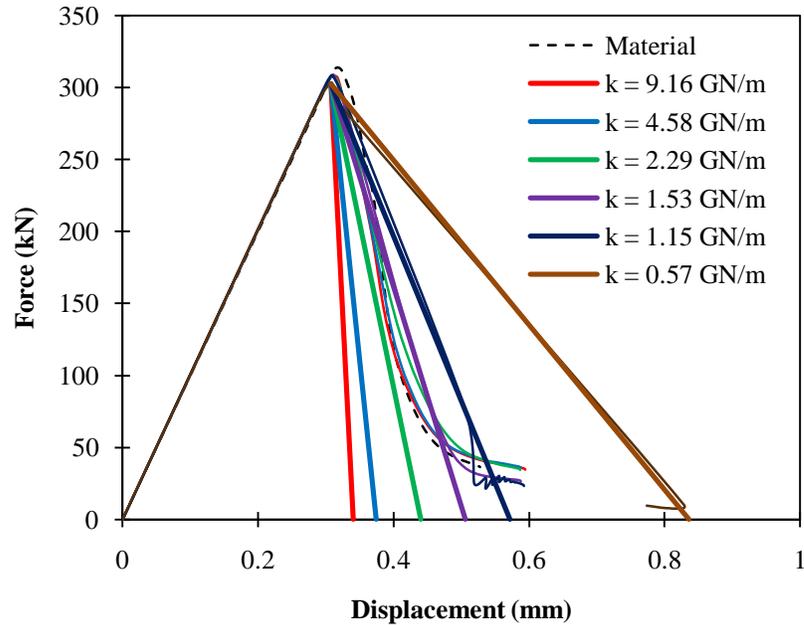
Figure 3-5: Force–displacement curves with different loading system stiffness simulated using Abaqus-Explicit. The thin and the thick lines for each LSS value represent the response of the specimen and loading system, respectively.

brown line) is not the same as the material behavior (black dash line) but matches the loading system behavior (thick brown line). Therefore, it can be concluded that the instability shown in the modeling results is due to instability of the physics of the problem, not instability of the numerical solution.

3.3.3   Loading System Reaction Intensity (LSRI)

When a rock fails, the stored strain energy in the loading system is released and part of that energy is transferred to the rock. If the rock is capable of absorbing the transferred energy then the failure is stable; otherwise, the excessive energy from the loading system will cause the rock to fail in an unstable manner. In other words, rock failure can cause a sudden reaction of the loading system which will then push the failing rock and potentially cause rapid ejection of

fractured rocks (as seen in some laboratory tests or in the field). This push action can cause ejection of fractured rocks at an ejection velocity up to a few meters per second (He et al., 2010; Milev et al., 2001).

Previous experimental and numerical studies have shown that softer loading systems lead to more violent failure (Garvey, 2013; Hedley, 1992; Kias and Ozbay, 2013; Salamon, 1970; Wawersik and Fairhurst, 1970). Thus, it can be inferred that the larger the excessive energy is, the faster and stronger the reaction will be from the loading system. Videos recorded from laboratory tests show that when a rock fails violently, a noticeable reaction of the platens of the loading system can be observed. In contrast, the reaction of the platens during a stable failure is not obvious and only sensitive monitoring equipment can capture the movement of the platens. The loading system reaction can thus be used to identify unstable failure.

The reaction of the platen during rock failure is examined in this study. In the numerical models, velocities at all nodes can be tracked, which can be used to identify the change of velocity over time. In this research, an indicator, called the Loading System Reaction Intensity (LSRI), is proposed to identify unstable failure. LSRI is defined as the ratio of the maximum velocity (V_{max}) of the platen (Figure 3-6) to the applied loading velocity (V_0 at the platen's top end), i.e.,

$$LSRI = \frac{V_{max}}{V_0}$$
(3-1)
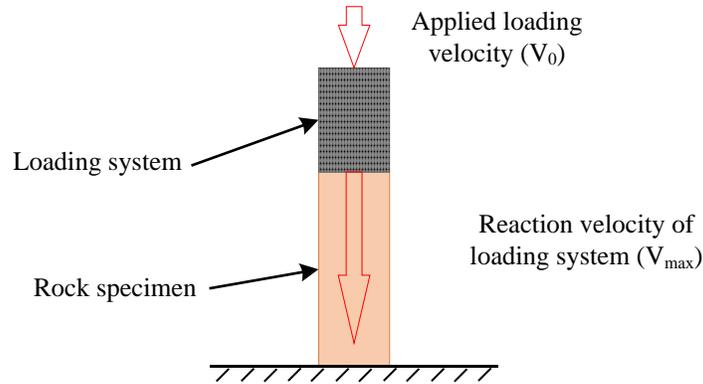
Figure 3-6: A schematic drawing showing the velocity applied to the loading system and the velocity at the platen-rock interface.

V_{max} often occurs at the contact between the platens and the specimen. Using the model parameters listed in Table 3-1 and Table 3-2, the model shown in Figure 3-3 is simulated and LSRI values with different LSS values are calculated and the results are presented in Figure 3-7. When the LSS values are much smaller than the rock's post-peak stiffness, the failure is unstable and the post-peak curve deviates significantly from the rock's characteristic post-peak curve (Figure 3-4). In this case, the LSRI values are very high (>> 1). When the LSS value is much larger than the rock's post-peak stiffness, failure is stable and the LSRI values are small (< 2). When the LSS value is only slightly smaller than the rock's post-peak stiffness, theoretically the failure is unstable. However, when the data points are plotted in Figure 3-7, it shows that the change from low LSRI values to high ones is not abrupt, but rather than gradual. It seems that there is a transition zone as indicated in Figure 3-7. When the data points are in this transition zone, it means that the rock failure will not necessarily result in violent rock ejection. In other words, if the LSS value is slightly smaller than the material's post-peak stiffness, the failure may be in a mode of transition between stable and unstable failures. In reality, this condition can occur in the form of sudden spalling of the skins of the specimen in laboratory or sudden spalling of rock slabs at excavation boundaries. This type of rock failure is not violent and should not be
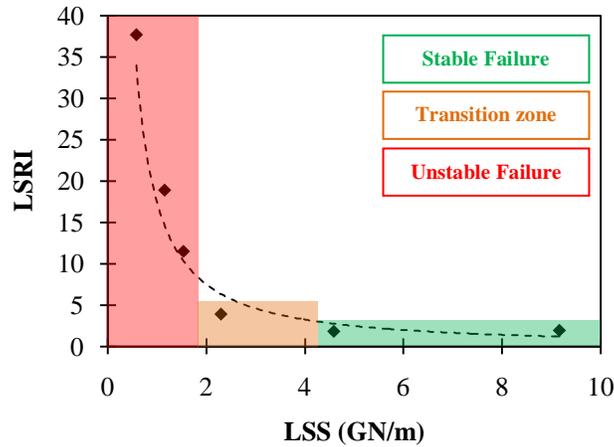
Figure 3-7: Relation between the loading system reaction intensity (LSRI) and LSS.

classified as rockbursts. The numerical simulation result implies that there is no clear boundary between stable and unstable failures. According to the data shown in Figure 3-7, LSRI values between 2 and 6 most likely show a less violent transitional failure of the rock under uniaxial compression.

3.3.4 The maximum kinetic energy (KE_{max})

When a rock fails, part of the strain energy stored in the loading system and the rock is released in the form of kinetic energy. If the stiffness of the loading system is smaller than that of the rock's post-peak stiffness, then more energy is released from the loading system than what the rock can absorb during failure and the failure process will be unstable. Otherwise, the rock can fail in a stable manner. In other words, unstable rock failure is influenced and caused by a large amount of energy transferred from the loading system. Hence, the rock failure behavior is governed by both the amount of energy stored in the rock and the loading system before failure and the loading system stiffness.
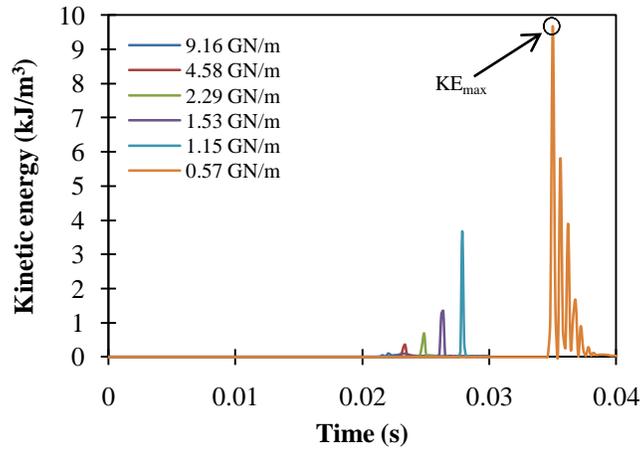
Figure 3-8: The released unit energy from the specimen in UCS test models with different LSS.
Numerical simulation allows the kinetic energy to be calculated. In this study, the kinetic energy

from the failing rock is calculated. Figure 3-8 illustrates the released unit energy from the rock

specimen in the UCS test models with different LSS. This figure shows that more kinetic energy

is released when LSS is smaller. In this study, the released maximum kinetic energy is

normalized by the volume of the specimen to give a maximum unit kinetic energy (KE_{max}) and is

used to interpret the modeling results.

Figure 3-9 presents the relation between KE_{max} and LSS in uniaxial compression. It shows that

when LSS is much smaller than the material's post-peak stiffness (4.23 GN/m), unstable failure

occurs and the corresponding KE_{max} is high (i.e. > 1.0 kJ/m^3). When the LSS is greater than the

material's post-peak stiffness (4.23 GN/m), the failure is stable and the KE_{max} value is small (i.e.

< 0.1 kJ/m^3). Because the specimen's post-peak curve is not deviated significantly from the

rock's characteristic post-peak curve when LSS is equal to 2.29 GN/m (Figure 3-4), this case is

called the "transition" zone that is indicated in and Figure 3-9.
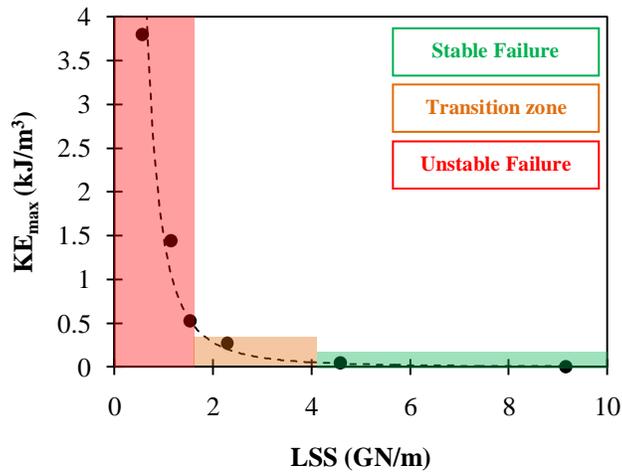
Figure 3-9: Relation between the maximum unit kinetic energy and LSS.

Figure 3-7 and Figure 3-9 show similar trends; similar to LSRI, KE_{max} can be used for identifying unstable rock failure in numerical simulation. The advantage of using LSRI is that it is simple and straightforward, and the LSRI value can be directly observed or measured in laboratory tests. In complex loading conditions, the identification of the reaction velocity during unstable rock failure may not be easy and the energy approach provides an alternative for unstable rock failure identification.

In this research, a platen with steel properties was used in numerical models to apply load to the rock specimen and the LSS was varied by changing the platen's length (*L*) (See Eq. (2-13)). An alternative approach to change LSS in numerical models is changing the platen's Young's modulus (*E*) while keeping the platen's size (*A* and *L*) constant. In the method used in this research, the mass of the loading system was varied by changing the LSS while in the second approach the mass was constant. Stavrogin and Tarasov (1995) noted that the dynamic behavior of a specimen in UCS tests depends on the mass of the loading system. Therefore, the calculated KE_{max} and LSRI from these two approaches will be different for the same LSS.

The influence of loading system mass on rock dynamic response is briefly addressed in Appendix B. Numerical results presented in Appendix B approves that the dynamic behavior of rocks depends on both the stiffness and the mass of the loading system. The numerical results presented in Figure 3-6 to Figure 3-8 show the dynamic behavior of rock due to changes in LSS and the mass of the loading system at same time. Because the purpose of this research is capturing unstable rock failure in numerical models; hence, the influence of different testing conditions on dynamic behavior of rock was not investigated in details.

3.4 Polyaxial unloading test simulation

Changes in stress state associated with underground excavation can be simulated using polyaxial unloading tests in laboratory (Figure 3-10). After excavation, the minimum principal stress is reduced to zero at the excavation boundary, the intermediate principal stress is unchanged, and the maximum principal stress is increased. Displacement and rock ejection are only possible on the free surface of the tunnel and this has been simulated using the polyaxial test system shown in Figure 3-11.

Commonly used failure criteria for rocks, such as the Mohr-Coulomb and Hoek-Brown failure criteria, are expressed using the minimum and maximum principal stresses and the influence of the intermediate principal stress is ignored. Laboratory and numerical results (Brady and Brown, 2013; Cai, 2008a; Mogi, 1967; Wiebols and Cook, 1968) have shown that the intermediate principal stress influences the failure process by confining the cracks in rock specimens such that the cracks can be developed in the direction parallel to the $\sigma_1 - \sigma_2$ plane. The intermediate principal stress induces frictional stress on the surfaces between the specimen and the platens. The frictional stress changes the stress field inside the specimen and affects the failure process

64

and peak strength. If there is no frictional contact for σ_2 loading, increasing the intermediate principal stress produces small increases in the peak strengths of rocks. Hence, a simplification to ignore the influence of σ_2 on rock strength is justifiable (Brown, 2008).

In 3D models, the influence of the intermediate principal stress on rock strength by inducing frictional stress to confine cracks can be captured successfully using the Mohr-Coulomb and Hoek-Brown failure criteria without including the intermediate principal stress in the failure criteria (Cai, 2008a; Pan et al., 2012; Shi and Li, 2009). Thus, in this study a Mohr-Coulomb strain-softening failure criterion is used to simulate above mentioned polyaxial test system. The goal is to achieve a better understanding of the rock failure behavior under polyaxial unloading conditions.

In the following discussion, the laboratory test conducted by Zhao and Cai (2015) is simulated. In the numerical simulation, the stress path shown in Figure 3-12 is considered. Three pairs of platens in the three principal stress directions are used to apply the stresses (σ_1, σ_2, and σ_3). In the simulation, σ_1, σ_2 and σ_3 are increased to 20, 13 and 12 MPa, respectively. Then, the specimen is unloaded in the σ_3 direction by removing one of the platens in this direction. σ_2 is kept constant and σ_1 is increased until failure occurred. A friction coefficient of 0.2 is set for the contacts between the specimen and the platens. Hexahedral eight-node linear elements are used and the model geometry and meshes are presented in Figure 3-13. In the numerical models, the rock specimen size is 150 (height) $\times$ 60 (width) $\times$ 30 (thickness) mm^3. In the following sections, the influences of LSS, specimen's H/W ratio, and intermediate principal stress (σ_2) on the rock failure behavior are discussed.
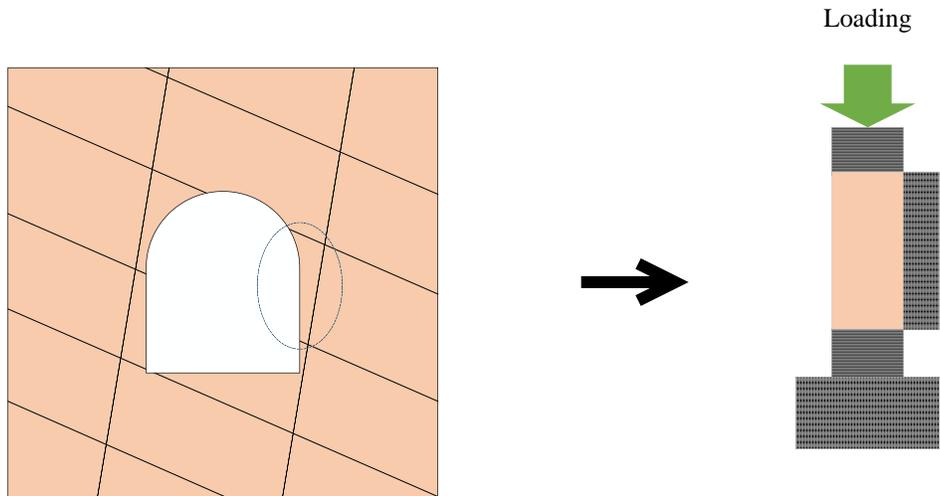
Figure 3-10: Representation of stress state at underground excavation boundaries in laboratory.
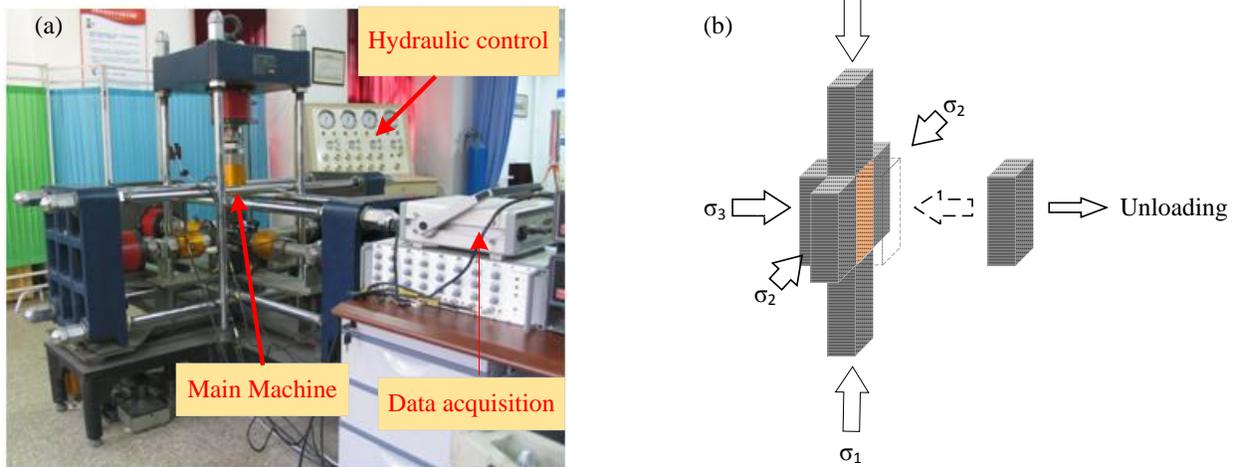
Figure 3-11: (a) The polyaxial test machine (He et al., 2012a); (b) a schematic diagram showing unloading in the σ_3 direction in the tests.
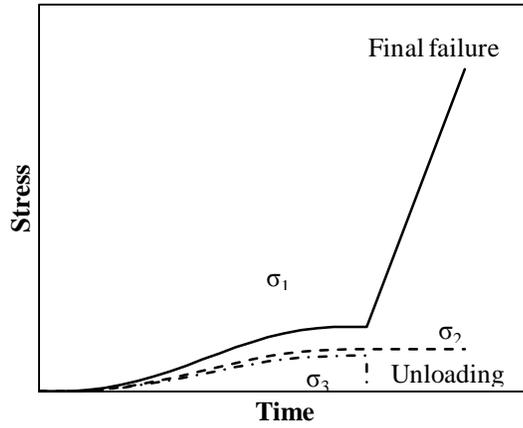
Figure 3-12: Designed stress path in the numerical simulation.
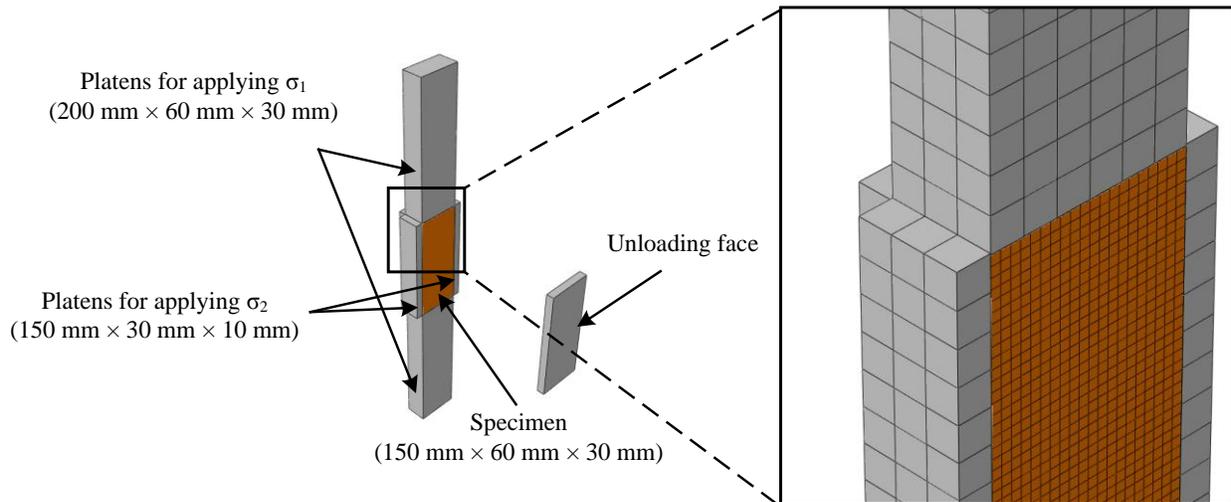
Figure 3-13: Polyaxial model geometry and mesh.

3.4.1　Influence of LSS on failure behavior

The total strain energy inside an elastic column under an axial loading can be calculated from

$$U = \frac{\sigma^2 AL}{2E} \qquad (3\text{-}4)$$

where σ is the axial stress, A is cross sectional area, L is the length, and E is the Young's modulus. Eq. (3-4) means that when a material is soft (e.g., with a small E), large or long (i.e., large A or L values), or under high stress, it stores more strain energy. Hence, when longer platens are used in the simulation while keeping A and E constant, more strain energy will be available for release from the loading system after the specimen fails. When A, E, and L are constant (i.e., the machine stiffness is constant) and the rock strength is high, more strain energy will be available for release from the loading system after the specimen fails. If the unstable failure condition is met, then the failure will be more violent in such conditions.

Five different loading systems consisting of three pairs of platens in the three principal stress directions are modeled to study the influence of LSS on the rock failure behavior and its effect on the released kinetic energy. It is difficult to calculate the loading system stiffness of the test machine shown in Figure 3-11a. The stiffness of the machine in the three principal stress directions is approximately equal. Because the load in the maximum principal stress direction drives rock failure, only LSS in this direction is varied in the numerical simulation and the LSS in the intermediate and the minimum principal stress directions are kept constant. The platen sizes in the maximum principal stress direction are 60 mm in width and 30 mm in thickness and the height varied from 200 to 1600 mm. This results in LSS values varying from 1.8 to 0.225 GN/m. Steel properties (i.e., $E = 200$ GPa, $v = 0.3$ and $\rho = 7700$ kg/m^3) are assigned to the platens. A loading velocity of 0.015 m/s is applied to the top end of the top platen.

The influence of LSS on the maximum released unit kinetic energy from the specimen (KE_{max}) and LSRI are presented in Figure 3-14 and Figure 3-15, respectively. According to Figure 3-14, when the specimen is loaded in a soft loading system the released kinetic energy from the specimen is larger than that from the specimen which is loaded in a stiff loading system. The peak kinetic energy can be as high as 70 kJ/m^3 for the case when the LSS is equal to 0.225 GN/m. Energy absorption rockbolts should be used to support tunnel walls under such a loading condition (Cai, 2013b; Cai and Champaigne, 2012).

Figure 3-15 indicates that the LSRI values for models with smaller LSS values are large. The post-peak stiffness of the rock obtained from the uniaxial compression test is 4.23 GN/m. In a uniaxial compression test, if the LSS value is smaller than the post-peak stiffness of the rock, unstable failure will occur. Without considering the difference in loading conditions, one may judge that failure should be unstable if the LSS value in the polyaxial unloading condition is smaller than the post-peak stiffness of the rock in uniaxial compression (i.e. 4.23 GN/m). However, confinement in the intermediate principal stress direction and friction between the platens and the rock affect the failure behavior of the rock, making it less brittle. As a result, the post-peak failure behavior in the polyaxial unloading is different from that in uniaxial compression. In the case of LSS = 1.8 GN/m, the LSRI is 1.71.
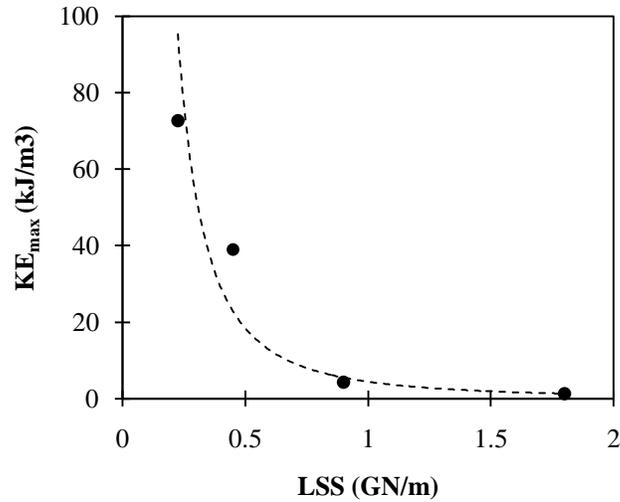
Figure 3-14: Influence of LSS on the maximum released unit kinetic energy (H/W= 2.5, σ_2 = 13 MPa).

Based on the understanding from the uniaxial compression test simulation, the rock failure is stable when LSRI is less than 2. Hence, it is possible to state that the rock failure is stable for LSS = 1.8 GN/m. When the LSS value is very small at 0.225 GN/m, the LSRI value is 54.4. In this case, more kinetic energy is transferred from the platens (or the loading system) to the specimen and the failure is unstable. In this study, LSS was varied by changing the platen length which results in a change of the mass of the loading system. Hence, the results presented in Figure 3-14 and Figure 3-15 show the dynamic behavior of rock due to a change of LSS and the mass of the loading system at the same time.
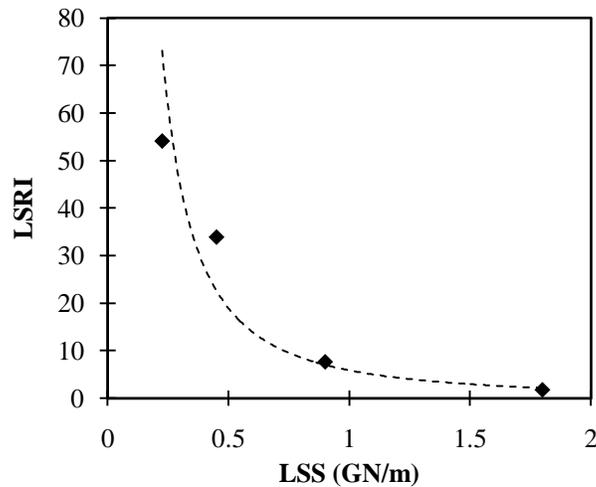
Figure 3-15: Relation between LSS and the loading system reaction intensity (LSRI) obtained from the polyaxial unloading test simulation (H/W= 2.5, σ_2 = 13 MPa).

3.4.2 Influence of H/W ratio on failure behavior

The mechanical behaviors of rocks are size or scale dependent. Many researchers have studied the influences of specimen size and shape on the strength and fracturing characteristics of rocks in laboratory (Bazant and Xiang, 1997; Bieniawski, 1968; Hoek and Brown, 1980; Hudson et al., 1972a; Hudson et al., 1972b; Li et al., 2011a; Mogi, 1962, 2007). Test results have shown that specimens with a lower height to width (H/W) ratio fail at a higher stress. On the other hand, when a specimen is shorter, the post-peak portion of the complete stress–strain curve is more ductile (Hudson et al., 1972a).

Four rectangular prism specimens with different H/W ratios are modeled to understand the influence of specimen height to width ratio (H/W) on the rock failure behavior and the released kinetic energy. In this simulation, all specimens are 60 mm in width and 30 mm in thickness. The height of the specimens is varied at 60, 90, 120, and 150 mm, resulting in H/W ratios of 1, 1.5, 2, and 2.5. The rock mechanical parameters listed in Table 3-1 and Table 3-2 are used. The specimens are subjected to an intermediate principal stress of 13 MPa, the same as that used in

71

the laboratory test (Zhao and Cai, 2015). A LSS of 0.45 GN/m (with a total platen length of 800 mm) in the maximum principal stress direction is set for all models, and the same modeling procedure described in Section 3.4.1 is used.

Figure 3-16 presents relation between the H/W ratio and the rock strength (σ_1) obtained from the experiment (Zhao and Cai, 2015) and the simulation. It is seen that the H/W ratio influences the peak strengths of the specimens. When the H/W ratios vary from 2.5 to 1.5, the peak strengths increase slightly but the peak strength for the specimen with H/W = 1 is high. The trend that the peak strength decreases and approaches a constant strength value as the H/W ratio increases from 1 to 2.5 can be seen from the figure. This is in good agreement with the results from the laboratory tests (Zhao and Cai, 2015). The influence of the H/W ratio on rock strength is mainly due to the end effect caused by the friction between the platens and the specimens.

Figure 3-17 presents the maximum released kinetic energy from the specimens with different H/W ratios, for LSS = 0.45 GN/m and σ_2 = 13 MPa. The figure shows that the maximum released kinetic energy from the specimen is large when the H/W ratio is high. This is due to shape effect that makes a taller specimen more brittle than a shorter one. In fact, confinement can affect a larger volume of the rock in a shorter specimen and thus the failure mode is less violent. The LSRI values calculated from the numerical modeling (Figure 3-18) indicate that more platen reactions occur for specimens with a higher H/W ratio. This also means that the failure in a taller specimen is more violent than that in a shorter one.
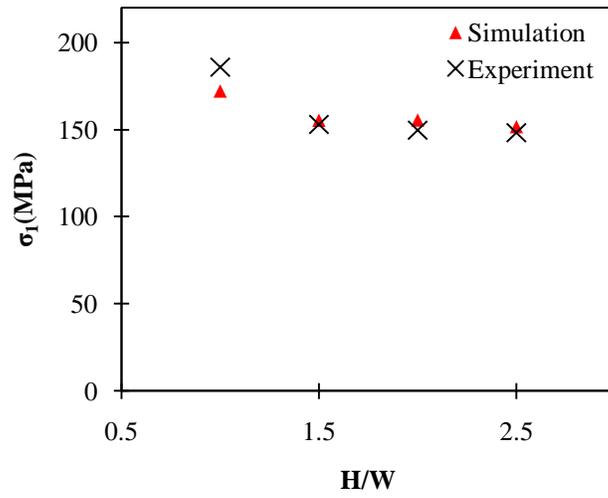
Figure 3-16: Influence of the H/W ratio on peak strength (σ_2 = 13 MPa, σ_3 = 0 MPa).
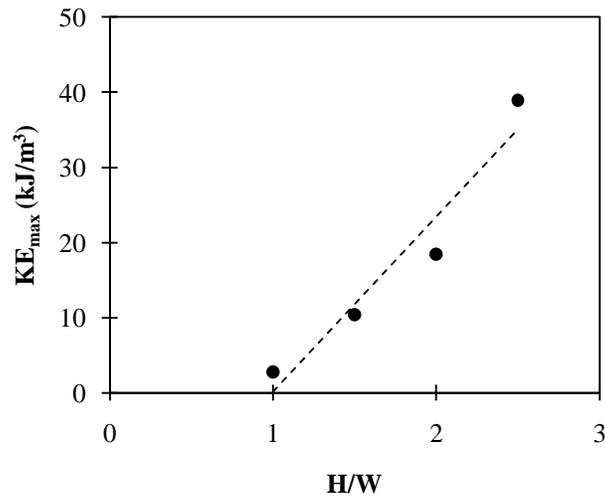
Figure 3-17: Influence of the H/W ratio on KE_{max} (LSS = 0.45 GN/m, σ_2 = 13 MPa).
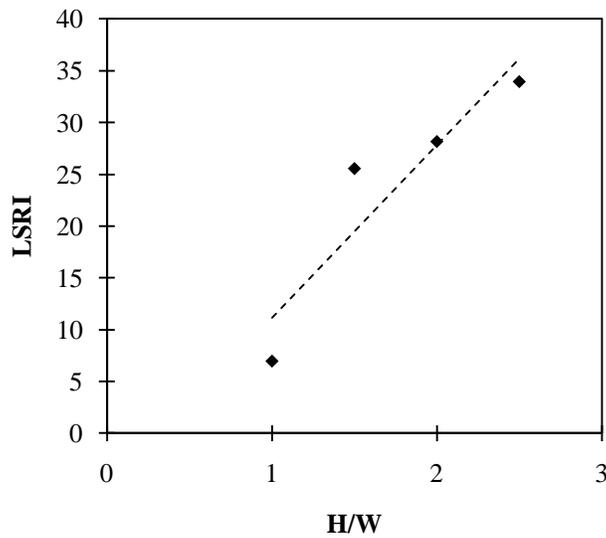
Figure 3-18: Influence of the specimen H/W ratio on the loading system reaction intensity (LSRI) (LSS = 0.45 GN/m, σ_2 = 13 MPa).

3.4.3 Influence of intermediate principal stress on failure behavior

At the underground excavation boundaries a biaxial stress state ($\sigma_1 \neq 0$, $\sigma_2 \neq 0$, and $\sigma_3 = 0$) exists. Comprehensive studies have been carried out to investigate the influence of intermediate principal stress on rock failure and fracturing behaviors (Cai, 2008a; Manouchehrian et al., 2014; Mogi, 1967; Mogi, 1981; Pan et al., 2012; Wiebols and Cook, 1968). Results from experimental and numerical studies have shown that the intermediate principal stress increases the rock strength and affects the mode of rock fracturing. However, there is no systematic investigation on how the intermediate principal stress influences the intensity of rockbursts.

Polyaxial unloading tests are simulated with five different σ_2 values (0, 13, 26, 39, and 52 MPa) to study the influence of intermediate principal stress σ_2 on the rock failure behavior. The specimen size is 150 mm in height, 60 mm in width, and 30 mm in thickness. The LSS in the maximum principal stress direction for all models is 0.45 GN/m. The modeling procedure

74
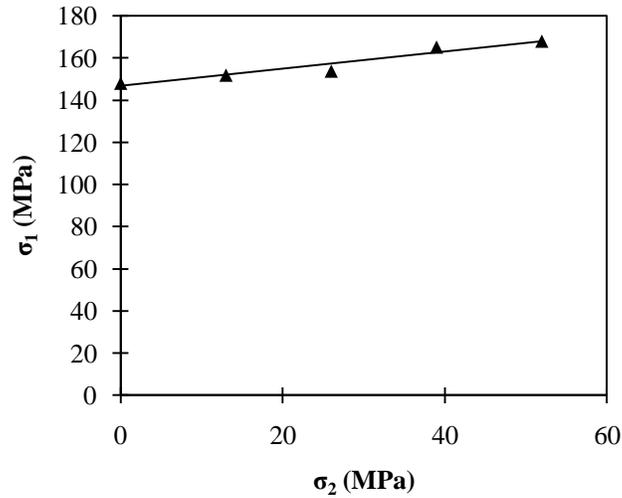
Figure 3-19: Influence of the intermediate principal stress on peak strength ($\sigma_3 = 0$ MPa).

described in Section 3.4.1 is used. Figure 3-19 presents the relation between the intermediate principal stress (σ_2) and the strength (σ_1) of the rock. It is seen that with an increase of σ_2, the peak strengths increase, which is in agreement with laboratory results (Haimson and Chang, 2000; Mogi, 1971, 2007). However, because a small friction coefficient ($\mu = 0.2$) is assigned to the contact between the platens and the rock in the numerical model, the degree of σ_1 variation with σ_2 is not as obvious as that seen in the experimental results.

Figure 3-20 presents relation between the intermediate principal stress and KE_{max} from the specimens, for $\sigma_2 = 13, 26, 39, 52$ MPa, and LSS = 0.45 GN/m. When the intermediate principal stress is low, more kinetic energy is released from the specimens. The calculated LSRI values are presented in Figure 3-21, respectively. The results show that as the intermediate principal stresses increase, LSRI decreases which means that the failure is less violent. The reason is that as the intermediate principal stress increases, the post-peak stiffness of the rock is reduced. This is
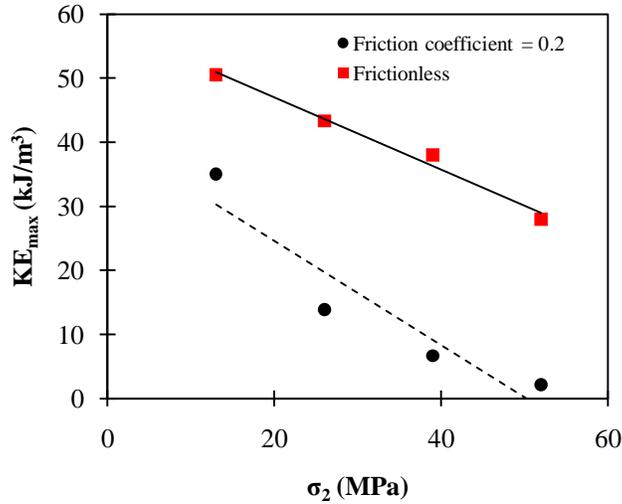
Figure 3-20: Influence of the intermediate principal stress on KE_{max} (LSS = 0.45 GN/m, H/W= 2.5).

similar to the results from conventional triaxial tests that generally show a reduced post-peak stiffness as confinements increase (Wawersik and Fairhurst, 1970). Hence, it is concluded that the intermediate principal stress can reduce the intensity of unstable rock failure. This insight is obtained from numerical modeling and needed to be confirmed in laboratory using the rockburst test system.

As presented in (Cai, 2008a), the large influence of the intermediate principal stress on rock strength, as seen in laboratory test results, is largely due to the end effect because very stiff loading platens are used and the friction between the platens and the specimen cannot be completely eliminated. As seen in Figure 3-20 and Figure 3-21, if frictionless contacts between the platens and the specimen is used to apply the intermediate principal stress, the failure is more violent than that with friction contacts (μ = 0.2). However, the KE_{max} and LSRI values are less affected by σ_2 in this case.
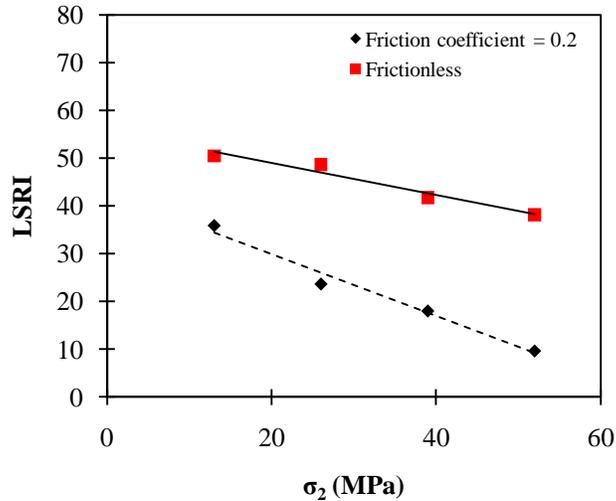
Figure 3-21: Influence of the intermediate principal stress on the loading system reaction intensity (LSRI) (LSS = 0.45 GN/m, H/W= 2.5).

3.5 Final remarks

Rocks near underground opening boundaries are under a polyaxial stress state. Excavating the openings reduces the radial stress and increases the tangential stress. Rockbursts can occur if the tangential stress is high and the loading system stiffness is small. Rockburst is a complex phenomenon and the mechanism that governs rockburst is not well understood yet.

In this chapter, an explicit FEM tool was used to simulate rock failure under uniaxial compression and polyaxial unloading conditions. The suitability of the adopted numerical model to simulate unstable rock failure was tested and confirmed. Depending on the relative values of the loading system stiffness and the post-peak stiffness of the rock, stable and unstable rock failures can occur. In particular, it was observed from the modeling outputs that unstable rock failure is associated with a sudden movement of the loading platens or a sudden release of excessive energy, which can be observed directly or indirectly in laboratory tests using

monitoring equipment. It is proposed to use the Loading System Reaction Intensity (LSRI) and the maximum unit kinetic energy (KE_{max}) as indicators of unstable failure in numerical modeling. It is seen from the results that LSRI is smaller than 2 for stable rock failure and greater than 6 for unstable rock failure under uniaxial compression. A transition zone with LSRI values between 2 and 6 may exist, indicating that the failure is less violent when the LSRI values are not sufficiently high.

Polyaxial loading can change the post-peak stiffness of rocks obtained in uniaxial compression tests and hence alter the failure characteristics. The simulation results under polyaxial unloading conditions showed that the LSRI and KE_{max} values are very high if the loading system stiffness is low. The simulation results showed that the failure in taller specimens was more violent than that in shorter ones. In addition, it was found that higher intermediate principal stresses may lead to less violent failures of rocks.

One advantage of using numerical simulation to study unstable rock failure is that the loading system stiffness can be varied easily and the boundary conditions can be honoured. Another advantage is that the energy can be examined. Violent rock failures are often associated with energy release and the ability to calculate the kinetic energy is critical in engineering design. The modeling approach presented in this research can be useful for predicting unstable rock failure and estimating released kinetic energy in an underground setting which includes mine openings and geological structures, which is important for designing rock support in deep tunnels.

From a micro-structural point of view, rocks are heterogeneous materials which contain various minerals and microcracks. A simplification was made to consider rocks as a homogeneous material in the meso-scale or macro-scale in this study. If the objective is to analyze the failure

process, the use of homogenous material models may not be appropriate because even if the overall stress–strain curve properly reflects the prescribed mechanical properties, the failure process and pattern can be unrealistic. However, this study has demonstrated that a homogeneous model can be used to study the unstable rock failure and associated released kinetic energy in Abaqus. In the next chapter, the material heterogeneity is introduced into Abaqus models and the influence of rock heterogeneity on dynamic rock failure and associated energy release is investigated.

Chapter 4

4 Influence of material heterogeneity on failure intensity in unstable rock failure

4.1 Introduction

Studies have demonstrated that numerical methods can be used to simulate rock failure (Bardet, 1989; Jiang et al., 2010; Kias and Ozbay, 2013; Mitri et al., 1999; Müller, 1991; Oelfke et al., 1996; Salamon et al., 2003; Zubelewicz and Mróz, 1983). Continuum (e.g. FEM and FDM) and discontinuum (e.g. DEM) methods have been used to model rock failure. Many numerical models consider a continuous, isotropic, homogeneous, and linearly elastic medium in simulation. Despite these simplifications, these models are useful for solving some geomechanical problems. In homogeneous models, it is implicitly assumed that shear failure is the dominant failure mechanism (Kaiser and Kim, 2015; Valley et al., 2010). When the major failure mode is tensile splitting, a homogeneous model cannot produce realistic results even if it properly reflects the prescribed mechanical properties such as peak strength. Hajiabdolmajid et al. (2002) showed that traditional homogeneous models were not capable of simulating failure zone around excavations. They developed a cohesion weakening and frictional strengthening (CWFS) model to capture the failure zone around AECL's Mine-by tunnel in Lac du Bonnet granite. In their model, the failure zones were captured as shear failure zones. Despite the capability of this model for simulating the damage zone around the tunnel, it was not capable of capturing the gradual tensile failure process. Hence, homogeneous models may not be suitable

for rock failure process analysis (stable and/or unstable) around excavation boundaries where failure predominantly occurs in tensile splitting.

Heterogeneity is a characteristic of rocks and rock-like materials such as concrete, which makes this group of materials behave differently from others. Heterogeneity affects rock behavior under mechanical loads. The key function of heterogeneity is the formation of local stress concentration inside the body which leads to local tensile stresses even if the whole rock is under compression (Blair and Cook, 1998a, 1998b; Gallagher et al., 1974). It is understood from previous studies that the process of crack development is initiated due to tensile micro-cracking. Shear failure becomes dominant in a later deformation stage when sufficient numbers of tensile fractures have been generated (Brace et al., 1966; Fairhurst and Cook, 1966; Fonseka et al., 1985; Hallbauer et al., 1973; Manouchehrian and Marji, 2012; Martin and Chandler, 1994; Tapponnier and Brace, 1976). Hence, material heterogeneity needs to be introduced into the models to capture tensile splitting failure of rocks.

Over the years, efforts have been made to develop numerical codes that can consider discontinuity, heterogeneity, anisotropy, and non-elasticity of rocks. Advanced numerical tools such as PFC, RFPA, UDEC, EPCA (Elasto-Plastic Cellular Automaton) (Feng et al., 2006), and ELFEN have been developed for simulating rocks as heterogeneous media. Application of these numerical tools demonstrated that consideration of rock heterogeneity is essential in simulating rock failure processes (Cai, 2008a, 2013a; Feng et al., 2006; Gong et al., 2006; Itasca, 2000; Manouchehrian et al., 2014; Munjiza et al., 1995; Potyondy and Cundall, 2004; Tang, 1997; Tang and Kaiser, 1998). In addition, some advanced numerical tools have been utilized to study unstable rock failure which showed the suitability of heterogeneous models to simulate rock failure (Bardet, 1989; Chen et al., 1997; Fujii et al., 1997; Garvey, 2013; Gu, 2013; Gu and

Ozbay, 2015; Kaiser and Tang, 1998; Kias and Ozbay, 2013; Mitri et al., 1999; Müller, 1991; Oelfke et al., 1996; Salamon et al., 2003; Sharan, 2007; Sun et al., 2007; Tan et al., 2009; Zhang et al., 2013). However, previous studies did not focus on the effect of heterogeneity on unstable rock failure.

In this chapter, simulation results of unstable rock failure of heterogeneous rocks under unconfined and confined conditions using Abaqus-Explicit code are presented. Introduction of heterogeneity using Python scripting into Abaqus models is explained in Section 4.2. In the developed heterogeneous models, mechanical properties of Young's modulus (E), cohesion (c), and friction angle (φ), which follow normal distribution functions, are set randomly in each element. A parametric study is conducted to understand the effect of each parameter's heterogeneity on the mechanical behavior of rocks. Effect of LSS and confinement on failure intensity is investigated. A comparison of results between the homogeneous and the heterogeneous models is presented in Section 4.3.

4.2   Abaqus models for rock failure simulation

Despite Abaqus's capability for simulating physical problems, its application in the geomechanical field is limited. A key characteristic of geomaterials is material heterogeneity, which cannot be readily modeled in Abaqus. Fortunately, Abaqus provides windows for adding and improving its capability using scripting. Hence, for modeling rock-like materials, it is possible to introduce material heterogeneity into the models to produce more realistic results. In this section, a simulation of rock failure processes in compression using homogeneous material models is presented first, followed by an introduction of material heterogeneity into Abaqus

models and a simulation of rock failure processes in compression using heterogeneous material models.

4.2.1 Compression test simulation using homogenous models

This study investigates the effect of material heterogeneity on unstable rock failure. For this purpose, the tested mechanical properties of T_{2b} marble (Table 4-1) are used as the base case. T_{2b} marble is the host rock of the diversion tunnels at the Jinping II hydropower station in China, which have experienced violent rock failures during construction (Zhang et al., 2014).

Table 4-1: Physical and mechanical properties of the T_{2b} marble (Zhang et al., 2014)

Parameter	Test value
Density, ρ (kg/m^3)	2780
Young's modulus, E (GPa)	55
Poisson's ratio, v	0.27
Uniaxial compressive strength, UCS (MPa)	110.7[*]
Cohesion, c (MPa)	32.6
Friction angle, φ (°)	29.0
Post-peak modulus, E_{pp} (GPa)	150[**]

[*] UCS of the T_{2b} marble was reported between 100 and 160 MPa in (Zhang et al., 2014). This value was calculated according to $UCS = \frac{2c.cos\varphi}{(1-sin\varphi)}$ for the present study.

[**] Post-peak modulus (K_{pp}) of the T_{2b} marble is extracted by digitizing curves presented in (Zhang et al., 2014).

Table 4-2: Strain-softening parameters of the homogeneous model

Cohesion		Tension cut-off	
Cohesion yield stress (MPa)	Shear plastic strain	Tension cut-off stress (MPa)	Tensile plastic strain
32.2	0	5.5	0
0.01	0.2	0.1	0.001

Unconfined and confined compression tests are simulated using Abaqus[2D] to investigate the failure mechanism of rocks in homogeneous models. An elasto-plastic Mohr-Coulomb strain-softening model with homogeneous material properties is used to model the strength behavior of the T_{2b} marble. Table 4-2 presents the adjusted parameters for defining the strain-softening behavior of the rock in the homogeneous model. A rectangular specimen with a height of 250 mm and a width of 100 mm is used for the simulation. In the unconfined compression test simulation, one end of the specimen is fixed in the maximum stress direction and the other direction is free (roller constraint) and a constant velocity of 0.03 m/s is applied directly to the other end to load the specimen. The same end boundary conditions are applied to the specimens in the confined compression test simulation and the confinements applied are 5, 10, 20, and 40 MPa. In the unconfined and confined compression test simulations, a friction angle of 30° and a cohesion of 32.9 MPa are used, which are based on the reported laboratory test data. A post-peak modulus of 150 GPa is obtained for unconfined tests based on the test values.

Table 4-3: Physical and mechanical properties of the simulated rock

Parameter	Homogeneous model	Heterogeneous model
Density, ρ (kg/m^3)	2780	2780
Young's modulus, E (GPa)	55.0	54.8
Poisson's ratio, ν	0.27	0.27
Uniaxial compressive strength, UCS (MPa)	113.6	113.5
Cohesion, c (MPa)	32.9	32.7
Friction angle, φ (°)	30.0	29.7
Post-peak modulus, E_{pp} (GPa)	166	146

Evaluated peak strength and elastic modulus from the homogeneous model are summarized in Table 4-3. Figure 4-1a and Figure 4-2 present the stress–strain curves and snapshots of the failure pattern at different confinements. Figure 4-1a indicates that the post-peak slopes of the specimens are almost the same as confinement increases. Laboratory test results show a change in deformation behavior from brittle to ductile with the increase of confinement (Paterson, 1958). Furthermore, Figure 4-2 shows that confinement does not affect the failure pattern in the homogeneous model because all of them show distinct shear failure. Despite that the peak uniaxial compressive strength (UCS) of the T_{2b} marble is captured by the homogeneous model, it fails to capture the splitting failure under low confinement and the failure mode transition from brittle to ductile as confinement increases.
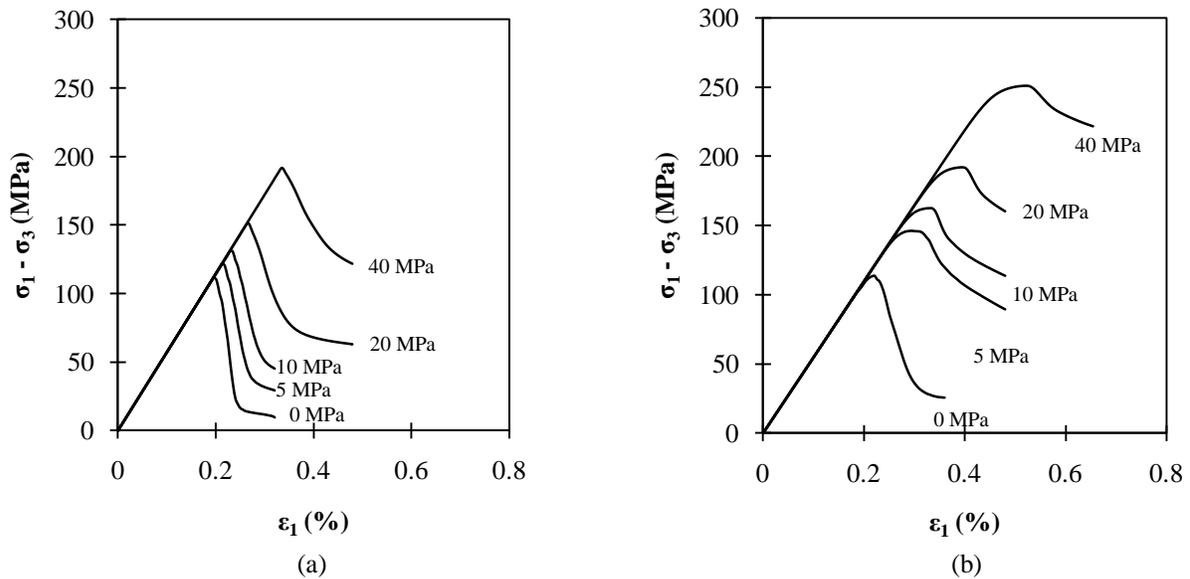
Figure 4-1: Stress–strain curves at different confinements: (a) homogeneous model; (b) heterogeneous model.

σ₃ = 0 MPa σ₃ = 5 MPa σ₃ = 10 MPa σ₃ = 20 MPa σ₃ = 40 MPa
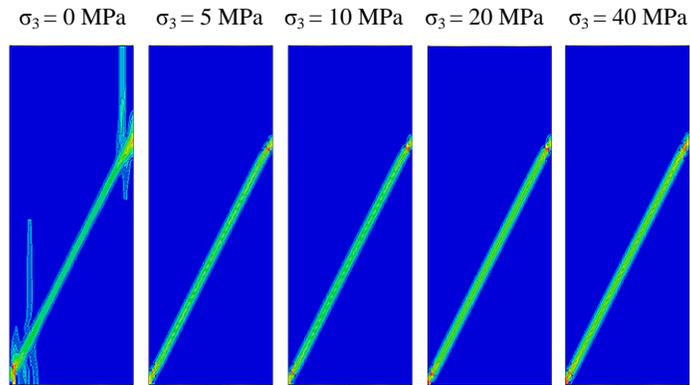
Figure 4-2: Failure patterns at different confinements (homogeneous model).

4.2.2 Compression test simulation using heterogeneous models

The material properties of each element are assigned randomly following normal distribution functions to introduce heterogeneity into Abaqus models. The introduction of material heterogeneity cannot be conducted using Abaqus's GUI and Python scripting is needed. Using Python scripts in Abaqus, it is possible to automate a repetitive task, vary parameters of a simulation as part of an optimization study, and extract information from outputs (Puri, 2011). The following pseudo-code summarizes a technique for introducing material heterogeneity into Abaqus models using Python scripting.

(1) **[Mesh generation**] Define mesh size at different locations of the model and generate mesh.
(2) **[Element bin]** Find the number of elements (*nElems*) and divide it by a bin number (*nElemsBin)* to create *nElems/nHet* element bins (to decrease the computation time).
(3) **[Material]** Generate *nElems/nElemsBin* random material definitions.
(4) **[Section]** Create *nElems/nElemsBin* sections with *nElemsBin* random element members and material property.
(5) **[Shuffling]** Generate a list of *nElems* integers (1 to *nElems*) that represent element number.
(6) **[Set]** Generate *nElems*/*nElemsBin* sets with *nElemsBin* elements in each set.

Rectangular specimen with 4000 elements and 100 different materials

$\mu_E = 52$ GPa, $\sigma_E = 7.80$ GPa
$\mu_c = 39$ MPa, $\sigma_c = 5.85$ MPa
$\mu_\varphi = 37°$, $\sigma_\varphi = 1.85°$
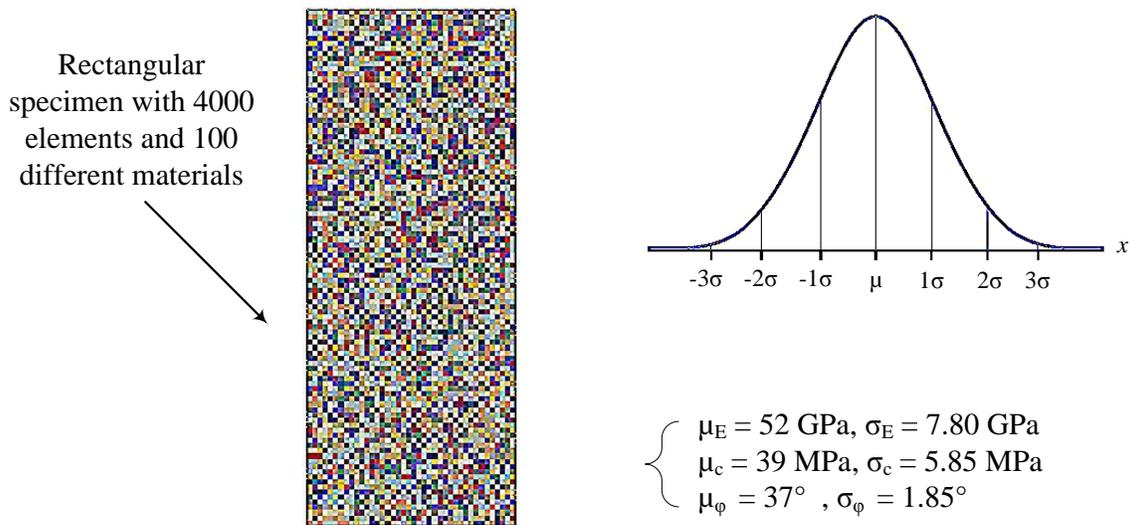
Figure 4-3: Generated heterogeneous material in Abaqus by Python scripting.

The introduction of material heterogeneity increases computation time significantly. Element bins are defined and material properties are assigned to members of each element bin instead of each element individually to reduce computation time. The developed Python script assigns randomly distributed material properties of E, c, and φ to the elements and the properties follow normal distribution functions. One example of execution of the explained technique to simulate a rectangular model with 4000 elements and 100 materials is presented in Figure 4-3 (each color represents one material).

Rocks contain different minerals that have different mechanical properties. A change in the mechanical properties of rock forming elements will affect the mechanical behavior of the rock. A parametric study is conducted to examine how heterogeneity of the mechanical properties influences the mechanical behavior of rocks. For this purpose, coefficients of variation (COV) of E, c, and φ are varied from 0 to 20 % individually.

Figure 4-4 shows the sensitivity of the heterogeneous models to the variation of parameters E, c, and φ. The heterogeneity of Young's modulus influences the yield stress and modulus of the rock (Figure 4-4a). More heterogeneous materials show a non-linear deformation behavior before peak. Figure 4-4b indicates that the heterogeneity of cohesion affects the uniaxial compressive strength and post-peak behavior of the models. As the COV of cohesion increases, the peak strength reduces and the post-peak behavior becomes more brittle. The heterogeneity of the friction angle affects only the peak strength of the rocks (Figure 4-4c).

Next, unconfined and confined compression test simulations are conducted using the heterogeneous model (Figure 4-3). It should be noted that although the introduction of probability distributions for the rock properties resulted in different results for each model run, the overall model responses show a similar trend. Figure 4-5 shows the stress–strain curves of ten unconfined compression test simulations with one set of probability distribution parameters (Heterogeneous-1 in Table 4-4). A basic descriptive statistical analysis (Table 4-5) shows that the average values for uniaxial compressive strength (*UCS*), Young's modulus (*E*), and post-
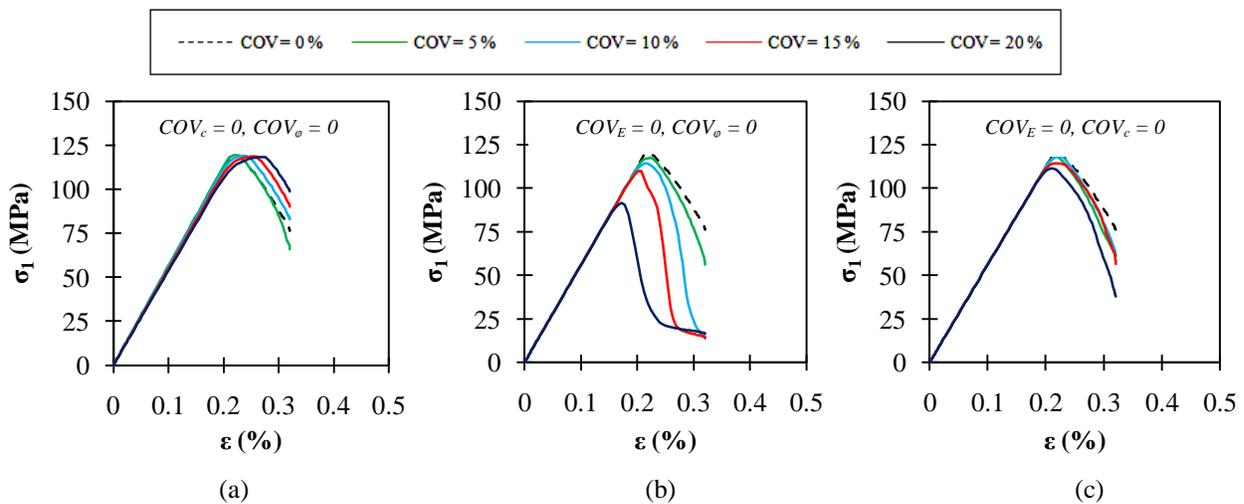
Figure 4-4: Sensitivity of the heterogeneous model to the variation of (a) Young's modulus E, (b) cohesion c and (c) friction angle φ.

88

peak modulus (E_{pp}) are 113.4 MPa, 54.8 GPa, and 151 GPa respectively for Heterogeneous-1 model.

Heterogeneous-1 model is used to simulate the mechanical properties of the T_{2b} marble (Table 4-1). Stress–strain curves of the specimens in confined test simulations are presented in Figure 4-1b. A friction angle of 29.7° and a cohesion of 32.7 MPa are calculated for the heterogeneous model, which are similar to the test results. A calculated post-peak modulus of 146 GPa is close to the value obtained from the test data. All calculated material parameters from the Heterogeneous-1 model are also summarized in Table 4-3.

Table 4-4: Probability distribution parameters of two heterogeneous models

Parameter	Heterogeneous-1		Heterogeneous-2	
	Mean	COV (%)	Mean	COV (%)
Young's modulus, E (GPa)	52	15	52	25
Cohesion, c (MPa)	39	15	39	20
Friction angle, φ (°)	37	5	37	10

Table 4-5: Basic statistical description of evaluated mechanical properties of the simulated rock (Heterogeneous-1 model)

	UCS (MPa)	E (GPa)	E_{pp} (GPa)
Min	101.6	51.7	84.9
Max	121.7	56.1	291.1
Mean	113.4	54.8	151.0
COV (%)	5.2	2.4	44.1
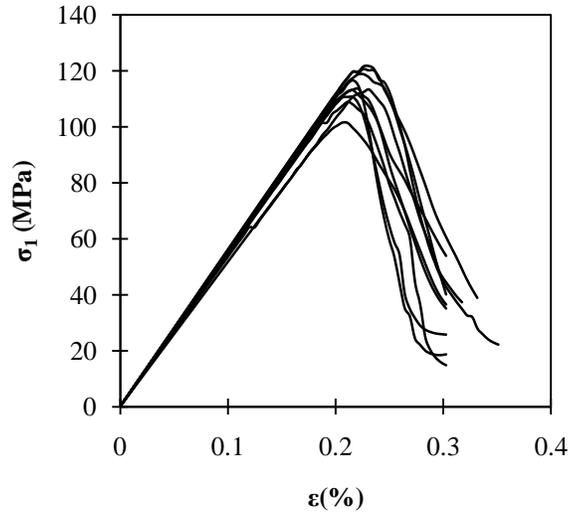
Figure 4-5: Stress–strain curves of specimens from ten simulations.

$\sigma_3 = 0$ MPa $\sigma_3 = 5$ MPa $\sigma_3 = 10$ MPa $\sigma_3 = 20$ MPa $\sigma_3 = 40$ MPa
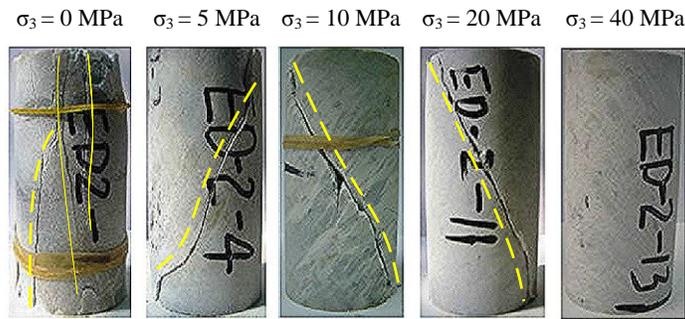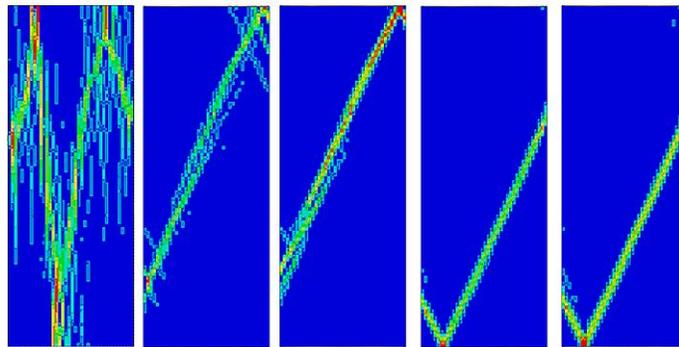
(a) Laboratory tests

(b) Heterogeneous model

Figure 4-6: Failure patterns at different confinements from (a) laboratory tests (Zhang et al., 2014) and (b) numerical modeling (Heterogeneous-1 model).

Figure 4-6 shows photographs of the failed T_{2b} marble specimens in laboratory tests (Zhang et al., 2014) and snapshots of the maximum principal plastic strain obtained by the Heterogeneous-1 model. The failure modes change from splitting failure at zero confinement to shear failure at high confinements. Figure 4-7 presents the shear and tensile modes indicated by the maximum principal plastic strain at peak stress under different confinements. It shows that an increase of confinement limits the tensile cracks and makes shear failure the dominant failure mode. The homogeneous material models cannot capture axial splitting at zero confinement (Figure 4-2) but the heterogeneous material model successfully captures this failure mode. Hence, the developed heterogeneous material model in Abaqus enhances its capability for solving geotechnical engineering problems.

$\sigma_3 = 0$ MPa $\sigma_3 = 5$ MPa $\sigma_3 = 10$ MPa $\sigma_3 = 20$ MPa $\sigma_3 = 40$ MPa

(a) Shear failure
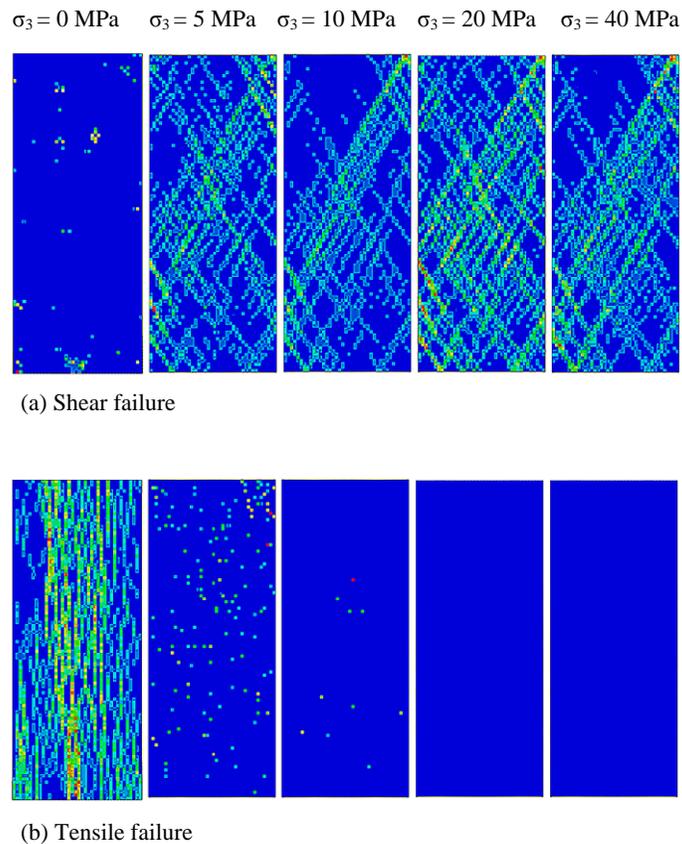
(b) Tensile failure

Figure 4-7: (a) Shear and (b) tensile failures at peak stress under different confinements (Heterogeneous-1 model).

91

4.3 Simulation of unstable rock failure

Failure intensity is a term that refers to the amount of released energy and the velocity of platens which can be potentially linked to the velocity of ejected rocks. High failure intensity means that the amount of released energy is large or the velocity of platens is high. In the current study, LSRI and KE_{max} are used to investigate the failure intensity of unstable rock failure. The results of the influence of the LSS and confinement on failure intensity in homogeneous and heterogeneous material models are compared and discussed.

4.3.1 Effect of loading system stiffness on failure intensity

A comparison of the LSS with the material's post-peak stiffness is conducted to study the mechanism of unstable rock failure in homogeneous and heterogeneous models. First, unconfined compression test setup shown in Figure 4-8 with different LSS values are simulated. The homogeneous and heterogeneous model parameters presented in Section 4.2 are used. Rectangular specimens with a width of 100 mm a height of 250 mm are simulated. A rectangular platen with a width of 150 mm and varying height is modeled. The height of the platen is varied from 100 to 3200 mm, which resulted in LSS of 0.94 to 30 GN/m. One specimen's end is fixed in the loading direction with a roller constraint. One point at this end is fixed in the direction perpendicular to loading direction with a pin constraint to avoid model movement. The specimen is loaded by applying a constant velocity of 0.03 m/s to the platen end. A frictionless contact is assigned between the specimen and the platen to exclude the end effect.
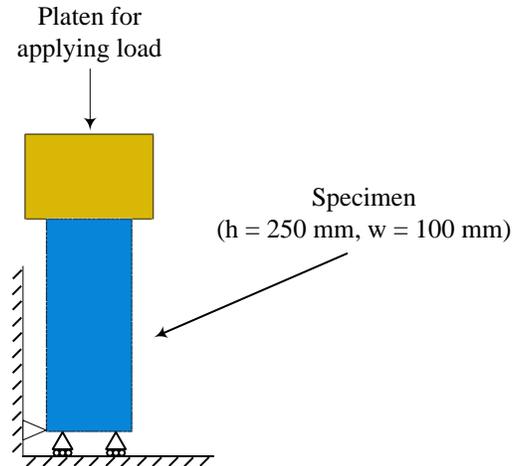
Figure 4-8: Model geometry in unconfined compression tests.
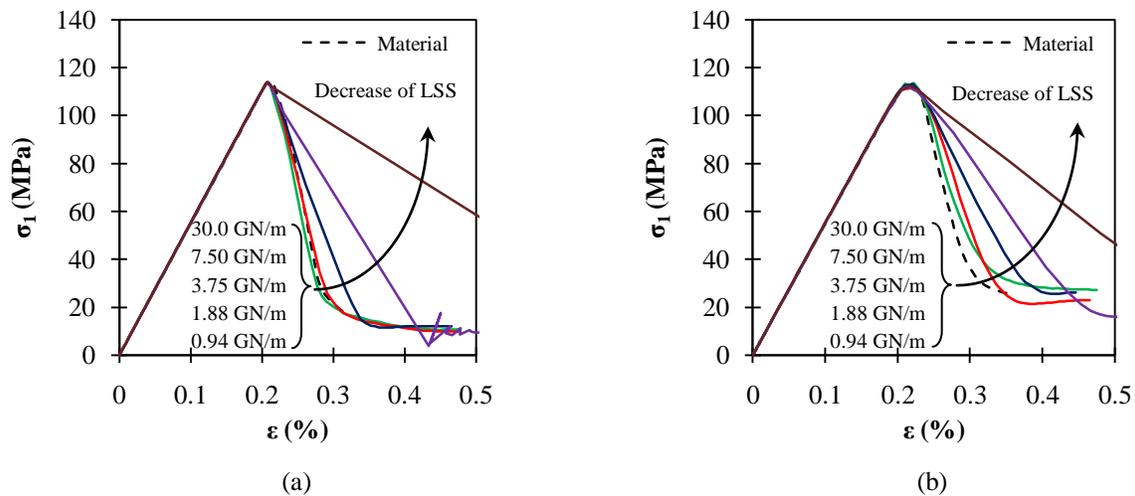
Figure 4-9: Stress–strain curves of (a) the homogeneous and (b) the Heterogeneous-1 models with different LSS.

Figure 4-9 shows the effect of LSS on the stress–strain curves of the homogeneous and the Heterogeneous-1 models. One case with a rigid loading system is simulated for both the homogeneous and the Heterogeneous-1 models to obtain the rock's characteristic behavior in unconfined compressions. This is achieved by applying a constant velocity of 0.03 m/s directly to the specimen's top end. This rigid loading condition is equivalent to a loading system with

infinite loading system stiffness. The responses of the material under infinite loading system stiffness are shown in Figure 4-9 by the dashed lines (labeled as "Material"). The rigid loading results in post-peak stiffness (k_{pp}) of 6.6 and 5.9 GN/m for the homogeneous and Heterogeneous-1 models, respectively. When the LSS is less than k_{pp}, the post-peak stress–strain curves deviates from the rock's characteristic post-peak curves (Figure 4-9).

In this study, the homogeneous and the heterogeneous model parameters are chosen based on the test data of the T_{2b} marble (Table 4-1). Figure 4-10 shows the stress–strain curves of the homogeneous and heterogeneous models and, the associated failure patterns. Two sets of heterogeneous model parameters with the same means of E, c and φ but different COVs are considered (Table 4-4). The second heterogeneous model, which is more heterogeneous, is referenced as "Heterogeneous-2." Figure 4-10 shows that with the increase of material heterogeneity, the peak strength is reduced (UCS = 90 MPa) and the post-peak behavior becomes less brittle (k_{pp} = 2.5 GN/m). Figure 4-11a presents the maximum unit released kinetic energy (KE_{max}) from the models during failure with different LSS. The calculated kinetic energy in the heterogeneous models is higher than that in the homogeneous models when the LSS is high. This is due to tensile failure in the heterogeneous models that causes more lateral deformation. Furthermore, Figure 4-11a shows that less energy is released when the model becomes more heterogeneous.

In this research LSRI is used as the indicator of unstable failure. Figure 4-11b shows that when the LSS is softer than the rock's post-peak stiffness, the failure is unstable and the LSRI values is high (>> 2). On the other hand, if the LSS is stiffer than the rock's post-peak stiffness, the failure is stable and LSRI is small (< 2). Studies have shown that heterogeneous rocks are less burst-prone than homogeneous rocks (Zengchao and Yangsheng, 2003). Figure 4-11b and

Figure 4-11c demonstrate that when a rock is more heterogeneous, its failure is less violent. When the degree of material heterogeneity increases, crack damage starts at a lower stress and the peak strength of the rock is generally lower than that of a less heterogeneous rock. In addition, pre-peak cracking can reduce the peak strength of the rock so that the rock can store less strain energy and is hence less prone to unstable failure. This is because that when a rock fails at a lower stress, less strain energy is stored in the loading system and consequently there is less energy from the loading system to push the failing rock. As a result, the failure is less violent. Moreover, the post-peak behavior of a rock becomes less brittle as the heterogeneity increases. For example, for an LSS of 3.75 GN/m failure in Heterogeneous-1 model (k_{pp} = 5.9 GN/m) is unstable but is stable in Heterogeneous-2 model (k_{pp} = 2.5 GN/m).
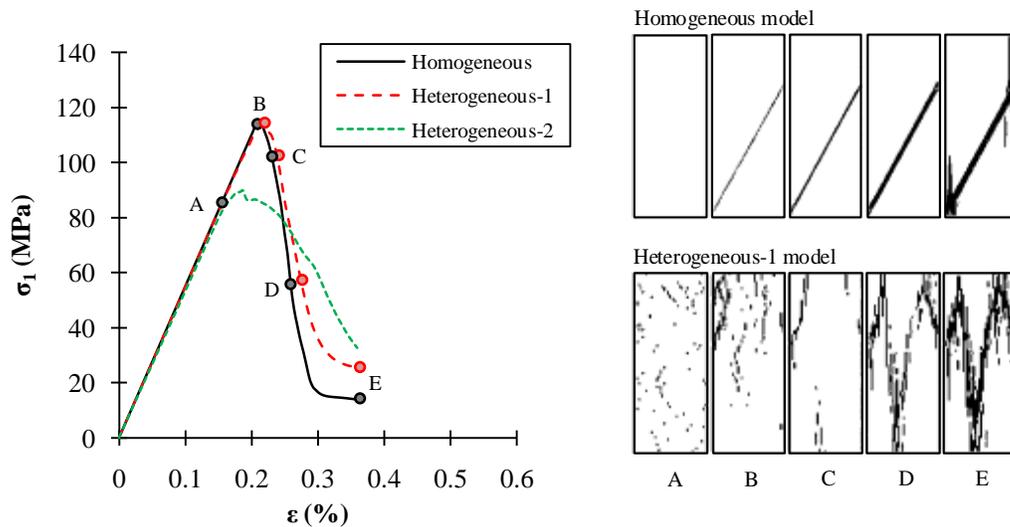
Figure 4-10: Comparison of stress–strain curves of the homogeneous and heterogeneous models and the associated failure patterns.

(a)   (b)
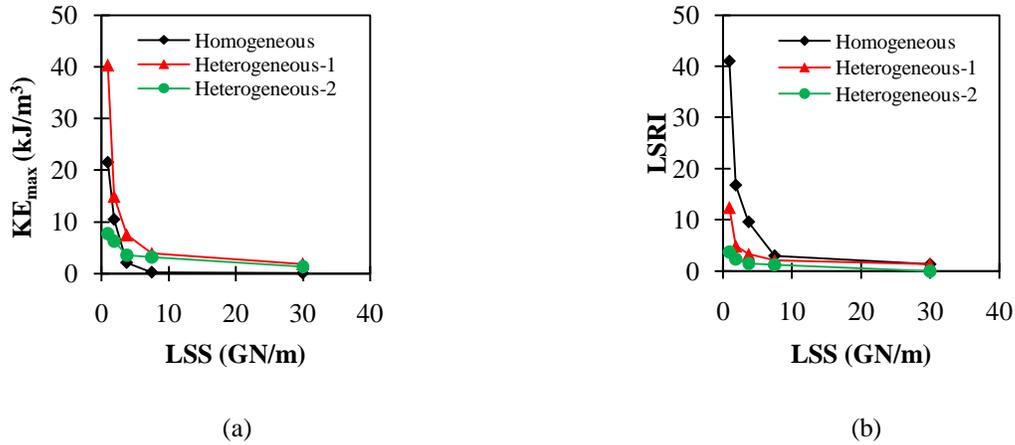
Figure 4-11: Relation between relative loading stiffness and (a) maximum unit kinetic energy, and (b) the loading system reaction intensity (LSRI) in unconfined compression tests.

4.3.2 Effect of confinement on failure intensity

Many studies have been carried out to understand the effect of confinement on rock deformation behaviors (Griggs, 1936; Jaeger et al., 2009; Klein et al., 2001; Tiwari and Rao, 2006). Laboratory test results have shown that confinement strengthens a rock and affects the failure behavior.

A systematic study of the effect of confinement on the intensity of rock failure is conducted. Confined compression tests with confinements of 0, 5, 10, 15, and 20 MPa are simulated using the homogeneous and heterogeneous models. The specimen size is 100 mm in width and 250 mm in height. The LSS in σ_1 direction for all models is 0.94 GN/m. The modeling procedure described in Section 4.3.1 is used.

Figure 4-12a presents the relation between confinement and KE_{max}. When the confinement is low, more energy is released from the specimen. The peak strengths of the Heterogeneous-1 and the homogeneous model are similar (Figure 4-10), but the released energy from the heterogeneous model is higher than that from the homogeneous model (Figure 4-12a). This is

due to the difference in failure mode; tensile splitting in the heterogeneous model leads to more dilation of the specimen. Hence, the total released energy is higher in the heterogeneous model. As confinement increases, there is a transition of failure mode from tensile splitting to shear and KE_{max} from both the homogeneous and the heterogeneous models are similar. Heterogeneous-2 model has a lower peak strength compared with the other two models. Hence, the released maximum unit kinetic energy is smaller than these from the homogeneous model and the Heterogeneous-1 model.

The calculated LSRI values are presented in Figure 4-12b. The results indicate that LSRI decreases as confinement increases, meaning that the failure is less violent under confined conditions. Figure 4-12b shows that at zero confinement the LSRI of the heterogeneous models is low. The LSRI values of the Heterogeneous-1 model at higher confinements are larger than the values of the homogeneous model, due to the difference in failure mode under unconfined and confined conditions. Figure 4-13 illustrates the displacement vectors of the rocks failed in shear and tensile splitting. In the shear failure mode, broken rocks move predominantly in the loading

(a)   (a)
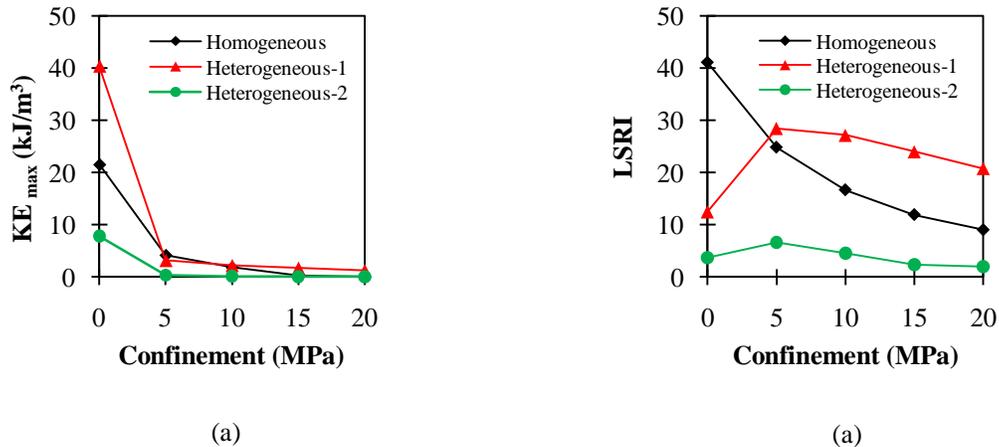
Figure 4-12: Relation between relative loading stiffness and (a) maximum unit kinetic energy, and (b) the loading system reaction intensity (LSRI) in confined compression tests.

97

<div align="center">(a) Shear failure   (b) Tensile failure</div>
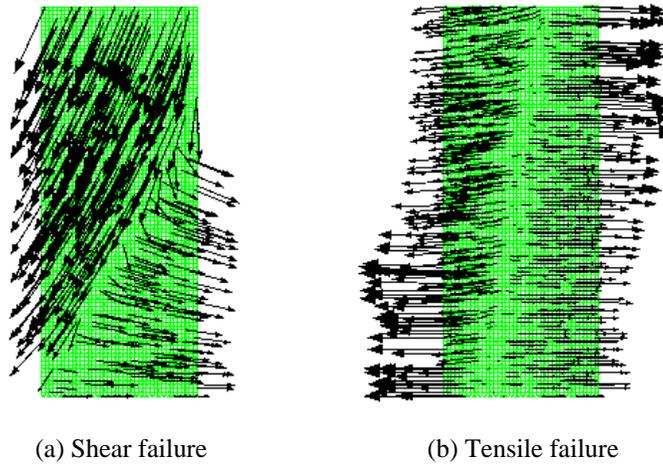
Figure 4-13: Displacement vectors in (a) shear and (b) tensile failures.

direction but in the tensile failure mode broken rocks move predominantly in the horizontal direction. Hence, the LSRI value is lower when splitting failure occurs at zero confinement. For the Heterogeneous-1 model, the overall peak strength of the rock is the same as that of the homogeneous model. When the rock fails in shear under high confinements, the platen's end moves more and the LSRI values are higher than those of the homogeneous model. For the Heterogeneous-2 model, the overall peak strength of the rock is lower than that of the Heterogeneous-1 model; as a result, the LSRI values are lower. The simulation results agree with field observations that strainbursts occur frequently in more competent and relatively homogeneous rocks.

4.4 Final remarks

Rockbursts caused by unstable rock failure are hazardous in deep underground construction. A good understanding of the failure mechanism is important for anticipating and controlling unstable rock failures. Brittle rock failure near excavation boundaries occurs predominantly in tensile splitting and it is important to consider this failure mode in numerical simulations of

unstable rock failure. Previous studies have shown that both homogeneous and heterogeneous models are able to reflect properly the prescribed mechanical properties of rock. In homogeneous models it is implicitly assumed that shear failure is the predominant failure mechanism. Hence, homogeneous models may give unrealistic results in conditions that the major failure mode is in fact tensile splitting. Heterogeneous models are capable of capturing tensile splitting failure at low confinements. A question that may arise is that how a change in failure mechanism influences the failure intensity because the released energy and the ejection velocity of broken rocks are concerns in unstable failure analyses.

In this study, the Abaqus-Explicit code was employed to simulate unstable rock failure. Heterogeneity of materials was introduced into Abaqus models using Python scripts. In the heterogeneous models, mechanical properties of rocks were assigned to each element randomly following normal distribution functions. A parametric study was conducted to reveal the model response of different material heterogeneities. The simulation results show that the pre-peak behavior of rocks is controlled by the heterogeneity of Young's modulus, and peak and post-peak behaviors are controlled mainly by the heterogeneities of cohesion and friction angle. By introducing heterogeneity into the models, tensile and shear failure mechanisms and the mechanical response of the models can be captured satisfactorily.

Effect of material heterogeneity on failure intensity in compression tests was investigated. The simulation results from both homogeneous and heterogeneous models show that rock failure is more violent when the loading system is softer and the confinement is lower. However, it is observed when two materials have the same peak strength, the heterogeneous model releases more energy than the homogeneous model due to the difference in the failure modes. The tensile splitting failure mode of the heterogeneous model releases more energy than the shear failure

99

mode of the homogeneous model. Furthermore, results show that more heterogeneous rocks, which usually have lower rock strengths, tend to be less violent if the rocks fail in an unstable fashion. This is in good agreement with field observation results that strainbursts occur frequently in more competent and relatively homogeneous rocks.

In the present study, it was showed that a change in failure mode may influence the failure intensity and this emphasized the importance of considering failure mode in unstable rock failure analysis. In the next chapter, the developed heterogeneous modeling approach in Abaqus is used to study rockburst near underground excavations.

Chapter 5

5 Influence of geological weak planes on rockburst occurrence and damage

5.1 Introduction

Rockburst is a great danger to the safety of miners and investment (Cai, 2013b; Chen et al., 1997; Whyatt et al., 2006; Zhang et al., 2013; Zhu et al., 2009) and many efforts have been made to understand why rockburst occurs. Many factors that influence rockburst damage have been identified (Lee et al., 2004; Mansurov, 2001; Wang and Park, 2001). Kaiser and Cai (2012) categorized the main influencing factors systematically into four groups as seismic event, geology, geotechnical property, and mining activity. Research has been conducted to understand the influence of these factors on rockburst damage (Kaiser et al., 1996; Reddy and Spottiswoode, 2001; Salamon, 1983; Zhang et al., 2013; Zhu et al., 2010). Unfortunately, there is still a long way to go to go, partially due to a lack of tools that can be used to investigate rockburst mechanism and damage but most importantly due to the fact that rockburst is a very complex phenomenon.

Dynamic disturbance due to seismic activities (e.g. explosion, vibration, stress impact from nearby rockbursts) does influence rockburst damage. Studies have shown that external disturbances during underground mining can induce rockbursts (Blair, 1993; Kaiser et al., 1996; Zhu et al., 2010). In addition, mining provides conditions for rockburst occurrence by changing the stress field and loading system stiffness in the ground around underground openings (Mitri et

al., 1999; Ozbay, 1989; Salamon, 1983). Geotechnical factors such as rock strength and rock brittleness affect strain energy storage and release. Rocks that have higher strengths and are more brittle tend to be more burst-prone. Other geotechnical factors that influence rockburst damage are in situ stress and discontinuities (Reddy and Spottiswoode, 2001; Snelling et al., 2013; Yeryomenko and Sklyar, 1999). In particular, discontinuities such as shears and faults can alter the stress field and the loading system stiffness such that rock failure becomes more violent.

It has been recognized that a deep underground opening is more burst-prone when it approaches a geological discontinuity such as fault, dyke, and contact (Hedley, 1992; Snelling et al., 2013). Durrheim et al. (1998) investigated 21 rockbursts in some deep South African gold mines and identified regional structures such as faults and dykes as a major controlling factor that influenced the occurrence of the rockbursts. They concluded that mining near major faults and dykes might have resulted in rockbursts. Jiang et al. (2010) studied the rockburst characteristic of the pilot tunnels of the Jinping II hydropower station in China and noticed that rockbursts tended to occur at places where faults and large joints were presence.

Hence, it is logical to study the influence of structural planes on rockburst. For instance, Zhang et al. (2013) conducted a numerical study that considered a fault near the drainage tunnel of the Jinping II hydropower station to explain a rockburst that occurred in the drainage tunnel. Their results showed that the fault influenced rock failure around the tunnel but they did not provide ejection velocity and kinetic energy release analysis. Zhou et al. (2015) conducted laboratory shear tests to explain the role of weak planes on rockburst damage observed in the intake tunnels of the Jinping II hydropower station. Based on their test results, they hypothesized three possible mechanisms (fault-slip, shear rupture, and buckling) for rockburst occurrence.

As reviewed and demonstrated in previous chapters, unstable rock failure can be simulated using continuum and discontinuum models. Some numerical simulations were carried out to study unstable rock failure in laboratory tests such as uniaxial and triaxial compression tests (Garvey, 2013; Manouchehrian and Cai, 2016d). Moreover, some researchers investigated unstable rock failure around underground openings using numerical methods (Jiang et al., 2010; Jiang et al., 2015; Kias and Ozbay, 2013; Zhang et al., 2014). Results from the above mentioned studies and other similar studies have been used to explain rockbursting phenomenon around deep underground openings. However, it is still not clear how the presence of weak planes near an opening influences rockburst damage.

In this chapter, the influence of geological weak planes on rockburst occurrence and damage around underground openings is investigated using Abaqus. A discussion of rockbursts induced by weak planes is presented in Section 5.2. In Section 5.3, simulation of rockburst in a tunnel with a nearby weak plane or fault is conducted using the Abaqus-Explicit code with heterogeneous material properties. A parametric study with different fault lengths (l), inclinations (θ), and positions relative to the tunnel (d) is conducted. A comparison of results between models with and without a weak plane is also presented.

5.2 Rockbursts near weak planes

Case histories from civil and mine tunneling have shown that rockburst occurrence locations are not uniform along the tunnels. Both the rockburst occurrence and the damage extent in a tunnel varies as the result of the influence of many factors such as geology and mining activities (Kaiser and Cai, 2012). The presence of weak planes such as faults, shears, and bedding planes near or at rockburst damage locations has been noticed. Weak planes can change stress field and loading system stiffness locally, making a rock mass more burst-prone. In highly stressed grounds, weak

planes may induce rockburst through slab buckling and rock rupture, depending on the position of the weak plane relative to the excavation walls and the stress condition.

5.2.1 Slab buckling

Slab buckling has been identified as a mechanism of rockburst (Bardet, 1991; Nemat-Nasser and Horii, 1982; Ortlepp, 1993). The concept of buckling rockburst is illustrated in Figure 5-1. Weak planes parallel to the tunnel boundaries and the maximum principal in situ stress may cause buckling type rockburst. When the rocks in the slab are highly stressed, a small increase of stress due to tunnel advance or a dynamic disturbance from nearby blasting and rockbursts or remote seismic events may trigger rockburst. The rock slab can fail violently and the stored energy in the rock slab is released suddenly and broken pieces of rocks are ejected into the excavation. Some rockbursts occurred in some South African mines and at the Jinping II tunnels in China
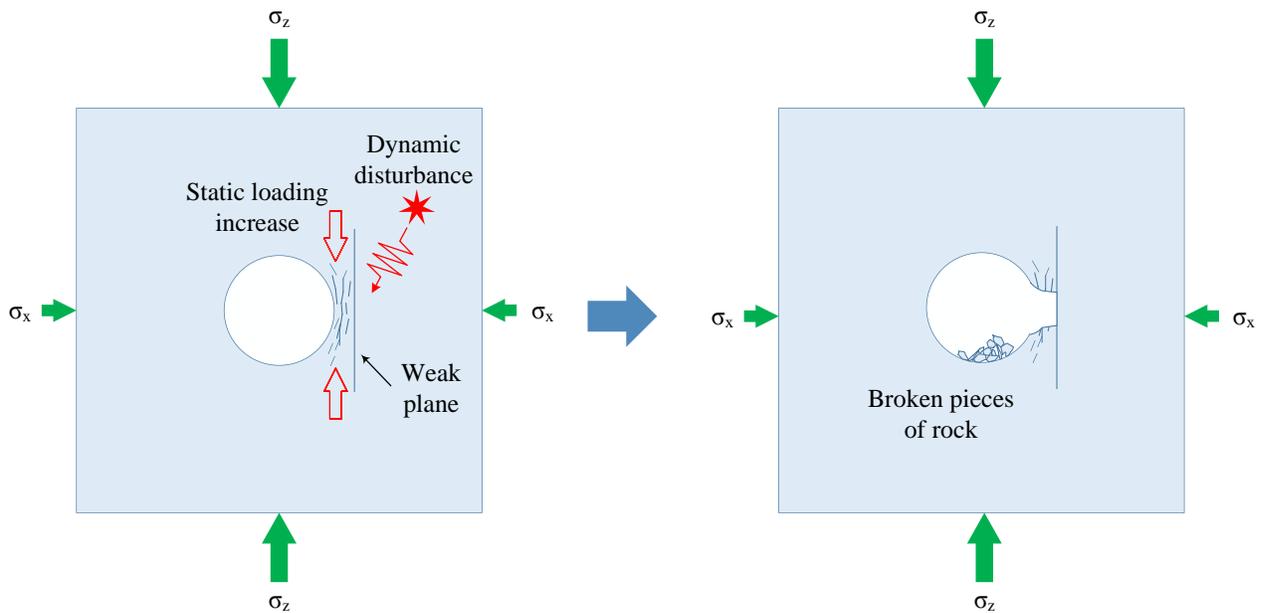
Figure 5-1: Schematic sketch of rockburst induced by slab buckling.

were resulted from slab buckling (Ortlepp, 1997; Qiu et al., 2014). Rock slabs are normally created by high stress in a 3D stress state with the intermediate principal stress playing an important role (Cai, 2008a). It should be noted that in this thesis, only rockbursts induced by static loading are investigated.

5.2.2   Intact rock rupture

Experimental and numerical studies have shown that in a loaded rock specimen with pre-existing weak planes such as cracks and fractures, new fractures nucleate from the tips of the pre-existing fractures (Bobet and Einstein, 1998a; Bobet and Einstein, 1998b; Cai, 2013a; Tang and Kou, 1998). When an underground opening is excavated, rocks around the excavation boundary are subjected to a stress change; the radial stress is decreased while the tangential stress is increased. This stress change due to excavation may activate a nearby fault as shown in Figure 5-2, causing
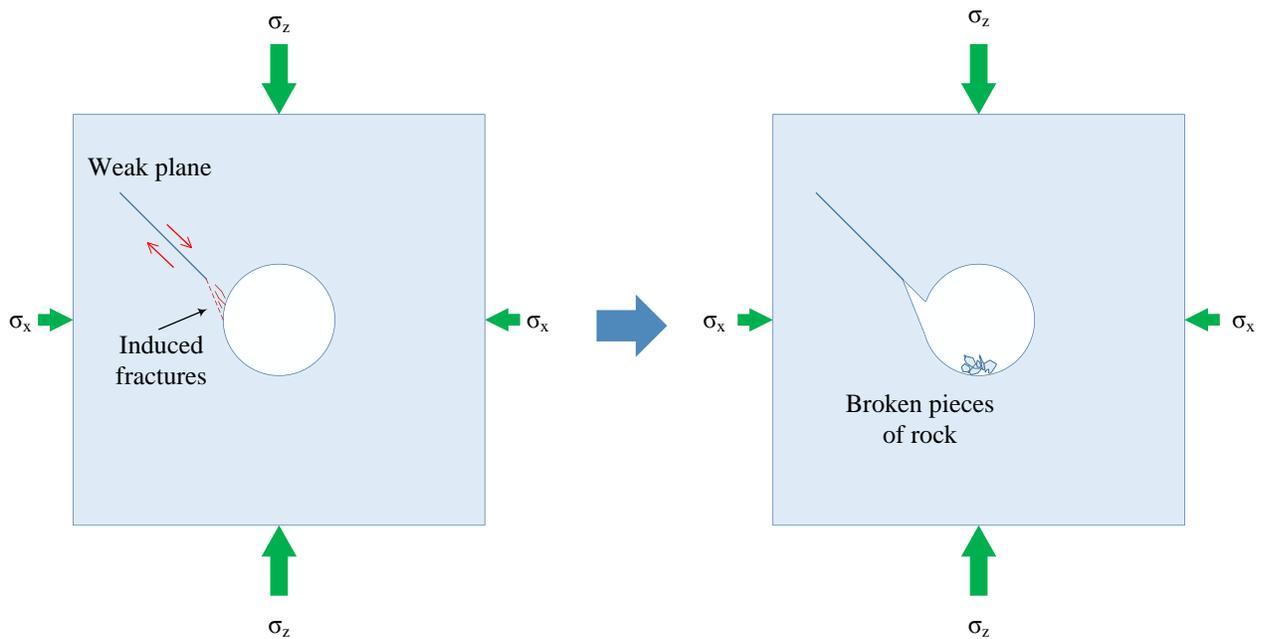
Figure 5-2: Schematic sketch of rockburst induced by intact rock rupture and fault slip.

rocks to fracture ahead of the fault. As loads increase, the fractures propagate until they reach the tunnel wall and rupture the rocks. The rupture of the rocks will, in turn, cause a sudden fault slip. Strain energy, which is accumulated gradually during the deformation process, can be released suddenly when the fault slips. When the fault slips suddenly (unstable fault shear failure) with a large amount of strain energy stored in the rocks released, it may cause rock failure in other parts of the tunnel. Thus, weak planes around underground excavations can influence tunnel stability (Barton et al., 1974; Jeon et al., 2004; Yeung and Leong, 1997).

5.3 Influence of weak planes on rockburst occurrence and damage

In this section, models are developed to study the influence of weak planes on rockburst occurrence and damage numerically. A systematic study is conducted to understand the influence of weak plane length (l), orientation (θ), and relative position of a weak plane to a tunnel (d) on rockburst damage. In this study, Abaqus^{2D} is used to simulate rockburst in deep tunnels.

5.3.1 Model setup and tunnel excavation simulation method

5.3.1.1 Material properties and boundary conditions

A circular tunnel with a radius (r) of 5 m is modeled. In the numerical models, the outside boundary width and height should be at least ten times of the tunnel diameter to exclude the effect of the outer boundary on stress redistribution around the tunnel. In this study, the models also include a fault with a varying length and orientation because the main objective of this research is to study the influence of weak planes on rockburst in deep underground excavations. Hence, the external boundary width and height are 15 times of the tunnel diameter to make sure that stress redistribution around the fault does not affect the modeling results. Figure 5-3

illustrates the model geometry. Before excavation, in situ stresses are applied to the external boundaries and then the boundaries are fixed with roller constraints. Tunnel excavation is then simulated. The horizontal (σ_x) and vertical (σ_z) in situ stresses are assumed to be 30 and 60 MPa, respectively.

An elasto-plastic Mohr-Coulomb strain-softening model with heterogeneous material properties is used to model the rock mass with its physical and mechanical properties presented in Table 5-1. The heterogeneous model is illustrated in Figure 5-4, showing the normal distributions of Young's modulus E, cohesion c, and friction angle φ in the model. In the heterogeneous model, the mean values of E, c, and φ are 21 GPa, 22 MPa, and 31°, respectively and the coefficients of variation (COV) for all three values are set to 5%. The parameters for defining the strain-softening behavior of the rock mass are presented in Table 5-2.

Table 5-1: Rock mass physical and mechanical properties

Parameter	Value
Density, ρ (kg/m^3)	2500
Young's modulus, E (GPa)	20
Poisson's ratio, v	0.2
Uniaxial compressive strength, UCS (MPa)	69.3
Cohesion, c (MPa)	20
Friction angle, φ (°)	30

Table 5-2: Parameters with COV = 5% for defining the post-peak behavior of the rock

Cohesion		Tension cut-off	
Cohesion yield stress (MPa)	Shear plastic strain	Tension cut-off stress (MPa)	Tensile plastic strain
22.0	0	3.0	0
0.01	0.2	0.01	0.005

σz = 60 MPa

Host rock
(150 m × 150 m)

Fault

l

θ

d

σx

σx = 30 MPa

Tunnel
(r = 5 m)

σz
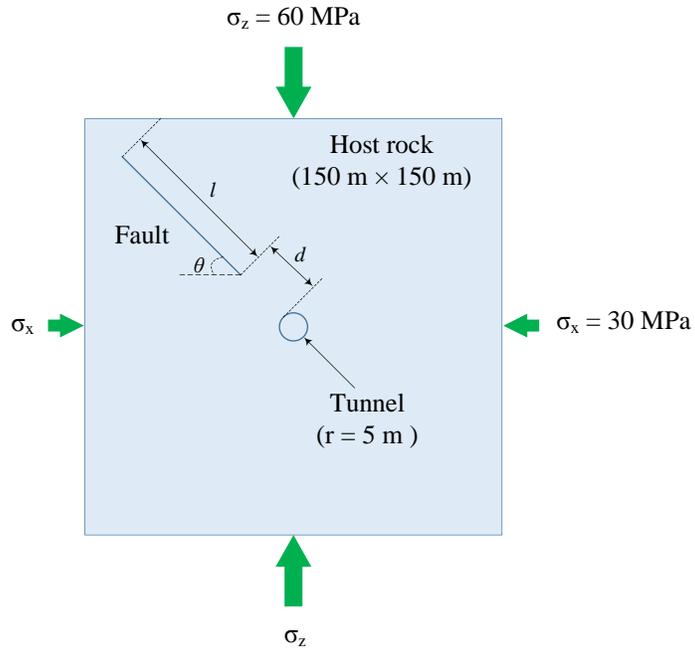
Figure 5-3: Model geometry and boundary conditions.

Tunnel

Normal
distribution

$\mu_E = 21$ GPa, $\sigma_E = 1.05$ GPa
$\mu_c = 22$ MPa, $\sigma_c = 1.1$ MPa
$\mu_\varphi = 31°$, $\sigma_\varphi = 1.55°$

-3σ -2σ -1σ μ 1σ 2σ 3σ

x
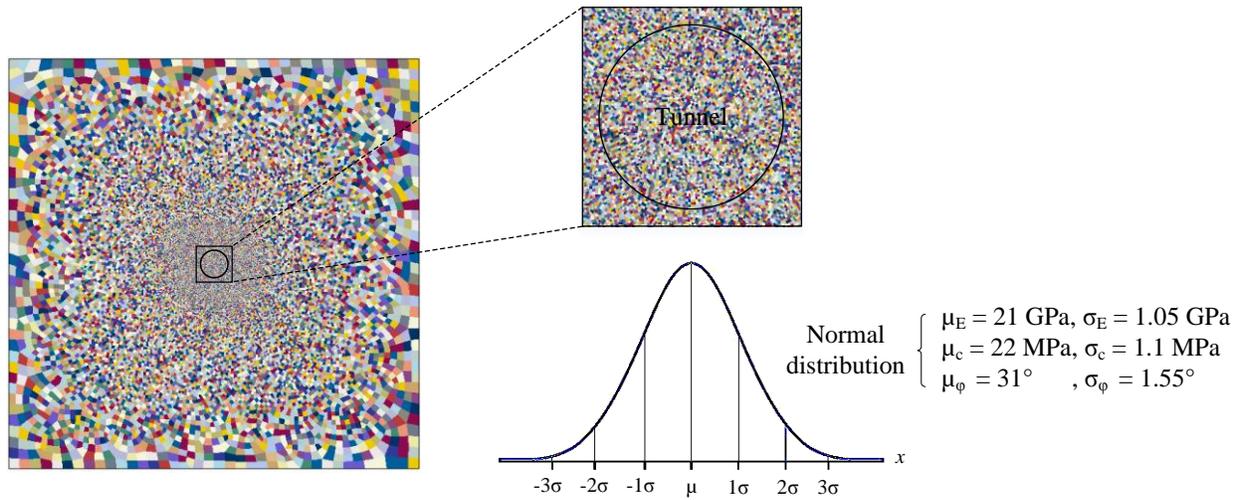
Figure 5-4: Heterogeneous model with normal distributions of Young's modulus E, cohesion c, and friction angle φ.

5.3.1.2 Tunnel excavation simulation

If a tunnel is excavated by the long-round drill and blast method, the tunnel portion of the model can be deleted in one stage to simulate excavation in numerical modeling. A dynamic unloading condition is created by this excavation method. If a tunnel is excavated by the short-round drill and blast method or by TBM, gradual tunnel excavation needs to be considered in numerical modeling to avoid dynamic shockwave around the excavation (Cai, 2008b).

Two approaches can be used to simulate gradual excavation of a tunnel in two dimensional (2D) models. In the first approach, the tunnel is excavated at once and equivalent pressures are applied to the tunnel boundary. The pressures are then reduced step-by-step to reach to zero to simulate gradual tunnel excavation (Azevedo et al., 2002). In the second approach, the material in the tunnel portion is degraded (by reducing Young's modulus) step-by-step to reach to empty to simulate gradual tunnel excavation (Cai, 2008b). Implementation of these techniques in Abaqus requires complicated FORTRAN programming. A new and simple technique is proposed in this study to simulate gradual tunnel excavation.

In numerical models, when two separated surfaces touch each other, they interact according to the normal and tangential contact types assigned. In many practical problems, the normal and tangential contact behaviors between two surfaces are defined by the normal contact stiffness (k) and friction coefficient (μ), respectively. The normal force (F) between the surfaces is,

$$F = k.\Delta x \qquad \qquad (5\text{-}1)$$

where Δx is the penetration of surfaces. For a given contact force (F), the resulting penetration (Δx) increases as the normal contact stiffness (k) decreases. In the current model simulation, a
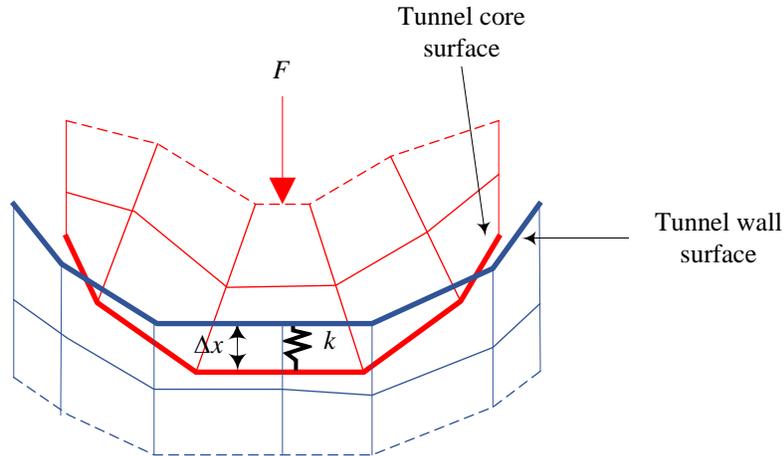
Figure 5-5: Surface penetration proportional to normal contact stiffness.

contact is assigned to the boundary between the tunnel core and the tunnel wall (Figure 5-5). The

normal contact stiffness (k) of the contact is reduced step-by-step to reach to zero to simulate

gradual tunnel excavation. In this method, the surfaces of the tunnel core and the tunnel wall are

allowed to penetrate each other in a controlled fashion, and this results in stress reduction which

is equivalent to that caused by actual tunnel excavation.

This method is implemented in Abaqus and an elastic stress analysis is conducted to verify its

suitability for gradual tunnel excavation simulation in 2D models. Excavation of the circular

tunnel (Figure 5-3) in a ground with σ_z = 60 MPa and σ_x = 60 MPa is considered. Before any

excavation, hard contact (i.e., $k = \infty$) and rough contact (i.e., $\mu = \infty$) are assigned to define the

normal and tangential contact behaviors, respectively. In this way, no relative movement is

allowed between contacted elements in the tunnel portion and the host rock. Figure 5-6 presents

the stress distributions before excavation, showing uniform stresses in the model which are equal

to the applied stresses (i.e., σ_z = 60 MPa and σ_x = 60 MPa).
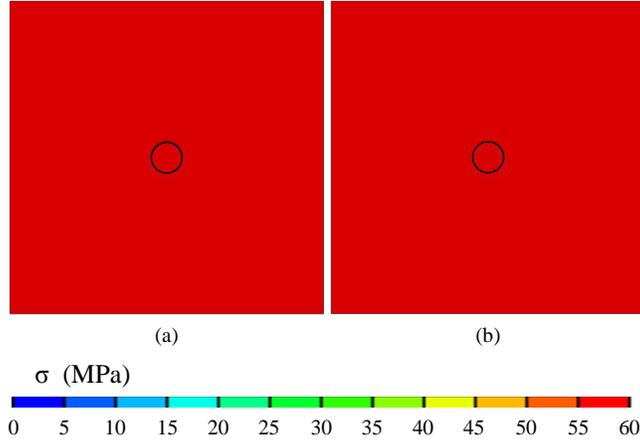
Figure 5-6: (a) Horizontal stress σ_x and (b) vertical stress σ_z in the model before tunnel excavation.

The contact stiffness between elements in the tunnel core and the tunnel wall is reduced from 20 GN/m to zero in ten steps to mimic the sequence of gradual excavation in 2D models. The contact stiffness 20 GN/m, which is equal to the Young's modulus of 20 GPa in value, is selected to ensure uniform stress distribution before excavation (Figure 5-6).

The stress state at a circular tunnel wall in an infinite plate is (Brady and Brown, 2013)

$$\sigma_r = 0 \tag{5-1}$$

$$\sigma_\theta = \sigma_z + \sigma_x + 2(\sigma_z - \sigma_x)cos2\theta \tag{5-2}$$

$$\tau_{r\theta} = 0 \tag{5-3}$$

where σ_r, σ_θ and $\tau_{r\theta}$ are radial, tangential and shear stresses, respectively. For the given hydrostatic far-field stresses, the analytical solution gives $\sigma_\theta = 120.0$ MPa at the tunnel surface. Figure 5-7 shows the tangential stress distribution around the tunnel after excavation. This figure shows $\sigma_\theta = 117.4$ MPa at the tunnel surface, which is in good agreement with the analytical
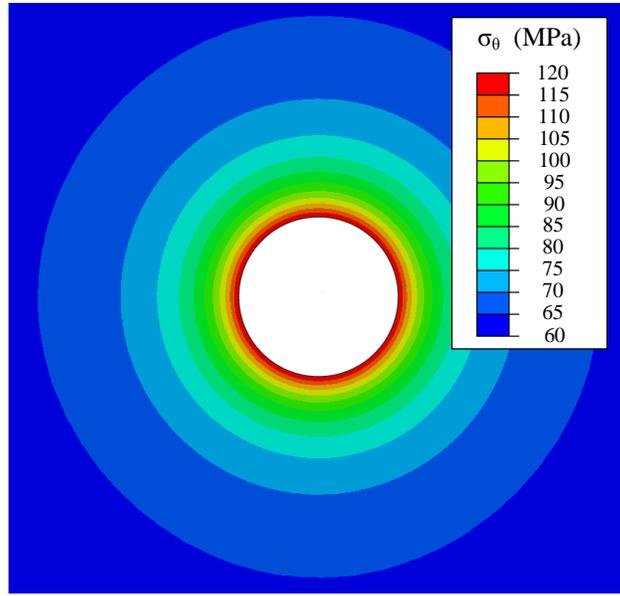
Figure 5-7: Maximum principal stress distribution around the tunnel after excavation.

solution. This verifies that the proposed tunnel excavation technique in Abaqus is suitable for gradual tunnel excavation simulation in 2D models.

Figure 5-8 presents the ground reaction curve for the simulated 2D tunneling process. In Figure 5-8, the vertical axis shows the vertical pressure at the top of the tunnel and the horizontal axis shows the tunnel convergence in σ_z direction between two points at the top and the bottom of the tunnel. Figure 5-8 indicates that when there is no excavation, the vertical stress at the top of the tunnel is 60 MPa, which is equal to the applied σ_z. By decreasing the normal contact stiffness step-by-step, the vertical stress at the top of the tunnel wall is decreased and reaches zero at the last step. The analytical solution gives a maximum convergence of 0.39% in σ_z direction. Figure 5-8 shows that the calculated convergence is 0.388%. The gradual excavation process implicitly implies that the tunnel face has advanced more than three tunnel diameters and the maximum tunnel convergence has been reached (Panet and Guenot, 1983).

For an elastic analysis, the results are independent of the excavation rate. Because an elasto-plastic Mohr-Coulomb model is used in this study, it is needed to verify the applicability of the proposed gradual excavation method for the Mohr-Coulomb models. The same modeling approach explained above in an elasto-perfectly plastic Mohr-Coulomb model is considered. A cohesion of 20 MPa and a friction angle of 30 are assigned. The ground reaction curve is shown by the red dash line in Figure 5-8. The analytical solution gives a maximum convergence of 0.46% in the σ_z direction and the calculated convergence in the elasto-plastic model is 0.47%. This verification confirms that the proposed approach is suitable for simulating gradual tunnel excavation process in 2D models using both elastic and elasto-plastic models.
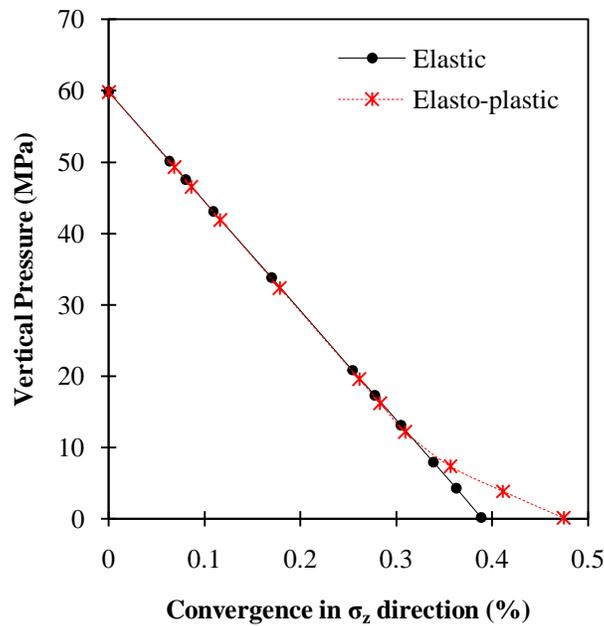
Figure 5-8: Ground reaction curve for tunnel excavation simulation in 2D.

5.3.2 Effect of weak planes on rockburst occurrence and damage

A tunnel without any adjacent geological structure is modeled firstly to study the effect of weak planes on rockburst occurrence and damage. Shear and tensile failures around the tunnel,

indicated by plastic strains, are illustrated in Figure 5-9. The figures show symmetric failures around the tunnel, with shear failure zones located at 3 and 9 o'clock because the maximum in situ principal stress direction is vertical.

Figure 5-10a shows the velocity distribution in elements around the tunnel at the beginning of excavation Step 10. The figure shows a maximum velocity of 1.78 m/s in one node at the tunnel surface. The minimum velocity in the failed elements is 0.14 m/s. The velocities of all failed elements around the tunnel during the model running time (or the tunnel excavation process) are tracked and an average velocity ($\overline{V}$) is calculated. The maximum of the average velocity ($\overline{V}_{max}$) during the running time is picked to interpret the results. It should be noted that this velocity is the modeling velocity not the ejection velocity. Figure 5-11 shows the velocity vectors of nodes around the tunnel at the beginning of Step 10. As it is seen, not all the vectors in the failure zone are perpendicular to the tunnel wall. Hence, the ejection velocity, which is the radial velocity of failed rocks, would be slightly smaller than the calculated velocity in the models. However, the modeling velocity can give an approximation of the ejection velocity. When failure is stable, the ejection velocity of failed rocks is low (Milev et al., 2002). $\overline{V}_{max}$ is 0.58 m/s at the tunnel wall, which means that the rock failure can be considered as stable in this case. The maximum kinetic

(a) Shear failure   (b) Tensile failure
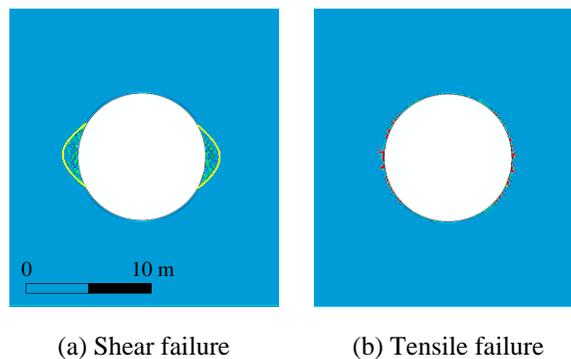
Figure 5-9: Failure zones around the tunnel without any nearby geological structures: (a) shear failure, (b) tensile failure.

energy per unit volume (KE_{max}) from the failed rocks, which can be used as an indicator of the rock failure intensity, is 0.65 kJ/m^3. In this case, the maximum unit kinetic energy is also small, which again means that the rock failure is stable; if it were in the field, the failure would be in the form of spalling, spitting or shallow slabbing.
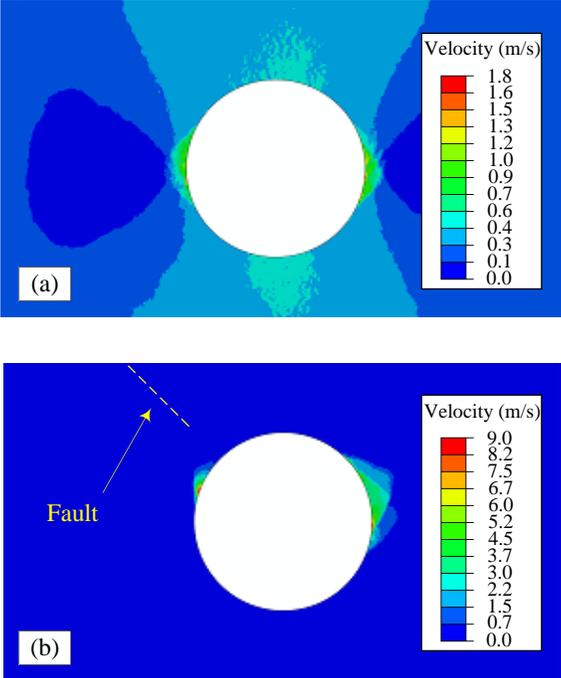
Figure 5-10: Velocity distributions in the elements: (a) without and (b) with a nearby fault at the beginning of Step 10 (for l = 80 m, d = 2.5 m, and θ = 45°).
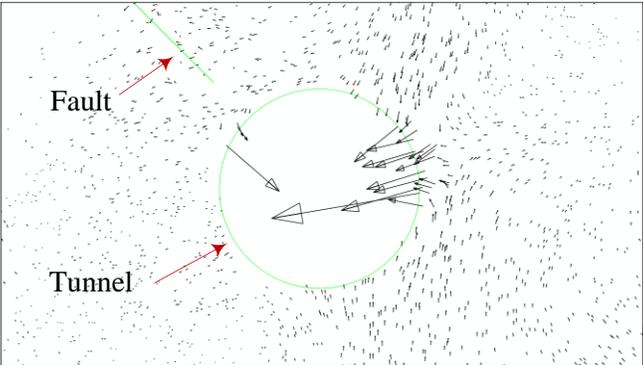
Figure 5-11: The vectors of velocity at the beginning of Step 10 (for l = 80 m, d = 2.5 m, and θ = 45°).

Next, a fault with a dip of $\theta = 45°$, a length of $l = 80$ m, at a position of $d = 2.5$ m from the tunnel wall (see Figure 5-3) is added to the model. It is assumed that the modeled fault is straight. A Coulomb model with a friction coefficient (μ) of 0.4 and a zero cohesion is used to model the fault. The Coulomb model is suitable for modeling filled and sheared faults (Tonon et al., 2001). The same modeling approach for gradual tunnel excavation explained above is applied and the tunnel is excavated in ten steps.

Figure 5-10b shows the velocity distribution in elements around the tunnel at the beginning of excavation Step 10. Development of failure around the tunnel at Steps 1, 4, 9, and 10 is shown in Figure 5-12. The figure shows the initiation of tensile and shear fractures at the lower end of the fault at Step 1 excavation. Afterwards, the shear fractures propagate toward the tunnel face (Step 4) and rocks between the fault and the tunnel are ruptured. Meanwhile, tensile fractures are initiated at the bottom of the tunnel. Figure 5-13 shows the relative movement of the foot wall

Step 1   Step 4   Step 9   Step 10

(a) Shear failure

0   10 m
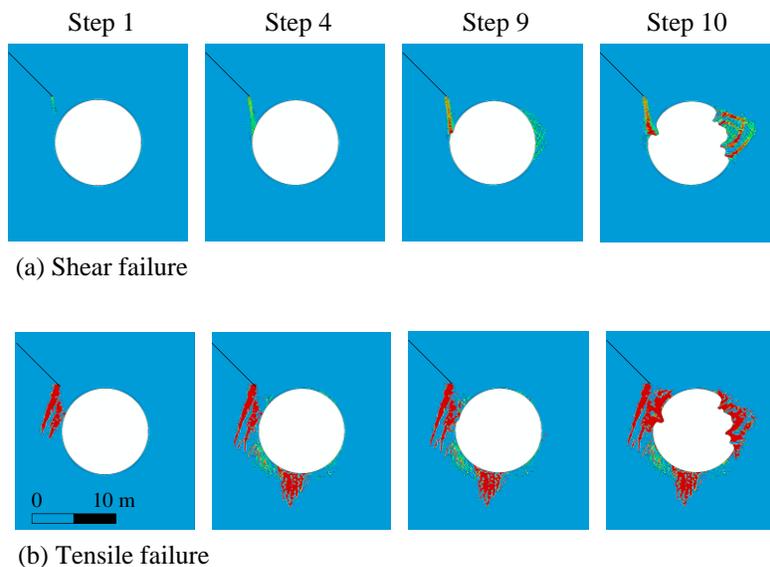
(b) Tensile failure

Figure 5-12: Failure development around the tunnel with a nearby fault: (a) shear failure, (b) tensile failure (for l = 80 m, d = 2.5 m, and θ = 45°).

116
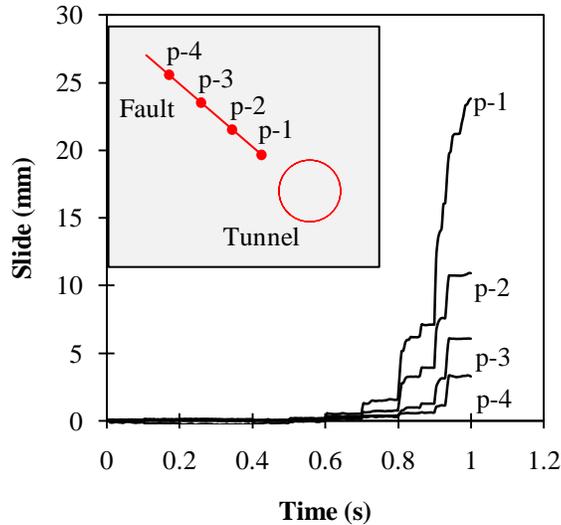
Figure 5-13: Relative movements of the fault during the running time. The spacings of the points are not to scale in the insert.

and the hanging wall of the fault at four points (the fault tip and three points at 1 m spacing). A relative slip of the fault of about 25 mm occurs at point-1 after the excavation is completed. The slip rate is the highest at Step 9. Slip of the fault due to excavation causes compression at positions of 1 to 4 o'clock (Step 9). When the contact stiffness reaches zero or the tunnel face advances sufficiently ahead (Step 10), the failed rocks on the right tunnel wall blow out with a $\bar{V}_{max}$ = 3.4 m/s and a failure pit with a depth of 3 m is created. The maximum unit kinetic energy is 6.97 kJ/m^3.

When rock failure occurs, the broken rock pieces can spall non-violently or be ejected violently. Rock failure is usually classified into two groups: stable and unstable failures based on the ejection velocity of broken rocks, volume of damaged rock, and released energy. However, there is no exact border between stable and unstable failures and a transition between the two should exist (Manouchehrian and Cai, 2016d).

Recognition of stable and unstable rock failures is not straightforward in numerical modeling. Usually, the failure mode in numerical modeling is judged by comparing the model response with a known model response that is considered as stable failure. For example, it is widely accepted that failure in an Uniaxial Compression Strength (UCS) test simulation is stable if a rigid loading system is used (Garvey, 2013; Kias and Ozbay, 2013; Manouchehrian and Cai, 2016d). Using this modeling result as the base, other UCS modeling results with different loading systems can be compared and the failure mode judged. Model responses such as stress–strain curve, energy components, velocity etc., can be used to judge failure mode.

In tunnel excavation modeling, the failure mode in a model without geological structures can be considered as stable (base model). Therefore, responses from models with geological structures can be compared with the response of the model without geological structures to distinguish between the stable and unstable failures. Hence, we can track the velocity of failed elements, the volume of failed rock, the amount of released kinetic energy, and the deformed mesh and compare them with these from the base model to judge the failure mode. The results presented in Figure 5-10 and Figure 5-12 show that the presence of the fault results in higher modeling velocity, more kinetic energy release, and larger failure zones. Comparing with the results shown in Figure 5-9, it can be concluded that the presence of the fault changes the failure mode from stable to unstable.

5.3.2.1 *Influence of fault length on rockburst damage*

In fracture mechanics, the term "critical crack size" refers to the size of a crack (weak plane) in a structure that causes failure at a particular stress level. Wong et al. (2002) showed that in rock specimens, new cracks are easier to initiate from longer pre-existing cracks than from shorter

ones. Thus, it can be expected that longer faults in a rock mass can affect the stability of underground openings more than short ones can do.

Tunneling process near a fault with different lengths is simulated to understand the influence of fault length (l) on rockburst damage. A circular tunnel with a radius of $r = 5$ m is excavated in ten steps. A fault with a dip of $\theta = 45°$, located at a position of $d = 2.5$ m from the tunnel wall (Figure 5-3) is included in the model. The length of the fault (l) is varied at $l = 0$, 20, 40, 60, and 80 m, resulting in l/r ratios of 0, 4, 8, 12, and 16, respectively. The rock mass properties listed in Table 5-1 and the in situ stress field of $\sigma_z = 60$ MPa and $\sigma_x = 30$ MPa are used. The same modeling procedure for gradual tunnel excavation described in Section 5.3.1 is used.

The influence of l on $\bar{V}_{max}$ and KE_{max} is presented in Figure 5-14 and Figure 5-15, respectively. Figure 5-14 and Figure 5-15 indicate that as the fault length increases, both $\bar{V}_{max}$ and KE_{max} increase. Figure 5-14 shows that when $l = 0$ m (i.e., there is no fault), the $\bar{V}_{max}$ is low (0.58 m/s) and the rock failure can be considered as stable. $\bar{V}_{max}$ and KE_{max} increase rapidly as the l/r ratio
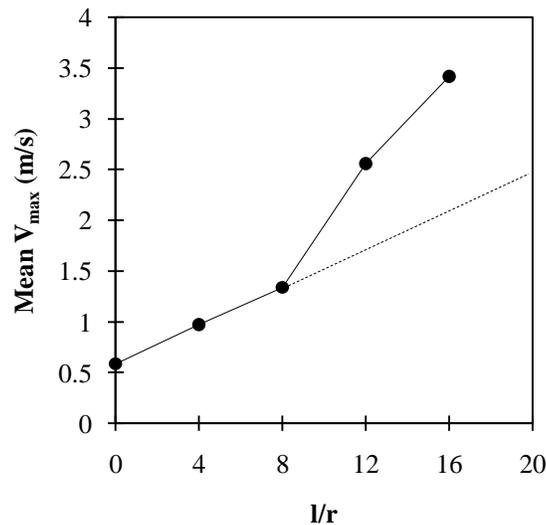
Figure 5-14: Influence of fault length on $\bar{V}_{max}$ (for d/r = 0.5 and θ = 45°).

119

increases. In Figure 5-14 and Figure 5-15, a trend change exists when l/r changes from 8 to 12. When the fault is longer (e.g. l/r = 12 and 16), its end is closer to the model boundary, and this can influence the results. As stated above, the outside boundary width and height should be at least ten times of the modeled structure to exclude the effect of the outer boundary on stress redistribution around the structure. In this study, in addition to the tunnel a fault is included in the model. In this case, building a model which is large enough to exclude the boundary effect is computationally expensive. In Figure 5-14 and Figure 5-15, the dash line may be used to correct the boundary effect. For example, for l/r = 16, we have $\bar{V}_{max}$ = 3.4 m/s and KE_{max} = 6.97 kJ/m^3 from modeling results, which can be modified to $\bar{V}_{max}$ = 2.2 m/s and KE_{max} = 2.8 kJ/m^3 from the dashed line. Figure 5-16 illustrates the failure zones in the models. This figure shows that when the fault is longer, a larger fracture zone is formed at the ends of the fault. The failure zones around the tunnel for various l/r ratios are presented in Figure 5-17, with tensile and shear failure zones shown separately. It is seen that as the l/r ratio increases, the failure zones become larger.
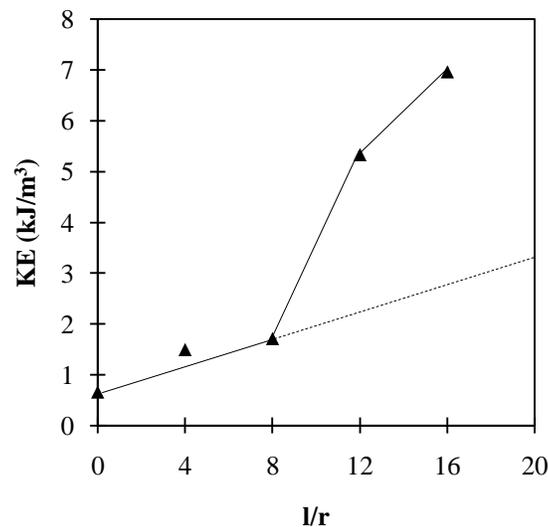
Figure 5-15: Influence of fault length on KE$_{max}$ (for d/r = 0.5 and θ = 45°).
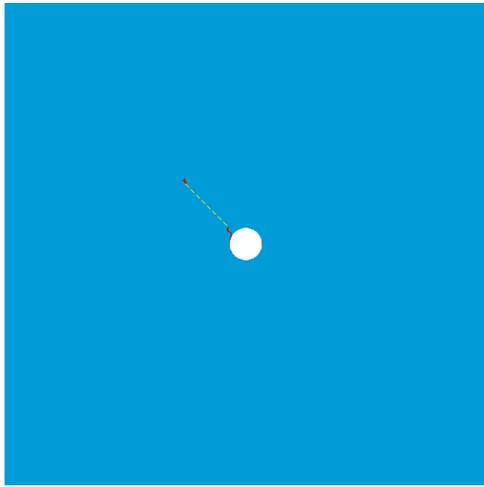
l/r = 4
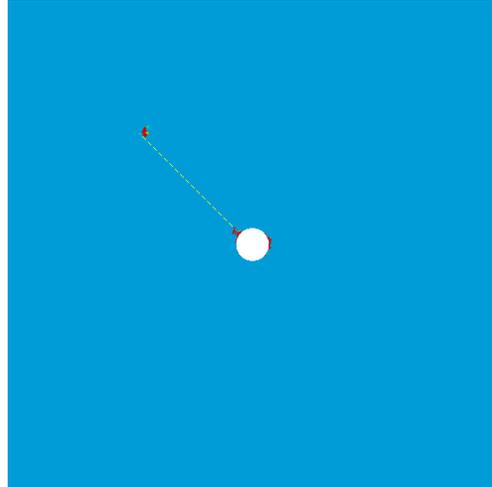
l/r = 8
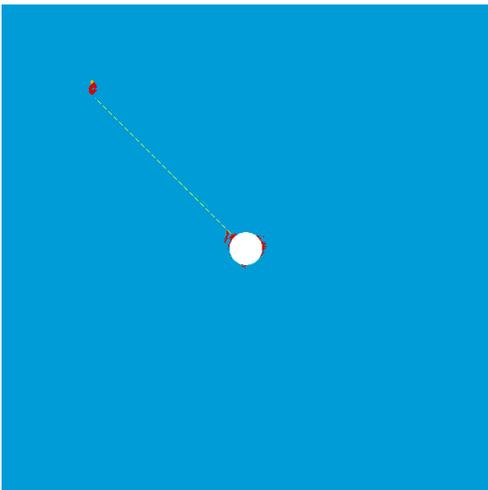
l/r = 12
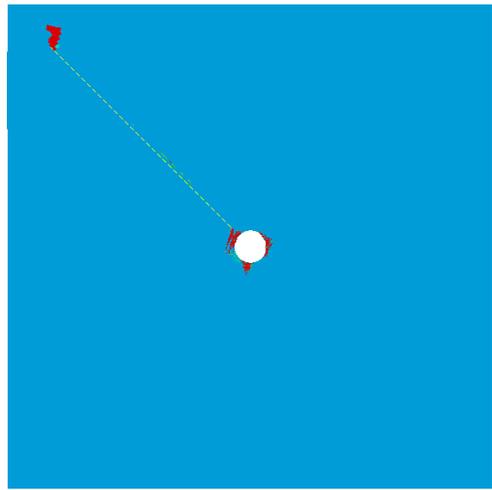
l/r = 16

Figure 5-16. Failure zones in models with different fault lengths.
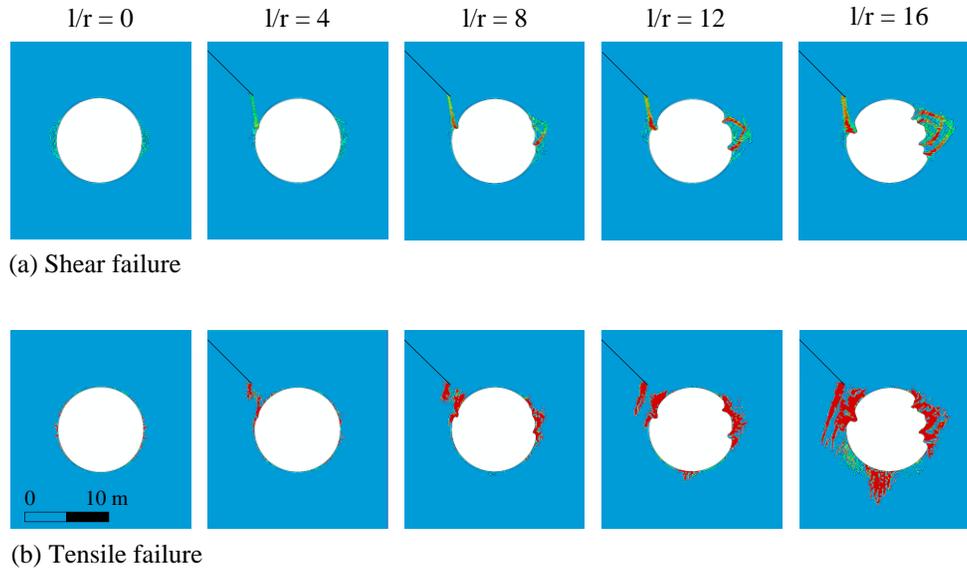
Figure 5-17: Failure zones around the tunnel in models with different fault lengths: (a) shear failure, (b) tensile failure (for d/r = 0.5 and θ = 45°).

Figure 5-18 shows the total displacement distribution around the tunnel at the end of Step 9 excavation (before the sidewall fails). The figure shows that when the fault is longer, a larger volume of hanging wall rock can move toward the tunnel and push the rock near the tunnel wall boundary, particularly the rock on the right wall side. Hence, more strain energy release is possible if there is a sudden rock failure. This explains why the maximum unit kinetic energy is high for large l/r ratios. Furthermore, the displacement field also indicates that the mine system stiffness is low when the l/r ratio is high because the rocks surrounding the failed rocks can have more deformation.

The concept of mine system stiffness has been used by some researchers to explain rockburst in underground mines (Aglawe, 1999; Wiles, 2002). Although it is difficult to calculate mine system stiffness quantitatively in a tunnel setting, an analogy to Loading System Stiffness (LSS) in laboratory testing can be made. Laboratory test results show that the modes of failure (stable

and unstable) depends on the relative stiffness of the rock in the post-peak deformation stage and the loading system (Wawersik and Fairhurst, 1970). A soft loading system is capable of storing more strain energy than a stiff loading system. Thus, when a rock specimen fails, the failure is stable under a stiff loading system condition and unstable under a soft loading system condition. Figure 5-19a shows the concept of LSS by changing the length of the loading platen and Figure 5-19b shows the failure modes changing from stable to unstable as LSS decreases. Despite of loading condition difference in the field and in laboratory, it can be seen that an increase of l decreases the mine system stiffness and as a result, unstable rock failure can occur around the tunnel. This can be clearly seen from the results presented in Figure 5-14 to Figure 5-18.
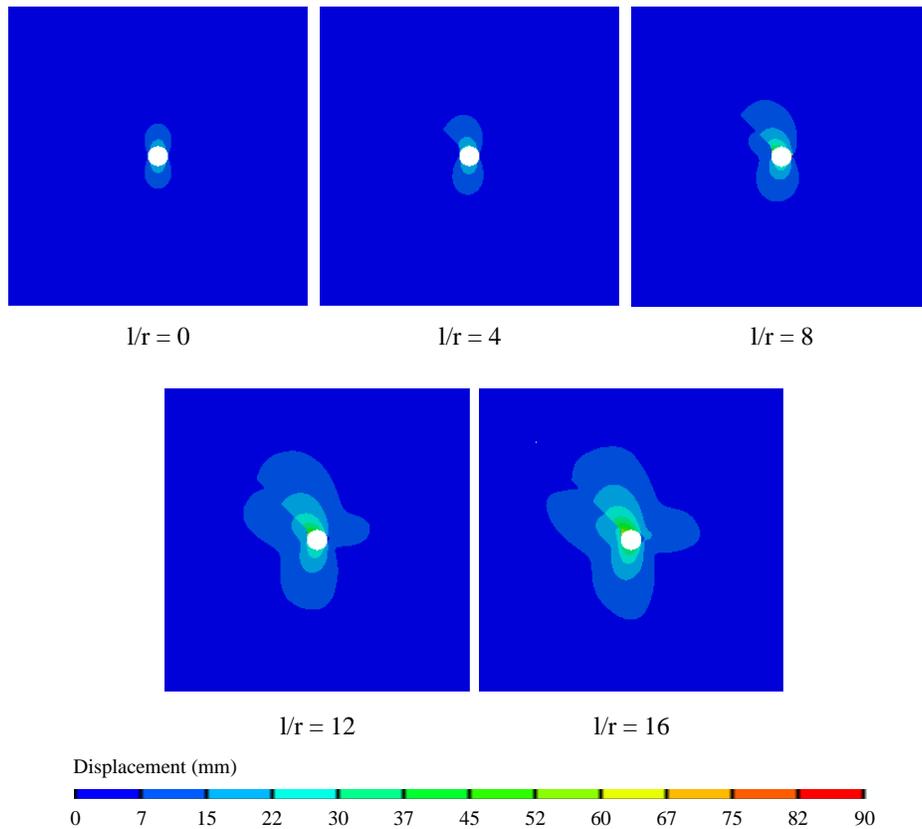
Figure 5-18: Displacement around the tunnel in models with different fault lengths at the beginning of Step 10 (for d/r = 0.5 and θ = 45°).
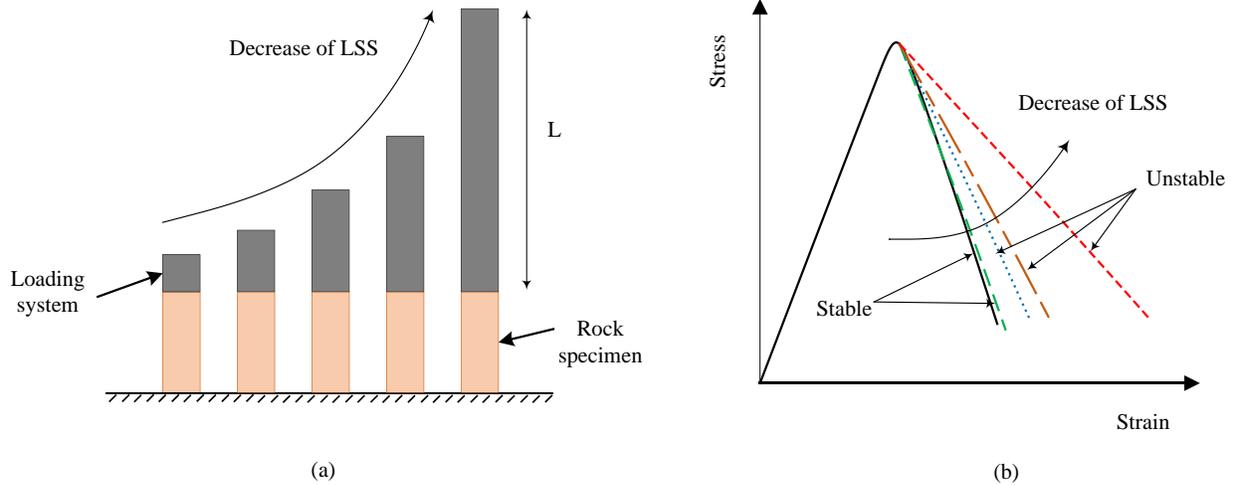
Figure 5-19: Illustration of loading system stiffness change in (a) laboratory UCS test and (b) the corresponding stress–strain curves.

Reduced mine system stiffness can be considered as a main effect of weak planes near openings in deep underground mines that can potentially cause rockburst. According to the simulation results, it is seen that the size of a weak plane is an important factor that influences rockburst damage.

5.3.2.2 *Influence of fault position relative to tunnel on rockburst occurrence and damage*

When an opening is excavated near weak planes, excavation-induced stress concentration can affect the stability of the weak planes and the opening. The relative position of the opening to the weak planes can influence the failure mode. For example, when a fault is very close to the tunnel wall buckling failures may appear (Ortlepp and Stacey, 1994). Hence, a systematic study on the influence of the relative position of a fault to the tunnel on rockburst occurrence and damage is conducted.

A circular tunnel with a radius of $r = 5$ m is considered. The relative position of a fault to the tunnel is defined by d (see Figure 5-3). A fault with a dip of $\theta = 45°$ and a length of $l = 60$ m (l/r

= 12) at different positions to the tunnel wall (d = 0, 5, 10, 15, and 20 m) is modeled. The modeling procedure for gradual tunnel excavation explained in Section 5.3.1 is used.

Figure 5-20 and Figure 5-21 present $\bar{V}_{max}$ and KE_{max} values for different position distances normalized by r. As d increases, the $\bar{V}_{max}$ and KE_{max} values first increase and then decrease. When the fault daylights (d/r = 0), there is no intact rock to prevent fault slip and the fault can slide toward the tunnel easily. In this case, the rock mass near the fault is less stressed and less energy is accumulated in the rock mass. The stress (Mises stress) states around the tunnel before excavation in the models with d/r = 0, 1, and 2 are shown in Figure 5-22 and the failure zones after tunnel excavation are shown in Figure 5-23 for different d/r ratios. When d/r = 0, only rock masses on the right tunnel wall fail and the maximum velocity $\bar{V}_{max}$ the maximum velocity is 2.0 m/s. Because the volume of the failed rock is small, less kinetic energy is released and KE_{max} is 2.1 kJ/m^3. Intact rock exists between the fault and the tunnel for non-zero d, and the rock has to be ruptured before the fault can slip freely. Coupled with stress concentration due to the fault geometry, more energy can be stored inside the rock mass before it fails. As a result, a large amount of energy is released when the rock fails and the failure can be more violent. For d/r = 1, both $\bar{V}_{max}$ and KE_{max} are the highest in the five cases simulated. However, when the fault is further away from the tunnel, its influence on rock failure and energy release is small. Hence, the position distance of weak planes to an opening is an important factor that influences rockburst damage.
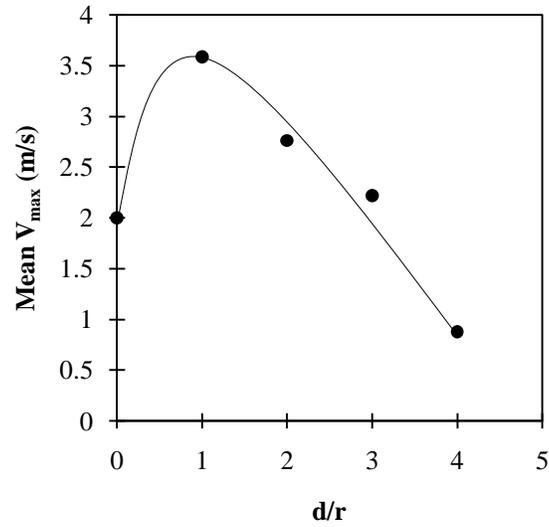
Figure 5-20: Influence of the relative position of the fault to the tunnel on $\overline{V}_{max}$ (for l/r = 12 and θ = 45°).
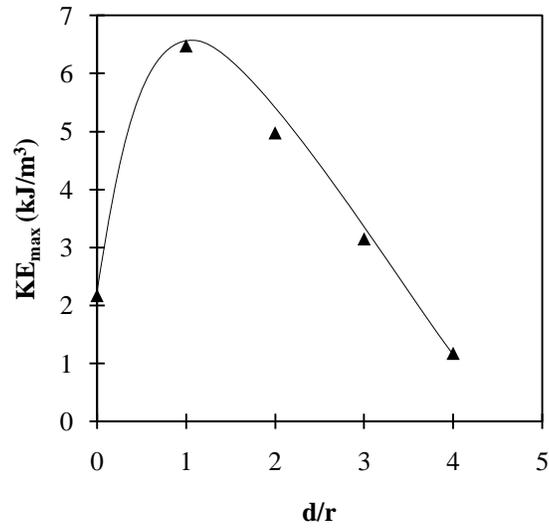
Figure 5-21: Influence of the relative position of the fault to the tunnel on KE_{max} (for l/r = 12 and θ = 45°).

126
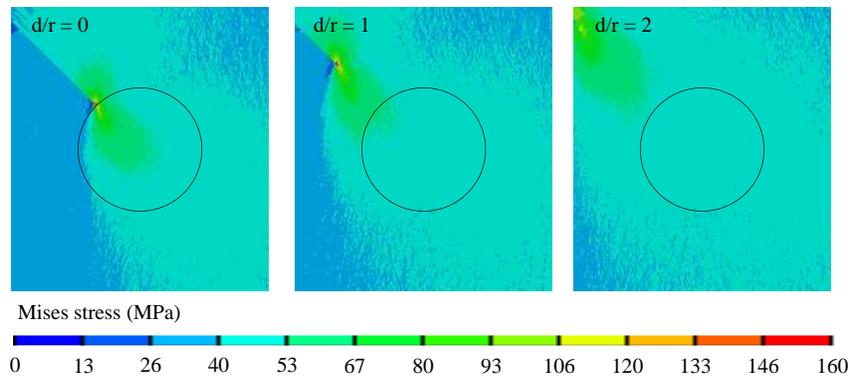
Figure 5-22: Stress around the tunnel before excavation for d/r = 0, 1, and 2.

(a) Shear failure
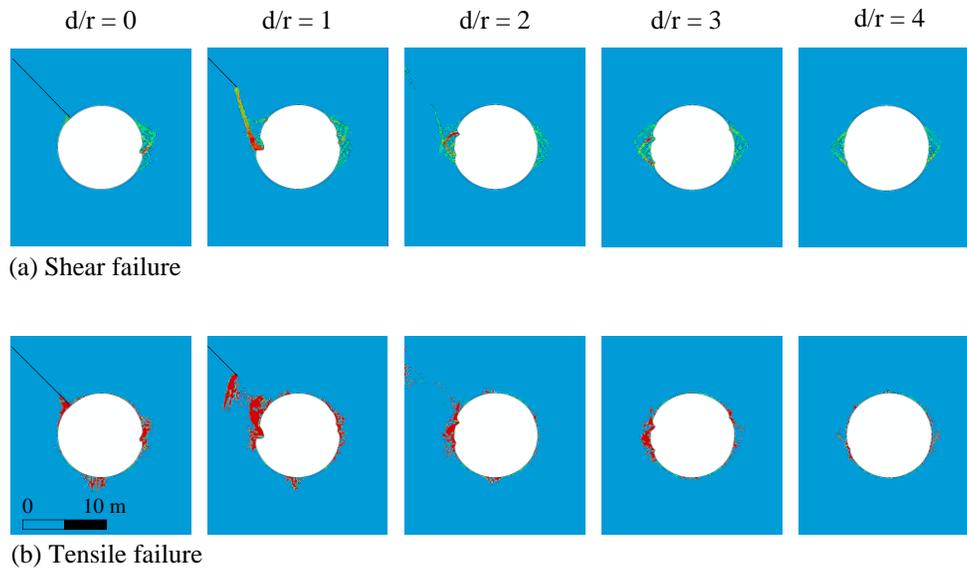
(b) Tensile failure

Figure 5-23: Failure patterns around the tunnel in models with different d/r values: (a) shear failure, (b) tensile failure (for l/r = 12 and θ = 45°).

5.3.2.3 *Influence of fault orientation on rockburst occurrence and damage*

Discontinuities alter stress distribution in rock masses and they also affect tunnel stability. Studies have shown that the orientation of discontinuities is an important factor that influences mechanical behaviors of rock masses (Barton, 2000; He et al., 2012a; Hoek, 1983). For instance, it has been observed in triaxial laboratory tests that the strength of a jointed specimen is

controlled by the orientation of discontinuities (Hoek, 1983). Thus, attention must be paid to the orientation of discontinuities in rock engineering problems.

A systematic study is carried out to understand the influence of fault dip (θ) on rockburst damage. For this purpose, the tunneling process near a fault with different dips is simulated. Excavation of a circular tunnel with a radius of $r = 5$ m is modeled in ten steps. A fault with a length of $l = 60$ m and a distance to the tunnel of $d = 2.5$ m is modeled. The dip is varied at $\theta = 0°$, 30°, 45°, 60°, and 90°. The modeling procedure for gradual tunnel excavation described in Section 5.3.1 is used.

Figure 5-24 presents the relation between θ and $\bar{V}_{max}$. It shows that when the dip of the fault is $0°$, $\bar{V}_{max}$ is low (0.63 m/s). In this case the fault is perpendicular to the maximum in situ stress (σ_z) and the presence of the fault has little influence on the degree of violence of rock failure. As θ changes from 0° to 90°, $\bar{V}_{max}$ first increases (from 0° to 45°) and then decreases (from 45° to 90°), with the maximum occurring around 45°.

The relation between θ and KE_{max} is shown in Figure 5-25. KE_{max} has a similar trend of variation with respect to θ as $\bar{V}_{max}$. As θ changes from 0° to 90°, KE_{max} first increases (from 0° to 45°) and then decreases (from 45° to 90°). The failure zones for different θ values are illustrated in Figure 5-26, showing that the largest failure zone occurs when the dip θ is 45°. For the given stress state in the model ($\sigma_z = 60$ MPa, $\sigma_x = 30$ MPa, and $\tau_{xz} = 0$ MPa), the shear stress along the fault is the maximum at $\theta = 45°$. The results shown in Figure 5-24 to Figure 5-26 imply that failure is more violent when shear stress along the fault is the maximum. Hence, the inclination of weak planes relative to the maximum principal in situ stress direction is an important factor

that influences rockburst damage. Rock masses around an underground opening are more burst-prone when the shear stress along an existing weak plane near the excavation is high.

The study above shows that the presence of weak planes around a tunnel may induce rockburst through changing the loading system stiffness of the failed rocks. It is demonstrated that the weak plane must be positioned in such a way that it favors stress buildup in the rocks that are about to fail and energy release if the rocks do fail. If failure occurs when the fault is critically positioned and oriented, more stored energy can be released, which can change the failure mode from stable to unstable.
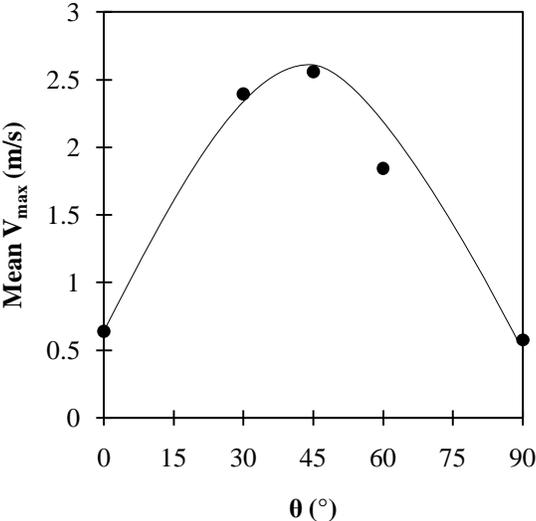
Figure 5-24: Influence of fault dip on $\overline{V}_{max}$ (for l/r = 12 and d/r = 0.5).
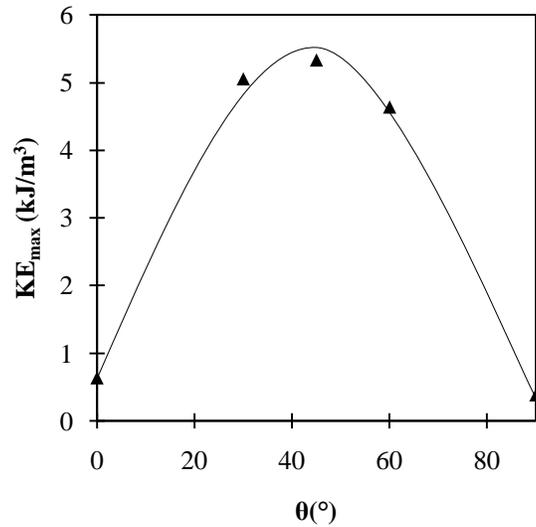
Figure 5-25: Influence of fault dip on KE_{max} (for l/r = 12 and d/r = 0.5).

(a) Shear failure
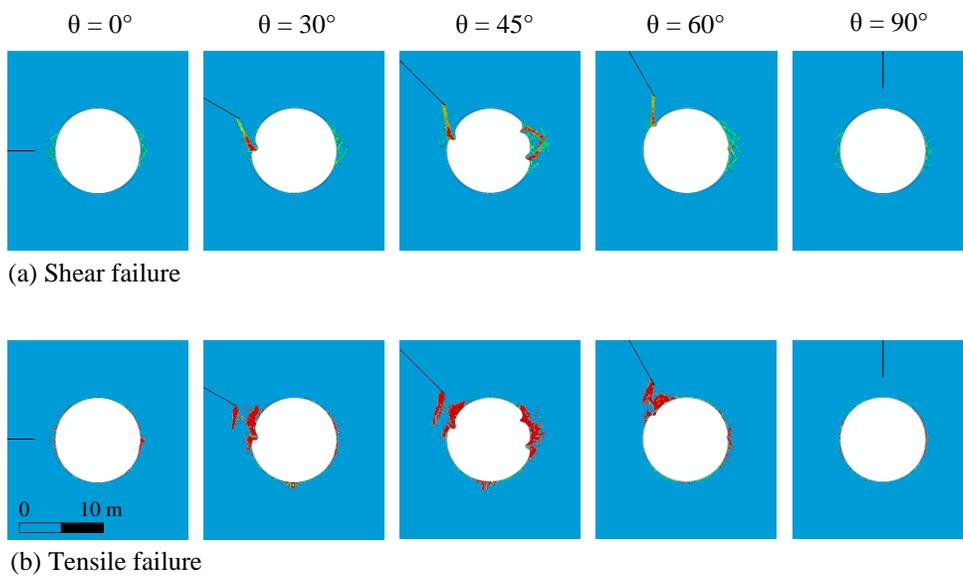
(b) Tensile failure

Figure 5-26: Failure zone around the tunnel in models with different fault orientations: (a) shear failure, (b) tensile failure (for l/r = 12 and d/r = 0.5).

5.4   Final remarks

Rockburst is a hazardous problem in deep underground mines and civil tunnels. Many factors that influence rockburst damage have been identified. Among them, the presence of geological discontinuities such as faults and shears is considered a key factor but their role in influencing

rockburst occurrence and damage is not fully understood. A good understanding of the role of geological structures on rockburst occurrence and damage is important for anticipating and controlling rockburst.

In this chapter, the Abaqus-Explicit code with heterogeneous material properties was used to study the role of weak planes in rockburst occurrence and damage. Firstly, a new approach was presented for simulating the tunnel gradual excavation process in 2D models using Abaqus. Models with and without fault planes were developed and simulated. The influence of weak plane length (l) and orientation (θ) as well as relative position of a weak plane to a tunnel (d) on rockburst damage was systematically studied. The maximum average velocity of failed elements ($\bar{V}_{max}$), the maximum unit kinetic energy of failed elements (KE_{max}), failure zone, and deformed mesh were obtained and analyzed. It is shown that weak planes around a tunnel may change the loading system stiffness of the failed rocks and induce rockburst because when there is a weak plane near an underground opening, a large volume of rock is able to move more freely than that without a weak plane. It is also demonstrated that a weak plane must be in such a position that favors stress buildup in the rocks that are about to fail. If failure occurs when a fault is critically positioned and oriented, more stored energy can be released, which can change the failure mode from stable to unstable. High stress, relatively soft loading system, and free surface (deformation potential) are necessary conditions for unstable rock failure to occur.

This study shows that weak planes around deep tunnels may influence rockburst damage if they are critically positioned and oriented. Hence, it is important to conduct detailed geological survey before and during excavation to identify these types of geological discontinuities because this will allow for anticipating potential burst-prone zones along the tunnels and taking appropriate actions to control rockburst. The approach presented in this study can capture

dynamic response of a rock mass. In particular, the ability to approximate the ejection velocity and released kinetic energy provides a new approach for dynamic rock support design.

In the next chapter, a rockburst occurred in the Jinping II drainage tunnel with an observed nearby fault is simulated to confirm that the presence of weak planes in the vicinity of deep tunnels is a necessary condition for the occurrence of rockburst.

Chapter 6

6 Case study: 11.28 rockburst in the Jinping II drainage tunnel

6.1 Introduction

In Chapter 5, numerical models were developed to explore the role of geological weak planes in rockburst occurrence and damage. The modeling results showed that weak planes around a tunnel may change the loading system stiffness of the failed rocks and induce unstable rock failure or rockburst. However, the developed models need to be verified through case studies.

A minor fault near the Jinping II drainage tunnel in China was revealed after a rockburst (the 11.28 rockburst). In this Chapter, numerical models are developed to simulate the 11.28 rockburst. This case study validates the developed models and adds value to the results. In Section 6.2, a brief description of the tunneling project is presented. Some important features of the 11.28 rockburst are explained in Section 6.3. Simulation of the 11.28 rockburst and results are presented in Section 6.4.

6.2 Project overview

For decades, it has been in planning the installation of harnessing hydropower on the Jinping bend of the Yalong River to produce energy. The river makes a hairpin bend of 150 km long, but the downstream part of the river on the opposite side of the mountain is only 16 km away. In that distance, an elevation drop of 310 m exists, which creates an excellent location for hydroelectricity production. Two projects, named Jinping I and Jinping II, were planned for the

bend to produce hydroelectric power with a total capacity of 8,400 MW (Shiyong et al., 2010). In the 1960s, the former Sichuan and Shanghai design institutes, and the Ministry of Water Resources and Electric Power started planning for Jinping I and II projects.

Constructions of the Jinping II hydropower station started on January 30, 2007. In December 2012, the dam's first generator was set up and the second one was installed in January 2013. The fifth generator went online in May 2014 and the seventh in October 2014. The Jinping II project was completed when the final generator (the 8th generator) went online on November 26, 2014 (https://en.wikipedia.org/wiki/Jinping-II_Dam).
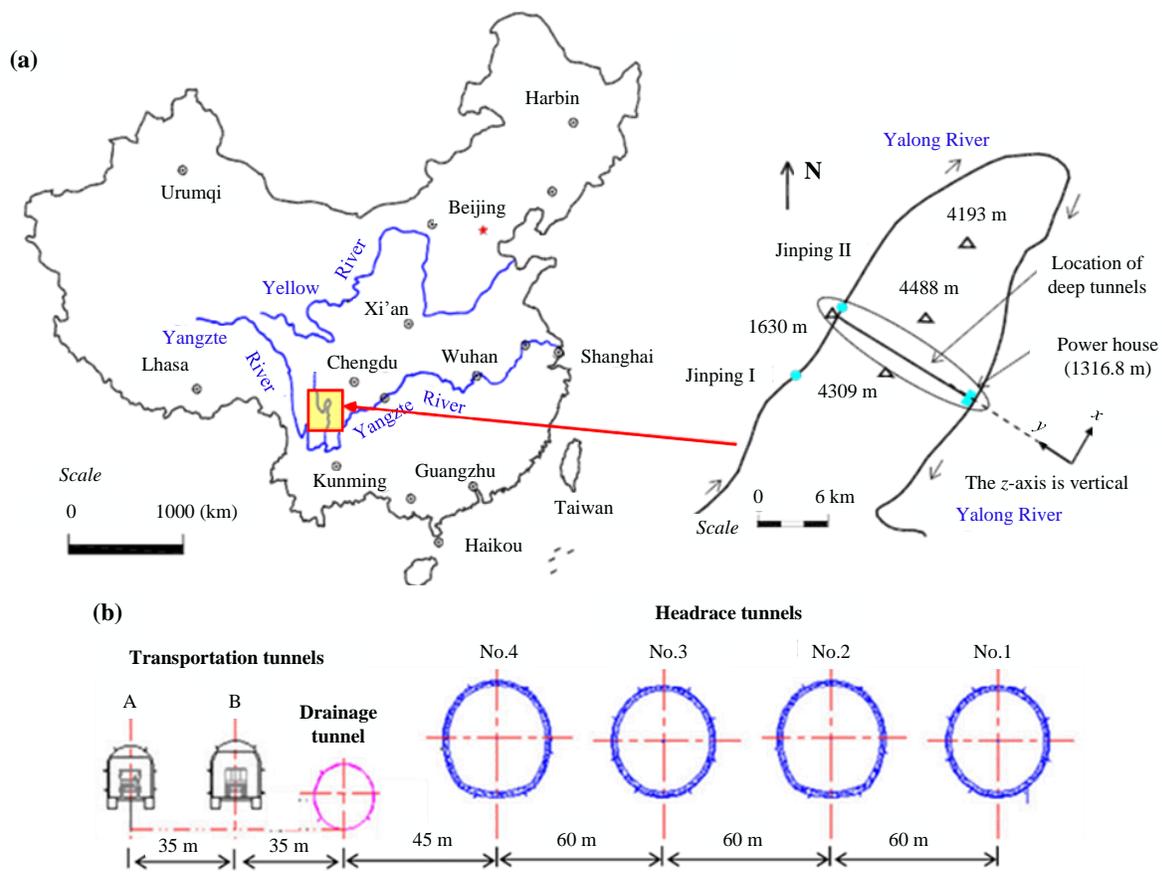
Figure 6-1: (a) Location and (b) layout of the tunnels at the Jinping II hydropower station (Li et al., 2012).

Rockburst was a hazardous problem during the construction of the Jinping II hydropower station in China. The location of the Jinping II hydropower station and the layout of the tunnels are presented in Figure 6-1. Construction of the intake tunnels at the Jinping II hydropower station is one of the deepest tunneling projects in the world. The project consists of seven parallel tunnels (two auxiliary tunnels, four headrace tunnels, and one drainage tunnel), each 17 km long with a maximum overburden of 2,525 m (Zhang et al., 2013). The axes of the tunnels are oriented at N58°W. The entrances of the tunnels at both ends are called the east end and the west end (Figure 6-2). The clock calibration method was used to describe different positions at the cross section of the circular tunnels. The tunnels were excavated using TBM and the drill and blast methods. TBMs were used to excavate the drainage tunnel with a diameter of 7.2 m and the headrace tunnels No. 1 and 3, each with a diameter of 12.4 m. The drill and blast method was used to excavate the headrace tunnels No. 2 and 4, each with a diameter of 13 m.
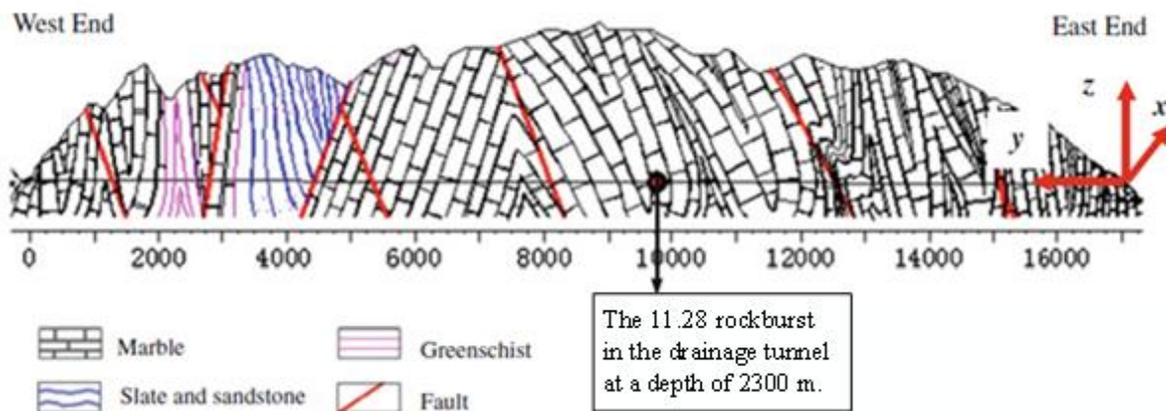
Figure 6-2: Lithology found along the drainage tunnel path and location of the 11.28 rockburst in the drainage tunnel (Zhang et al., 2012).

135

6.3 The 11.28 rockburst in the drainage tunnel

A number of rockbursts occurred during the excavation of the headrace tunnels and the drainage tunnel. Fatalities, injuries, and loss of construction equipment due to rockburst have been reported (Zhang et al., 2012). Zhang et al. (2012) conducted an investigation on four intense rockburst events. Among them the rockburst occurred on November 28, 2009 at Stake SK9+283-9+322 in the drainage tunnel, which was referred as the 11.28 rockburst, was the most intense. The location of the 11.28 rockburst along the tunnel path is shown in Figure 6-2. This event caused seven fatalities and one injury. A TBM machine was completely destroyed and buried under more than 400 m^3 of rock fragments. This rockburst caused a seismic event with a Richter magnitude of 2.0. It should be noted that several intense rockbursts had already occurred in the drainage tunnel before the 11.28 rockburst (Figure 6-3). These rockbursts are listed in Table 6-1 and the associated failure zones are sketched in Figure 6-4.
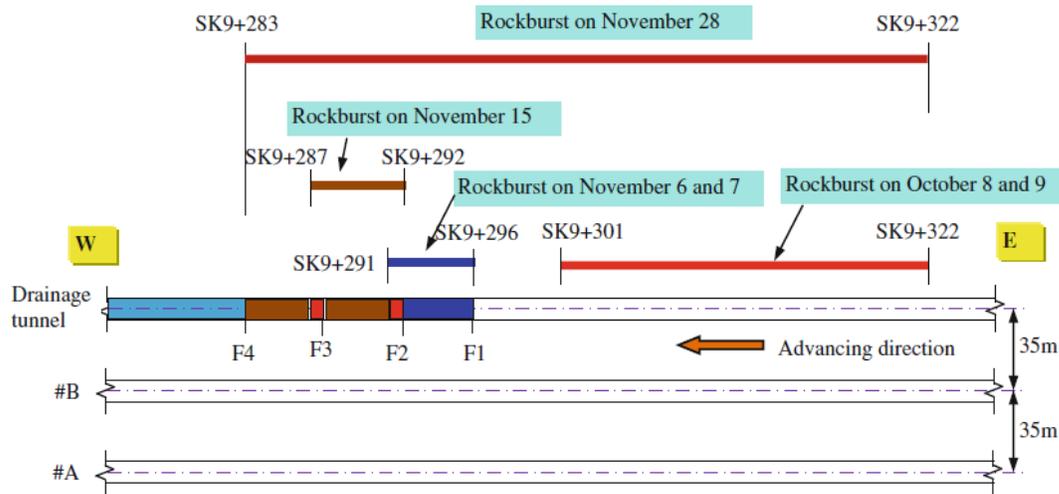
Figure 6-3: Development of the ''11.28'' rockburst in the drainage tunnel. F1 to F4 are the locations of the advancing tunnel faces (Zhang et al., 2012).

Table 6-1: Several rockbursts before the 11.28 rockburst (Zhang et al., 2012)

Date	Number	Stake	Position	Failure depth	Other information
October 8, 2009	1	SK9+302	About 1 o'clock north	1.7 m	A sound similar to blasting
	2	SK9+314	About 1-2 o'clock north	1.2-1.7 m	Extending to the tunnel face
	3	SK9+31 - 9+322	About 7-10 o'clock north	About 1 m	
October 8, 2009	1	SK9+301 - 9+314	10-2 o'clock on the crown	2-3 m	The tunnel face was located at SK9+296. Due to the huge impact of the rockburst, severe buckling was caused to the 14-beam steel sets. Loud blast-like sounds
	2	SK9+311 - 9+322	10-7 o'clock	1 m	A collapse induced by the seismic waves from the major rockburst zone
November 6, 2009		SK9+292	About 6-10 o'clock north	2-3 m	The tunnel face advanced 4 m at Stake SK9+292. It led to the migration of the TBM centerline with a 13.4 mm horizontal displacement and a 8.9 mm height difference
November 7, 2009		SK9+296 - 9+291	Near the cutter head and shield		Extending 1 m in front of the tunnel face. Very loud sounds
November 15, 2009		SK9+288	7-3 o'clock	2-3 m	Extending 1 m in front of the tunnel face. Huge sounds
		SK9+292	12-4 o'clock		

Figure 6-2 illustrates the lithology found along the tunnel path. As shown in Figure 6-2, T_{2b} marble is the host rock of the drainage tunnel at the section that the 11.28 rockburst occurred. The mechanical properties of the rock mass are summarized in Table 6-2. A minor fault in the vicinity of the 11.28 rockburst location in the drainage tunnel was revealed after the rockburst event. The fault was sub-parallel to the tunnel axis with a dip direction of N27°E and a dip of 50°. Table 6-3 and Figure 6-5 summarize the in situ stress field at the 11.28 rockburst section (Zhang et al., 2013). This rockburst is simulated numerically in the next section.
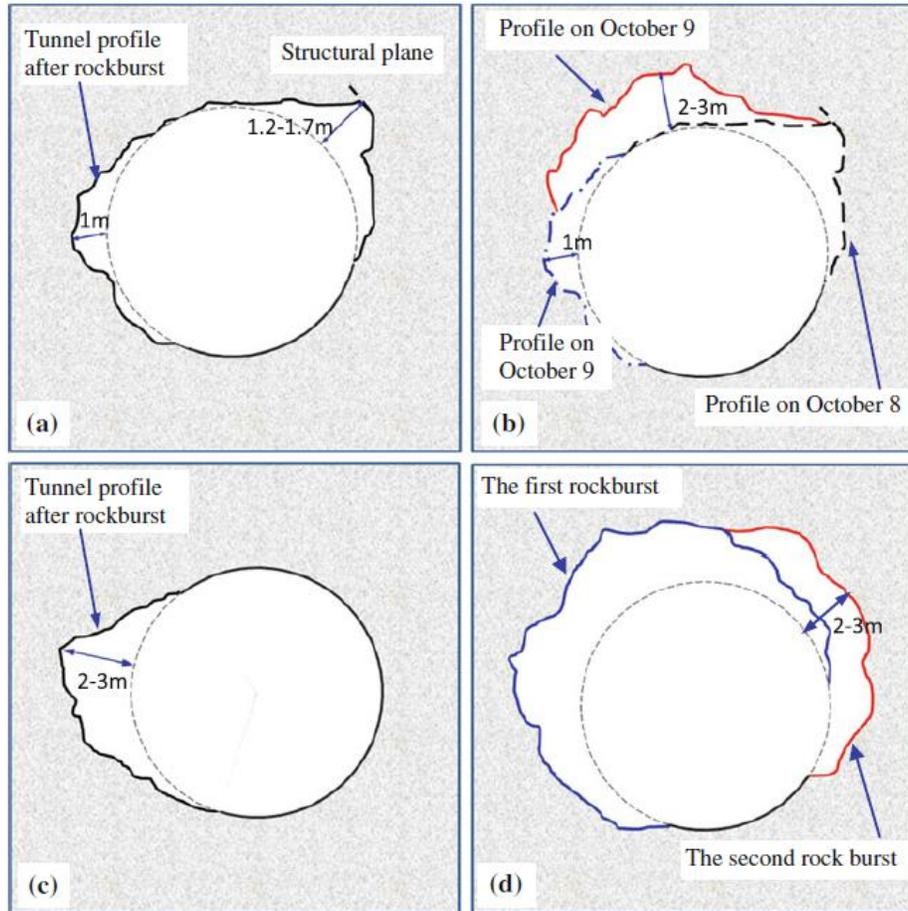
Figure 6-4: Failure zone morphologies in the drainage tunnel: (a) rockburst on October 8, 2009 (b) rockburst on October 9, (c) rockburst on November 6, 2009 and (d) rockburst on November 15, 2009 (Zhang et al., 2012).

Table 6-2: Physical and mechanical properties of rock mass at the 11.28 rockburst section (Zhang et al., 2013)

Parameter	Value
Density, ρ (kg/m^3)	2780
Young's modulus, E (GPa)	18.9
Poisson's ratio, ν	0.23
Uniaxial compressive strength, UCS (MPa)	49.7[*]
Cohesion, c (MPa)	15.6
Friction angle, φ (°)	25.8

[*] This value was calculated according to $UCS = \frac{2c.cos\varphi}{(1-sin\varphi)}$ for the present study.

Table 6-3: In situ stress field at the 11.28 rockburst section (Zhang et al., 2013)

σ_x (MPa)	σ_y (MPa)	σ_z (MPa)	τ_{xy} (MPa)	τ_{yz} (MPa)	τ_{xz} (MPa)
-46.42	-51.68	-61.48	-2.37	-0.64	3.45

Table 6-4: Parameters for defining the post-peak behavior of the rock

Cohesion		Tension cut-off	
Cohesion yield stress (MPa)	Shear plastic strain	Tension cut-off stress (MPa)	Tensile plastic strain
18.0	0	2.8	0
0.01	0.3	0.01	0.005
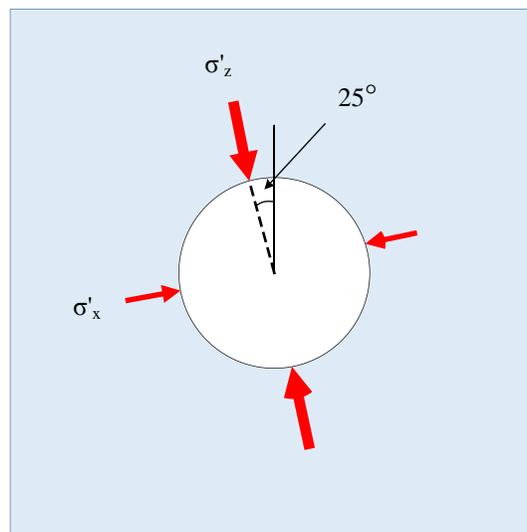
Figure 6-5: The in situ stress in the rockburst section.

139

6.4 Rockburst simulation model, results, and discussion

An Abaqus model, which considers heterogeneous rock properties, is built to simulate the 11.28 rockburst occurred in the drainage tunnel. The physical and mechanical properties of the rock mass are calibrated based on the data shown in Table 6-2. The mean values of E, c, and φ are 18 GPa, 18 MPa, and 28°, respectively. The coefficients of variation (COV) are 15% for E and c, and 5% for φ. The strain-softening behavior of the rock mass is defined using parameters presented in Table 6-4. The model geometry and boundary conditions are shown in Figure 6-6. The modeling procedure for gradual tunnel excavation explained in Section 5.3.1 is used. The total number of excavation steps is 10.

As mentioned above, a minor fault near the rockburst damage location was revealed after the
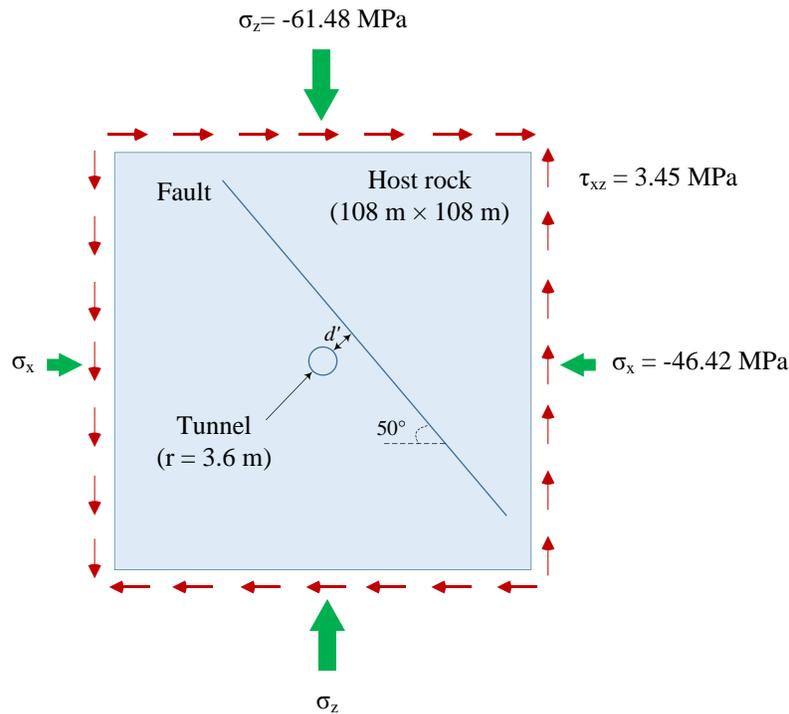
Figure 6-6: Tunnel excavation model geometry and boundary conditions.

11.28 rockburst. The fault was straight and smooth with no infilling (Zhou et al., 2015). This fault is considered in the numerical model to understand the role of the fault on the rockburst damage. The length of the observed fault near the tunnel was not measured. In the model the length of the fault (*l*) is set to 90 m, resulting in a *l/r* ratio of 25. The fault's length of 90 m can be considered as a relatively long fault relative to the size of the tunnel. Because the mechanical properties of this fault were not reported, the friction coefficient has to be estimated. Laboratory test results have shown that depending on the infilling material and surface roughness, the friction coefficient (*μ*) of a fault lies between 0.2 and 0.85 (Collettini, 2011). The lower end values would suit more for faults with smooth surface and soft infilling materials. Because the fault located at the 11.28 rockburst event site has no soft infilling, *μ* values varied between 0.4 and 0.8 are considered in this study to consider the uncertainty of the contact property of the fault. It should be noted that the modeled fault is assumed to be straight and the faults waviness that exists in reality is neglected. Therefore, interlocking between two faces of the fault is not considered. This simplification makes the fault easier to slide. Hence, this model can be considered as an extreme case and the calculated $\overline{V}_{max}$ and KE_{max} are the upper bound values.

For comparison, rock failure in the drainage tunnel without any adjacent geological structure is simulated first and the shear and tensile failure zones are presented in Figure 6-7. Symmetric shear failure around the tunnel at 7 to 10 and 1 to 4 o'clock positions can be seen. It is in the same direction of the minimum principal in situ stress (Figure 6-5). Tensile failure is more or less uniformly distrusted around the tunnel.

(a) Shear failure   (b) Tensile failure
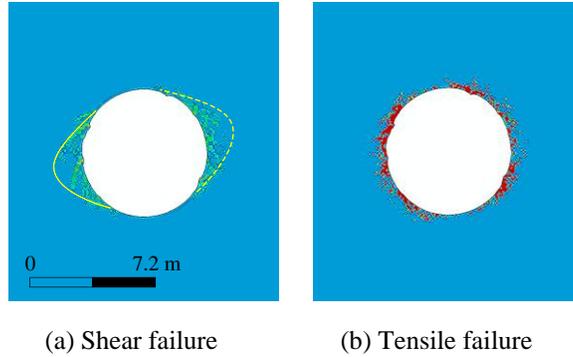
Figure 6-7: (a) Shear and (b) tensile failure zones around the drainage tunnel without any nearby structures.

Figure 6-8 and Figure 6-9 show the average velocity ($\overline{V}$) and the maximum unit kinetic energy (*KE*) of the failed elements at excavation Step 10, respectively. For the model without any adjacent geological structure, $\overline{V}_{max}$ is 0.63 m/s and KE_{max} is equal to 0.84 kJ/m^3. Under this condition, stable failure in the form of spalling is expected and this model is referred as the "base model."
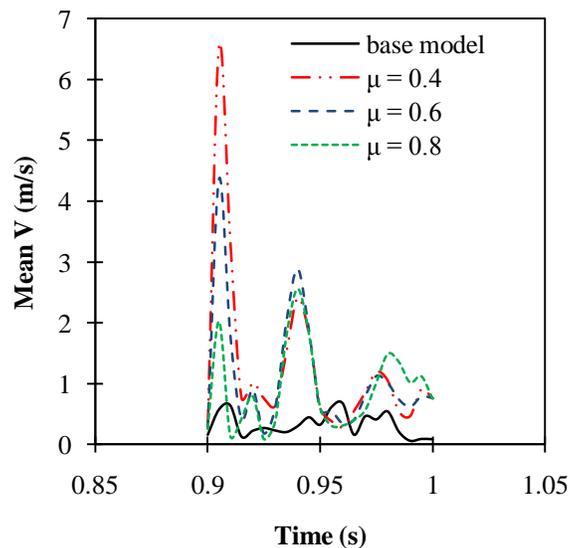
Figure 6-8: Average velocity of failed elements during Step 10.
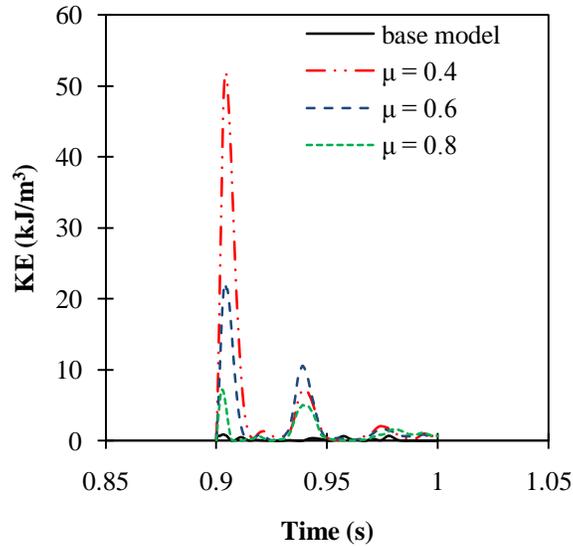
Figure 6-9: The maximum unit kinetic energy during Step 10.

Failure development around the tunnel in the models that include the minor fault with $\mu = 0.4$ is illustrated in Figure 6-10. During the excavation at Step 7, stress concentrates in the rock mass at the position of 1 to 3 o'clock in the footwall on the right tunnel wall due to the presence of the fault; as a result, fractures initiate and propagate in this zone. As excavation continues to Step 9, the tangential stresses increase and some fractures are formed in the rock mass at the position of 7 and 10 o'clock and the fractures in the rock mass at the position of 1 to 3 o'clock propagate further.

Step 1   Step 7   Step 9   Step 10-1   Step 10-2

(a) Shear failure
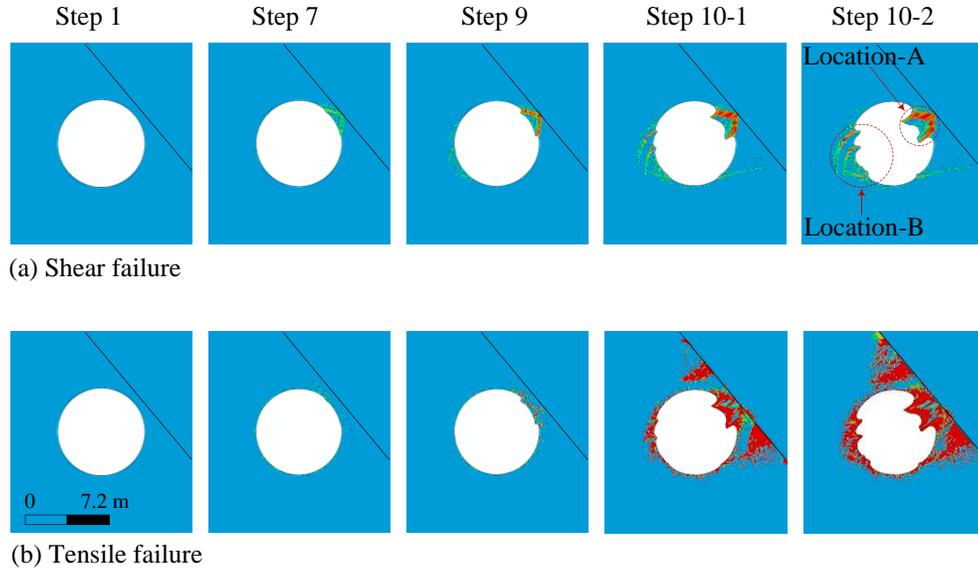
(b) Tensile failure

Figure 6-10: (a) Shear and (b) tensile failure developments around the drainage tunnel in the 11.28 rockburst event (for μ = 0.4).

When the tunnel is fully excavated (or the tunnel face advances sufficiently away from the cross section of analysis), the fractured rock mass at the position of 1 to 3 o'clock fails in an unstable fashion, evidenced by the large modeling velocity and released kinetic energy captured in the numerical modeling (Step 10-1). For a better understanding of failure development in Step 10, this step is divided in two steps (Step 10-1 and Step 10-2). The locations at the positions of 1 to 3 and 7 to 10 o'clock are referenced as "Location-A" and "Location-B", respectively. Figure 6-11 presents the relation between $\bar{V}_{max}$ and μ at both locations, showing a trend of $\bar{V}_{max}$ decrease as μ increase. The $\bar{V}_{max}$ for $\mu = 0.6$ is 4.3 m/s, which is much higher than the $\bar{V}_{max}$ value of 0.63 m/s in the base model. The maximum released kinetic energy per unit volume KE_{max} at Location-A during Step 10 excavation is presented in Figure 6-12, showing a trend of KE_{max} decrease as μ increases. For example, the maximum unit kinetic energy KE_{max} for $\mu = 0.6$ is 22.3 kJ/m^3, much higher than the maximum unit kinetic energy of 0.84 kJ/m^3 in the base model.
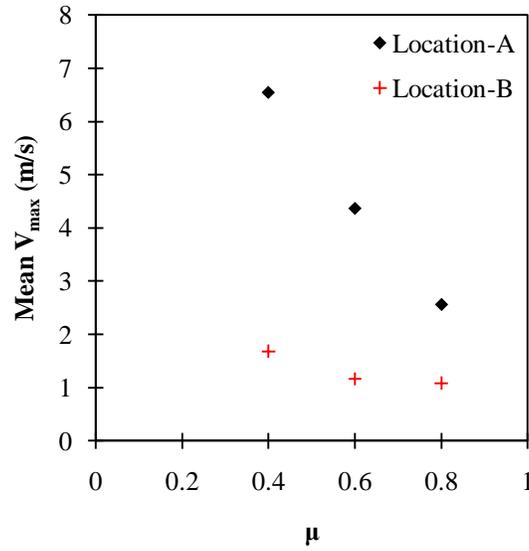
Figure 6-11: Influence of µ on $\overline{V}_{max}$.
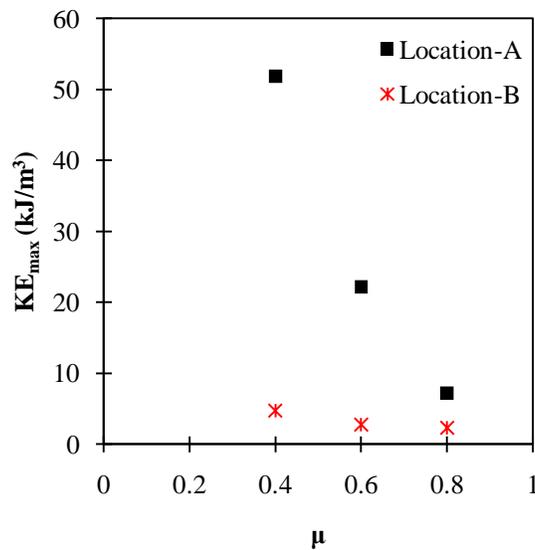
Figure 6-12: Influence of µ on the maximum unit kinetic energy.

The released kinetic energy per unit volume at Location-A are 51.8 kJ/m^3, 22.2 kJ/m^3, and 7.3 kJ/m^3 for μ equal to 0.4, 0.6, and 0.8, respectively. The maximum unit kinetic energy is large when the μ value is small. In this case, energy absorption rockbolts should be used to support tunnel walls (Cai and Champaigne, 2012). At the Jinping II construction site, standard rock
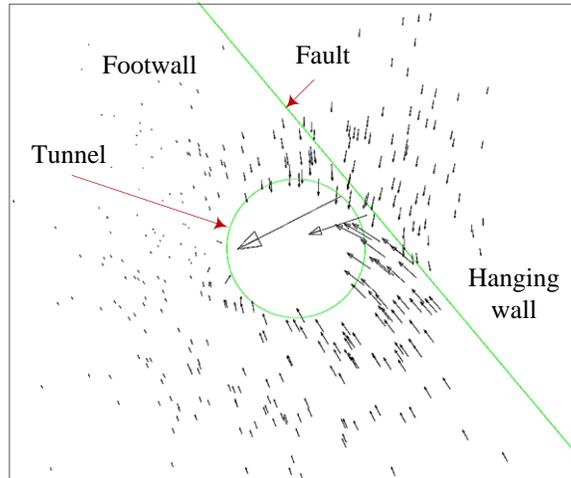
Figure 6-13: The displacement field around the tunnel at the beginning of Step 10.

supports were used and they did not have enough capacity to absorb high released energy (e.g., > 15 kJ/m^3). As a result, severe rockburst damage occurred.

After the footwall rock failure, stresses increase further at the position of 7 to 10 o'clock, causing additional rock failure at Location-B (Step 10-2). As can be seen from Figure 6-11 and Figure 6-12, the $\bar{V}_{max}$ and KE_{max} values are smaller at Location-B than at Location-A, implying that rock failure is more violent at location where the influence of the geological structure is large. This is because that the mine system stiffness for rock masses at Location-A is softer than that at Location-B due to the proximity of Location-A to the fault.

The sudden rock failure at the footwall (Location-A) destroys the closed ring of rocks and causes the rock mass around the tunnel to lose its load bearing capacity. Figure 6-10 shows that there is a sudden increase of tensile fractures around the tunnel after the footwall rock fails at Step 10-1. Figure 6-13 illustrates the displacement field around the tunnel at the beginning of Step 10. The figure shows that the hanging wall pushes the footwall and induces these tensile fractures due to bending (slab flexure mechanism). These tensile fractures further degrade the rock mass and

combined with pre-existing joints in the rock mass, rock blocks can move freely. Because the rock support installed at the site was insufficient, fall of ground eventually occurred in the roof of the tunnel, forming a V-shape failure zone with a depth of 6 m as shown in Figure 6-14a. Figure 6-14b overlaps both the shear and the tensile failure zones from the numerical modeling. It shows that the numerical model captures the V-shape failure zone well. Because Abaqus is a continuum tool, the process of the collapse of the rock mass cannot be well captured. No field monitoring was conducted at the site to record what happened during the rockburst; the failure process described above is gained from the numerical modeling and it most likely represents what might had happened in the field during the 11.28 rockburst event.

The normal distance of the fault plane shown in Figure 6-6 to the tunnel (d') was not reported in the publications. In the above simulation, a d' value of 0.72 m ($d'/r = 0.2$) is used. The stiffness of the rock mass between the fault and the tunnel depends on d'. Due to the complex geometry of the tunnel and geology, it is difficult to calculate the exact stiffness value of the rock mass and an approximation using the elastic column theory can be considered. The stiffness of an elastic column with a uniform cross section and material properties can be calculated from Eq. (2-13).

(a)   (b)
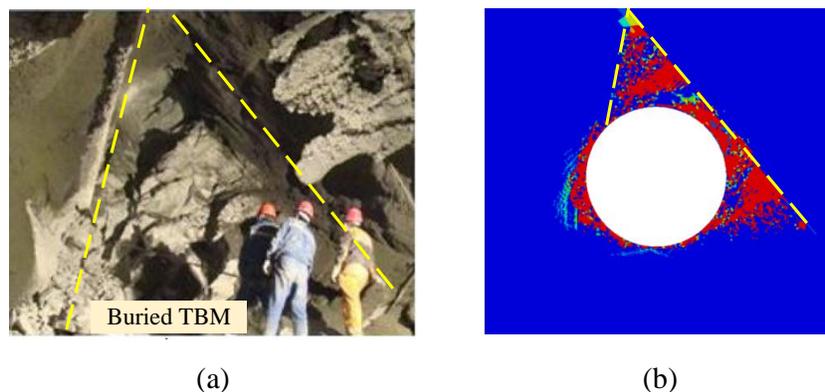
Figure 6-14: Comparison of failure zone in the 11.28 rockburst in the field (Zhang et al., 2012) (a) with that from the numerical simulation (b).

For the same column length, changing d' changes the cross section area A, thus affecting the stiffness. Another two d' values (1.44 and 2.16 m, resulting in d'/r ratios of 0.4 and 0.6, respectively) are considered and model simulations are conducted to understand the influence of d' on failure mode. Figure 6-15 and Figure 6-16 present the influence of d' on $\bar{V}_{max}$ and KE_{max}, respectively. The results show that the d' value influences rock failure at Location-A significantly and failure becomes less violent when the fault is located further away from the tunnel. Based on the field observation of failure zones (Figure 6-14a), it is seen that the distance from the tunnel wall to the fault is likely in the range of 0.7 to 1.5 m.
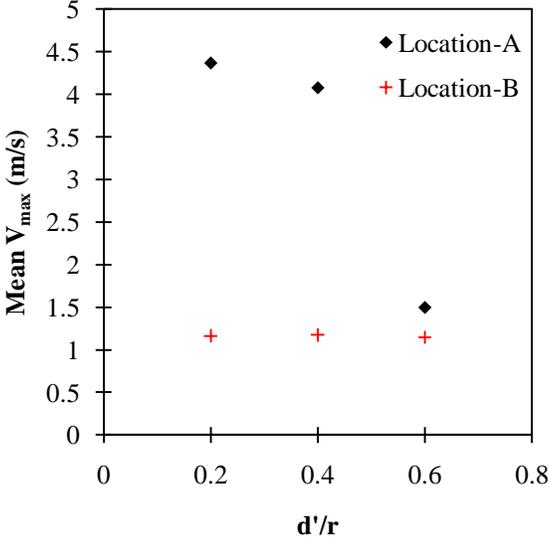
Figure 6-15: Influence of d'/r on $\bar{V}_{max}$.
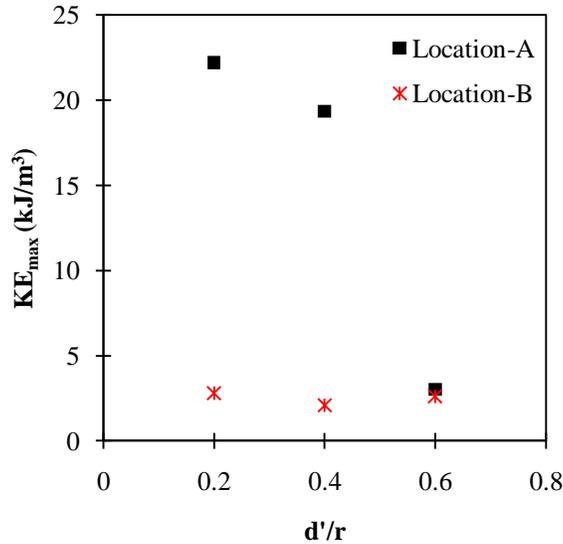
Figure 6-16: Influence of d'/r on the maximum unit kinetic energy (for μ = 0.6).

6.5 Final remarks

Several extremely intense rockbursts occurred during the tunnel construction at the Jinping II hydropower station in China. Several construction workers were killed and many more were injured. Moreover, some equipment was damaged.

In this chapter, the role of weak plane on the 11.28 rockburst in the Jinping II drainage tunnel was studied. The modeling results of a model without any weak plane show symmetric failure with low $\bar{V}_{max}$ and KE_{max} values. Because a fault was observed near the tunnel after the 11.28 rockburst event, this fault was included in the subsequent models, which resulted in asymmetric failure around the tunnel with high values of $\bar{V}_{max}$ and KE_{max}. The modeling results captured important characteristics of the 11.28 rockburst such as failure pattern and unstable violent rock failure. Considering the uncertainty in the mechanical properties of the fault and its distance to the tunnel, the average ejection velocity of the right tunnel wall rock is estimated in a range of 1.5 to 6.6 m/s and the maximum unit kinetic energy is between 3.1 and 51.8 kJ/m^3.

In this study, the modeled fault is assumed to be straight and the fault waviness is neglected. This simplification makes the fault easier to slide. Hence, the calculated $\overline{V}_{max}$ and KE_{max} are the upper bound values. In other words, the ejection velocity and the released kinetic energy might be smaller than the values calculated by the model. Although the approximated ejection velocity and maximum unit kinetic energy cannot be verified by field measurement data (no quantitative data were available), these values correspond well with the post-event observation of the field damage condition. This implies that the adopted numerical tool is useful to study unstable rock failure problems in underground excavations.

Chapter 7

7 Conclusions and future research

7.1 Summary

Rockburst is a hazardous problem in deep underground mines and civil tunnels, which imposes a great danger to safety of personnel and investment. Many factors that influence rockburst damage have been identified. The presence of geological structures such as faults, shear zones, joints and dykes has been observed near excavation boundaries in many rockburst case histories but still their role in rockburst occurrence is not fully understood.

This thesis aims at making a contribution to better understanding of rockburst occurrences in deep mines and tunnels. In this thesis, an explicit finite element tool (Abaqus) is employed to study rockburst and an emphasis is placed on exploration of the roles of loading system stiffness and geological structures in rockburst events.

A literature review was conducted in Chapter 2 to answer the questions why rockbursts occur and what approach can be taken to address the problem. In Chapter 3, unstable rock failures under uniaxial compression and polyaxial unloading conditions were simulated to verify the suitability of the selected numerical tool for studying rockburst. The influences of the loading system stiffness, specimen's height to width ratio, and intermediate principal stress on rock failure intensity were investigated.

Hypotheses	Conclusions
•Unstable rock failure can be simulated using advanced numerical tools;	•Unstable rock failure **can be** simulated using advanced numerical tools (Ch.3);
•For unstable failure to occur, some necessary conditions must be met;	•For unstable failure to occur, some necessary conditions **must be** met (Ch.5);
•Geological structures affect the rock failure mode (stable or unstable) by modifying the loading system stiffness;	•Geological structures **affect** the rock failure mode (stable or unstable) by modifying the loading system stiffness (Ch. 5 and Ch.6);
•The released energy from unstable rock failure can be estimated.	•The released energy from unstable rock failure can be **estimated** (Ch.5 and Ch.6).

Figure 7-1: Research hypotheses and the main conclusions from the research.

In Chapter 4, the capability of Abaqus for modeling geomaterials was extended by introducing material heterogeneity using Python scripting. Moreover, the effect of material heterogeneity on rock failure intensity in unconfined and confined compression tests was investigated.

In Chapter 5, models with and without fault planes were developed to study the role of weak planes in rockburst occurrence and damage in tunnels. The influence of weak plane length and orientation as well as relative position of a weak plane to a tunnel on rockburst damage was systematically studied. Finally, in Chapter 6, a case study of rockburst with an observed nearby fault in the Jinping II drainage tunnel in China was conducted to demonstrate the applicability of the developed Abaqus models for studying rockburst.

The main conclusions from the thesis work (Figure 7-1) are presented in Section 7.2, which are structured according to the thesis chapters. Recommendations for future work are presented in Section 7.3.

7.2 Conclusion

The key findings of the literature review and the research conducted in this study are summarized below.

Chapter 2 - Literature review

- Rockburst is a hazardous problem in deep mines and tunnels.

- The main factors that influence rockburst damage can be categorized into four groups: (i) seismic event, (ii) geology, (iii) geotechnical property, and (iv) mining activity.

- In general, many simplifications are made to develop analytical solutions. Hence, analytical methods could not provide solutions for complex problems such as rockburst.

- Empirical methods are too simplistic and do not consider all the necessary conditions for a rockburst to occur. Therefore, predictions made from empirical methods are not reliable.

- Data-based methods such as statistical and artificial intelligence methods are capable of developing input-output relations for analyzing complex systems. However, a large dataset is needed to find reliable solutions. Collection of more information from rockburst case histories may make it possible to predict rockburst using data-based methods at an acceptable level of confidence.

- Experimental methods can reproduce the process of unstable rock failure and help to analyze the dynamic response of rocks; however, it is rather difficult to simulate rockbursts that truly mimic conditions underground.

- Some numerical studies proved the suitability of using numerical method to study unstable rock failure and rockburst. However, a missing factor in the previous numerical works is the effect of geological structures on rockburst occurrence and damage.

Chapter 3 - Simulation of unstable rock failure in laboratory tests

- Abaqus is capable of capturing unstable rock failure. This was tested and confirmed through simulations of unstable rock failure in uniaxial compression and polyaxial unloading tests.

- Unstable rock failure is associated with a sudden movement of the loading platens or a sudden release of excessive energy, which can be observed directly or indirectly in laboratory tests using monitoring equipment; it can be calculated directly in numerical modeling. This study proposed to use the Loading System Reaction Intensity (LSRI) and the maximum unit kinetic energy (KE_{max}) as indicators of unstable rock failure in numerical modeling.

- The numerical modeling results show that there is no clear boundary between stable and unstable failures. It seems that a transition failure mode exists between stable and unstable rock failure. In reality, this condition can occur in the form of sudden spalling of the skins of the specimen in laboratory or sudden spalling of rock slabs at excavation boundaries. This type of rock failure is not violent and should not be classified as rockbursts.

- In polyaxial test, failure is more violent when a specimen is taller, the confinement is lower, and the loading system stiffness is lower.

Chapter 4 - Influence of material heterogeneity on failure intensity in unstable rock failure

- In homogeneous models it is implicitly assumed that shear failure is the predominant failure mechanism. Hence, homogeneous models may give unrealistic results in conditions that the major failure mode is in fact tensile splitting.

- Material heterogeneity was introduced into Abaqus models by Python scripting. In the heterogeneous models, mechanical properties of rocks were assigned to each element randomly following normal distribution functions. The modeling results show that by introducing material heterogeneity into the models, tensile and shear failures and the mechanical response of the models can be captured satisfactorily.

- The simulation results show that the pre-peak behavior of rocks is controlled by the heterogeneity of Young's modulus, and the peak and post-peak behaviors are controlled mainly by the heterogeneities of cohesion and friction angle.

- The simulation results from both homogeneous and heterogeneous models show that rock failure is more violent when the loading system is softer and the confinement is lower. However, it is observed that when two materials have the same peak strength, the heterogeneous model releases more energy than the homogeneous model due to the difference in the failure mode. The tensile splitting failure mode of the heterogeneous model releases more energy than the shear failure mode of the homogeneous model.

- It is observed from the numerical results that more heterogeneous rocks, normally have lower rock strengths, tend to be less violent if the rocks fail in an unstable fashion. This is in good agreement with field observation results that rockbursts occur frequently in more competent and relatively homogeneous rocks.

- This study shows that a change in failure mode may influence the failure intensity and emphasized the importance of considering failure mode in unstable rock failure analysis.

155

Chapter 5 - Influence of geological weak planes on rockburst occurrence and damage

- A new approach was presented for simulating the tunnel gradual excavation process in 2D models using Abaqus. In this approach, the contact stiffness assigned to the boundary between the tunnel core and the tunnel wall was reduced step-by-step to reach to zero to simulate gradual tunnel excavation.

- It is shown that weak planes around a tunnel may change the loading system stiffness of the failed rocks and induce rockburst because when there is a weak plane near an underground opening, a large volume of rock is able to move more freely than that without a weak plane.

- The study demonstrates that a weak plane must be in such a position that favors stress build up in the rocks that are about to fail. If failure occurs when a fault is critically positioned and oriented, more stored energy can be released, which can change the failure mode from stable to unstable.

- High stress, relatively soft loading system, and free surface (deformation potential) are necessary conditions for unstable rock failure to occur. Rockburst occurs if all of these necessary conditions are satisfied.

- The approach presented in this study can capture the dynamic response of a rock mass. In particular, the ability to approximate ejection velocity and released kinetic energy provides a new approach for dynamic rock support design.

Chapter 6 - Case study: 11.28 rockburst in the Jinping II drainage tunnel

- The role of weak plane on the 11.28 rockburst in the Jinping II drainage tunnel was investigated. The modeling results captured important characteristics of the 11.28 rockburst such as failure pattern and unstable violent rock failure.

- Considering the uncertainty in the mechanical properties of the fault and its distance to the tunnel, the average ejection velocity of the right tunnel wall rock is approximated in a range of 1.5 to 6.6 m/s and the maximum unit released kinetic energy is between 3.1 and 51.8 kJ/m^3. Although the approximated ejection velocity and the maximum unit kinetic energy cannot be verified by field measurement data (no quantitative data were available), the simulated rock failure zone (with an approximated ejection velocity of 6.5 m/s and the maximum unit kinetic energy of 51.8 kJ/m^3) that corresponds well with the post-event observation of the damage condition in the field indicates that the friction coefficient of the fault is most likely 0.4.

- The case study results imply that the adopted numerical tool is useful to study unstable rock failure problems in underground excavations.

The results from this thesis provide some important and enlightening insights to addressing rockburst problems in deep mines and tunnels. However, due to time and computation resource constraints, some questions could not be addressed in the thesis and they are recommended for future research.

7.3 Future work

Some recommendations for future research are suggested below.

- Conduct polyaxial unloading test simulation using heterogeneous models in Abaqus[3D] for a better understanding of spalling at tunnel walls.

- Investigate the influence of dykes on rockburst occurrence and damage. Presence of dykes near many rockbursts has been confirmed. The numerical approach can be extended to study the role of dykes on rockburst damage.

- Simulate rockbursts due to dynamic disturbances. Dynamic disturbance due to seismic activities (e.g. explosion, vibration, stress impact from nearby rockbursts) does influence rockburst damage. This thesis focuses on the simulation of rockburst due to static loading. Simulation of rockburst due to dynamic loading may reveal new features of rockbursts.

- Apply the numerical modeling approach to the design support system in burst-prone grounds. The role of rock support in reducing the degree of rock damage due to failure can be studied.

- Develop 3D models to study rockbursts in tunnels. The thesis focuses on 2D rockburst simulations in tunnels, which are useful to gain insight into rockburst occurrence and damage; however, a more comprehensive understanding of rockburst in mines and tunnels can be made using 3D models.

References

Adoko, A. C., Gokceoglu, C., Wu, L., and Zuo, Q. J. (2013). Knowledge-based and data-driven fuzzy modeling for rockburst prediction. International Journal of Rock Mechanics and Mining Sciences, 61, 86-95.

Aga, I., Shettigar, P., and Krishnamurthy, R. (1990). Rockburst hazard and its alleviation in Kolar Gold Mines-a review in Rock Bursts-Global Experiences (pp. 43-69): Oxford and IBH Publishing Co. Pvt. Ltd.

Aglawe, J. P. (1999). Unstable and violent failure around underground openings in highly stressed ground. (PhD Thesis), Queen's University, Kingston, Canada.

Ahmed, A., Ali, H., ElAraby, S., ElKateb, M., and Noureldin, S. (2008). Non-deterministic tunneling analysis using AI based techniques genetic programming vs ANNs. Paper presented at the 12th International Colloquium on Structural and Geotechnical Engineering (ICSGE), Cairo.

Andrieux, P., Blake, W., Hedley, D., Nordlund, E., Phipps, D., Simser, B., and Swan, G. (2013). Rockburst case histories: 1985, 1990, 2001 & 2013. CAMIRO Mining Division for the Deep Mining Research Consortium, Sudbury, Ont.

Azevedo, R. F., Parreira, A. B., and Zornberg, J. G. (2002). Numerical analysis of a tunnel in residual soils. Journal of geotechnical and geoenvironmental engineering, 128(3), 227-236.

Bardet, J. (1989). Finite element analysis of rockburst as surface instability. Computers and Geotechnics, 8(3), 177-193.

Bardet, J. (1991). Numerical modeling of a rockburst as surface buckling: Proc 2nd International Symposium on Rockbursts and Seismicity in Mines, Minneapolis, 8–10 June 1988 P81–85. Publ Rotterdam: AA Balkema, 1990. Paper presented at the International Journal of Rock Mechanics and Mining Sciences & Geomechanics Abstracts,A397.

Barton, N., Lien, R., and Lunde, J. (1974). Engineering classification of rock masses for the design of tunnel support. Rock mechanics, 6(4), 189-236.

Barton, N. R. (2000). TBM tunnelling in jointed and faulted rock. Rotterdam, Netherlands: A.A.Balkema.

Bazant, Z. P., Belytschko, T. B., and Chang, T. (1984). Continuum theory for strain-softening. Journal of Engineering Mechanics, 110(12), 1666-1692.

Bazant, Z. P., and Oh, B. H. (1985). Microplane model for progressive fracture of concrete and rock. Journal of Engineering Mechanics, 111(4), 559-582.

Bazant, Z. P., and Pijaudier-Cabot, G. (1988). Nonlocal continuum damage, localization instability and convergence. Journal of applied mechanics, 55(2), 287-293.

Bazant, Z. P., and Xiang, Y. (1997). Size effect in compression fracture: splitting crack band propagation. Journal of Engineering Mechanics, 123(2), 162-172.

Beer, G., Smith, I., and Duenser, C. (2008). The boundary element method with programming: for engineers and scientists. Germany: Springer Science & Business Media.

Bieniawski, Z. (1968). Propagation of brittle fracture in rock. Paper presented at the The 10th US Symposium on Rock Mechanics (USRMS).

Blair, D. (1993). Blast vibration control in the presence of delay scatter and random fluctuations between blastholes. International journal for numerical and analytical methods in geomechanics, 17(2), 95-118.

Blair, S., and Cook, N. (1998a). Analysis of compressive fracture in rock using statistical techniques: Part I. A non-linear rule-based model. International Journal of Rock Mechanics and Mining Sciences, 35(7), 837-848.

Blair, S., and Cook, N. (1998b). Analysis of compressive fracture in rock using statistical techniques: Part II. Effect of microscale heterogeneity on macroscopic deformation. International Journal of Rock Mechanics and Mining Sciences, 35(7), 849-861.

Blake, W. (1972). Rock-burst mechanics. Colorado School of Mine Quarterly, 67(1).

Blake, W., and Hedley, D. G. (2003). Rockbursts: case studies from North American hard-rock mines. Littleton, Colorado: SME.

Bobet, A. (2010). Numerical methods in geomechanics. The Arabian Journal for Science and Engineering, 35(1B), 27-48.

Bobet, A., and Einstein, H. (1998a). Fracture coalescence in rock-type materials under uniaxial and biaxial compression. International Journal of Rock Mechanics and Mining Sciences, 35(7), 863-888.

Bobet, A., and Einstein, H. H. (1998b). Numerical modeling of fracture coalescence in a model rock material. International Journal of Fracture, 92(3), 221-252.

Brace, W., and Bombolakis, E. (1963). A note on brittle crack growth in compression. Journal of Geophysical Research, 68, 3709-3713.

Brace, W., Paulding, B., and Scholz, C. (1966). Dilatancy in the fracture of crystalline rocks. Journal of Geophysical Research, 71(16), 3939-3953.

Brady, B. H., and Brown, E. T. (2013). Rock mechanics: for underground mining: Springer Science & Business Media.

Brown, E. (2008). Estimating the mechanical properties of rock masses. Paper presented at the Proceedings of the 1st southern hemisphere international rock mechanics symposium: SHIRMS,3-21.

Brune, J. F. (2010). Extracting the Science: A Century of Mining Research: SME.

Burgert, W., and Lippmann, H. (1981). Models of translatory rock bursting in coal. Paper presented at the International Journal of Rock Mechanics and Mining Sciences & Geomechanics Abstracts,285-294.

Cai, M. (2008a). Influence of intermediate principal stress on rock fracturing and strength near excavation boundaries—insight from numerical modeling. International Journal of Rock Mechanics and Mining Sciences, 45(5), 763-772.

Cai, M. (2008b). Influence of stress path on tunnel excavation response–Numerical tool selection and modeling strategy. Tunnelling and Underground Space Technology, 23(6), 618-628.

Cai, M. (2013a). Fracture initiation and propagation in a Brazilian disc with a plane interface: a numerical study. Rock mechanics and rock engineering, 46(2), 289-302.

Cai, M. (2013b). Principles of rock support in burst-prone ground. Tunnelling and Underground Space Technology, 36, 46-56.

Cai, M., and Champaigne, D. (2012). Influence of bolt-grout bonding on MCB conebolt performance. International Journal of Rock Mechanics and Mining Sciences, 49, 165-175.

Cai, M., and Kaiser, P. K. (2015). A Guide to Rockburst Support Selection. Sudbury, Ontario: Geomechanics Research Center.

Cai, M., and Manouchehrian, A. (2015). Numerical analysis of released energy during unstable rock failure under true-triaxial unloading condition. Paper presented at the ISRM 2015,Paper 179.

Chen, Z., Tang, C., and Huang, R. (1997). A double rock sample model for rockbursts. International Journal of Rock Mechanics and Mining Sciences, 34(6), 991-1000.

Coates, D. F. (1966). Rock mechanics principles. Geoscience Abstracts.

Collettini, C. (2011). The mechanical paradox of low-angle normal faults: Current understanding and open questions. Tectonophysics, 510(3), 253-268.

Cook, N. (1965). A note on rockbursts considered as a problem of stability. J South Afr Inst Min Metall, 65, 437-446.

Cook, N., Hoek, E., Pretoriu, J., Ortlepp, W., and Salamon, M. (1966). Rock mechanics applied to the study of rockbursts. 66(12), 435-528.

de Borst, R. (2013). Computational Methods for Generalised Continua Generalized Continua from the Theory to Engineering Applications (pp. 361-388): Springer.

Diederichs, M. S. (2001). Instability of hard rockmasses: the role of tensile damage and relaxation: National Library of Canada= Bibliothèque nationale du Canada.

Durrheim, R. (2010). Mitigating the risk of rockbursts in the deep hard rock mines of South Africa: 100 years of research. Extracting the Science: a century of mining research, Brune J (eds), Society for Mining, Metallurgy, and Exploration, Inc, 156-171.

Durrheim, R., Roberts, M., Haile, A., Hagan, T., Jager, A., Handley, M., Spottiswoode, S., and Ortlepp, W. (1998). Factors influencing the severity of rockburst damage in South African gold mines. Journal of the South African Institute of Mining and Metallurgy, 98, 53-58.

Fairhurst, C., and Cook, N. (1966). The phenomenon of rock splitting parallel to the direction of maximum compression in the neighborhood of a surface. Paper presented at the Proceedings of the first congress on the international society of rock mechanics,687-692.

Fakhimi, A., Hosseini, O., and Theodore, R. (2016). Physical and numerical study of strain burst of mine pillars. Computers and Geotechnics, 74, 36-44. doi: http://dx.doi.org/10.1016/j.compgeo.2015.12.018

Feng, X. T., Pan, P., and Zhou, H. (2006). Simulation of the rock microfracturing process under uniaxial compression using an elasto-plastic cellular automaton. International Journal of Rock Mechanics and Mining Sciences, 43(7), 1091-1108.

Fonseka, G., Murrell, S., and Barnes, P. (1985). Scanning electron microscope and acoustic emission studies of crack development in rocks. Paper presented at the International Journal of Rock Mechanics and Mining Sciences & Geomechanics Abstracts,273-289.

Fujii, Y., Ishijima, Y., and Deguchi, G. (1997). Prediction of coal face rockbursts and microseismicity in deep longwall coal mining. International Journal of Rock Mechanics and Mining Sciences, 34(1), 85-96.

Gallagher, J., Friedman, M., Handin, J., and Sowers, G. (1974). Experimental studies relating to microfracture in sandstone. Tectonophysics, 21(3), 203-247.

Garvey, R. J. (2013). A study of unstable rock failures using finite difference and discrete element methods. (PhD Thesis), Colorado School of Mines, Golden, Colorado.

Ghaei, A., and Movahhedy, M. R. (2007). Die design for the radial forging process using 3D FEM. Journal of materials processing technology, 182(1), 534-539.

Ghose, A. K., and Rao, H. S. (1990). Rockbursts: Global Experiences: Papers Presented at the 5th Plenary Scientific Session of Working Group on Rockbursts of International Bureau of Strata Mechanics, February, 1988: AA Balkema.

Gibowicz, S. J., and Lasocki, S. (1997). Rockbursts and seismicity in mines: proceedings of the 4th International Symposium on Rockbursts and Seismicity in Mines, Kraków, Poland, 11-14 August 1997. Krakow, Poland: AA Balkema.

Giner, E., Sukumar, N., Tarancon, J., and Fuenmayor, F. (2009). An Abaqus implementation of the extended finite element method. Engineering fracture mechanics, 76(3), 347-368.

Gong, Q., Jiao, Y., and Zhao, J. (2006). Numerical modelling of the effects of joint spacing on rock fragmentation by TBM cutters. Tunnelling and Underground Space Technology, 21(1), 46-55.

Goodman, R. E. (1989). Introduction to rock mechanics (Vol. 2): Wiley New York.

Griggs, D. T. (1936). Deformation of rocks under high confining pressures: I. Experiments at room temperature. The Journal of Geology, 541-577.

Gu, R. (2013). Distinct element model analyses of unstable failures in underground coal mines. (PhD Thesis), Colorado School of Mines, Golden, Colorado.

Gu, R., and Ozbay, U. (2015). Numerical investigation of unstable rock failure in underground mining condition. Computers and Geotechnics, 63, 171-182.

Hadamard, J. (1902). Sur les problèmes aux dérivées partielles et leur signification physique. Princeton university bulletin, 13(49-52), 28.

Hagan, T., Miley, A., Spottiswoode, S., Hildyard, M., Grodner, M., Rorke, A., Finnie, G., Reddy, N., Haile, A., and Le Bron, K. (2001). Simulated rockburst experiment-an overview. Journal of the South African Institute of Mining and Metallurgy, 101(5), 217-222.

Haijun, C., Nenghui, L., Dexin, N., and Yuequan, S. (2003). Prediction of rockburst by artificial neural network. Chinese Journal of Rock Mechanics and Engineering, 22(5), 762-768.

Haimson, B., and Chang, C. (2000). A new true triaxial cell for testing mechanical properties of rock, and its use to determine rock strength and deformability of Westerly granite. International Journal of Rock Mechanics and Mining Sciences, 37(1), 285-296.

Hajiabdolmajid, V., Kaiser, P., and Martin, C. (2002). Modelling brittle failure of rock. International Journal of Rock Mechanics and Mining Sciences, 39(6), 731-741.

Hallbauer, D., Wagner, H., and Cook, N. (1973). Some observations concerning the microscopic and mechanical behaviour of quartzite specimens in stiff, triaxial compression tests. Paper presented at the International Journal of Rock Mechanics and Mining Sciences & Geomechanics Abstracts,713-726.

Harewood, F., and McHugh, P. (2007). Comparison of the implicit and explicit finite element methods using crystal plasticity. Computational Materials Science, 39(2), 481-494.

Hastings, J., Juds, M., and Brauer, J. (1985). Accuracy and economy of finite element magnetic analysis. Paper presented at the 33rd Annual National Relay Conference.

Hazzard, J. F., Collins, D. S., Pettitt, W. S., and Young, R. P. (2002). Simulation of unstable fault slip in granite using a bonded-particle model The Mechanism of Induced Seismicity (pp. 221-245): Springer.

He, B. G., Zelig, R., Hatzor, Y. H., and Feng, X. T. (2016). Rockburst Generation in Discontinuous Rock Masses. Rock mechanics and rock engineering, In Press. doi: 10.1007/s00603-015-0906-8

He, M., Miao, J., and Feng, J. (2010). Rock burst process of limestone and its acoustic emission characteristics under true-triaxial unloading conditions. International Journal of Rock Mechanics and Mining Sciences, 47(2), 286-298.

He, M., Nie, W., Zhao, Z., and Guo, W. (2012a). Experimental investigation of bedding plane orientation on the rockburst behavior of sandstone. Rock mechanics and rock engineering, 45(3), 311-326.

He, M., Xia, H., Jia, X., Gong, W., Zhao, F., and Liang, K. (2012b). Studies on classification, criteria and control of rockbursts. J Rock Mech Geotech Eng, 4(2), 97-114.

Heal, D. (2010). Observations and analysis of incidences of rockburst damage in underground mines. (PhD Thesis), University of Western Australia, Australia.

Hedley, D. (1988). Rockbursts in Ontario mines during 1985 (Vol. 87). Ottawa, Canada: Canada Centre for Mineral and Energy Technology.

Hedley, D. (1992). Rockburst handbook for Ontario hard rock mines. Ottawa, Canada.

Helwany, S. (2007). Applied soil mechanics with ABAQUS applications. Hoboken, New Jersey: John Wiley & Sons.

Henley, S. (1976). Catastrophe theory models in geology. Journal of the International Association for Mathematical Geology, 8(6), 649-655.

Hoek, E. (1983). Strength of jointed rock masses. Geotechnique, 33(3), 187-223.

Hoek, E., and Brown, E. (1997). Practical estimates of rock mass strength. International Journal of Rock Mechanics and Mining Sciences, 34(8), 1165-1186.

Hoek, E., and Brown, E. T. (1980). Underground excavations in rock. London: Institution of Mining and Metallurgy.

http://serc.carleton.edu/NAGTWorkshops/petrology/index.html.   Retrieved November 22, 2015

http://whattherockstellus.blogspot.ca/2012_03_01_archive.html.   Retrieved November 22, 2015

http://www.affordablegranite.co.uk/salt-pepper-granite.html.   Retrieved November 22, 2015

https://en.wikipedia.org/wiki/Empirical_research.   Retrieved September 3, 2014

https://en.wikipedia.org/wiki/Jinping-II_Dam.   Retrieved February 27, 2016

Hua, A. Z., and You, M. Q. (2001). Rock failure due to energy release during unloading and application to underground rock burst control. Tunnelling and Underground Space Technology, 16(3), 241-246.

Hudson, J. A., Brown, E. T., and Fairhurst, C. (1972a). Shape of the complete stress-strain curve for rock. Paper presented at the Stability of Rock Slopes,773-795.

Hudson, J. A., Crouch, S. L., and Fairhurst, C. (1972b). Soft, stiff and servo-controlled testing machines: a review with reference to rock failure. Engineering Geology, 6(3), 155-189.

Itasca, U. (2000). Universal Distinct Element Code User's Guide: USA.

Jaeger, J. C., Cook, N. G., and Zimmerman, R. (2009). Fundamentals of rock mechanics: John Wiley & Sons.

Jager, A., Wojno, L., and Henderson, N. (1990). New developments in the design and support of tunnels under high stress. Paper presented at the Proc. Int. Deep Conf.: Technical Challenges in Deep Level Mining,1155-1172.

Jeon, S., Kim, J., Seo, Y., and Hong, C. (2004). Effect of a fault and weak plane on the stability of a tunnel in rock—a scaled model test and numerical analysis. International Journal of Rock Mechanics and Mining Sciences, 41, 658-663.

Jia, P., and Zhu, W. C. (2012). Dynamic-static coupling analysis on rockburst mechanism in jointed rock mass. Journal of Central South University, 19, 3285-3290.

Jiang, Q., Feng, X. T., Xiang, T. B., and Su, G. S. (2010). Rockburst characteristics and numerical simulation based on a new energy index: a case study of a tunnel at 2,500 m depth. Bulletin of engineering geology and the environment, 69(3), 381-388.

Jiang, Q., Su, G. S., Feng, X. T., Cui, J., Pan, P. Z., and Jiang, J. Q. (2015). Observation of rock fragment ejection in post-failure response. International Journal of Rock Mechanics and Mining Sciences(74), 30-37.

Jing, L. (2003). A review of techniques, advances and outstanding issues in numerical modelling for rock mechanics and rock engineering. International Journal of Rock Mechanics and Mining Sciences, 40(3), 283-353.

Jiong, W., Yubiao, Y., Zhengjun, J., Ping, Q., and Chen, C. (2011). Mechanism of energy limit equilibrium of rock burst in coal mine. Mining Science and Technology (China), 21(2), 197-200.

Johnston, J. C. (1988). A survey of mining associated rockbursts. (MSc Thesis), Massachusetts Institute of Technology, Cambridge, Massachusetts.

Kaiser, P. (1993). Keynote address: support of tunnels in burst prone ground—toward a rational design methodology. Rockbursts and seismicity in mines, 13-27.

Kaiser, P., McCreath, D., and Tannant, D. (1996). Rockburst support handbook. Geomechanics Research Centre, Laurentian University, Canada.

Kaiser, P., and Tang, C. (1998). Numerical simulation of damage accumulation and seismic energy release during brittle rock failure—part II: rib pillar collapse. International Journal of Rock Mechanics and Mining Sciences, 35(2), 123-134.

Kaiser, P. K., and Cai, M. (2012). Design of rock support system under rockburst condition. Journal of Rock Mechanics and Geotechnical Engineering, 4(3), 215-227.

Kaiser, P. K., and Kim, B. H. (2015). Characterization of strength of intact brittle rock considering confinement-dependent failure processes. Rock mechanics and rock engineering, 48(1), 107-119.

Kias, E. (2013). Investigation of unstable failure in underground coal mining using the discrete element method. (PhD Thesis), Colorado School of Mines, Golden, Colorado.

Kias, E., and Ozbay, U. (2013). Modeling unstable failure of coal pillars in underground mining using the discrete element method. Paper presented at the 47th US Rock Mechanics/Geomechanics Symposium,Paper 165.

Klein, E., Baud, P., Reuschlé, T., and Wong, T. (2001). Mechanical behaviour and failure mode of Bentheim sandstone under triaxial compression. Physics and Chemistry of the Earth, Part A: Solid Earth and Geodesy, 26(1), 21-25.

Kwasniewski, M., Szutkowski, I., and Wang, J. (1994). Study of ability of coal from seam 510 for storing elastic energy in the aspect of assessment of hazard in Porabka-Klimontow Colliery. (MSc Thesis), Silesian Technical University.

Lee, S. M., Park, B. S., and Lee, S. W. (2004). Analysis of rockbursts that have occurred in a waterway tunnel in Korea. International Journal of Rock Mechanics and Mining Sciences, 41, 911-916.

Li, D., Li, C. C., and Li, X. (2011a). Influence of sample height-to-width ratios on failure mode for rectangular prism samples of hard rock loaded in uniaxial compression. Rock mechanics and rock engineering, 44(3), 253-267.

Li, J., Fan, P., and Wang, M. (2013). Failure behavior of highly stressed rocks under quasi-static and intensive unloading conditions. Journal of Rock Mechanics and Geotechnical Engineering, 5(4), 287-293.

Li, S., Feng, X.-T., Li, Z., Chen, B., Zhang, C., and Zhou, H. (2012). In situ monitoring of rockburst nucleation and evolution in the deeply buried tunnels of Jinping II hydropower station. Engineering Geology, 137, 85-96.

Li, T., Cai, M., and Cai, M. (2007). A review of mining-induced seismicity in China. International Journal of Rock Mechanics and Mining Sciences, 44(8), 1149-1171.

Li, T., Wang, X., and Meng, L. (2011b). A physical simulation test for the rockburst in tunnels. Journal of Mountain Science, 8(2), 278-285.

Li, X., Cao, W., Zhou, Z., and Zou, Y. (2014). Influence of stress path on excavation unloading response. Tunnelling and Underground Space Technology, 42, 237-246.

Li, X., Wang, X., Kang, Y., and He, Z. (2005). Artificial neural network for prediction of rockburst in deep-buried long tunnel Advances in Neural Networks–ISNN 2005 (pp. 983-986): Springer.

Manouchehrian, A., and Cai, M. (2016a). Influence of material heterogeneity on failure intensity in unstable rock failure. Computers and Geotechnics, 71, 237-246. doi: http://dx.doi.org/10.1016/j.compgeo.2015.10.004

Manouchehrian, A., and Cai, M. (2016b). Influence of weak planes on rockburst occurrence. Paper presented at the the 3rd International Symposium on Mine Safety Science and Engineering,Paper 110 Montreal, Canada.

Manouchehrian, A., and Cai, M. (2016c). Numerical modeling of rockburst in deep tunnels. Rock Mechanics and Rock Engineering, Submitted.

Manouchehrian, A., and Cai, M. (2016d). Simulation of unstable rock failure under unloading conditions. Canadian Geotechnical Journal, 53(1), 22-34. doi: 10.1139/cgj-2015-0126

Manouchehrian, A., and Marji, M. F. (2012). Numerical analysis of confinement effect on crack propagation mechanism from a flaw in a pre-cracked rock under compression. Acta Mechanica Sinica, 28(5), 1389-1397.

Manouchehrian, A., Sharifzadeh, M., Marji, M. F., and Gholamnejad, J. (2014). A bonded particle model for analysis of the flaw orientation effect on crack propagation mechanism in brittle materials under compression. Archives of Civil and Mechanical Engineering, 14(1), 40-52. doi: http://dx.doi.org/10.1016/j.acme.2013.05.008

Mansurov, V. (2001). Prediction of rockbursts by analysis of induced seismicity data. International Journal of Rock Mechanics and Mining Sciences, 38(6), 893-901.

Martin, C., and Chandler, N. (1994). The progressive fracture of Lac du Bonnet granite. Paper presented at the International Journal of Rock Mechanics and Mining Sciences & Geomechanics Abstracts,643-659.

Miao, S.-J., Cai, M.-F., Guo, Q.-F., and Huang, Z.-J. (2016). Rock burst prediction based on in-situ stress and energy accumulation theory. International Journal of Rock Mechanics and Mining Sciences, 83, 86-94. doi: http://dx.doi.org/10.1016/j.ijrmms.2016.01.001

Milev, A., Spottiswoode, S., Noble, B., Linzer, L., Van Zyl, M., Daehnke, A., and Acheampong, E. (2002). The meaningful use of peak particle velocities at excavation surfaces for the optimisation of the rockburst criteria for tunnels and stopes. SIMRAC Final Project Report GAP, 709.

Milev, A., Spottiswoode, S., Rorke, A., and Finnie, G. (2001). Seismic monitoring of a simulated rockburst on a wall of an underground tunnel. Journal of the South African Institute of Mining and Metallurgy, 101(5), 253-260.

Mitri, H., Tang, B., and Simon, R. (1999). FE modelling of mining-induced energy release and storage rates. Journal of the South African Institute of Mining and Metallurgy, 99(2), 103-110.

Mogi, K. (1962). The influence of the dimensions of specimens on the fracture strength of rocks: comparison between the strength of rock specimens and that of the Earth's crust. Bulletin of the Earthquake Research Institute, 40, 831-853.

Mogi, K. (1967). Effect of the intermediate principal stress on rock failure. Journal of Geophysical Research, 72(20), 5117-5131.

Mogi, K. (1971). Fracture and flow of rocks under high triaxial compression. Journal of Geophysical Research, 76(5), 1255-1269.

Mogi, K. (1981). Flow and fracture of rocks under general triaxial compression. Applied Mathematics and Mechanics, 2(6), 635-651.

Mogi, K. (2007). Experimental rock mechanics. London: Taylor $ Francis.

Müller, W. (1991). Numerical simulation of rock bursts. Mining science and technology, 12(1), 27-42.

Munjiza, A., Owen, D., and Bicanic, N. (1995). A combined finite-discrete element method in transient dynamics of fracturing solids. Engineering computations, 12(2), 145-174.

Nemat‐Nasser, S., and Horii, H. (1982). Compression‐induced nonplanar crack extension with application to splitting, exfoliation, and rockburst. Journal of Geophysical Research: Solid Earth (1978–2012), 87(B8), 6805-6821.

Oelfke, S. M., Mustoe, G. G., and Kripakov, N. (1996). Yielding Gate Pillar Design With an Elasto-plastic Discrete Element Code. Paper presented at the 2nd North American Rock Mechanics Symposium.

Ortlepp, W. (1993). High ground displacement velocities associated with rockburst damage. Rockbursts and seismicity in mines, 5, 101-106.

Ortlepp, W., and Stacey, T. (1994). Rockburst mechanisms in tunnels and shafts. Tunnelling and Underground Space Technology, 9(1), 59-65.

Ortlepp, W. D. (1997). Rock fracture and rockbursts: an illustrative study: South African Institute of Mining and Metallurgy.

Ozbay, M. (1989). The stability and design of yield pillars located at shallow and moderate depths. Journal of the South African Institute of Mining and Metallurgy, 89(3), 73-79.

Palmström, A. (1995). Characterizing rock burst and squeezing by the rock mass index. Paper presented at the International conference in design and construction of underground structures.

Pan, P. Z., Feng, X. T., and Hudson, J. A. (2012). The influence of the intermediate principal stress on rock failure behaviour: A numerical study. Engineering Geology, 124, 109-118.

Pan, Y., Li, A. W., and Qi, Y. S. (2009). Fold catastrophe model of dynamic pillar failure in asymmetric mining. Mining Science and Technology (China), 19(1), 49-57.

Pan, Y., Zhang, Y., and Yu, G. M. (2006). Mechanism and catastrophe theory analysis of circular tunnel rockburst. Applied Mathematics and Mechanics, 27, 841-852.

Panet, M., and Guenot, A. (1983). Analysis of convergence behind the face of a tunnel: Tunnelling 82, proceedings of the 3rd international symposium, Brighton, 7–11 June 1982, P197–204. Publ London: IMM, 1982. Paper presented at the International Journal of Rock Mechanics and Mining Sciences & Geomechanics Abstracts,A16.

Paterson, M. (1958). Experimental deformation and faulting in Wombeyan marble. Geological Society of America Bulletin, 69(4), 465-476.

Potyondy, D., and Cundall, P. (2004). A bonded-particle model for rock. International Journal of Rock Mechanics and Mining Sciences, 41(8), 1329-1364.

Puri, G. (2011). Python scripts for Abaqus: learn by example. Uinted States: Kan Sasana Printer.

Qian, Q., and Zhou, X. (2011). Quantitative analysis of rockburst for surrounding rocks and zonal disintegration mechanism in deep tunnels. J Rock Mech Geotech Eng, 3(1), 1-9.

Qiao, C., and Tian, Z. (1998). Study of the possibility of rockburst in Donggua-shan Copper Mine. Chinese J. Rock Mech. Eng. Žexp, 17, 917-921.

Qin, S., Jiao, J. J., Tang, C., and Li, Z. (2006). Instability leading to coal bumps and nonlinear evolutionary mechanisms for a coal-pillar-and-roof system. International journal of solids and structures, 43(25), 7407-7423.

Qiu, S., Feng, X., Zhang, C., and Xiang, T. (2014). Estimation of rockburst wall-rock velocity invoked by slab flexure sources in deep tunnels. Canadian Geotechnical Journal, 51(5), 520-539.

Rahimdel, M. J., Mirzaii, H., Mahdevari, S., and Bagherpour, R. (2011). Evaluation of Rock Burst Potential in Beheshtabad Water Transition Tunnel and It's Control. Paper presented at the at the The 7th Iranian conference of engineering geology and the Environmen, Shahrood, Iran.

Read, H. E., and Hegemier, G. (1984). Strain softening of rock, soil and concrete—a review article. Mechanics of Materials, 3(4), 271-294.

Reddy, N., and Spottiswoode, S. (2001). The influence of geology on a simulated rockburst. Journal of the South African Institute of Mining and Metallurgy, 101(5), 267-274.

Riefenberg, J. S. (1991). Statistical evaluation and time series analysis of microseismicity, mining, and rock bursts in a hard-rock mine: US Department of the Interior, Bureau of Mines.

Salamon, M. (1970). Stability, instability and design of pillar workings. Paper presented at the International Journal of Rock Mechanics and Mining Sciences & Geomechanics Abstracts,613-631.

Salamon, M. (1974). Rock mechanics of underground excavations. Advances in rock mechanics, Proc. 3rd Cong. ISRM., Denver B, 1, 951-1009.

Salamon, M. (1983). Rockburst hazard and the fight for its alleviation in South African gold mines. Rockbursts: prediction and control. IMM, London, 11-36.

Salamon, M. (1984). Energy considerations in rock mechanics: fundamental results. Journal of the South African Institute of Mining and Metallurgy, 84(8), 233-246.

Salamon, M. (1993). Keynote address: Some applications of geomechanical modelling in rockburst and related research. Paper presented at the Proceedings of the 3rd International Symposium on Rockbursts and Seismicity in Mines,297-309.

Salamon, M., Badr, S., Mendoza, R., and Ozbay, M. (2003). Pillar failure in deep coal seams: numerical simulation. Paper presented at the 10th ISRM Congress.

Samui, P., Das, S. K., and Sitharam, T. (2009). Application of soft computing techniques to expansive soil characterization Intelligent and Soft Computing in Infrastructure Systems Engineering (pp. 305-323): Springer.

Selvadurai, A. (2007). The analytical method in geomechanics. Applied Mechanics Reviews, 60(3), 87-106.

Sharan, S. (2007). A finite element perturbation method for the prediction of rockburst. Computers & Structures, 85(17), 1304-1309.

Shepherd, J., Rixon, L., and Griffiths, L. (1981). Outbursts and geological structures in coal mines: a review. Paper presented at the International Journal of Rock Mechanics and Mining Sciences & Geomechanics Abstracts,267-283.

Shi, L., and Li, X. C. (2009). Analysis of end friction effect in true triaxial test. Rock and Soil Mechanics, 4, 068.

Shiyong, W., Manbin, S., and Jian, W. (2010). Jinping hydropower project: main technical issues on engineering geology and rock mechanics. Bulletin of engineering geology and the environment, 69(3), 325-332. doi: 10.1007/s10064-010-0272-4

Snelling, P. E., Godin, L., and McKinnon, S. D. (2013). The role of geologic structure and stress in triggering remote seismicity in Creighton Mine, Sudbury, Canada. International Journal of Rock Mechanics and Mining Sciences, 58, 166-179. doi: http://dx.doi.org/10.1016/j.ijrmms.2012.10.005

Stacey, T., Ortlepp, W., and Kirsten, H. (1995). Energy-absorbing capacity of reinforced shotcrete, with reference to the containment of rockburst damage. Journal of the South African Institute of Mining and Metallurgy, 95(3), 137-140.

Stacey, T., and Rojas, E. (2013). A potential method of containing rockburst damage and enhancing safety using a sacrificial layer. Journal of the Southern African Institute of Mining and Metallurgy, 113(7), 565-573.

Starfield, A. M., and Cundall, P. (1988). Towards a methodology for rock mechanics modelling. Paper presented at the International Journal of Rock Mechanics and Mining Sciences & Geomechanics Abstracts,99-106.

Stavrogin, A., and Tarasov, B. (1995). Some results obtained with high-stiffness rock testing systems. Int. Soc. Rock Mech. News J, 3(2), 6-19.

Sun, J., Lee, K., and Lee, H. (2000). Comparison of implicit and explicit finite element methods for dynamic problems. Journal of materials processing technology, 105(1), 110-118.

Sun, J. S., Zhu, Q. H., and Lu, W. B. (2007). Numerical simulation of rock burst in circular tunnels under unloading conditions. Journal of China University of Mining and Technology, 17(4), 552-556.

Tan, Y. L., Sun, C. J., and Zhang, Z. Y. (2009). 2D-ball simulations on stiffness influences for coal bump. Journal of Coal Science and Engineering (China), 15(2), 161-165. doi: 10.1007/s12404-009-0210-x

Tang, C. (1997). Numerical simulation of progressive rock failure and associated seismicity. International Journal of Rock Mechanics and Mining Sciences, 34(2), 249-261.

Tang, C., and Kaiser, P. (1998). Numerical simulation of cumulative damage and seismic energy release during brittle rock failure—part I: fundamentals. International Journal of Rock Mechanics and Mining Sciences, 35(2), 113-121.

Tang, C., and Kou, S. (1998). Crack propagation and coalescence in brittle materials under compression. Engineering fracture mechanics, 61(3), 311-324.

Tao, M., Li, X., and Wu, C. (2012). Characteristics of the unloading process of rocks under high initial stress. Computers and Geotechnics, 45, 83-92. doi: http://dx.doi.org/10.1016/j.compgeo.2012.05.002

Tapponnier, P., and Brace, W. (1976). Development of stress-induced microcracks in Westerly granite. Paper presented at the International Journal of Rock Mechanics and Mining Sciences & Geomechanics Abstracts,103-112.

Tiwari, R. P., and Rao, K. S. (2006). Post failure behaviour of a rock mass under the influence of triaxial and true triaxial confinement. Engineering Geology, 84(3), 112-129.

Tonon, F., Amadei, B., Pan, E., and Frangopol, D. (2001). Bayesian estimation of rock mass boundary conditions with applications to the AECL underground research laboratory. International Journal of Rock Mechanics and Mining Sciences, 38(7), 995-1027.

Udd, J. E., and Hedley, D. (1987). Rockburst Research In Canada-1987. Paper presented at the 6th ISRM Congress.

Valley, B., Suorineni, F., and Kaiser, P. (2010). Numerical analyses of the effect of heterogeneities on rock failure process. Paper presented at the 44th US Rock Mechanics Symposium and 5th US-Canada Rock Mechanics Symposium.

Wang, J., and Park, H. (2001). Comprehensive prediction of rockburst based on analysis of strain energy in rocks. Tunnelling and Underground Space Technology, 16(1), 49-57.

Wang, S., Zheng, H., Li, C., and Ge, X. (2011a). A finite element implementation of strain-softening rock mass. International Journal of Rock Mechanics and Mining Sciences, 48(1), 67-76.

Wang, S. Y., Lam, K. C., Au, S. K., Tang, C. A., Zhu, W. C., and Yang, T. H. (2006). Analytical and Numerical Study on the Pillar Rockbursts Mechanism. Rock mechanics and rock engineering, 39(5), 445-467. doi: 10.1007/s00603-005-0075-2

Wang, Y. H., Li, W. D., and Li, Q. G. (1998). Fuzzy estimation method of rockburst prediction. Chinese Journal of Rock Mechanics and Engineering, 17, 493-501.

Wang, Z. Q., Zhang, L. X., and Guo, H. B. (2011b). Catastrophe Theory Analysis on Asymmetric Mining Pillar Dynamic Failure. Paper presented at the Applied Mechanics and Materials,4662-4667.

Wattimena, R., SIRAIT, B., P. Widodo, N., and MATSUI, K. (2012). Evaluation of rockburst potential in a cut-and-fill mine using energy balance. International Journal of the JCRM, 8(1), 19-23.

Wawersik, W. R., and Fairhurst, C. (1970). A study of brittle rock fracture in laboratory compression experiments. International Journal of Rock Mechanics and Mining Sciences & Geomechanics Abstracts, 7(5), 561-575. doi: http://dx.doi.org/10.1016/0148-9062(70)90007-0

White, R., and Rose, B. (2012). Rockburst support in high stress areas in Brunswick Mines.

Whyatt, J. (2008). Dynamic failure in deep coal: recent trends and a path forward. Paper presented at the Proceedings 27th International Conference on Ground Control in Mining,37-45.

Whyatt, J., Blake, W., Williams, T., and White, B. (2006). 60 Years of rockbursting in the Coeurd'Alene District of Northern Idaho, USA: lessons learned and remaining issues. Paper presented at the Presentation at 109th annual exhibit and meeting, Society for Mining, Metallurgy, and Exploration,25-27.

Wiebols, G. A., and Cook, N. G. W. (1968). An energy criterion for the strength of rock in polyaxial compression. International Journal of Rock Mechanics and Mining Sciences & Geomechanics Abstracts, 5(6), 529-549. doi: http://dx.doi.org/10.1016/0148-9062(68)90040-5

Wiles, T. (2002). Loading system stiffness-a parameter to evaluate rockburst potential. Paper presented at the First International Seminar on Deep and High Stress Mining, Australian Centre for Geomechanics, Perth, Australia.

Wong, R., Tang, C., Chau, K., and Lin, P. (2002). Splitting failure in brittle rocks containing pre-existing flaws under uniaxial compression. Engineering fracture mechanics, 69(17), 1853-1871.

Wu, Y., and Zhang, W. (1997). Prevention of rockbursts in coal mines in China. Paper presented at the Proceedings of the 4th International Symposium on Rockbursts and Seismicity in Mines, Rotterdam,361-366 Poland.

Yang, D. Y., Jung, D. W., Song, I. S., Yoo, D. J., and Lee, J. H. (1995). Comparative investigation into implicit, explicit, and iterative implicit/explicit schemes for the simulation of sheet-metal forming processes. Journal of materials processing technology, 50(1–4), 39-53. doi: http://dx.doi.org/10.1016/0924-0136(94)01368-B

Yeryomenko, A., and Sklyar, N. (1999). Effect of geological disturbances on the danger of rock bursts in a rock mass. Journal of Mining Science, 35(1), 12-18.

Yeung, M., and Leong, L. (1997). Effects of joint attributes on tunnel stability. International Journal of Rock Mechanics and Mining Sciences, 34(3), 348. e341-348. e318.

Young, R. P. (1993). Rockbursts and Seismicity in Mines 93: Proceedings of the 3rd international symposium, Kingston, Ontario, 16-18 August 1993. Kingston, Canada: Taylor & Francis.

Yu, H. C., Liu, H. N., Lu, X. S., and Liu, H. D. (2009). Prediction method of rock burst proneness based on rough set and genetic algorithm. Journal of Coal Science and Engineering (China), 15(4), 367-373.

Zengchao, F., and Yangsheng, Z. (2003). Correlativity of rock inhomogeneity and rock burst trend. Chinese Journal of Rock Mechanics and Engineering, 11, 027.

Zhang, C., Feng, X. T., Zhou, H., Qiu, S., and Wu, W. (2012). Case Histories of Four Extremely Intense Rockbursts in Deep Tunnels. Rock mechanics and rock engineering, 45(3), 275-288. doi: 10.1007/s00603-011-0218-6

Zhang, C., Feng, X. T., Zhou, H., Qiu, S., and Wu, W. (2013). Rockmass damage development following two extremely intense rockbursts in deep tunnels at Jinping II hydropower station, southwestern China. Bulletin of engineering geology and the environment, 72(2), 237-247.

Zhang, C., Feng, X. T., Zhou, H., Qiu, S., and Yang, Y. (2014). Rock mass damage induced by rockbursts occurring on tunnel floors: a case study of two tunnels at the Jinping II Hydropower Station. Environmental earth sciences, 71(1), 441-450.

Zhang, X., and Vu-Quoc, L. (2002). Modeling the dependence of the coefficient of restitution on the impact velocity in elasto-plastic collisions. International journal of impact engineering, 27(3), 317-341.

Zhao, X. G., and Cai, M. (2015). Influence of specimen height-to-width ratio on the strainburst characteristics of Tianhu granite under true-triaxial unloading conditions. Canadian Geotechnical Journal, 52(7), 890-902. doi: 10.1139/cgj-2014-0355

Zheng, H., Liu, D., Lee, C. F., and Ge, X. (2005). Principle of analysis of brittle-plastic rock mass. International journal of solids and structures, 42(1), 139-158.

Zhou, H., Meng, F., Zhang, C., Hu, D., Yang, F., and Lu, J. (2015). Analysis of rockburst mechanisms induced by structural planes in deep tunnels. Bulletin of engineering geology and the environment, 74(4), 1435-1451. doi: 10.1007/s10064-014-0696-3

Zhou, J., Li, X., and Shi, X. (2012). Long-term prediction model of rockburst in underground openings using heuristic algorithms and support vector machines. Safety science, 50(4), 629-644.

Zhou, X. P., Qian, Q. H., and Yang, H. Q. (2011). Rock burst of deep circular tunnels surrounded by weakened rock mass with cracks. Theoretical and Applied Fracture Mechanics, 56(2), 79-88. doi: http://dx.doi.org/10.1016/j.tafmec.2011.10.003

Zhu, Q. H., Lu, W. B., Sun, J. S., Yi, L., and Ming, C. (2009). Prevention of rockburst by guide holes based on numerical simulations. Mining Science and Technology (China), 19(3), 346-351.

Zhu, W., Yang, W., Li, X., Xiang, L., and Yu, D. (2014). Study on splitting failure in rock masses by simulation test, site monitoring and energy model. Tunnelling and Underground Space Technology, 41, 152-164. doi: http://dx.doi.org/10.1016/j.tust.2013.12.007

Zhu, W. C., Li, Z. H., Zhu, L., and Tang, C. A. (2010). Numerical simulation on rockburst of underground opening triggered by dynamic disturbance. Tunnelling and Underground Space Technology, 25(5), 587-599. doi: http://dx.doi.org/10.1016/j.tust.2010.04.004

Zubelewicz, A., and Mróz, Z. (1983). Numerical simulation of rock burst processes treated as problems of dynamic instability. Rock mechanics and rock engineering, 16(4), 253-274. doi: 10.1007/BF01042360

Appendix A: Review of methods for studying rockburst

In Chapter 2, a review on the numerical methods for studying the unstable rock failure and rockburst was presented. In this appendix, a review of the other common methods for studying the unstable rock failure and rockburst is presented.

A.1   Analytical methods

Analytical methods play an important role for developing concise results of practical value for preliminary design. This is important to geotechnical engineering because, in most instances, preliminary designs are carried out with only a limited knowledge of the range of values associated with geotechnical material parameters.

Furthermore, analytical solutions provide geotechnical engineers with a tool to examine plausible engineering solutions to what are undoubtedly very complex problems in geomechanics and to assess more conveniently the issue of geotechnical parameter variability. They also provide computational modelers with valuable benchmarking tools that will assist in the verification of the capabilities and reliability of computational approaches (Selvadurai, 2007). On the other hand, analytical methods assume that a rock mass is continuous, homogeneous, isotropic, and linearly elastic. In reality, rock masses are discontinuous, heterogeneous, anisotropic, and non-elastic. In spite of these simplifications, analytical solutions are useful for solving some geomechanical problems.

Several theories have been employed for analyzing rockburst. Catastrophe theory is a mathematical technique for analyzing natural phenomena that involve discontinuities or sudden changes in parameters (Henley, 1976). Several studies have been performed to analyze rockburst using this theory (Pan et al., 2009; Pan et al., 2006; Qin et al., 2006; Wang et al., 2006; Wang et al., 2011b). For instance, Wang et al. (2011b) used the catastrophe theory to analyze the mechanism of unstable failure of pillars. Using the catastrophe theory in a rock-rock model, they analyzed the system stability by studying the energy import rate (J). They showed that failure is unstable when $J \leq 0$ which implied that rockburst occurs when the Loading System Stiffness (LSS) is less than the rock's post-peak stiffness.

Because rockburst is the result of violent release of energy, it is logical that an analysis of energy can be used to explain the mechanism of violent failure. Initially only the energy stored within a rock was considered as the source of the released energy. Later, it was realized that there was a change in potential energy of the surrounding rock mass because of mining operations. This led to the concept of energy balance that was originally developed by Cook (1965) and later refined by Salamon (1970, 1974, 1984). It later became the principle based on which many researches on rockburst were carried out. For example, Wattimena et al. (2012) used the energy balance concept to evaluate rockburst potential in a cut-and-fill mine. In another study, Jiong et al. (2011), based on the energy theory, studied the energy limit equilibrium of a roof-coal-roof rockburst system, and determined the conditions that a rockburst might occur. Qiu et al. (2014) proposed an analytical approach based on the energy balance principle to estimate the wall-rock velocity in a rockburst. In their proposed method, the slabbing thickness of an intact rock mass was assessed analytically and then the wall-rock velocity was calculated.

176

Fracture mechanics is another theoretical approach that has been employed for analyzing rockburst. In brittle rocks, the dissipated energy from microcrack growth is small, but the elastic strain energy stored in the rocks is larger than the dissipated energy for growth of pre-existing and secondary microcracks. A sudden release of the residual elastic strain energy may lead to rockburst. Based on this understanding, Qian and Zhou (2011) established some criteria for rockburst occurrence. They studied the relation between rockburst and zonal disintegration in rock masses surrounding deep tunnels and investigated the influence of in situ stress and the physical and mechanical parameters on the distribution of rockburst zones and the ejection velocity of rock fragments. In another work, Zhou et al. (2011) studied rockbursts in deep circular tunnels surrounded by weakened rock masses with cracks using the fracture mechanics theory. They established a criterion of rockburst occurrence in crack-weakened rock masses based on energy analysis and investigated the influence of in situ stress on the distribution and area of rockburst zones.

In summary, analytical methods are very useful in geomechanics because they provide results with less effort and highlight the most important variables that affect the solution of a problem. Analytical solutions, however, often have limited application and they must be used within the range of assumptions made for their development. Such assumptions usually include elastic, homogeneous, isotropic material, time independent behavior, quasi-static loading, etc. (Bobet, 2010). Hence, analytical methods could not provide solutions for complex problems such as rockburst.

A.2 Empirical methods

Even with many resources available for site investigation, it remains a problem in applying theories in practical engineering, and some decisions are often made based on experience and engineering judgments. Empirical research is a way of gaining knowledge by means of direct and indirect observation or experience. Empirical evidence (direct observation or experience) can be analyzed quantitatively or qualitatively (https://en.wikipedia.org/wiki/Empirical_research). Through quantifying the evidence or making sense of it in a qualitative form, a researcher can answer questions empirically.

Many researchers have proposed empirical criteria for predicting rockburst intensity. For instance Kwasniewski et al. (1994) proposed an elastic strain energy criterion for analyzing rockburst. They showed that the potential energy of elastic strain (PES), i.e., the elastic strain energy in a unit volume of rock, can be used for predicting rockburst intensity. The elastic strain energy stored in a rock before the peak strength is reached can be calculated using the equation below:

$$PES = \frac{{\sigma_c}^2}{2E_s} \tag{A-1}$$

where σ_c is the uniaxial compressive strength and E_s is the unloading deformation modulus. The PES value can be used for assessing rockburst potential (Wang and Park, 2001):

- PES = 50 kJ/m^3, rockburst hazard is very low;

- 50 < PES = 100 kJ/m^3, rockburst hazard is low;

- 100 < PES < 150 kJ/m^3, rockburst hazard is moderate;

- 150 < PES = 200 kJ/m^3, rockburst hazard is high; and

- PES > 200 kJ/m^3, rockburst hazard is very high.

Another criterion for rockburst potential assessment, which is based on rock brittleness, was proposed by Qiao and Tian (1998). Rock brittleness is defined by the ratio of uniaxial compressive strength (σ_c) to uniaxial tensile strength (σ_T):

$$B = \frac{\sigma_c}{\sigma_T} \qquad \text{(A-2)}$$

Their experiences showed that for:

- B > 40, no rockburst;

- B = 40 - 26.7, weak rockburst;

- B = 26.7 - 14.5, strong rockburst; and

- B < 14.5, violent rockburst.

A criterion based on tangential stress was proposed by Wang et al. (1998). Stress state and rock mechanical properties were considered. This criterion was defined by:

$$T_s = \frac{\sigma_\theta}{\sigma_c} \qquad \text{(A-3)}$$

where, σ_θ is the maximum tangential stress in the rock mass around the opening and σ_c is the uniaxial compressive strength of the rock. In their view rockburst could be categorized by the following:

- T_s < 0.3, no rockburst;

- T_s = 0.3 - 0.5, weak rockburst;

- T_s = 0.5 - 0.7, strong rockburst; and

- T_s > 0.7, violent rockburst.

In general, high stress and strain energy could be less concentrated and accumulated in densely fractured and jointed rock mass. From this point of view, the intensity of fractures and joints developed in a rock mass can elaborate the tendency of rockburst indirectly. Palmström (1995) used the Rock Mass index (RMi) for predicting rockburst by defining a term called competency factor C_g:

$$C_g = \frac{RMi}{\sigma_\theta} \tag{A-4}$$

where, σ_θ is the maximum tangential stress around the underground opening. Then following scaling system for rockburst was proposed by Palmström (1995):

- If $C_g > 2.5$, no rock stress induced instability;
- If $1 < C_g < 2.5$, high stress, slightly loosening;
- If $0.5 < C_g < 1$, light rockburst or spalling; and
- If $C_g < 0.5$, heavy rockburst.

RQD is an index for describing the degree of rock mass integrity. Wang and Park (2001) used RQD for assessing the possibility of rockburst at Linglong gold mine in China. They believed that in the shallow part of the mine where RQD was 25, there was little possibility of rockburst occurrence while in the deeper part (H > 400 m) of the mine where RQD was 90 to 98, there was a high possibility of rockburst.

Empirical methods are simple techniques for analyzing rockburst problems. This approach is based on some criteria and each criterion comes from experiments, experiences, and personal judgments. Results have shown that for a particular case, the assessment results from different criteria are not necessarily the same, i.e., a criterion may evaluate a light rockburst while another may predict a violent one (Miao et al., 2016; Rahimdel et al., 2011). The most important point

about empirical methods is that they are too simplistic and do not consider all the necessary and sufficient conditions for a rockburst to occur. Therefore, predictions made from empirical methods are not reliable.

A.3   Data-based methods

When sufficient information is available, data-based modeling techniques can be used successfully to develop input–output relations for analyzing complex systems. These techniques are mostly comprised of statistical and artificial intelligence methods.

A.3.1   Statistical methods

Statistical methods have been used for solving many problems in various branches of science such as medicine, economics, sociology, and engineering. Among all engineering fields, geotechnical engineering always deals with uncertainties; thus, statistical methods suit for solving problems in this field.

Some researchers have used statistical methods to study rockburst. For instance, Riefenberg (1991) presented a statistical analysis method for describing the occurrence of rockburst in a deep hard-rock mine and quantified the relations among microseismicity, mining, geometry, and stress. A dataset comprising 101 rockburst events during a period of 1,079 days of mining in a deep western U.S. silver-lead-zinc mine was compiled. Statistical analyses were conducted to find the relation among four individual parameters including blasting, rock mass damage, average microseismicity rate, and local mine geometry. According to the results, 91% of the rockbursts occurred with blasting while only 3% occurred independent of blasting. The results also showed that local mine geometry and geology appeared to affect rockburst activity. Moreover, it seemed that the time of rockburst occurrence was dictated by the long-term average

daily rates of microseismicity. Time series analysis on the daily microseismic activities resulted in a model that might be used to forecast the daily microseismic activity. This analysis showed non-randomness in the data of microseismic event rate and a strong correlation between rockburst occurrences and daily microseismic events.

A.3.2 Artificial intelligence methods

The use of artificial intelligence (AI) methods in solving geomechanical problems increased significantly in the last two decades. AI methods are powerful and versatile for organizing and correlating information in ways that have been proven useful for solving certain types of problems that are too complex, too poorly understood, or too resource-intensive to tackle using more-traditional computational methods (Samui et al., 2009). Moreover, successful application of AI methods for solving problems in decision-making sciences, computer engineering, and electrical engineering is expected to increase interest and reliability on AI methods in the field of geotechnical engineering. The expert judgements that must routinely be made in solving geotechnical problems make it an excellent field for AI application (Ahmed et al., 2008).

Regarding the ability of AI methods, many data-based models using methods such as Artificial Neural Networks (ANN), Genetic Algorithms (GA), Fuzzy Logic, and Particle Swarm Optimization (PSO) have been proposed for rockburst prediction. Haijun et al. (2003) developed an ANN model for the prediction of rockburst and rockburst intensity. Their ANN model was designed with four input parameters consisting of uniaxial compressive strength, tensile strength, elastic energy index of rock and maximum tangential stress of tunnel walls and two binary outputs. The results showed that the established ANN model was capable of predicting rockburst in four groups: violent, medium, light, and no rockburst. In their work, they used a dataset including only 13 rockburst cases from China to train the ANN models, which was not large

enough. In another work, Li et al. (2005) established an ANN model using the same approach as Haijun et al. (2003) did. They used a slightly larger training dataset (20 cases), which was still not efficient. Adoko et al. (2013) used fuzzy modeling for rockburst prediction. They collected a dataset comprised of 174 rockburst events and proposed five models based on Fuzzy Inference System (FIS), Adaptive Neuro-Fuzzy Inference System (ANFIS), and field measurement data. Because a larger dataset was used in their study, the results may be more reliable. He et al. (2012b) used a Bayesian Network (BN) model to predict rockburst. The BN model was trained using 30 well-documented rockburst case histories. This BN model can predict the intensity of rockburst in four groups: (i) overbreak, (ii) slight rockburst, (iii) medium rockburst, and (iv) strong rockburst.

In some researches, metaheuristic algorithms have been employed for analyzing rockburst. For instance, Yu et al. (2009) proposed a method, which is based on Rough Set Theory and Genetic Algorithm (GA), to predict rockburst proneness. Comparing the prediction with the actual field data, they showed that the proposed method was feasible and effective. In another work a predictive model was developed by Zhou et al. (2012) using Support Vector Machines (SVM) in combination with GA and PSO algorithms as metaheuristic algorithms for long-term prediction of rockburst. They used PSO and GA to improve the SVM for rockburst prediction.

In general, data which hold valuable information such as trends and patterns of rockbursts can be used to improve decision-making and optimize mining processes. However, the interaction among different factors that influence rockburst is complex and a large number of data are needed to predict rockburst. There is an extraordinary expansion of data collection activities nowadays with respect to the advances in information and communication technologies. The

183

collected data need to be stored and analyzed to develop useful intelligent models for rockburst prediction.

A.4   Experimental methods

Physical testing is essential for studying rock mechanics and rock engineering problems by providing necessary information about rock properties. Physical tests are also helpful to observe the response of rock to different mechanical loads. Experimental methods (laboratory and in situ tests) have been used to study different rock engineering problems and can be employed to investigate different aspects of unstable rock failure.

Laboratory testing can reproduce the process of unstable rock failure and help to analyze the internal changing characteristics of rockburst; however, it is rather difficult to simulate rockbursts that truly mimic conditions underground. Burgert and Lippmann (1981) conducted some laboratory tests using epoxy resin specimens (as a model material) to study typical features of rockburst in coal mines. The test results showed that there were a fractured zone and two elastic zones in the specimens before the rockburst. They proposed an index called "proneness to bursting" to evaluate the possibility of rockburst in their model test.

A simulated rockburst was conducted by Milev et al. (2001) underground at Kopanang mine in
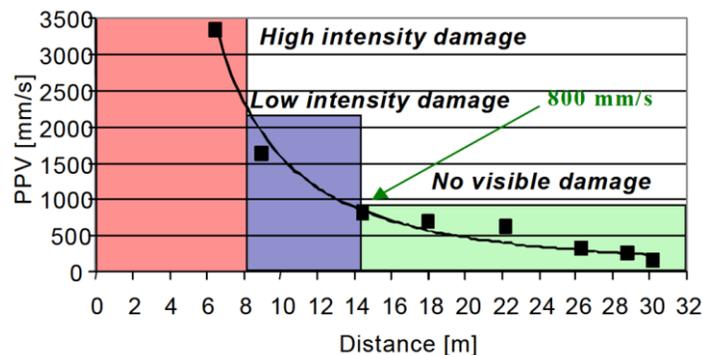
Figure A-1: The attenuation of the PPVs in the wall of an underground tunnel (Milev et al., 2002).

South Africa by means of a large blast near a crosscut sidewall. This experiment was carried out to study the seismicity in the near and far fields, to monitor rock ejection, and to study rock mass conditions. Using installed accelerometers and a high-speed camera, they monitored ground motion velocities and ejected rocks, respectively. In that experiment the Peak Particle Velocity (PPV) generated by the simulated rockburst along the tunnel wall was monitored. PPV values were used to categorize rockburst damage into three groups: "no visible damage" when PPV < 800 mm/s, "low intensity damage" when 800 mm/s $\leq$ PPV $\leq$ 2100 mm/s, and "high intensity damage" when PPV > 2100 mm/s (Figure A-1) (Milev et al., 2002; Milev et al., 2001). In another work, Hagan et al. (2001) conducted a similar experiment underground at a deep level in the Kopanang Gold Mine in South Africa. The test results showed that rock damage occurred on the tunnel wall where the PPV exceeded 0.7 m/s.

He et al. (2010) developed a true-triaxial rockburst test system at China University of Mining Technology in Beijing. This setup was designed to provide dynamic unloading at the minimum principal stress direction. They used this testing system to study the rockburst process of limestone along with acoustic emission characteristics under true-triaxial unloading condition. They showed that this testing system can be employed for reproducing strainburst in laboratory
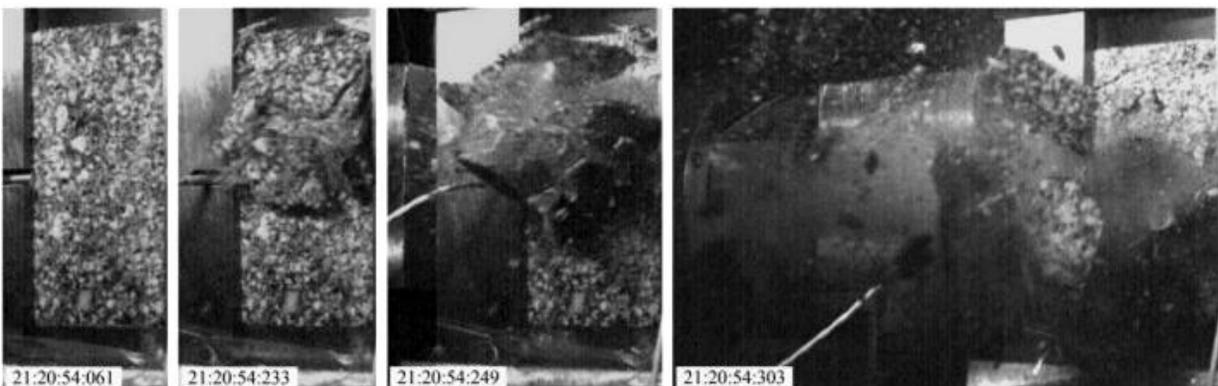
Figure A-2: Strainburst process of Tianhu granite (Zhao and Cai, 2015).

185

for rocks under polyaxial stress loading; it can also be used for calibrating numerical tools such as PFC. This apparatus was employed to study other aspects of rockburst such as the effect of bedding plane orientation on the rockburst behavior (He et al., 2012a). Their test results showed that when the bedding orientation was perpendicular to the unloading surface, the rockburst was controlled by the specimen's strength. This test facility was recently used by Zhao and Cai (2015) to study rockbursting behavior of Tianhu granite under polyaxial unloading condition (Figure A-2).

Li et al. (2011b) carried out a physical model test to study rockburst in tunnels (Figure A-3). The prototype model was built to simulate rockburst in a section of the diversion tunnels at Jinping II hydropower station in China. A hole was opened in the model after loading the model to simulate the tunnel excavation. The physical modeling results showed that the arch top, spandrel and side walls of the tunnel showed an obvious jump change of stress and strain several times after the excavation. In addition, the acoustic emission counts of the surrounding rock increased rapidly several times after the hole was opened. These observations were interpreted as features
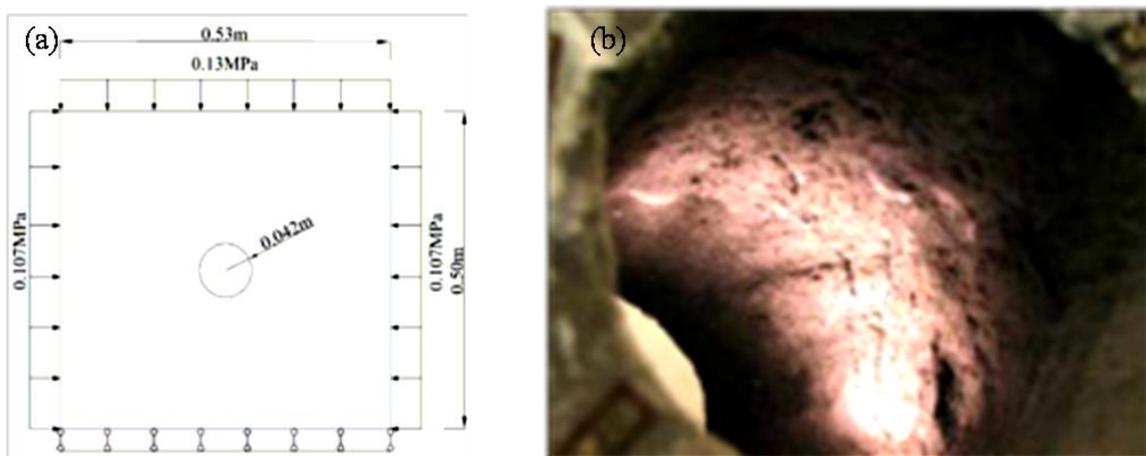
Figure A-3: (a) Schematic diagram of the model geometry and loading condition, and (b) the photograph of fractures on the tunnel wall (Li et al., 2011b).
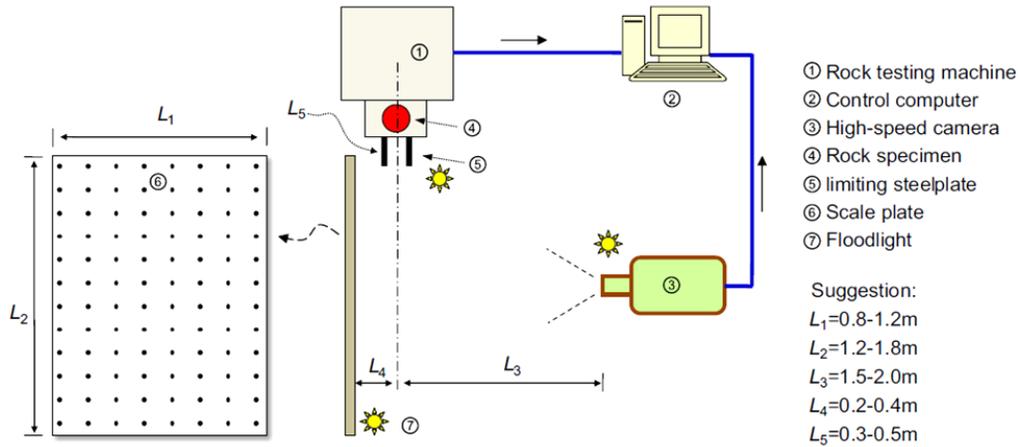
Figure A-4: Observation scheme for rock fragment ejection in post-failure (Jiang et al., 2015).

of rockburst. When the model was overloaded, spalling, buckling and breaking occurred in the surrounding rock of the model (Figure A-3b). It was concluded that the modeled segment of the tunnel in the Jinping II hydropower station is expected to experience the rockburst with the pattern of spalling, buckling, and breaking.

Zhou et al. (2015) conducted some laboratory shear tests to explain the role of weak planes on rockburst damage in tunnels of the Jinping II hydropower station. Based on their observations in the shear tests, they hypothesized three possible mechanisms including fault-slip burst, shear rupture burst, and buckling burst for rockburst occurrence. Jiang et al. (2015) conducted an experiment to study ejection velocity of broken rocks in unstable rock failure. In their experiment, rock specimens were loaded to fail while a high-speed camera was used to record the ejection process (Figure A-4). They used an algorithm to calculate the initial ejection velocity and initial ejection angle. Their observation showed the initial ejection velocities range from 1.1 to 7.9 m/s and the initial ejection angles range from −30° to 30°, and there is an approximate linear relation between the elastic modulus of the rock specimens and the ejection velocities.

In general, experimental studies are time-consuming and costly. In addition, for a successful analysis of the mechanism that drives a rockburst, a clear understanding of stress distribution and energy changes inside the rock body is needed, which is difficult to be achieved by the experimental approach. Some researchers had used photo-elastic stress analysis technique to measure stress field on the surface of specimens directly (Brace and Bombolakis, 1963) but direct measurement of energy change in laboratory tests is still difficult and is possible only under simple loading conditions by measuring stress and strain in rock (Hua and You, 2001). These practical difficulties force engineers to turn to other methods for analyzing rockburst.

Numerical methods are useful tools for analyzing stress field and energy inside a deformable body and can be used to observe and calculate parameters that are not possible to be obtained from experiments (Manouchehrian and Marji, 2012). Use of numerical methods can give new insight to the rockburst mechanism.

Appendix B: Influence of loading system mass on the rock dynamic response

In Chapters 3 and 4, a platen with steel properties was used in the numerical models to apply load to the rock specimen and LSS was varied by changing the platen's length (L) (See Eq. (2-13)). An alternative approach to change LSS in numerical models is changing the platen's Young's modulus (E) while keeping the platen size (A and L) constant. In the method used in this research, the mass of the loading system is varied by changing LSS while in the second approach the mass is constant. Stavrogin and Tarasov (1995) noted that the dynamic behavior of a specimen in UCS test depends on the mass of the loading system. Therefore, the kinetic energy from these two approaches might be different even if the LSS values are the same. In this appendix, the influence of loading system mass on the rock dynamic response is briefly investigated.

UCS tests with different LSS values are simulated. Firstly, the mechanical and physical properties (Table 3-1) of Tianhu granite (Zhao and Cai, 2015) are used to calibrate the models. Two approaches are used to build models with different LSS values. In the first approach, which was used in Chapters 3 and 4, the platen length is varied and its elastic modulus is kept constant at $E = 200$ GPa to account different loading system stiffness in the numerical modeling. A cylindrical platen with a diameter of 54 mm and a length between 50 and 800 mm is simulated, and the dimension of the cylindrical specimen is 100 mm (height) × 50 mm (diameter). The model geometry and mesh size is illustrated in Figure B-1. The LSS is calculated using Eq. (2-13). The mechanical and physical properties of the rock listed in Table 3-1 and steel properties

(i.e., $E = 200$ GPa, $v = 0.3$ and $\rho = 7700$ kg/m^3) are assigned to the rock and the platen, respectively. Frictionless contact is assigned to the contact between the platen and the specimen to exclude the friction effect. This approach is referenced as "Approach A." Figure B-2 presents the stress–strain curves for with different LSS values in UCS tests simulated using Approach A.

Approach B

E = 50, 100, 133, 200, 400, 800 GPa (Variable)

L = 200 mm (Constant)

Approach A

E = 200 GPa (Constant)

L = 50, 100, 200, 300, 400, 800 mm (Variable)

Rigid disc
(E = 20000 GPa)

Fixed end
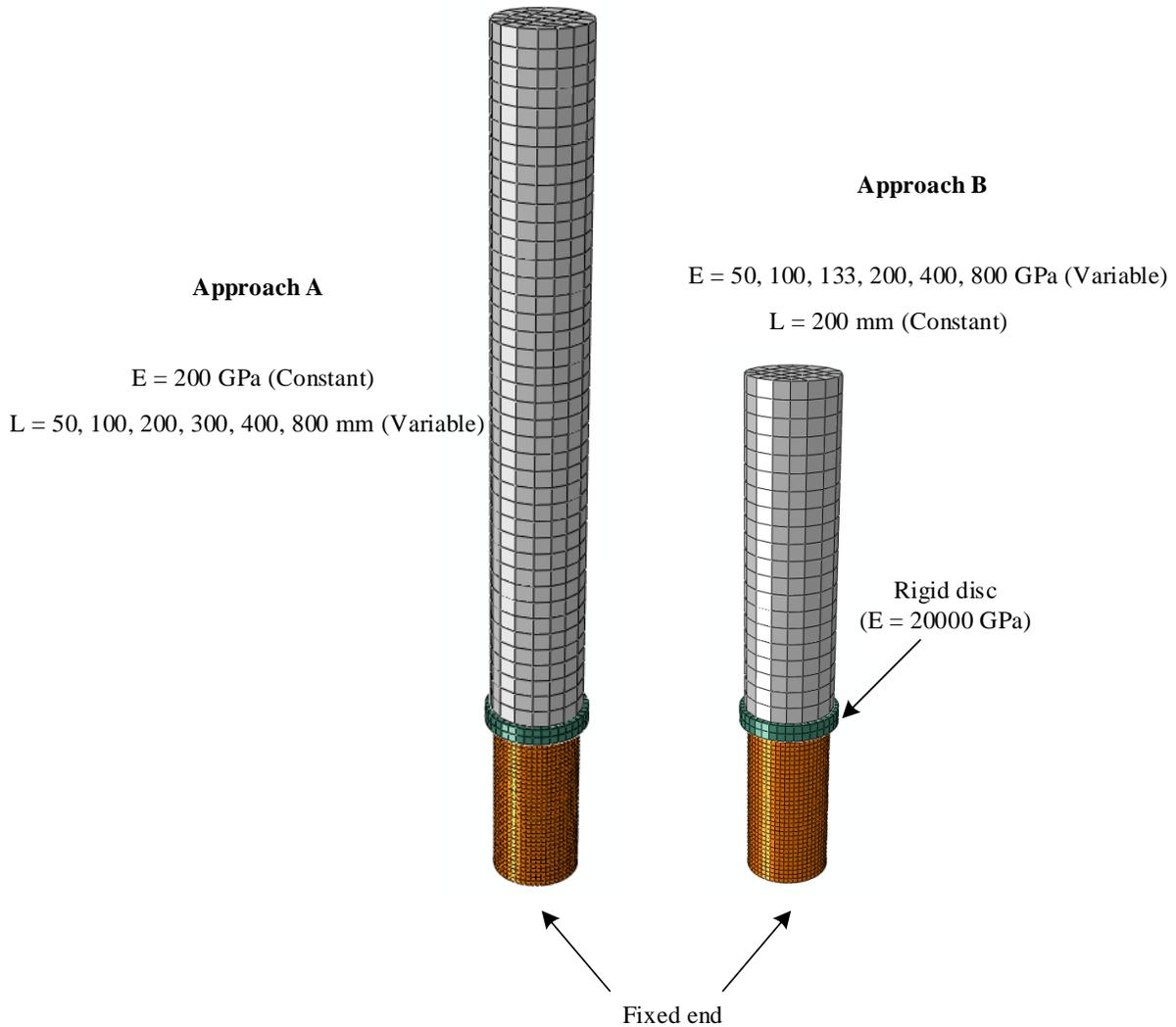
Figure B-1: Model geometry in two approaches.
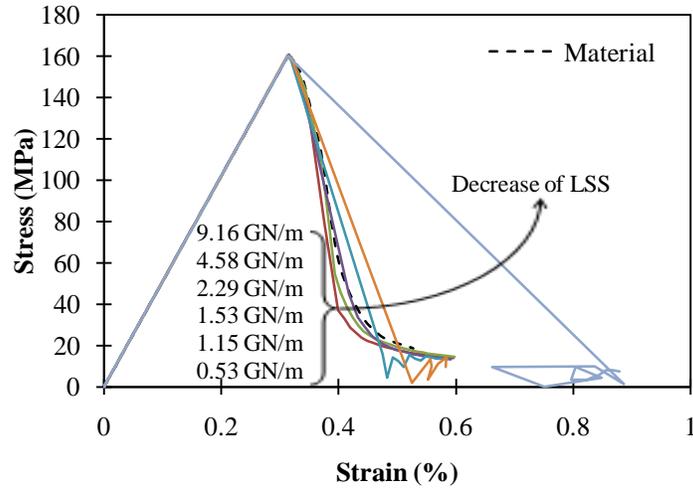
Figure B-2: Stress-strain curves with different LSS values (Approach A).
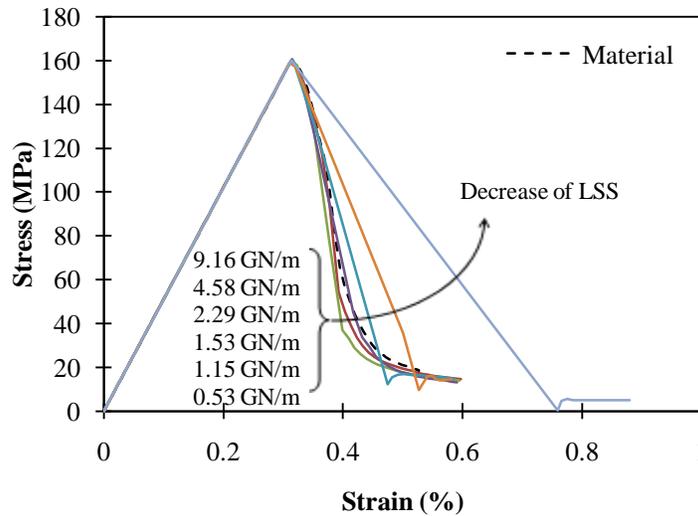
Figure B-3: Stress-strain curves with different LSS values (Approach B).

In the second approach, a cylindrical platen with a diameter of 54 mm and a constant length (L) of 200 mm is simulated. In this approach, E is varied between 50 to 800 GPa to change LSS from 0.57 to 9.16 GN/m. The platen has the properties of $v = 0.3$ and $\rho = 7700$ kg/m3. To avoid the Poisson's ratio effect when the Young's modulus of the platen is small (e.g. $E = 50$ GPa), a very stiff disc ($E = 20000$ GPa) is placed between the platen and the rock specimen. This
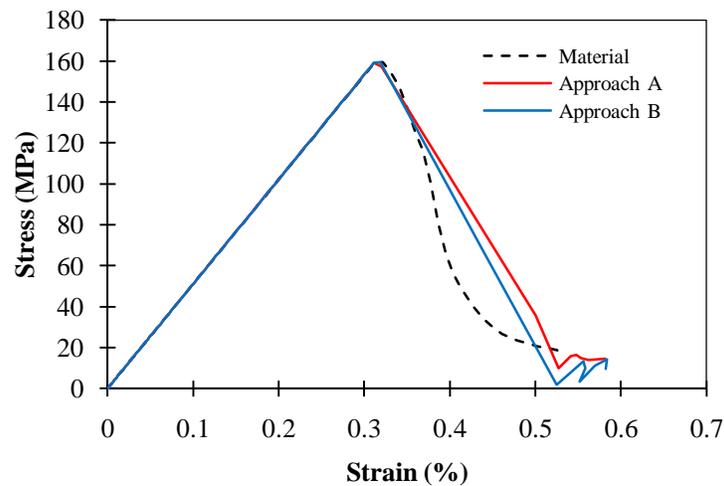
Figure B-4: Stress-strain curves of two models with k = 1.15 GN/m simulated using Approaches A and B.

approach is referenced as "Approach B." Figure B-3 presents the stress–strain curves for with different LSS values in UCS tests simulated using Approach B. Note that the rigid disc is included in both approaches to have the same boundary conditions in all models.

Figure B-2 and Figure B-3 indicate that when LSS is smaller than the post-peak stiffness of the rock, the specimen's post-peak curve deviates significantly from the rock's characteristic post-peak curve due to a strong reaction of the platen caused by rock failure. When LSS is greater than the post-peak stiffness of the rock, there is only a very small deviation of the specimen's post-peak curve from the rock's characteristic post-peak curve.

Figure B-4 shows stress–strain curves from two models with the same stiffness ($k = 1.15$ GN/m) but different modeling approaches (or masses). In this figure, the curves resulted from Approach A (in which the loading system mass is larger) is deviated slightly more from the rock's characteristic post-peak curve than the curves resulted from Approach B. The figure implies that even if LSS values are the same, the modeling results are slightly different if the masses of the loading system are different.

Figure B-5 shows the mass of the platen in Approaches A and B. In Approach A, longer platens are used to decrease the LSS; therefore, the mass increases from 0.88 to 14.1 kg when the LSS is decreased from 9.16 to 0.57 GN/m. In Approach B, the volume of the platen is constant at all LSS values; hence, the mass of the platen is constant in all models (m_L = 3.52 kg). As stated by Stavrogin and Tarasov (1995), the dynamic behavior of a specimen in UCS test depends on the mass of the loading system. The influence of LSS on the maximum released unit kinetic energy from the specimen (KE_{max}) is presented in Figure B-6. According to Figure B-6, in both approaches when the specimen is loaded in a soft loading system the released kinetic energy from the specimen is larger than that from the specimen loaded in a stiff loading system. However, for a given LSS value more kinetic energy is released when the mass of the loading system is larger. For example when LSS is equal to 0.57 GN/m, KE_{max} values are 10.6 and 8.3 kJ/m^3 from modeling Approaches A and B, respectively.

Figure B-7 shows the relations between LSS and the maximum velocity at the time of failure, at the platen end which is in contact with the specimen. According to Figure B-7, when the specimen is loaded in a soft loading system, V_{max} is larger than that from the specimen loaded in a stiff loading system in both approaches. However, for a given LSS value, V_{max} is larger when the mass of the loading system is larger. For example, when LSS is equal to 0.57 GN/m, V_{max} values are 2.03 and 1.73 m/s from the modeling Approaches A and B, respectively. The numerical results imply that the mass of the loading system can influence the dynamic behavior of the rock specimen.
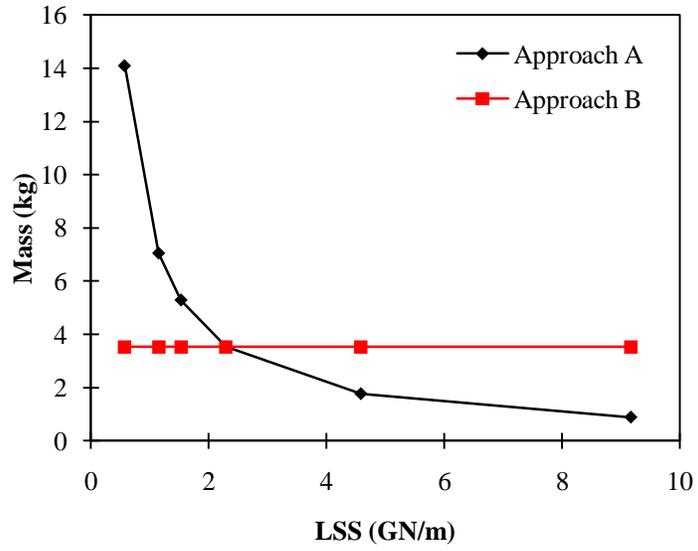
Figure B-5: The loading system mass in two approaches.
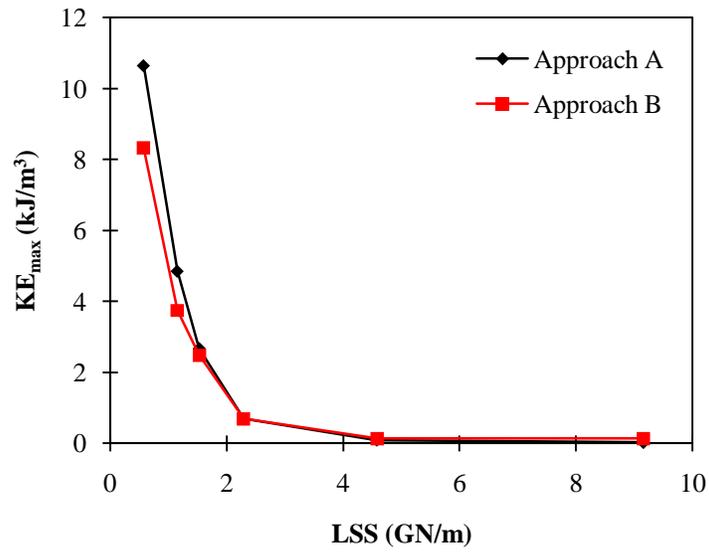
Figure B-6: Calculated *KE*$_{max}$ from two approaches.
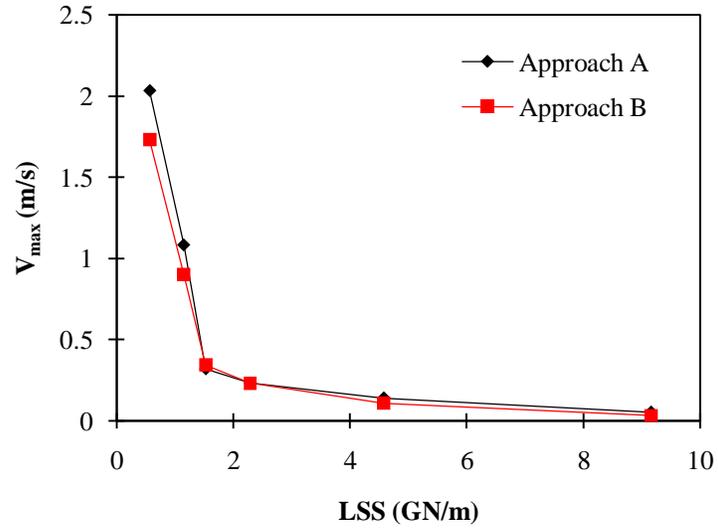
Figure B-7: Relations between LSS and the maximum velocity at the time of failure, at the platen end which is in contact with the specimen.

Appendix C: Input files for simulation of laboratory tests (*.inp)

In this appendix, the input files (*.inp) for the implementation of the numerical simulations explained in Chapter 3 are presented. The following input files (C.1 – C.3) are used to simulate UCS test with platen, Brazilian test, and polyaxial test, respectively.

C.1 UCS test

```
*Heading
 *Node
 *Element, type=C3D8R
 *Nset, nset=ASSEMBLY_SPECIMEN-1_BOTTOM
 *Nset, nset=ASSEMBLY_SPECIMEN-1_TOP
 *Nset, nset=ASSEMBLY_SPECIMEN-1__PICKEDSET5
 *Elset, elset=ASSEMBLY_SPECIMEN-1_BOTTOM
 *Elset, elset=ASSEMBLY_SPECIMEN-1_TOP
 *Elset, elset=ASSEMBLY_SPECIMEN-1__PICKEDSET5
 *Node
 *Element, type=C3D8R
 *Nset, nset=ASSEMBLY_PLATEN-2_PLATEN
 *Nset, nset=ASSEMBLY_PLATEN-2__PICKEDSET2
 *Elset, elset=ASSEMBLY_PLATEN-2_PLATEN
 *Elset, elset=ASSEMBLY_PLATEN-2__PICKEDSET2
 *Nset, nset=ASSEMBLY_SAMPLE
 *Nset, nset=ASSEMBLY__PICKEDSET118
 *Nset, nset=ASSEMBLY__PICKEDSET142
 *Nset, nset=ASSEMBLY__PICKEDSET143
 *Nset, nset=ASSEMBLY__PICKEDSET158
 *Nset, nset=ASSEMBLY__PICKEDSET165
 *Nset, nset=ASSEMBLY__PICKEDSET66
 *Elset, elset=ASSEMBLY_SAMPLE
 *Elset, elset=ASSEMBLY__PICKEDSET158
 *Elset, elset=ASSEMBLY__PICKEDSET165
 *Elset, elset=ASSEMBLY__PICKEDSET66
 *Elset, elset=ASSEMBLY___PICKEDSURF121_S1
 *Elset, elset=ASSEMBLY___PICKEDSURF124_S1
```

```
*Elset, elset=ASSEMBLY___PICKEDSURF156_S2
*surface, type=ELEMENT, name=ASSEMBLY__PICKEDSURF121
*surface, type=ELEMENT, name=ASSEMBLY__PICKEDSURF124
*surface, type=ELEMENT, name=ASSEMBLY__PICKEDSURF156
*surface, type=ELEMENT, name=ASSEMBLY__PICKEDSURF121
*surface, type=ELEMENT, name=ASSEMBLY__PICKEDSURF124
*surface, type=ELEMENT, name=ASSEMBLY__PICKEDSURF156
*material, name=ROCK
*density
*elastic
*mohrcoulomb
*mohrcoulombhardening
*tensioncutoff
*material, name=STEEL
*density
*elastic
*surfaceinteraction, name=FRICTION
*friction
*surfaceinteraction, name=INTPROP-1
*friction
*solidsection, elset=ASSEMBLY_SPECIMEN-1__PICKEDSET5, controls=EC-1,
material=ROCK
*solidsection, elset=ASSEMBLY_PLATEN-2__PICKEDSET2, material=STEEL
*sectioncontrols, name=EC-1, kinematicsplit=ORTHOGONAL
*solidsection, elset=ASSEMBLY_SPECIMEN-1__PICKEDSET5, controls=EC-1,
material=ROCK
*solidsection, elset=ASSEMBLY_PLATEN-2__PICKEDSET2, material=STEEL
*solidsection, elset=ASSEMBLY_SPECIMEN-1__PICKEDSET5, controls=EC-1,
material=ROCK
*solidsection, elset=ASSEMBLY_PLATEN-2__PICKEDSET2, material=STEEL
*friction
*friction
*elementoutput, elset=ASSEMBLY_SAMPLE, variable=PRESELECT
*integratedoutput, elset=ASSEMBLY_SAMPLE, variable=PRESELECT
*amplitude, name=CM-0O03SEC, definition=SMOOTHSTEP
*output, field, variable=PRESELECT, numberinterval=100
*output, history
*Step, name=Loading
*Step, name=Loading
*dynamic, explicit
*boundary
*boundary, amplitude=CM-0O03SEC
*output, field, variable=PRESELECT, numberinterval=100
```

```
*output, history
*elementoutput, elset=ASSEMBLY_SAMPLE, variable=PRESELECT
*integratedoutput, elset=ASSEMBLY_SAMPLE, variable=PRESELECT
*energyoutput, elset=ASSEMBLY_SAMPLE, variable=PRESELECT
*incrementationoutput, variable=PRESELECT
*endstep
*surface, type=ELEMENT, name=ASSEMBLY__PICKEDSURF121
*surface, type=ELEMENT, name=ASSEMBLY__PICKEDSURF124
*surface, type=ELEMENT, name=ASSEMBLY__PICKEDSURF156
*surfaceinteraction, name=FRICTION
*friction
*surfacebehavior, pressure-overclosure=HARD
*surfaceinteraction, name=INTPROP-1
*friction
*surfacebehavior, pressure-overclosure=HARD
*boundary
*Step, name=Loading
*dynamic, explicit
*boundary
*boundary, amplitude=CM-0O03SEC
*contactpair, interaction=INTPROP-1, mechanicalconstraint=KINEMATIC,
cpset=NODISK
*output, field, variable=PRESELECT, numberinterval=100
*output, history
*nodeoutput, nset=ASSEMBLY_SAMPLE, variable=PRESELECT
*endstep
```

C.2 Brazilian test

```
*Heading
*Node
*Element, type=C3D8R
*Nset, nset=ASSEMBLY_SPECIMEN-1_BOTTOM
*Nset, nset=ASSEMBLY_SPECIMEN-1_TOP
*Nset, nset=ASSEMBLY_SPECIMEN-1__PICKEDSET2
*Elset, elset=ASSEMBLY_SPECIMEN-1_BOTTOM
*Elset, elset=ASSEMBLY_SPECIMEN-1_TOP
*Elset, elset=ASSEMBLY_SPECIMEN-1__PICKEDSET2
*Node
*Element, type=C3D8R
*Nset, nset=ASSEMBLY_LODINGPART-1__PICKEDSET2
*Elset, elset=ASSEMBLY_LODINGPART-1__PICKEDSET2
```

```
*Node
*Element, type=C3D8R
*Nset, nset=ASSEMBLY_LODINGPART-2__PICKEDSET2
*Elset, elset=ASSEMBLY_LODINGPART-2__PICKEDSET2
*Nset, nset=ASSEMBLY__PICKEDSET30
*Nset, nset=ASSEMBLY__PICKEDSET31
*Nset, nset=ASSEMBLY__PICKEDSET35
*Elset, elset=ASSEMBLY__PICKEDSET30
*Elset, elset=ASSEMBLY__PICKEDSET31
*Elset, elset=ASSEMBLY__PICKEDSET35
*Elset, elset=ASSEMBLY___PICKEDSURF26_S4
*Elset, elset=ASSEMBLY___PICKEDSURF26_S5
*Elset, elset=ASSEMBLY___PICKEDSURF27_S4
*Elset, elset=ASSEMBLY___PICKEDSURF28_S4
*Elset, elset=ASSEMBLY___PICKEDSURF28_S5
*Elset, elset=ASSEMBLY___PICKEDSURF29_S6
*surface, type=ELEMENT, name=ASSEMBLY__PICKEDSURF26
*surface, type=ELEMENT, name=ASSEMBLY__PICKEDSURF27
*surface, type=ELEMENT, name=ASSEMBLY__PICKEDSURF28
*surface, type=ELEMENT, name=ASSEMBLY__PICKEDSURF29
*surface, type=ELEMENT, name=ASSEMBLY__PICKEDSURF26
*surface, type=ELEMENT, name=ASSEMBLY__PICKEDSURF27
*surface, type=ELEMENT, name=ASSEMBLY__PICKEDSURF28
*surface, type=ELEMENT, name=ASSEMBLY__PICKEDSURF29
*material, name=ROCK
*density
*elastic
*mohrcoulomb
*mohrcoulombhardening
*tensioncutoff
*material, name=STEEL
*density
*elastic
*surfaceinteraction, name=INTPROP-1
*friction
*solidsection, elset=ASSEMBLY_SPECIMEN-1__PICKEDSET2, controls=EC-1,
material=ROCK
*solidsection, elset=ASSEMBLY_LODINGPART-1__PICKEDSET2, controls=EC-1,
material=STEEL
*solidsection, elset=ASSEMBLY_LODINGPART-2__PICKEDSET2, controls=EC-1,
material=STEEL
*sectioncontrols, name=EC-1, kinematicsplit=ORTHOGONAL
```

```
  *solidsection, elset=ASSEMBLY_SPECIMEN-1__PICKEDSET2, controls=EC-1,
material=ROCK
  *solidsection, elset=ASSEMBLY_LODINGPART-1__PICKEDSET2, controls=EC-1,
material=STEEL
  *solidsection, elset=ASSEMBLY_LODINGPART-2__PICKEDSET2, controls=EC-1,
material=STEEL
  *solidsection, elset=ASSEMBLY_SPECIMEN-1__PICKEDSET2, controls=EC-1,
material=ROCK
  *solidsection, elset=ASSEMBLY_LODINGPART-1__PICKEDSET2, controls=EC-1,
material=STEEL
  *solidsection, elset=ASSEMBLY_LODINGPART-2__PICKEDSET2, controls=EC-1,
material=STEEL
  *friction
  *amplitude, name=NOPLATEN, definition=SMOOTHSTEP
  *amplitude, name=CM-0O03SEC, definition=SMOOTHSTEP
  *output, field, variable=PRESELECT, numberinterval=100
  *output, history, variable=PRESELECT
  *Step, name=Loading
  *Step, name=Loading
  *dynamic, explicit
  *boundary, type=VELOCITY
  *output, field, variable=PRESELECT, numberinterval=100
  *output, history, variable=PRESELECT
  *endstep
  *surface, type=ELEMENT, name=ASSEMBLY__PICKEDSURF26
  *surface, type=ELEMENT, name=ASSEMBLY__PICKEDSURF27
  *surface, type=ELEMENT, name=ASSEMBLY__PICKEDSURF28
  *surface, type=ELEMENT, name=ASSEMBLY__PICKEDSURF29
  *surfaceinteraction, name=INTPROP-1
  *friction
  *surfacebehavior, pressure-overclosure=HARD
  *boundary
  *boundary
  *Step, name=Loading
  *dynamic, explicit
  *boundary, type=VELOCITY
  *contactpair, interaction=INTPROP-1, mechanicalconstraint=KINEMATIC,
cpset=DOWN
  *contactpair, interaction=INTPROP-1, mechanicalconstraint=KINEMATIC,
cpset=UP
  *output, field, variable=PRESELECT, numberinterval=100
  *output, history, variable=PRESELECT
  *endstep
```

C.3   Polyaxial test

```
*Heading
*Node
*Element, type=C3D8R
*Nset, nset=ASSEMBLY_SAMPLE-1__PICKEDSET2
*Elset, elset=ASSEMBLY_SAMPLE-1__PICKEDSET2
*Node
*Element, type=C3D8R
*Nset, nset=ASSEMBLY_PLATEN-DIR1-1__PICKEDSET2
*Elset, elset=ASSEMBLY_PLATEN-DIR1-1__PICKEDSET2
*Node
*Element, type=C3D8R
*Nset, nset=ASSEMBLY_PLATEN-DIR1-2__PICKEDSET2
*Elset, elset=ASSEMBLY_PLATEN-DIR1-2__PICKEDSET2
*Node
*Element, type=C3D8R
*Nset, nset=ASSEMBLY_PLATEN-DIR3-1__PICKEDSET7
*Elset, elset=ASSEMBLY_PLATEN-DIR3-1__PICKEDSET7
*Node
*Element, type=C3D8R
*Nset, nset=ASSEMBLY_PLATEN-DIR3-2__PICKEDSET7
*Elset, elset=ASSEMBLY_PLATEN-DIR3-2__PICKEDSET7
*Node
*Element, type=C3D8R
*Nset, nset=ASSEMBLY_PLATEN-DIR2-1__PICKEDSET10
*Elset, elset=ASSEMBLY_PLATEN-DIR2-1__PICKEDSET10
*Node
*Element, type=C3D8R
*Nset, nset=ASSEMBLY_PLATEN-DIR2-2__PICKEDSET10
*Elset, elset=ASSEMBLY_PLATEN-DIR2-2__PICKEDSET10
*Nset, nset=ASSEMBLY_PLATEN
*Nset, nset=ASSEMBLY_SAMPLE
*Nset, nset=ASSEMBLY_TOP
*Nset, nset=ASSEMBLY_VELOCITY
*Nset, nset=ASSEMBLY__PICKEDSET205
*Nset, nset=ASSEMBLY__PICKEDSET257
*Nset, nset=ASSEMBLY__PICKEDSET258
*Nset, nset=ASSEMBLY__PICKEDSET262
*Nset, nset=ASSEMBLY__PICKEDSET266
*Nset, nset=ASSEMBLY__PICKEDSET267
*Nset, nset=ASSEMBLY__PICKEDSET57
```

```
*Nset, nset=ASSEMBLY__PICKEDSET58
*Nset, nset=ASSEMBLY__PICKEDSET76
*Nset, nset=ASSEMBLY__PICKEDSET78
*Elset, elset=ASSEMBLY_PLATEN
*Elset, elset=ASSEMBLY_SAMPLE
*Elset, elset=ASSEMBLY_TOP
*Elset, elset=ASSEMBLY_VELOCITY
*Elset, elset=ASSEMBLY__PICKEDSET205
*Elset, elset=ASSEMBLY__PICKEDSET257
*Elset, elset=ASSEMBLY__PICKEDSET258
*Elset, elset=ASSEMBLY__PICKEDSET262
*Elset, elset=ASSEMBLY__PICKEDSET266
*Elset, elset=ASSEMBLY__PICKEDSET267
*Elset, elset=ASSEMBLY__PICKEDSET57
*Elset, elset=ASSEMBLY__PICKEDSET58
*Elset, elset=ASSEMBLY__PICKEDSET76
*Elset, elset=ASSEMBLY__PICKEDSET78
*Elset, elset=ASSEMBLY___PICKEDSURF10_S3
*Elset, elset=ASSEMBLY___PICKEDSURF11_S6
*Elset, elset=ASSEMBLY___PICKEDSURF139_S5
*Elset, elset=ASSEMBLY___PICKEDSURF13_S5
*Elset, elset=ASSEMBLY___PICKEDSURF14_S4
*Elset, elset=ASSEMBLY___PICKEDSURF173_S3
*Elset, elset=ASSEMBLY___PICKEDSURF178_S5
*Elset, elset=ASSEMBLY___PICKEDSURF203_S3
*Elset, elset=ASSEMBLY___PICKEDSURF203_S5
*Elset, elset=ASSEMBLY___PICKEDSURF30_S3
*Elset, elset=ASSEMBLY___PICKEDSURF31_S2
*Elset, elset=ASSEMBLY___PICKEDSURF35_S3
*Elset, elset=ASSEMBLY___PICKEDSURF36_S1
*Elset, elset=ASSEMBLY___PICKEDSURF41_S5
*Elset, elset=ASSEMBLY___PICKEDSURF63_S5
*Elset, elset=ASSEMBLY___PICKEDSURF64_S3
*Elset, elset=ASSEMBLY___PICKEDSURF68_S3
*Elset, elset=ASSEMBLY___PICKEDSURF69_S5
*surface, type=ELEMENT, name=ASSEMBLY__PICKEDSURF10
*surface, type=ELEMENT, name=ASSEMBLY__PICKEDSURF11
*surface, type=ELEMENT, name=ASSEMBLY__PICKEDSURF13
*surface, type=ELEMENT, name=ASSEMBLY__PICKEDSURF14
*surface, type=ELEMENT, name=ASSEMBLY__PICKEDSURF30
*surface, type=ELEMENT, name=ASSEMBLY__PICKEDSURF31
*surface, type=ELEMENT, name=ASSEMBLY__PICKEDSURF35
*surface, type=ELEMENT, name=ASSEMBLY__PICKEDSURF36
```

```
*surface, type=ELEMENT, name=ASSEMBLY__PICKEDSURF41
*surface, type=ELEMENT, name=ASSEMBLY__PICKEDSURF63
*surface, type=ELEMENT, name=ASSEMBLY__PICKEDSURF64
*surface, type=ELEMENT, name=ASSEMBLY__PICKEDSURF68
*surface, type=ELEMENT, name=ASSEMBLY__PICKEDSURF69
*surface, type=ELEMENT, name=ASSEMBLY__PICKEDSURF139
*surface, type=ELEMENT, name=ASSEMBLY__PICKEDSURF173
*surface, type=ELEMENT, name=ASSEMBLY__PICKEDSURF178
*surface, type=ELEMENT, name=ASSEMBLY__PICKEDSURF203
*surface, type=ELEMENT, name=ASSEMBLY__PICKEDSURF10
*surface, type=ELEMENT, name=ASSEMBLY__PICKEDSURF11
*surface, type=ELEMENT, name=ASSEMBLY__PICKEDSURF13
*surface, type=ELEMENT, name=ASSEMBLY__PICKEDSURF14
*surface, type=ELEMENT, name=ASSEMBLY__PICKEDSURF30
*surface, type=ELEMENT, name=ASSEMBLY__PICKEDSURF31
*surface, type=ELEMENT, name=ASSEMBLY__PICKEDSURF35
*surface, type=ELEMENT, name=ASSEMBLY__PICKEDSURF36
*surface, type=ELEMENT, name=ASSEMBLY__PICKEDSURF41
*surface, type=ELEMENT, name=ASSEMBLY__PICKEDSURF63
*surface, type=ELEMENT, name=ASSEMBLY__PICKEDSURF64
*surface, type=ELEMENT, name=ASSEMBLY__PICKEDSURF68
*surface, type=ELEMENT, name=ASSEMBLY__PICKEDSURF69
*surface, type=ELEMENT, name=ASSEMBLY__PICKEDSURF139
*surface, type=ELEMENT, name=ASSEMBLY__PICKEDSURF173
*surface, type=ELEMENT, name=ASSEMBLY__PICKEDSURF178
*surface, type=ELEMENT, name=ASSEMBLY__PICKEDSURF203
*material, name=PLATEN-1
*density
*elastic
*material, name=PLATEN-2
*density
*elastic
*material, name=RIGIDPLATE
*density
*elastic
*material, name=ROCK
*density
*elastic
*mohrcoulomb
*mohrcoulombhardening
*tensioncutoff
*surfaceinteraction, name=CONTACT
*friction
```

```
*solidsection, elset=ASSEMBLY_SAMPLE-1__PICKEDSET2, material=ROCK
*solidsection, elset=ASSEMBLY_PLATEN-DIR1-1__PICKEDSET2, material=PLATEN-1
*solidsection, elset=ASSEMBLY_PLATEN-DIR1-2__PICKEDSET2, material=PLATEN-1
*solidsection, elset=ASSEMBLY_PLATEN-DIR3-1__PICKEDSET7, material=PLATEN-2
*solidsection, elset=ASSEMBLY_PLATEN-DIR3-2__PICKEDSET7, material=PLATEN-2
*solidsection, elset=ASSEMBLY_PLATEN-DIR2-1__PICKEDSET10,
material=RIGIDPLATE
*solidsection, elset=ASSEMBLY_PLATEN-DIR2-2__PICKEDSET10,
material=RIGIDPLATE
*solidsection, elset=ASSEMBLY_SAMPLE-1__PICKEDSET2, material=ROCK
*solidsection, elset=ASSEMBLY_PLATEN-DIR1-1__PICKEDSET2, material=PLATEN-1
*solidsection, elset=ASSEMBLY_PLATEN-DIR1-2__PICKEDSET2, material=PLATEN-1
*solidsection, elset=ASSEMBLY_PLATEN-DIR3-1__PICKEDSET7, material=PLATEN-2
*solidsection, elset=ASSEMBLY_PLATEN-DIR3-2__PICKEDSET7, material=PLATEN-2
*solidsection, elset=ASSEMBLY_PLATEN-DIR2-1__PICKEDSET10,
material=RIGIDPLATE
*solidsection, elset=ASSEMBLY_PLATEN-DIR2-2__PICKEDSET10,
material=RIGIDPLATE
*solidsection, elset=ASSEMBLY_SAMPLE-1__PICKEDSET2, material=ROCK
*solidsection, elset=ASSEMBLY_PLATEN-DIR1-1__PICKEDSET2, material=PLATEN-1
*solidsection, elset=ASSEMBLY_PLATEN-DIR1-2__PICKEDSET2, material=PLATEN-1
*solidsection, elset=ASSEMBLY_PLATEN-DIR3-1__PICKEDSET7, material=PLATEN-2
*solidsection, elset=ASSEMBLY_PLATEN-DIR3-2__PICKEDSET7, material=PLATEN-2
*solidsection, elset=ASSEMBLY_PLATEN-DIR2-1__PICKEDSET10,
material=RIGIDPLATE
*solidsection, elset=ASSEMBLY_PLATEN-DIR2-2__PICKEDSET10,
material=RIGIDPLATE
*friction
*elementoutput, elset=ASSEMBLY_SAMPLE, variable=PRESELECT
*elementoutput, elset=ASSEMBLY_SAMPLE, variable=PRESELECT
*integratedoutput, elset=ASSEMBLY_SAMPLE, variable=PRESELECT
*integratedoutput, elset=ASSEMBLY_SAMPLE, variable=PRESELECT
*amplitude, name=FRONTPLATENREMOVAL
*amplitude, name=LOADS, definition=SMOOTHSTEP
*amplitude, name=TOPLOAD, definition=SMOOTHSTEP
*output, field, variable=PRESELECT
*output, history
*output, history
*output, field, variable=PRESELECT, numberinterval=100
*output, history
*output, history
*Step, name=Loading
*Step, name=Unloading
```

```
*Step, name=Loading
*dynamic, explicit
*dsload, amplitude=LOADS
*dsload, amplitude=LOADS
*dsload, amplitude=LOADS
*output, field, variable=PRESELECT
*output, history
*energyoutput
*energyoutput, elset=ASSEMBLY_PLATEN
*output, history
*elementoutput, elset=ASSEMBLY_SAMPLE, variable=PRESELECT
*integratedoutput, elset=ASSEMBLY_SAMPLE, variable=PRESELECT
*energyoutput, elset=ASSEMBLY_SAMPLE, variable=PRESELECT
*incrementationoutput, variable=PRESELECT
*endstep
*Step, name=Unloading
*dynamic, explicit
*boundary
*boundary, amplitude=FRONTPLATENREMOVAL
*boundary, amplitude=TOPLOAD
*dsload, op=NEW
*dsload, op=NEW
*dsload, op=NEW
*output, field, variable=PRESELECT, numberinterval=100
*output, history
*energyoutput
*energyoutput, elset=ASSEMBLY_PLATEN
*output, history
*elementoutput, elset=ASSEMBLY_SAMPLE, variable=PRESELECT
*integratedoutput, elset=ASSEMBLY_SAMPLE, variable=PRESELECT
*energyoutput, elset=ASSEMBLY_SAMPLE, variable=PRESELECT
*incrementationoutput, variable=PRESELECT
*endstep
*surface, type=ELEMENT, name=ASSEMBLY__PICKEDSURF10
*surface, type=ELEMENT, name=ASSEMBLY__PICKEDSURF11
*surface, type=ELEMENT, name=ASSEMBLY__PICKEDSURF13
*surface, type=ELEMENT, name=ASSEMBLY__PICKEDSURF14
*surface, type=ELEMENT, name=ASSEMBLY__PICKEDSURF30
*surface, type=ELEMENT, name=ASSEMBLY__PICKEDSURF31
*surface, type=ELEMENT, name=ASSEMBLY__PICKEDSURF35
*surface, type=ELEMENT, name=ASSEMBLY__PICKEDSURF36
*surface, type=ELEMENT, name=ASSEMBLY__PICKEDSURF41
*surface, type=ELEMENT, name=ASSEMBLY__PICKEDSURF63
```

```
*surface, type=ELEMENT, name=ASSEMBLY__PICKEDSURF64
*surface, type=ELEMENT, name=ASSEMBLY__PICKEDSURF68
*surface, type=ELEMENT, name=ASSEMBLY__PICKEDSURF69
*surface, type=ELEMENT, name=ASSEMBLY__PICKEDSURF139
*surface, type=ELEMENT, name=ASSEMBLY__PICKEDSURF173
*surface, type=ELEMENT, name=ASSEMBLY__PICKEDSURF178
*surfaceinteraction, name=CONTACT
*friction
*surfacebehavior, pressure-overclosure=HARD
*boundary
*boundary
*Step, name=Loading
*dynamic, explicit
*contactpair, interaction=CONTACT, mechanicalconstraint=KINEMATIC,
cpset=DIR-1-BOTTOM
*contactpair, interaction=CONTACT, mechanicalconstraint=KINEMATIC,
cpset=DIR-1-TOP
*contactpair, interaction=CONTACT, mechanicalconstraint=KINEMATIC,
cpset=DIR2-NEGATIVE
*contactpair, interaction=CONTACT, mechanicalconstraint=KINEMATIC,
cpset=DIR2-POSITIVE
*contactpair, interaction=CONTACT, mechanicalconstraint=KINEMATIC,
cpset=DIR3-NEGATIVE
*contactpair, interaction=CONTACT, mechanicalconstraint=KINEMATIC,
cpset=DIR3-POSITIVE
*output, field, variable=PRESELECT
*output, history
*output, history
*nodeoutput, nset=ASSEMBLY_SAMPLE, variable=PRESELECT
*endstep
*Step, name=Unloading
*dynamic, explicit
*boundary
*boundary, amplitude=FRONTPLATENREMOVAL
*boundary, amplitude=TOPLOAD
*output, field, variable=PRESELECT, numberinterval=100
*output, history
*output, history
*nodeoutput, nset=ASSEMBLY_SAMPLE, variable=PRESELECT
*endstep
```

Appendix D: Python scripts for simulation using heterogeneous models (*.py)

In this appendix, the developed Python scripts (*.py) used for numerical simulations in Chapters 4 to 6 are presented. The following Python scripts (D.1 – D.3) are used to simulate heterogeneous UCS test without platen (Chapter 4), change the model geometry for parametric study (Chapter 5), and change contact properties at different steps (Chapters 5 and 6).

D.1   UCS test

```python
from abaqus import *
from abaqusConstants import *
from odbAccess import *
import visualization
from miscUtils import *
from part import *
from material import *
from section import *
from assembly import *
from step import *
from interaction import *
from load import *
from mesh import *
from job import *
from sketch import *
from visualization import *
from connectorBehavior import *
#from RandomArray import *
from random import *

import __main__
backwardCompatibility.setValues(includeDeprecated=ON)

# -------------------------------------------------------
def create_model():
    import section
```

```python
import regionToolset
import displayGroupMdbToolset as dgm
import part
import material
import assembly
import step
import interaction
import load
import mesh
import job
import sketch
import visualization
import xyPlot
import displayGroupOdbToolset as dgo
import connectorBehavior
s = mdb.models['Model-1'].ConstrainedSketch(name='__profile__',
    sheetSize=200.0)
g, v, d, c = s.geometry, s.vertices, s.dimensions, s.constraints
s.setPrimaryObject(option=STANDALONE)

# ---------------------------------------------------------------------
#                         Drawing part geometry
# ---------------------------------------------------------------------
s.rectangle(point1=(0.0, 0.0), point2=(sp_width, sp_height))
p = mdb.models['Model-1'].Part(name='specimen',
    dimensionality=TWO_D_PLANAR, type=DEFORMABLE_BODY)
p = mdb.models['Model-1'].parts['specimen']
p.BaseShell(sketch=s)
s.unsetPrimaryObject()
p = mdb.models['Model-1'].parts['specimen']
session.viewports['Viewport: 1'].setValues(displayedObject=p)
del mdb.models['Model-1'].sketches['__profile__']

# ---------------------------------------------------------------------
#    Define mesh size at different locations of geometry & generate mesh
# ---------------------------------------------------------------------
mdb.models['Model-1'].rootAssembly.DatumCsysByDefault(CARTESIAN)
mdb.models['Model-1'].rootAssembly.Instance(dependent=OFF,
name='specimen-1',
    part=mdb.models['Model-1'].parts['specimen'])
mdb.models['Model-1'].rootAssembly.setElementType(elemTypes=(ElemType(
    elemCode=CPE4R, elemLibrary=EXPLICIT, secondOrderAccuracy=OFF,
    hourglassControl=DEFAULT, distortionControl=DEFAULT), ElemType(
```

```
        elemCode=CPE3, elemLibrary=EXPLICIT)), regions=(
        mdb.models['Model-1'].rootAssembly.instances['specimen-
1'].faces.getSequenceFromMask(
        ('[#1 ]', ), ), ))
    mdb.models['Model-1'].rootAssembly.setMeshControls(algorithm=MEDIAL_AXIS,
        regions=
        mdb.models['Model-1'].rootAssembly.instances['specimen-
1'].faces.getSequenceFromMask(
        ('[#1 ]', ), ))
    mdb.models['Model-1'].rootAssembly.seedPartInstance(deviationFactor=0.1,
        regions=(mdb.models['Model-1'].rootAssembly.instances['specimen-1'],
), size=
        MeshSize)
    mdb.models['Model-1'].rootAssembly.generateMesh(regions=(
        mdb.models['Model-1'].rootAssembly.instances['specimen-1'], ))
# ----------------------------------------------------
def heterogeneity():
    import section
    import regionToolset
    import displayGroupMdbToolset as dgm
    import part
    import material
    import assembly
    import step
    import interaction
    import load
    import mesh
    import job
    import sketch
    import visualization
    import xyPlot
    import displayGroupOdbToolset as dgo
    import connectorBehavior

    a = mdb.models['Model-1']

### Finding the number of elements ###
    modelName =
session.sessionState[session.currentViewportName]['modelName']
    assy = mdb.models[modelName].rootAssembly
    nElems= len (assy.instances['specimen-1'].elements)

    if ( nElems % nHet ==0) :
```

```
        m = (nElems/nHet)
    else :
        m = (nElems/nHet + 1)

    z = range (0, m)

# Generate input file with (nElems/nHet) material definitions
    j=0
    for ys in z:
        j=j+1
        E_rand = normalvariate(E_mu, E_mu*E_std)
        alpha = E_rand/E_mu
        nu = normalvariate(1, std)
        beta_phi = std_angular/E_std
        beta_c = std/E_std
        gama_phi = beta_phi*(alpha-1)*phi_mu+phi_mu
        gama_c = beta_c * (alpha-1)+1
        myMat=a.Material('Material_'+str(j))
        myMat.Density(table=((density, ), ))
        myMat.Elastic(table=((E_rand, poisson),))
        myMat.MohrCoulombPlasticity(table=((gama_phi, gama_phi), ),
useTensionCutoff=True)
        myMat.mohrCoulombPlasticity.MohrCoulombHardening(
            table=((gama_c * cPeak_mu, 0.0),(gama_c * cResidual, gama_c *
C_PE)))
        myMat.mohrCoulombPlasticity.TensionCutOff(
            dependencies=0, table=((alpha*tPeak_mu, 0.0), (alpha*tResidual,
alpha*t_PE), ), temperatureDependency=OFF)


# Create nElems/nHet sections with nHet random element members & unique
material property
    a = mdb.models['Model-1']
    for i in xrange(0,m):
        a.HomogeneousSolidSection(name='section_'+str(i+1),
            material='Material_'+str(i+1),thickness=t)

    a = mdb.models['Model-1'].rootAssembly
    a.PartFromInstanceMesh(name='meshpart',
        partInstances=(a.instances['specimen-1'],))

# Generate a list of nElems integers (1 to nElems) representing element
number
```

```python
        ele_list = range(1,(nElems+1))
        shuffle(ele_list)


# Generate nElems/nHet sets with nHet elements each
        p = mdb.models['Model-1'].parts['meshpart']
        for i in xrange(0,(nElems/nHet)):
            ele_set=ele_list[(i*nHet):(i*nHet+nHet)]
            p.SetFromElementLabels(name='myeleset'+str(i+1),
                elementLabels=ele_set)
        ele_set=ele_list[(nElems//nHet) * nHet:(nElems)]
        p.SetFromElementLabels(name='myeleset'+str(i+2),
            elementLabels=ele_set)


        for i in xrange(0,m):
            myRegion= p.sets['myeleset'+str(i+1)]
            p.SectionAssignment(region=myRegion,
                sectionName='section_'+str(i+1), offset=0.0)
# ----------------------------------------------------------------------------
#                                 Direct Loading
# ----------------------------------------------------------------------------
def DirectLoading():
    import section
    import regionToolset
    import displayGroupMdbToolset as dgm
    import part
    import material
    import assembly
    import step
    import interaction
    import load
    import mesh
    import job
    import sketch
    import visualization
    import xyPlot
    import displayGroupOdbToolset as dgo
    import connectorBehavior

    a = mdb.models['Model-1'].rootAssembly
    session.viewports['Viewport: 1'].setValues(displayedObject=a)
    a.DatumCsysByDefault(CARTESIAN)
    p = mdb.models['Model-1'].parts['meshpart']
```

```python
    a.Instance(name='meshpart-1', part=p, dependent=OFF)

    del a.features['specimen-1']

    session.viewports['Viewport: 1'].assemblyDisplay.setValues(loads=ON,
bcs=ON,
        predefinedFields=ON, connectors=ON)
    session.viewports['Viewport:
1'].assemblyDisplay.setValues(step='Initial')

    n1 = a.instances['meshpart-1'].nodes
    bot_corner_node=[]
    bot_edge_nodes=[]
    top_edge_nodes=[]
    for n in n1:
        if (n.coordinates[0]==0) and (n.coordinates[1]==0):
            bot_corner_node.append(n.label)
        else:
            if (n.coordinates[1]==0):
                bot_edge_nodes.append(n.label)
            if (n.coordinates[1]==sp_height):
                top_edge_nodes.append(n.label)

    bn=mdb.models['Model-
1'].rootAssembly.SetFromNodeLabels(name='bottomNodes',
        nodeLabels=(('meshpart-1',bot_edge_nodes),))
    tn=mdb.models['Model-1'].rootAssembly.SetFromNodeLabels(name='topNodes',
        nodeLabels=(('meshpart-1',top_edge_nodes),))
    cn=mdb.models['Model-
1'].rootAssembly.SetFromNodeLabels(name='cornerNode',
        nodeLabels=(('meshpart-1',bot_corner_node),))

    region = regionToolset.Region(nodes=cn.nodes)
    mdb.models['Model-1'].DisplacementBC(name='fix-xy',
createStepName='Initial',
        region=region, u1=UNSET, u2=SET, ur3=SET, amplitude=UNSET,
        distributionType=UNIFORM, localCsys=None)

    region = regionToolset.Region(nodes=bn.nodes)
    mdb.models['Model-1'].DisplacementBC(name='Bottom',
createStepName='Initial',
        region=region, u1=UNSET, u2=SET, ur3=SET, amplitude=UNSET,
```

```
        distributionType=UNIFORM, localCsys=None)

    mdb.models['Model-1'].ExplicitDynamicsStep(name='Loading',
previous='Initial', timePeriod=3.0)
    mdb.models['Model-1'].fieldOutputRequests['F-Output-
1'].setValues(numIntervals=100)

    mdb.models['Model-1'].SmoothStepAmplitude(data=((0.0, 0.0), (2, 1.0)),
name=
        'Load', timeSpan=STEP)
    region = regionToolset.Region(nodes=tn.nodes)
    mdb.models['Model-1'].VelocityBC(name='TopLoad',
createStepName='Loading',
        region=region, v1=UNSET, v2=-0.03, vr3=UNSET, amplitude='Load',
        fieldName='', distributionType=UNIFORM, localCsys=None)
# -----------------------------------------------------------------------
#                           Model Parameters
# -----------------------------------------------------------------------
t =                      #Plane strain thickness
nHet =                   #Number of element in each pool
sp_width =               #Specimen width
sp_height =              #Specimen height
MeshSize =               #Mesh size
density =                #Density
E_mu =                   #Young's Modulus
poisson =                #Poisson's Ratio
cPeak_mu =               #Peak cohesion
cResidual =              #Residual cohesion
C_PE=                    #Cohesion plastic strain
tPeak_mu =               #Peak tension cut-off
tResidual =              #Residual tension cut-off
t_PE =                   #Tension cut-off plastic strain
phi_mu =                 #Friction angle
psi_mu =                 #Dilation angle
std =                    #Standard deviation for E, c and t
std_angular =            #Standard deviation for phi and psi
E_std =
myPath=''    #path for storage of files
# -----------------------------------------------------------------------
# Call routine to create model & obtain solution
# -----------------------------------------------------------------------
create_model()
heterogeneity()
```

```
DirectLoading()
#IndirectLoading ()
#mdb.saveAs(pathName=myPath+'heterogeneous.cae')
print 'Good job Amin! Program completed successfully.'
```

D.2   Changing the tunnel geometry for parametric study

```
from abaqus import *
from abaqusConstants import *
from odbAccess import *
import visualization
from miscUtils import *
from part import *
from material import *
from section import *
from assembly import *
from step import *
from interaction import *
from load import *
from mesh import *
from job import *
from sketch import *
from visualization import *
from connectorBehavior import *
#from RandomArray import *
from random import *
from math import *

import __main__
backwardCompatibility.setValues(includeDeprecated=ON)


def geometry():
    import section
    import regionToolset
    import displayGroupMdbToolset as dgm
    import part
    import material
    import assembly
    import step
    import interaction
    import load
    import mesh
```

```
    import job
    import sketch
    import visualization
    import xyPlot
    import displayGroupOdbToolset as dgo
    import connectorBehavior
    import math


### =======================================================================
###                              Geometry
### =======================================================================
    A_x = - dd * cos (Theta)
    A_y = dd * sin (Theta)

    B_x = A_x - L * cos (Theta)
    B_y = A_y + L * sin (Theta)

    C_x = B_x + sin (Theta)
    C_y = B_y + cos (Theta)



    D_x = A_x + sin (Theta)
    D_y = A_y + cos (Theta)

    E_x = (A_x + D_x) / 2
    E_y = (A_y + D_y) / 2

    F_x = (B_x + C_x) / 2
    F_y = (B_y + C_y) / 2


    ### Host_Rock
    mdb.models['Model-1'].ConstrainedSketch(name='__profile__',
sheetSize=500.0)
    mdb.models['Model-1'].sketches['__profile__'].rectangle(point1=(-
Model_Size, - Model_Size), point2=(Model_Size, Model_Size))

    mdb.models['Model-1'].Part(dimensionality=TWO_D_PLANAR, name='HostRock',
type=
        DEFORMABLE_BODY)
    mdb.models['Model-1'].parts['HostRock'].BaseShell(sketch=
        mdb.models['Model-1'].sketches['__profile__'])
    del mdb.models['Model-1'].sketches['__profile__']
```

```
    mdb.models['Model-1'].ConstrainedSketch(gridSpacing=1.41,
name='__profile__',
        sheetSize=56.56)
    mdb.models['Model-
1'].parts['HostRock'].projectReferencesOntoSketch(filter=
        COPLANAR_EDGES, sketch=mdb.models['Model-1'].sketches['__profile__'])
    mdb.models['Model-
1'].sketches['__profile__'].CircleByCenterPerimeter(center=(
    0, 0), point1=(0, TunRad))
    mdb.models['Model-1'].parts['HostRock'].Cut(sketch=
        mdb.models['Model-1'].sketches['__profile__'])
    del mdb.models['Model-1'].sketches['__profile__']


    mdb.models['Model-1'].ConstrainedSketch(gridSpacing=1.41,
name='__profile__',
        sheetSize=56.56)
    mdb.models['Model-
1'].parts['HostRock'].projectReferencesOntoSketch(filter=
        COPLANAR_EDGES, sketch=mdb.models['Model-1'].sketches['__profile__'])
    mdb.models['Model-1'].sketches['__profile__'].Line(point1=(A_x, A_y),
point2=(
        B_x, B_y))
    mdb.models['Model-1'].sketches['__profile__'].Line(point1=(B_x, B_y),
point2=
        (C_x, C_y))
    mdb.models['Model-1'].sketches['__profile__'].Line(point1=(C_x, C_y),
point2=
        (D_x, D_y))
    mdb.models['Model-1'].sketches['__profile__'].Line(point1=(D_x, D_y),
        point2=(A_x, A_y))
    mdb.models['Model-1'].parts['HostRock'].Cut(sketch=
        mdb.models['Model-1'].sketches['__profile__'])
    del mdb.models['Model-1'].sketches['__profile__']

### Tunnel
    mdb.models['Model-1'].ConstrainedSketch(name='__profile__',
sheetSize=200.0)
    mdb.models['Model-
1'].sketches['__profile__'].CircleByCenterPerimeter(center=(
```

```
    0, 0), point1=(0, TunRad))

    mdb.models['Model-1'].Part(dimensionality=TWO_D_PLANAR, name='Tunnel',
type=
        DEFORMABLE_BODY)
    mdb.models['Model-1'].parts['Tunnel'].BaseShell(sketch=
        mdb.models['Model-1'].sketches['__profile__'])
    del mdb.models['Model-1'].sketches['__profile__']


### Joint
    mdb.models['Model-1'].ConstrainedSketch(name='__profile__',
sheetSize=200.0)
    mdb.models['Model-1'].sketches['__profile__'].Line(point1=(A_x, A_y),
point2=(
        B_x, B_y))
    mdb.models['Model-1'].sketches['__profile__'].Line(point1=(B_x, B_y),
point2=
        (C_x, C_y))
    mdb.models['Model-1'].sketches['__profile__'].Line(point1=(C_x, C_y),
point2=
        (D_x, D_y))
    mdb.models['Model-1'].sketches['__profile__'].Line(point1=(D_x, D_y),
        point2=(A_x, A_y))

    mdb.models['Model-1'].Part(dimensionality=TWO_D_PLANAR, name='Joint',
type=
        DEFORMABLE_BODY)
    mdb.models['Model-1'].parts['Joint'].BaseShell(sketch=
        mdb.models['Model-1'].sketches['__profile__'])
    del mdb.models['Model-1'].sketches['__profile__']




    mdb.models['Model-1'].ConstrainedSketch(gridSpacing=1.41,
name='__profile__',
        sheetSize=56.56)
    mdb.models['Model-
1'].parts['HostRock'].projectReferencesOntoSketch(filter=
        COPLANAR_EDGES, sketch=mdb.models['Model-1'].sketches['__profile__'])
    mdb.models['Model-
1'].sketches['__profile__'].CircleByCenterPerimeter(center=(
    0, 0), point1=(0, TunRad))
    mdb.models['Model-1'].parts['HostRock'].Cut(sketch=
```

```
        mdb.models['Model-1'].sketches['__profile__'])
    del mdb.models['Model-1'].sketches['__profile__']


### Patition
    mdb.models['Model-1'].ConstrainedSketch(gridSpacing=500,
name='__profile__',
        sheetSize=141.42, transform=
        mdb.models['Model-1'].parts['Joint'].MakeSketchTransform(
        sketchPlane=mdb.models['Model-1'].parts['Joint'].faces[0],
        sketchPlaneSide=SIDE1, sketchOrientation=RIGHT, origin=((E_x + F_x) /
2, (E_y + F_y) / 2, 0.0)))
    mdb.models['Model-1'].parts['Joint'].projectReferencesOntoSketch(filter=
        COPLANAR_EDGES, sketch=mdb.models['Model-1'].sketches['__profile__'])
    mdb.models['Model-1'].sketches['__profile__'].rectangle(point1=( -(E_x +
F_x) / 2- 2 * TunRad, -(E_y + F_y) / 2 - 2 * TunRad), point2=(-(E_x + F_x) /
2+ 2 * TunRad,  -(E_y + F_y) / 2 + 2 * TunRad))
    mdb.models['Model-1'].parts['Joint'].PartitionFaceBySketch(faces=
        mdb.models['Model-1'].parts['Joint'].faces.getSequenceFromMask(('[#1
]',
        ), ), sketch=mdb.models['Model-1'].sketches['__profile__'])
    del mdb.models['Model-1'].sketches['__profile__']
### ========================================================================
###                      Define basic Model parameters
### ========================================================================
TunRad =
Model_Size = 15 * TunRad
d = 0.5 * TunRad
dd = TunRad + d
Theta =  1 * pi / 4
s =  Model_Size - (dd * cos (Theta))
L = 12 * TunRad
### ========================================================================
###           Call routine to create model & obtain solution
### ========================================================================
geometry()
```

D.3   Changing contact properties at different steps

```
from abaqus import *
from abaqusConstants import *
from odbAccess import *
import visualization
from miscUtils import *
```

```
from part import *
from material import *
from section import *
from assembly import *
from step import *
from interaction import *
from load import *
from mesh import *
from job import *
from sketch import *
from visualization import *
from connectorBehavior import *
#from RandomArray import *
from random import *
from math import *

import __main__
backwardCompatibility.setValues(includeDeprecated=ON)


def step():
    import section
    import regionToolset
    import displayGroupMdbToolset as dgm
    import part
    import material
    import assembly
    import step
    import interaction
    import load
    import mesh
    import job
    import sketch
    import visualization
    import xyPlot
    import displayGroupOdbToolset as dgo
    import connectorBehavior
    import math

### ========================================================================
### STEP
### ========================================================================
```

```
    mdb.models['Model-1'].ExplicitDynamicsStep(name='Loading',
previous='Initial', timePeriod= LoadingTime)
    mdb.models['Model-1'].ExplicitDynamicsStep(name='Step_1',
previous='Loading', timePeriod= StepTime)
    mdb.models['Model-1'].ExplicitDynamicsStep(name='Step_2',
previous='Step_1', timePeriod= StepTime)
    mdb.models['Model-1'].ExplicitDynamicsStep(name='Step_3',
previous='Step_2', timePeriod= StepTime)
    mdb.models['Model-1'].ExplicitDynamicsStep(name='Step_4',
previous='Step_3', timePeriod= StepTime)
    mdb.models['Model-1'].ExplicitDynamicsStep(name='Step_5',
previous='Step_4', timePeriod= StepTime)
    mdb.models['Model-1'].ExplicitDynamicsStep(name='Step_6',
previous='Step_5', timePeriod= StepTime)
    mdb.models['Model-1'].ExplicitDynamicsStep(name='Step_7',
previous='Step_6', timePeriod= StepTime)
    mdb.models['Model-1'].ExplicitDynamicsStep(name='Step_8',
previous='Step_7', timePeriod= StepTime)
    mdb.models['Model-1'].ExplicitDynamicsStep(name='Step_9',
previous='Step_8', timePeriod= StepTime)
    mdb.models['Model-1'].ExplicitDynamicsStep(name='Step_10',
previous='Step_9', timePeriod= StepTime)


    mdb.models['Model-1'].fieldOutputRequests['F-Output-
1'].setValues(numIntervals=20, variables=(
    'S', 'SVAVG', 'PE', 'PEVAVG', 'PEEQ', 'PEEQVAVG', 'PEEQT', 'LE', 'U',
'V',
    'A', 'RF', 'CSTRESS', 'EVF'))

    mdb.models['Model-1'].SmoothStepAmplitude(data=((0.0, 0.0), (1,
LoadingTime)), name=
        'Load', timeSpan=STEP)


    mdb.models['Model-1'].ContactProperty('Joint')
    mdb.models['Model-1'].interactionProperties['Joint'].TangentialBehavior(
        dependencies=0, directionality=ISOTROPIC, elasticSlipStiffness=None,
        formulation=PENALTY, fraction=0.005, maximumElasticSlip=FRACTION,
        pressureDependency=OFF, shearStressLimit=None,
slipRateDependency=OFF,
        table=((MyFriction, ), ), temperatureDependency=OFF)
    mdb.models['Model-1'].interactionProperties['Joint'].NormalBehavior(
```

```
    allowSeparation=ON, constraintEnforcementMethod=DEFAULT,
    pressureOverclosure=HARD)


mdb.models['Model-1'].ContactProperty('Tunnel')
mdb.models['Model-1'].interactionProperties['Tunnel'].NormalBehavior(
    allowSeparation=OFF, constraintEnforcementMethod=DEFAULT,
    pressureOverclosure=HARD)

mdb.models['Model-1'].ContactProperty('Step-1')
mdb.models['Model-1'].interactionProperties['Step-1'].NormalBehavior(
    constraintEnforcementMethod=DEFAULT, contactStiffness=10e9,
    pressureOverclosure=LINEAR)

mdb.models['Model-1'].ContactProperty('Step-2')
mdb.models['Model-1'].interactionProperties['Step-2'].NormalBehavior(
    constraintEnforcementMethod=DEFAULT, contactStiffness=7.5e9,
    pressureOverclosure=LINEAR)

mdb.models['Model-1'].ContactProperty('Step-3')
mdb.models['Model-1'].interactionProperties['Step-3'].NormalBehavior(
    constraintEnforcementMethod=DEFAULT, contactStiffness=5e9,
    pressureOverclosure=LINEAR)

mdb.models['Model-1'].ContactProperty('Step-4')
mdb.models['Model-1'].interactionProperties['Step-4'].NormalBehavior(
    constraintEnforcementMethod=DEFAULT, contactStiffness=2.5e9,
    pressureOverclosure=LINEAR)

mdb.models['Model-1'].ContactProperty('Step-5')
mdb.models['Model-1'].interactionProperties['Step-5'].NormalBehavior(
    constraintEnforcementMethod=DEFAULT, contactStiffness=1e9,
    pressureOverclosure=LINEAR)

mdb.models['Model-1'].ContactProperty('Step-6')
mdb.models['Model-1'].interactionProperties['Step-6'].NormalBehavior(
    constraintEnforcementMethod=DEFAULT, contactStiffness=0.75e9,
    pressureOverclosure=LINEAR)

mdb.models['Model-1'].ContactProperty('Step-7')
mdb.models['Model-1'].interactionProperties['Step-7'].NormalBehavior(
    constraintEnforcementMethod=DEFAULT, contactStiffness=0.5e9,
    pressureOverclosure=LINEAR)
```

```
    mdb.models['Model-1'].ContactProperty('Step-8')
    mdb.models['Model-1'].interactionProperties['Step-8'].NormalBehavior(
        constraintEnforcementMethod=DEFAULT, contactStiffness=0.25e9,
        pressureOverclosure=LINEAR)

    mdb.models['Model-1'].ContactProperty('Step-9')
    mdb.models['Model-1'].interactionProperties['Step-9'].NormalBehavior(
        constraintEnforcementMethod=DEFAULT, contactStiffness=0.1e9,
        pressureOverclosure=LINEAR)

    mdb.models['Model-1'].ContactProperty('Step-10')
    mdb.models['Model-1'].interactionProperties['Step-10'].NormalBehavior(
        constraintEnforcementMethod=DEFAULT, contactStiffness=1e1,
        pressureOverclosure=LINEAR)
### =======================================================================
### Define basic Model parameters
### =======================================================================
# Step Control
LoadingTime = 1
StepTime = 0.1
MyFriction = 0.6
### =======================================================================
### Call routine to create model & obtain solution
### =======================================================================
step()
```

Curriculum Vitae

Name:	Amin Manouchehrian

Post-secondary Education and Degrees:

Yazd University
Yazd, Iran
2004 - 2008 B.Sc.

Sahand University of Technology
Tabriz, Iran
2008 - 2010 M.Sc.

Laurentian University
Sudbury, Ontario, Canada
2013 - 2016 Ph.D.

Related Work Experience:

Research Assistant
Yazd University
2011 - 2012

Research Assistant
MIRARCO-Mining Innovation
Laurentian University
2013 - 2016

Publications Based on PhD Thesis:

Manouchehrian, A., Cai, M., 2016. Numerical modeling of rockburst in deep tunnels, Rock Mechanics and Rock Engineering, submitted.

Manouchehrian, A., Cai, M., 2016. Influence of material heterogeneity on failure intensity in unstable rock failure. Computers and Geotechnics **71**: 237-246.

Manouchehrian, A., Cai, M., 2016. Simulation of unstable rock failure under unloading conditions, Canadian Geotechnical Journal **53**: 22-34.

Manouchehrian, A., Cai, M., 2016. Influence of weak planes on rockburst occurrence. Paper-110. 3rd International Symposium on Mine Safety Science and Engineering, Montreal, Canada.

Cai, M., **Manouchehrian, A.**, 2015. Numerical analysis of released energy during unstable rock failure under true-triaxial unloading condition. Paper-179, 13th International ISRM Congress, Montreal, Canada.

Other Publications: **Manouchehrian, A.**, Gholamnejad, J., Sharifzadeh, M., 2014. Development of a model for analysis of the slope stability for circular mode failure using genetic algorithm, Environmental Earth Sciences **71**(3): 1267-1277.

Manouchehrian, A., Sharifzadeh, M., Fatehi Marji, M., Gholamnejad, J., 2014. A bonded particle model for analysis of flaw orientation effect on crack propagation mechanism in rocks under compression, Archives of Civil and Mechanical Engineering **14**(1): 40-52.

Manouchehrian, A., Sharifzadeh, M., Hamidzadeh, R., Nouri, T., 2013. Selection of regression models for predicting strength and deformability properties of rocks using GA, International Journal of Mining Science and Technology, **23**(4): 495-501.

Manouchehrian, A., Fatehi Marji, M., 2012. Numerical analysis of confinement effect on crack propagation mechanism of a flaw in a pre-cracked rock under compression, Acta Mechanica Sinica, **28**(5): 1389-1397.

Manouchehrian, A., Sharifzadeh, M., Hamidzadeh, R., 2012. Application of artificial neural networks and multivariate statistics to estimate UCS using textural characteristics, International Journal of Mining Science and Technology **22**(2): 229-236.

Manouchehrian, A., Fatehi Marji, M., Mohebbi, M., 2012. Comparison of indirect boundary element and finite element methods. A case study: Shiraz-Esfahan railway tunnel in Iran, Frontiers of Structural and Civil Engineering, **6**(4): 385-392.

Fatehi Marji, M., **Manouchehrian, A.,** 2012. Numerical prediction of crack path in pre-cracked rocks under uniaxial compression using a bonded particle model. 19th European Conference on Fracture, Kazan, Russia.

Manouchehrian, A., Sharifzadeh, M., Hamidzadeh, R., 2011. Estimation of UCS of rock from its textural characteristics using artificial neural networks, IAMG 2011, Salzburg, Austria

Fatehi Marji, M., **Manouchehrian, A.,** 2010. The effect of horizontal to vertical stress ratio (K) on displacement and stress concentration around underground excavations by using BEM, EUROCK 2010, Lausanne, Switzerland